DISPERSION OF EXPIRATORY AIRBORNE DROPLETS IN A MODEL SINGLE PATIENT HOSPITAL RECOVERY ROOM WITH STRATIFIED VENTILATION

by

Amir Abbas Aliabadi

B.A.Sc., The University of Toronto, 2006
M.A.Sc., The University of Toronto, 2008

A THESIS SUBMITTED IN PARTIAL FULFILLMENT OF
THE REQUIREMENTS FOR THE DEGREE OF

DOCTOR OF PHILOSOPHY

in

The Faculty of Graduate Studies

(Mechanical Engineering)

THE UNIVERSITY OF BRITISH COLUMBIA

(Vancouver)

January 2013

Abstract

Concerns about the environment, energy costs, and airborne infection risk have revived interest in ventilation systems for health care facilities. Low energy ventilation systems (e.g. stratified air ventilation) have received attention as a means of providing a better air quality at a lower energy cost. The sensitivity of such ventilation systems to boundary conditions in removing airborne contaminants produced by expiratory injections is of concern and studied experimentally and numerically in this work.

A three step methodology is adopted. First, an air-assist internally mixing atomizer is developed to generate a poly-disperse distribution of droplets for ventilation testing. A series of near-field experiments reveal droplet size, velocity, and diffusivity in radial and axial directions for steady and transient atomization. Second, the atomizer is used to inject droplets into a mock-up of a patient recovery room with an underfloor air distribution ventilation system. A series of far-field size-resolved concentration measurements are conducted at locations representative of an occupant (receptor). Third, Computational Fluid Dynamics (CFD) simulations are used to predict airborne droplet exposure among various cases in the far-field experiments. Both tracer gas and discrete phase approaches are implemented.

Based on the findings we recommend guidelines for ventilation design and room usage in real single patient hospital recovery rooms with stratified ventilation systems. It is desired to have expiratory injections at low momentum, preferably directed towards the walls or upwards. It is also advisable that occupant suspects spend most of their time away from the injection source, possibly at the corner of the room or behind the source. The variations in occupant thermal plume is not likely to affect exposure to airborne droplets in statistically significant ways. It is advisable to used air change rates greater than four since expiratory injections are likely to break down the vertical contaminant stratification. It is likely that dispersion rates be higher for sub micrometer droplets but lower for larger droplets. This has implications for ventilation design strategy as a function of pathogen or pathogen carrying droplet size.

Preface

Chapter 1 in part (section 1.1) and chapter 3 provide a thorough review of methods for ventilation design in consideration of preventing airborne infection risk. A holistic approach has been adopted, considering interconnections between fluid mechanics and epidemiology that describe airborne infection in a process originating from a source (infector) an ending in a receptor (infected). A version of these sections is published with Dr. S. N. Rogak, Dr. S. I. Green, and Dr. K. H. Bartlett [4]. A. Deylami has assisted with literature review in epidemiological studies of aerosol infection for this study.

Chapter 2 reviews the literature in near-field atomization process for steady and transient sprays. The review focuses on dispersion and velocity of droplets in sprays as a function of time and droplet size. A version of this chapter is published with K. W. J. Lim, Dr. S. N. Rogak, and Dr. S. I. Green [2].

Chapters 4 and 6 study in part (sections 4.1 and 6.1) the near-field experimental process of generating and dispersing contagious aerosols. These aerosols are produced by pseudo expiratory actions and later interact with the background ventilation to reach a potential receptor. A transient spray is used for which the droplet size, penetration, and velocity is characterized. A version of these sections are published with K. W. J. Lim, Dr. S. N. Rogak, and Dr. S. I. Green [2]. Dr. S. Kamal supported this study by providing guidance in setting up the Laser imaging system, and E. Faghani assisted with the pressure testing of the spray. A. Slade assisted with the early experimental setup in this study.

Chapters 4 and 6 also study in part (sections 4.2 and 6.2) the far-field experimental process for dispersion of aerosols in an underfloor air distribution ventilation system. Various room boundary conditions (air change rate, geometry, placement and strength of thermal plumes, direction of expiratory injection) and initial conditions (momentum and time duration of expiratory injection) are implemented. The measurement of aerosol mass concentration at the receptor site was a direct indicator for airborne infection risk. A version of these sections are published with Dr. S. N. Rogak,

and Dr. S. I. Green [5]. G. Smith provided air distribution equipment, at no charge, to support these experiments. A. C. Fabry, K. Asperin, and M. O'Brien assisted with the experimental effort in this study.

Chapters 5 and 7 study the far-field process for dispersion of aerosols in the same ventilation system numerically. ANSYS FLUENT 12.1 is used for Computational Fluid Dynamics (CFD) simulations. This study replicates the experiments and its results are later compared with the experimental restuls. A version of these chapters are published with Dr. S. N. Rogak, Dr. S. I. Green, and Dr. K. H. Bartlett [5, 6]. B. Thomas, B. Roehrl, and M. O'Brien assisted with mesh generation effort in this study.

Note, the terms 'particle', 'droplet', and 'aerosol' may be used interchangeably throughout the thesis. All these terms may refer to suspensions of liquid water, oral fluid, or oral fluid surrogate in air potentially carrying pathogens or non-volatile compounds in human oral fluid.

Table of Contents

Abstract ii

Preface iii

Table of Contents v

List of Tables x

List of Figures xii

List of Symbols xv

List of Abbreviations xx

Acknowledgements xxii

Dedication xxiii

1 Introduction 1
- 1.1 Predicting airborne infection risk: from source to receptor . 4
  - 1.1.1 Generation of aerosols 4
  - 1.1.2 Dispersion, heat and mass transfer 10
  - 1.1.3 Viability and infectivity 13
  - 1.1.4 Inhalation and deposition 18
  - 1.1.5 Summary: infection risk models 19
- 1.2 Mathematical framework and scaling analysis 23
  - 1.2.1 Continuum phase mass, momentum, and energy transport processes 24
  - 1.2.2 Discrete phase motion 27
  - 1.2.3 Scaling analysis for conservation and particle motion equations 28
- 1.3 Objectives and research plan 29

2 Review of Dispersion Mechanisms in Injections (Near-field) 33
2.1 Droplet dispersion in steady air-assist atomizers 33
2.2 Droplet dispersion in transient air-assist atomizers 38
2.3 Concluding remarks 38

3 Review of Building Ventilation Design Parameters on Infection Risk (Far-field) 40
3.1 Categories of ventilation systems 40
3.2 Ventilation performance indices 44
3.2.1 Temperature and relative humidity 44
3.2.2 Air changes per hour 45
3.2.3 Ventilation effectiveness 47
3.3 Parameters affecting ventilation performance 48
3.3.1 Ventilation type 48
3.3.2 Diffuser type 50
3.3.3 Contaminant type and injection 51
3.3.4 Heat gains and losses 53
3.3.5 Occupancy 53
3.3.6 Room geometry 54
3.4 Engineered disinfection of air 56
3.4.1 Filtration 56
3.4.2 Ultra violet radiation 56
3.5 Concluding remarks 57

4 Experimental Methodology 58
4.1 Near-field atomizer test methodology 58
4.1.1 Atomizer setup 58
4.1.2 Spray penetration test setup 61
4.1.3 Spray shadowgraphy test setup 64
4.1.4 Spray particle tracking velocimetry test setup 67
4.1.5 Valve actuation and rise time 69
4.1.6 Statistical analysis 71
4.1.7 Droplet size range for analysis 71
4.2 Far-field ventilation test methodology 71
4.2.1 Temperature measurement 72
4.2.2 Velocity measurement 76
4.2.3 Aerosol measurement 76
4.2.4 Thermal manikins 80
4.2.5 Room air change rate measurement 84
4.2.6 Oral fluid surrogate 84

4.2.7 Injection air temperature . . . 87
4.2.8 Parametric study . . . 87
4.2.9 Space-resolved ventilation tests . . . 94
4.2.10 Ventilation test protocol . . . 94
4.2.11 Performance indices . . . 94
4.2.12 Statistical analysis . . . 97

5 Numerical Methodology . . . 98
5.1 Modeling . . . 98
5.1.1 Turbulence: renormalization group $k-\epsilon$ . . . 98
5.1.2 Multicomponent mixture properties . . . 98
5.1.3 Discrete phase heat and mass transfer processes . . . 100
5.1.4 Discrete phase motion . . . 102
5.1.5 Coupling between the discrete and continuous phases 104
5.2 Boundary and initial conditions . . . 105
5.2.1 Injection . . . 105
5.2.2 Diffuser . . . 107
5.2.3 Initial conditions . . . 107
5.2.4 Exhaust . . . 108
5.2.5 Envelope . . . 108
5.3 Solution methods . . . 110
5.3.1 Coupled continuous and discrete phase calculations . 110
5.3.2 Pressure discretization . . . 110
5.3.3 Continuous phase solver . . . 111
5.3.4 Discrete phase solver . . . 112
5.4 Numerical errors . . . 112
5.5 Space and time discretization quality . . . 113
5.5.1 Time discretization . . . 113
5.5.2 Space discretization . . . 116
5.5.3 Time and space discretization error estimation . . . 120

6 Experimental Results and Discussion . . . 124
6.1 Near-field atomizer test results . . . 124
6.1.1 Spray penetration . . . 124
6.1.2 Sauter mean diameter, droplet size, and concentration distributions for steady spray . . . 127
6.1.3 Sauter mean diameter and concentration distribution for transient spray . . . 128
6.1.4 Droplet size distribution for transient spray . . . 128
6.1.5 Steady spray deceleration . . . 132

6.1.6 Velocity distribution for steady spray 132
6.1.7 Péclet number for steady spray 133
6.1.8 Velocity distribution for transient spray 135
6.2 Far-field ventilation test results 138
6.2.1 Reference case (1) 138
6.2.2 Parametric study 141
6.2.3 Space-resolved study 147

7 Numerical Results and Discussion 151
7.1 Far-field solution convergence 151
7.1.1 Reference case (1) 151
7.2 Far-field parametric study 156
7.2.1 Tracer gas model 156
7.2.2 Discrete phase model 156
7.3 Far-field space-resolved study 160
7.3.1 Tracer gas model 162
7.3.2 Discrete phase model 162
7.4 Limitations of eddy-viscosity turbulence models in ventilation space with injections 164

8 Conclusions and Recommendations 167
8.1 Conclusions 167
8.1.1 Near-field study 168
8.1.2 Far-field study 170
8.1.3 Adequacy of eddy-viscosity turbulence models for ventilation studies with injections 171
8.2 Recommendations 172

9 Future Work 174
9.1 Strengths and weaknesses of this thesis 174
9.2 Droplet dispersion experiments for air-assist internally mixing atomizers 174
9.3 Experiments to measure a wider droplet size range in ventilation flow 175
9.4 Empirical experiments with actual expiratory actions 175
9.5 Effect of ventilation type on transport of expiratory injected droplets 176
9.6 Effect of occupancy on aerosol transport 176
9.7 Prediction of airflow and contaminant distribution 176

Bibliography 178

Appendices 189
Appendix A: Far-field Tests Standard Operating Procedure (SOP) 189
Appendix B: MATLAB image processing algorithm 192
Appendix C: Room boundary and internal temperatures over 24 hours 193
Appendix D: Room boundary and internal conditions for reference case (1) 195
Appendix E: Further information 197

List of Tables

1.1 Experimental expiratory droplet size data 8
1.2 Summary of turbulence modeling approaches 12
1.3 Summary of most probable target molecules 15
1.4 Summary of the effect of temperature and relative humidity on airborne pathogen viability and infectivity [22, 23, 48] . . 15
1.5 Summary of advantages and disadvantages of different viability models 18
1.6 Dimensionless unknowns in the continuum phase conservation equations 27
1.7 Reference values for scaling analysis 28
1.8 Scaling analysis for non-dimensional terms in conservation and particle motion equations 29

2.1 Stokes numbers in spray droplet dispersion 37

3.1 Summary of advantages and disadvantages of different types of ventilation systems for hospitals 42
3.2 Functional spaces in health care facilities 46
3.3 Supply diffuser types 50

4.1 Flow conditions for the spray tests 61
4.2 Summary of shadowgraphy and particle tracking velocimetry parameters 66
4.3 Metabolic rate and manikin temperature 83
4.4 Log-linear rule for circular ducts 86
4.5 Oral fluid composition 86
4.6 Parametric study for the ventilation experiments 89
4.7 Object locations in the ventilation test setup 90
4.8 Atomizer flow conditions for the far-field ventilation test . . . 93

5.1 Surface temperature boundary conditions 109

5.2 Mesh generation parameters for coarse, mid and fine meshes in the ventilation simulation 116
5.3 Required length scale for wall control volumes in ventilation simulations according to the 'law of the wall' turbulent boundary layer theory 120

6.1 Summary of self-preserving properties for round turbulent starting jets and transient sprays 126

7.1 Comparison among experiments, tracer gas, and DPM in parametric study 162

List of Figures

1.1 Airborne infection process and influential environmental/ engineering controls . . . 3
1.2 Research plan . . . 30

4.1 Fluid mixing schematic (with permission of Spraying Systems Co.) . . . 59
4.2 Nozzle assembly . . . 60
4.3 Schematic for spray penetration test system . . . 62
4.4 Schematic for spray shadowgraphy/PTV test system . . . 63
4.5 Number size distribution for 6 μm diameter calibration microspheres measured by the shadowgraphy technique . . . 67
4.6 Sample droplet image and shadowgraphed droplet size . . . 68
4.7 Pressure rise time at a distance of 1 cm in front of the nozzle due to valve actuation . . . 70
4.8 Swirl diffuser . . . 72
4.9 Ventilation test room . . . 73
4.10 Schematic for ventilation test room . . . 74
4.11 Thermocouple calibration device . . . 75
4.12 Calibration curve for thermocouple number 1 . . . 76
4.13 Thermoelectric anemometer . . . 77
4.14 Aerodynamic particle sizer and sampling manifold . . . 78
4.15 APS aerosol sampling collection efficiency . . . 79
4.16 Vertical thermal manikin . . . 81
4.17 Horizontal thermal manikin . . . 82
4.18 Exhaust flow measurement setup for ventilation tests . . . 85
4.19 Diagram of ventilation test cases for winter experiments . . . 91
4.20 Atomizer orientation for the reference case (1) in the ventilation tests . . . 92
4.21 Diagram of ventilation test cases for winter experiments . . . 95

5.1 Injection volume fraction for experiment and CFD model . . . 106
5.2 Modeling swirl diffuser flow pattern . . . 107

5.3 Complete mesh for the reference case (1) in ventilation simulations . . . 117
5.4 Nozzle face mesh for the reference case in ventilation simulations 118
5.5 Diffuser face mesh for the reference case in ventilation simulations . . . 118
5.6 Exhaust face mesh for the reference case in ventilation simulations . . . 119

6.1 Spray at $t = 24\ ms$ for Test 1 showing raw and filtered binary images . . . 125
6.2 Dimensionless axial penetration versus dimensionless time and dimensionless radial penetration versus axial penetration . . . 126
6.3 Total radial concentration of droplets and d_{32} . . . 127
6.4 Schematic for leading and trailing edges of the transient spray 129
6.5 d_{32} and normalized concentration in the leading and trailing edges of the spray . . . 130
6.6 Volume size distribution on central axis in the leading and trailing edges of the spray . . . 131
6.7 Steady spray deceleration . . . 133
6.8 Axial velocity, normalized axial velocity, axial fluctuating velocity, and radial fluctuating velocity . . . 134
6.9 Turbulent Stokes number and Kolmogorov Stokes number . . . 135
6.10 Average Péclet number . . . 136
6.11 Axial velocity, axial fluctuating velocity, and radial fluctuating velocity for leading and trailing edges of the spray . . . 137
6.12 Background concentrations . . . 139
6.13 Experimental concentrations for the reference case (1) . . . 140
6.14 Experimental normalized concentrations for the reference case (1) . . . 142
6.15 Experimental normalized cumulative concentration fraction near injection and measurement points . . . 143
6.16 Short and long time measured (Exp.) relative exposure at all zones for parametric study . . . 144
6.17 Short and long time measured (Exp.) relative exposure at all zones for parametric study . . . 146
6.18 Short and long time measured (Exp.) relative exposure at all zones for space-resolved study . . . 148
6.19 Short and long time measured (Exp.) relative exposure at all zones for space-resolved study . . . 150

7.1 Velocity vectors and contours computed by CFD 5 s after injection for reference case (1) in parametric study 153
7.2 Velocity vectors and contours computed by CFD 600 s after injection for reference case (1) in parametric study 154
7.3 Droplet dispersion 120 s after injection simulated by CFD for the parametric study reference case 155
7.4 Modeled normalized concentrations for the reference case (1) 157
7.5 Modeled (top) and experimental (bottom) normalized cumulative concentration fraction near injection and measurement points 158
7.6 Short and long time measured (Exp.) and predicted (CFD DPM and tracer gas) relative exposure at all zones for parametric study 159
7.7 Short and long time predicted (CFD DPM) relative exposure for parametric study 161
7.8 Short and long time measured (Exp.) and predicted (CFD DPM and tracer gas) relative exposure for space-resolved study 163
7.9 Short and long time predicted (CFD DPM) relative exposure for space-resolved study 165

9.1 Room boundary temperature over 24 hours 193
9.2 Room internal temperature over 24 hours 194
9.3 Reference case (1) boundary temperatures 195
9.4 Reference case (1) internal temperatures 196
9.5 Reference case (1) internal air speed in the room 196
9.6 Reference case (1) room air changes per hour 197

List of Symbols

Alphabetical Symbols

A_g: Nozzle gas exit area
A_l: Nozzle liquid exit area
A_p: Aerosol/ particle/ droplet surface area
B: Spray self-similarity constant
C: Semi empirical coefficient for $k - \epsilon$ turbulence models, number of infection cases, constant, concentration
C_r: Jet radial dispersion self-preserving constant
$C(t)$: Real time volume concentration
$\overrightarrow{C(T)}$: Cumulative volume concentration
$\overrightarrow{C(T)}_{ref}$: Reference cumulative volume concentration
$\hat{C}(T)$: Normalized cumulative volume concentration (relative exposure)
C_x: Jet axial dispersion self-preserving constant, contaminant concentration under complete mixing conditions
C_s: Vapor concentration at aerosol/ particle/ droplet surface
C_∞: vapor concentration in the bulk gas
C_L: Aerosol/ particle/ droplet Lagrangian time scale coefficient
D_m: Mass diffusion coefficient
D_t: Effective mass diffusion coefficient in turbulent flow
D_T: Thermal diffusion coefficient
Dr: Aerosol/ particle/ droplet coefficient of drag
E: Discretization error
$E(x, T)$: Pathogen exposure at location x and time T
Ec: Eckert number
F: Flux integral
$\overrightarrow{F}$: Acceleration per unit mass
F_D: Drag acceleration per unit velocity
F_s: Grid convergence index factor of safety
Fr: Aerosol/ particle/ droplet Froude number
Gr: Grashof number
I: Number of infectors

J: Mass diffusion flux
L: Characteristic flow length, length scale
L_e: Eddy length scale
L_{ref}: Reference length scale
M_w: Molecular weight
N: Number of measurements, intake dose, molar flux of vapor, number of mesh elements
N_f: Number fraction
Nu: Nusselt number
P: Pressure, P value for statistical analysis
P^*: Non-dimensional pressure
P_I: Probability of infection
P_s: Actual pressure
P'_s: Hydrostatic pressure
P_{sat}: Saturated vapor pressure
$P(Z)$: Frequency distribution of the tolerance dose
Pe_L: Lagrangian Péclet number
Pr: Prandtl number
Q: Room ventilation rate, volumetric flow
R: Universal gas constant
R^2: Coefficient of determination
Re: Reynolds number
Re_g: Gas Reynolds number
Re_l: Liquid Reynolds number
Sc: Schmidt number
Sc_t: Effective Schmidt number in turbulent flow
Sh_{AB}: Sherwood number
St_k: Kolmogorov Stokes number
St_m: Mean Stokes number
St_t: Turbulent Stokes number
T: Local temperature, aerosol/ particle/ droplet integral time scale
T_{bp}: Boiling point
T_L: Flow Lagrangian integral time
T_p: Aerosol/ particle/ droplet temperature
T_{ref}: Reference temperature
T_{vap}: Vaporization temperature
T_∞: Far-field temperature
U: Axial aerosol/ particle/ droplet velocity
U_c: Axial aerosol/ particle/ droplet velocity in the center of spray
U_g: Nozzle gas exit velocity

U_l: Nozzle liquid exit velocity
U_r: Relative velocity between liquid and gas
U_{ref}: Reference velocity
V: Velocity, room volume, volume
V_0: Viability at time zero
V_f: Volume fraction
V_{ref}: Reference volume
V_t: Viability at time t
We_g: Aerodynamic Weber number
X: Local bulk mole fraction of species
Y: Species mass fraction
Z: Normalized tolerance dose
c: Pathogen concentration in the respiratory fluid
c_p: Aerosol/ particle/ droplet specific heat capacity, specific heat capacity
d: Aerosol/ particle/ droplet diameter
d_{10}: Number mean diameter
d_{32}: Volume to surface area ratio or Sauter Mean Diameter (SMD)
d_g: Nozzle gas exit diameter
d_l: Nozzle liquid exit diameter
d_p: Aerosol/ particle/ droplet diameter
ds: Aerosol/ particle/ droplet path
f: Numerical solution
$f(t)$: Viability function of the virus or bacteria in the aerosols
$f_{v,0}$: Volatile fraction of droplet
g: Gravitational acceleration
h: Convective heat transfer coefficient, mesh spacing
h_{fg}: Latent heat of vaporization
j: Size bin number
k: Turbulent kinetic energy, viability decay constant, thermal conductivity
k_c: Mass transfer coefficient
$\dot{m}_g$: Gas mass flow rate
$\dot{m}_l$: Liquid mass flow rate
m_p: Aerosol/ particle/ droplet mass
$m_{p,0}$: Aerosol/ particle/ droplet initial mass before evaporation
n: Continuous phase jet or spray axial dispersion self-preserving constant
p: Pulmonary ventilation rate, order of convergence
p_g: Nozzle gas exit momentum
p_l: Nozzle liquid exit momentum
q: Quanta generation rate
r: Radial distance from nozzle, infectivity of pathogens, mesh refinement

ratio
t: Time, t statistic
t^*: Non-dimensional time
t_d: Imaging time delay
t_f: Time delay to reach maximum liquid/gas flow
t_0: Time delay
t^*: Non-dimensional time
u: Uncertainty, fluid horizontal component of velocity, boundary layer tangential velocity
$\overline{u}$: Time averaged horizontal component of velocity
$\overrightarrow{u}$: Continuum phase velocity
$\overrightarrow{u^*}$: Non-dimensional continuum phase velocity
u^*: Non-dimensional velocity in horizontal coordinate
u^+: Boundary layer non-dimensional tangential velocity
u': Fluctuating horizontal component of velocity
$\overrightarrow{u}_p$: Aerosol/ particle/ droplet velocity
$\overrightarrow{u^*}_p$: Non-dimensional aerosol/ particle/ droplet velocity
u'_p: Aerosol/ particle/ droplet fluctuating horizontal velocity
v: Velocity in vertical coordinate
v^*: Non-dimensional velocity in vertical coordinate
v': Fluctuating vertical component of velocity
w^*: Non-dimensional velocity in horizontal coordinate
w': Fluctuating horizontal component of velocity
$v(x,t)$: Volume density of expiratory aerosols/ particles/ droplets at location x and time t
v_t: Terminal aerosol/ particle/ droplet velocity
x: Axial distance from nozzle, random variable, position, horizontal coordinate
x^*: Non-dimensional horizontal coordinate
x_0: Axial distance of virtual origin from nozzle tip
y: Vertical coordinate
y^*: Non-dimensional vertical coordinate
y^+: Boundary layer non-dimensional vertical coordinate
z: Horizontal coordinate
z^*: Non-dimensional horizontal coordinate
$\overline{x}$: Mean value statistic

Greek Symbols

β: Coefficient of thermal expansion, deposition fraction of infectious aerosols/ particles/ droplets in respiratory tract
ϵ: Turbulent dissipation rate, aerosol/ particle/ droplet diffusivity, discretization relative error
η: Aerosol/ particle/ droplet deposition efficiency on sampling tube walls
μ: Statistical mean, gas dynamic viscosity
μ_g: Gas dynamic viscosity
μ_l: Liquid dynamic viscosity
μ_t: Turbulent viscosity
ν: Degrees of freedom, kinematic viscosity
ν_g: Gas kinematic viscosity
ν_l: Liquid kinematic viscosity
ν_t: Turbulent kinematic viscosity
ρ: Continuum phase density
ρ_0: Operating density
ρ_g: Gas density
ρ_l: Liquid density
ρ_o: Outdoor air density
ρ_p: Aerosol/ particle/ droplet density
ρ_{ref}: Reference density
σ: Liquid surface tension, standard deviation
τ: Aerosol/ particle/ droplet relaxation time
τ_{cross}: Aerosol/ particle/ droplet eddy crossing time
τ_d: Aerosol/ particle/ droplet relaxation time
τ_g: Characteristic mean flow time scale
τ_e: Characteristic eddy time scale
τ_k: Characteristic Kolmogorov time scale
τ_w: Bounday layer wall shear

List of Abbreviations

ACH: Air Changes per Hour
ADPI: Air Diffusion Performance Index
AHU: Air Handling Unit
AII: Airborne Infection Isolation
ALR: Air to Liquid Mass Ratio
APS: Aerodynamic Particle Sizer
ASHRAE: American Society of Heating, Refrigerating and Air Conditioning Engineers
ATEM: Analytical Transmission Electron Microscope
CDC: Center for Disease Control
CSA: Canadian Standards Association
GCI: Grid Convergence Index
CEV: Cough Expired Volume
CFD: Computational Fluid Dynamics
CFL: Courant-Friedrich-Lewy
CFU: Colony Forming Unit
CPFR: Cough Peak Flow Rate
DES: Detached Eddy Simulation
DNS: Direct Numerical Simulation
DRW: Discrete Random Walk
HEPA: High Efficiency Particulate Air
HOT: Higher Order Terms
HVAC: Heating Ventilation and Air Conditioning
ID: Infection Dose
IMI: Interferometric Mie Imaging
LDA: Laser Doppler Anemometry
LES: Large Eddy Simulation
LACI: Local Air Change Index
MERV: Minimum Efficiency Reporting Value
NHS: National Health Service
OAF: Open Air Factor
OPC: Optical Particle Counter

PDC: Passive Down-draught Cooling
PE: Protective Environment
PFU: Plaque Forming Unit
PIV: Particle Image Velocimetry
PM: Particulate Matter
PRESTO!: PREssure STaggered Option
PTU: Programmable Timing Unit
PTV: Particle Tracking Velocimetry
PVT: Peak Velocity Time
RANS: Reynolds Averaged Navier-Stokes
RNG: Renormalization Group
RT−PCR: Reverse Transcriptase−Polymerase Chain Reaction
RSM: Reynolds Stress Model
SARS: Severe Acute Respiratory Syndrome
SMD: Sauter Mean Diameter
SMPS: Scanning Mobility Particle Spectrometer
SOP: Standard Operating Procedure
UV: Ultra Violet
WHO: World Health Organization

Acknowledgements

I offer my enduring gratitude to the faculty, staff and my fellow students at the University of British Columbia (UBC), who have inspired me to complete my work in this research. I owe particular thanks to Dr. S. N. Rogak and Dr. S. I. Green, whose scrutinizing questions taught me to question any aspect of this research more deeply. I thank Dr. K. H. Bartlett, Dr. N. Atabaki, Dr. M. Martinez, and Dr. S. Kamal at UBC, Mr. P. Marmion, Mr. J. Ng, and Mr. T. Amlani at Stantec Consulting, and Mr. G. Smith at EH Price for enhancing my visions in science, providing coherent answers to my endless questions, and supporting the experimental setup completion.

I thank my colleagues, M. Salehi, E. Chan, E. Faghani, S. M. Taghavi, A. Shadkam, C. Lin, A. Soewono, H. Arri, K. Alba, and P. Anderson for assisting me with their experience and valuable comments in my research. I also extend my gratitude for so many undergraduate students that assisted me in my work. Specific undergraduate students who collaborated with me are A. C. Fabry, K. Asperin, K. Lim, A. Deylami, A. Slade, M. O'Brien, B. Thomas, and B. Roehrl.

Completing this work would be impossible without the financial support of a few funding organizations. In particular I like to acknowledge the financial support of Natural Sciences and Engineering Council of Canada (NSERC), Institute for Computing, Information, and Cognitive Systems (ICICS), Faculty of Graduate Studies (FoGS), Sustainable Building Science Program (SBSP), and Stantec Consulting.

Special thanks are owed to my parents H. Ansari and F. Aliabadi, who have supported me throughout my years of education, both emotionally and financially. My brother R. Aliabadi has always been a source of inspiration for me in courage, creativity, and hard work. My aunt N. Ansari, uncle M. Tahmasebi, and cousin A. Tahmasebi have provided me the unending family support in Vancouver throughout my years at UBC. The last but not the least to thank is my best friend L. Sadraei who has been a major motivation to finish this work.

To mankind,
For the betterment of society.

Chapter 1

Introduction

The spread of infectious disease is of global concern for social and economic reasons. For example, seasonal influenza kills 200−500 thousand people annually. In 2009−2010, influenza A (H1N1) caused 17000 deaths worldwide, many among whom were healthy adults [101, 106]. In 2002−2003, Severe Acute Respiratory Syndrome (SARS) killed more than 700 people and spread into 37 countries causing a cost of $18 billion in Asia [11, 74, 75, 106]. These recent outbreaks remind us of the potential for a pandemic such as the Spanish flu of 1918−1920 which killed 50−100 million people [11].

Diseases can spread wherever people have direct or indirect contact, but this thesis focuses on infections that occur in health care facilities because they often contain a large proportion of infectious or vulnerable people, and because governments and other health care providers have a clear responsibility to mitigate infections that occur within their walls.

Human−human transmission of disease can result from direct contact with an infected person or an indirect contact through an intermediate object. A direct contact infection could be caused by caregivers not washing hands prior to attending patients [13]. Another common direct contact transmission is due to large infectious aerosols that travel a short distance from the source to the receptor (spray transmission). An important mode of indirect contact is airborne transmission occurring via the spread of fine aerosols and skin flakes in room air over long distances and time scales. Aerosols can be generated and released by human expiratory actions (speech, breathing, coughing, sneezing), skin shedding, or resuspension from surfaces [69].

Aerosol disease transmission is known to be the main route for many diseases such as *Tuberculosis* and *Aspergillosis*. Also, recent research has shown that the importance of aerosol infection is underrated for common diseases such as influenza, especially during cold and dry seasons [100]. For example, modern experimental techniques have detected infectious aerosols produced by infected patients while breathing, coughing, or sneezing [101].

Infection control involves blocking any stage of the infection pathway. For airborne transmission, this implies reducing the generation of pathogens

from an infectious person, using disinfection techniques to kill pathogens released to the air, or simply isolating infectious people in special rooms. Controls generally fall into three categories: administrative, personal protection, and environmental and engineering. Administrative controls aim to keep infectious people away from vulnerable people (infection detection, triage, communication, education) and ensure that technical controls (e.g. engineering and personal protection) are used correctly. For the airborne transmission pathway, personal protection consists of some form of mask or respirator aiming to prevent either the shedding or inhalation of pathogens [11]. Engineering and environmental controls primarily intervene after pathogens leave the breathing zone from one person before they enter the breathing zone of another. An important aspect of engineering and environmental controls is architectural programming. This involves proper design of hospital spaces and careful planning of medical procedures so that all transmission routes for diseases are considered and intervened.

At the simplest level, an engineering control might involve an increase in room ventilation rates. This would normally decrease pathogen concentrations, which would be expected to reduce infections. Nevertheless, it is still possible that increasing ventilation rates result in increased exposure. In any regard, rooms are not well-mixed, people do not breath in all parts of the room, and pathogen infectivity changes with time and environmental conditions. Furthermore, increased ventilation is not free because it normally requires larger and more energy intensive equipment. *How much should ventilation rates be increased? Which type of system is most helpful in reducing airborne infections? What factors in a ventilation system design affect airborne infection risk most significantly?* These questions cannot be answered without considering the entire airborne infection pathway in the first place. A suitable approach is to describe infection pathway using quantitative estimates of infection risk. Such quantitative estimation must include every process during infection from source to receptor.

Figure 1.1 shows the airborne infection pathway and the environmental and engineering controls that may influence the steps along the path. In section 1.1, we review each step of the infection pathway and provide the available models. Our focus is on factors that can influence the relative risks of different ventilation systems. In section 1.2, we lay the mathematical framework and scaling analysis in physics of airborne pathogen dispersion in a ventilation background. This section assists development of appropriate analytical, experimental, and numerical methodologies to guide ventilation design for airborne infection risk reduction. Subsequently, section 1.3 lays out the specific objectives of this research and a plan to fulfill them.

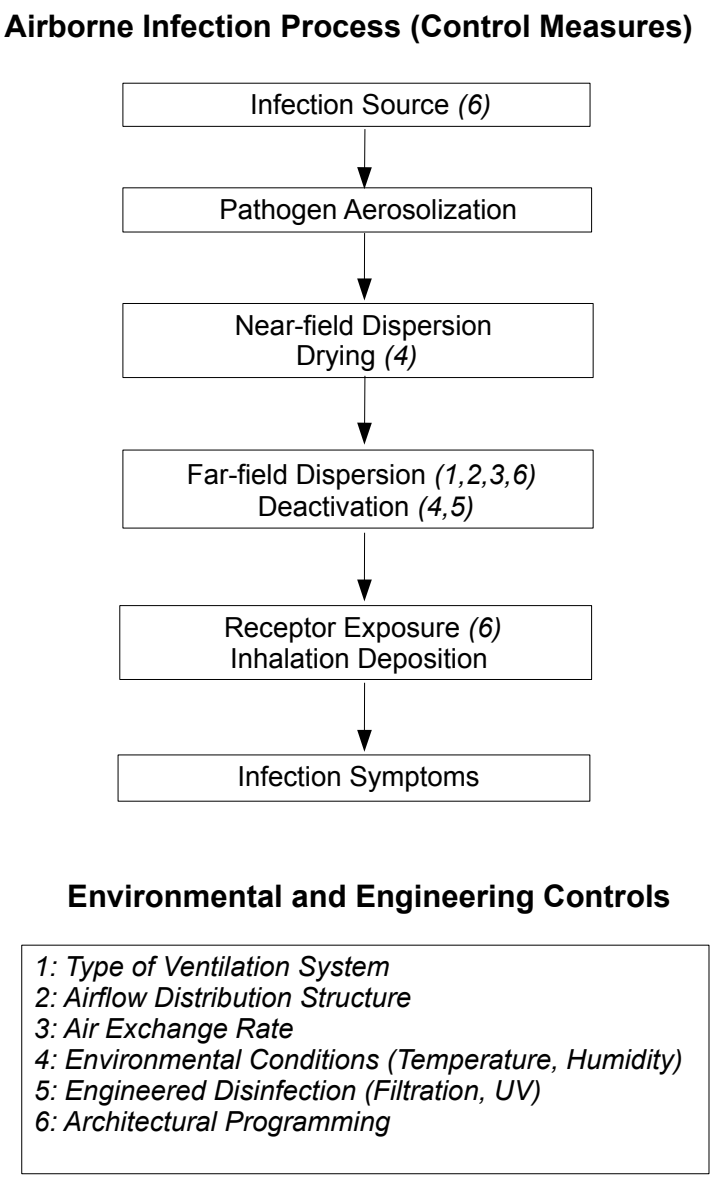

Figure 1.1: Airborne infection process and influential environmental/ engineering controls

1.1 Predicting airborne infection risk: from source to receptor

For effective ventilation design of a health care facility, one needs to be able to quantify and predict airborne infection risk. The informed selection of one ventilation design strategy over another requires the use of suitable metrics. To provide a useful prediction, many input parameters need to be supplied to an airborne infection risk model or experiment. The accuracy and extent of these parameters, of course, depend on the model or experiment complexity and the desired level of detail for the expected results. The key factors of the airborne infection process, which determine the organization of our discussion, are present in the Wells-Riley risk model for a well-mixed room [86]:

$$P_I = \frac{C}{S} = 1 - exp\left(\frac{Iqpt}{Q}\right) \tag{1.1}$$

where P_I is the probability of infection, C is the number of infection cases, S is the number of susceptible persons, I is the number of infectors, q is the quanta generation rate, p is the pulmonary ventilation rate of a person (inhalation), t is the exposure time interval, and Q is the room ventilation rate with clean air. As implied by this equation, one needs to know I, q, p, t, and Q in order to quantify infection risk.

This model is useful, but only for the simple case of a well-mixed room where airborne pathogens are randomly distributed in space. More parameters and complications arise for scenarios in which the air is not well-mixed. In addition, empirical data need to exist for q that quantifies a minimum dose of pathogens that has been observed to infect a person. In section 1.1.5 we will consider and compare more sophisticated risk models, but they all involve the same factors: aerosol generation, pathogen transport, infectivity loss, inhalation and deposition, and invasion of body tissues.

1.1.1 Generation of aerosols

1.1.1.1 Categories of airborne aerosols

Aerosols are suspensions of fine solid or liquid particles in a gas. The medical profession reserves the term *airborne* for aerosols that are transported by air currents over long time periods (minutes) and large distances (greater than 1 m). Thus, small aerosols contribute to the *airborne infection mode* while larger aerosols, which settle quickly, contribute to the *droplet infection*

mode. These are some variations in how the terms are used in the literature [11, 13].

There is agreement that aerosols smaller than 5 μm in aerodynamic diameter (also called droplet nuclei [11]) contribute to airborne infection [13, 101]. However, Tellier [101] considers aerosols larger than 20 μm while Tang et al. [99] consider aerosols larger than 60 μm as contributing to droplet infection. Some authors also define an intermediate size range where aerosols contribute to infection via both airborne and droplet modes. This intermediate behavior depends on particular geometrical settings, airflow patterns in ventilation, and also aerosol response to the surrounding environment [99, 101].

Particular care must be given to aerosols that change in size during the time of flight due to evaporation. An aerosol may move from the droplet regime towards the airborne regime due to mass loss. Aerosol composition and environmental factors such as temperature and relative humidity determine such changes and must be carefully considered in any study [13, 20, 69, 99, 101].

There are hundreds of airborne communicable pathogens [13, 55, 99] falling into three major categories: viruses, bacteria, and fungal spores. Viruses are the smallest with diameters in the range $0.02-0.3$ μm. Bacteria have diameters in the range $0.5-10$ μm. Spores are the largest with diameters in the range $0.5-30$ μm [55].

Human activities are key sources for generation and dispersal of airborne pathogens. These include respiratory activities (breathing, speaking, coughing, sneezing, etc.), showering, flushing, using tap water (atomization of infectious aerosols, particularly bacteria present in the water or in the local plumbing), sewage aerosolization from toilets and its transport in building down-pipe systems, and wet-cleaning of indoor surfaces [69]. Other human activities such as bed making, walking on carpet, or skin cell shedding, cause resuspension of aerosols from surfaces [100].

In addition, various medical procedures also contribute to airborne transmission. Some procedures that may increase droplet nuclei generation are intubation, cardiopulmonary resuscitation, bronchoscopy, autopsy, and surgery with high-speed devices. Presently, there is no precise list of such procedures, and neither has there been any study on the impact of ventilation design on the spread of pathogens released by high-risk procedures [11].

Aside from these sources, each building facility has its own microbial ecology that supports the growth of certain kinds of pathogens and suppresses the growth of others. For example, Heating Ventilation and Air Conditioning (HVAC) system components such as filters, cooling coils, air

intakes, and porous insulation in air ducts can support the growth and dissemination of spores in certain areas. On the other hand, sufficient sunlight and natural ventilation in other areas may disinfect pathogens [20, 55].

1.1.1.2 Expiratory aerosols

Expiratory droplets are particularly important in the spread of airborne infection. Human expirations (breathing, coughing, and sneezing) create the smallest aerosols compared to other sources. Particular attention is paid to human expiratory sources of aerosols for the remainder of this thesis.

Coughs and sneezes were studied by Jennison [51] who applied high-speed photography to track the size and motion of droplets as subjects sneezed. Seventy years ago, it was not possible to track aerosols smaller than 100 μm. Nevertheless, Jennison determined the important length and time scales of sneezes.

Duguid [29] studied the sizes of droplets produced by sneezing, coughing, and speaking using microscopic measurement of stain marks found on slides exposed directly to air exhaled from the mouth. He was able to detect droplets sized in the range $1-2000$ μm. Fairchild and Stamper [34] measured droplets in exhaled breath using an Optical Particle Counter (OPC) in the range $0.09-3.0$ μm. Papineni and Rosenthal [76] studied the size distribution of droplets exhaled by healthy individuals while mouth breathing, nose breathing, talking, and coughing. They used an OPC and an Analytical Transmission Electron Microscope (ATEM). The OPC indicated that the majority of droplets were under 1 μm. ATEM measurements were conducted by collecting droplets on slides and viewing their size under microscope after evaporation. The original droplet size was corrected with a calculation. They confirmed the existence of larger droplets in exhaled breath as opposed to nose breathing. Yang et al. [111] studied the size distribution of droplets experimentally using the Aerodynamic Particle Sizer (APS) and the Scanning Mobility Particle Spectrometer (SMPS). Their samples were bagged before analysis; hence, significant evaporation and droplet settling may have occurred. An experimental study by Chao et al. [16] considered characteristics of a real cough just after the mouth opening using Interferometric Mie Imaging (IMI). They found that droplets are in the range $2-2000$ μm (corresponding to the entire measurement range of IMI).

The large variation in reported droplet size can be attributed to three major causes: (i) the sensitivity of different measurement techniques, (ii) the unrepeatable nature of coughs and sneezes for each subject, as well as the variability of coughs and sneezes among different subjects, and (iii) the

evaporation of droplets at different time scales according to their initial size. Size distribution data found in the literature are summarized in table 1.1.

Study	Measurement Technique	Expiration Type	D_{min} $[\mu m]$	D_{max} $[\mu m]$	Geometric Mean $[\mu m]$	Geometric Standard Deviation $[\mu m]$
Duguid [29]	Microscopy	Coughing	1	2000	14	2.6
Duguid [29]	Microscopy	Sneezing	1	2000	8.1	2.3
Laudon and Roberts [64]	Microscopy	Coughing	1	>1471	12	8.4
Papineni and Rosenthal [76]	OPC[1]	Talking	<0.6	2.5	0.8	1.5
Papineni and Rosenthal [76]	OPC	Nose Breathing	<0.6	2.5	0.8	1.5
Papineni and Rosenthal [76]	OPC	Mouth Breathing	<0.6	2.5	0.7	1.4
Papineni and Rosenthal [76]	OPC	Coughing	<0.6	2.5	0.7	1.5
Papineni and Rosenthal [76]	ATEM[2]	Mouth Breathing	<0.6	2.5	1.2	1.6
Chao et al. [16]	IMI[3]	Talking	2	2000	12.6	3.2
Chao et al. [16]	IMI	Coughing	2	2000	13.1	3.6

Table 1.1: Experimental expiratory droplet size data ([1]OPC: Optical Particle Counter, [2]ATEM: Analytical Transmission Electron Microscope, [3]IMI: Interferometric Mie Imaging)

The physiology of coughing is described by McCool [66] as a three-phase reflex: inspiration, compression, and expiration. The peak flow rate in a cough may reach as high as 12 L/s. Piirilä and Sovijarvi [78] performed an objective assessment of coughing. They investigated the cough as a primitive reflex typically consisting of an initiating deep inspiration, glottal closure, and an explosive expiration accompanied by a sound. The flow characteristics of a cough were reported to vary from person to person. They reported that the durations of the different phases of the cough reflex can be easily measured on a graph of flow versus time. They suggested that the duration of the glottal closure during the compressive phase of cough varies in the range $0.09-1.01$ s. They also defined a useful parameter in characterizing the cough, the Cough Peak Flow Rate (CPFR). Nishino [73] explains the physiology of coughing and sneezing in detail and points out the similarities and differences between the two. The flow dynamics of a sneeze are similar to the cough in time variation of flow rate. However, the peak velocities are higher, and in addition to mouth exhalation, a small fraction of the exhalation exits the nose. For sneezes, Jennison [51] reported exit velocities as high as 90 m/s with Peak Velocity Time (PVT) of 57 ms. The total sneeze time was reported in the range $0.07-0.20$ s. Zhu et al. [116] performed Particle Image Velocimetry (PIV) measurements and Computational Fluid Dynamics (CFD) simulations of cough droplet dispersion in a calm background. Experimentally, they found that the initial velocity of coughs varies in the range $6-22$ m/s and the amount of saliva injected is in the range $6.1-7.7$ mg. Chao et al. [16] reported an average expiration air velocity of 11.7 m/s for coughing and 3.9 m/s for speaking at some distance away from the mouth opening.

Gupta et al. [39] performed an experimental study to characterize the flow rate versus time profile of a human exhalation. They have combined gamma-probability-distribution functions to fit experimental data. Such functions will be particularly useful for setting cough and sneeze boundary conditions for CFD studies. They characterize the complete distribution by only three parameters: Cough Peak Flow Rate (CPFR), Peak Velocity Time (PVT), and Cough Expired Volume (CEV). These boundary conditions were implemented in a CFD simulation by Aliabadi et al. [6]. They demonstrated that volatile cough and sneeze aerosols evaporate at different time scales according to their size. Small droplets (smaller than 20 μm) evaporate at much faster time scales (milliseconds) than larger droplets (larger than 50 μm) for which the evaporation time is in the order of seconds. The most important factors in evaporation rate are temperature and relative humidity in the ambient air.

Höppe [47] pioneered the measurement of expiration temperatures in different climatic conditions. He studied the nasal and oral exhalation temperatures as a function of environment temperature ($5-33\ ^oC$) and environment relative humidities ($10-90$ %). Noticeable variabilities in exhalation temperatures were observed. Similarly, McFadden et al. [67] provided thermal mapping of the human airways using measurements by inserting fine thermistor probes into the respiratory tract. They found that at normal to high rate breathing the temperature in the upper airway system is in the range $33.9-35.5\ ^oC$.

1.1.2 Dispersion, heat and mass transfer

After aerosol generation, the next step in the infection pathway is the dispersion of airborne pathogens in ventilation space, possibly towards potential subjects. This dispersion is a function of many variables such as aerosol size, mean and fluctuating velocities of air, temperature, and the rate at which the aerosol is transferring mass or heat with the environment (i.e. evaporation or cooling/heating). These processes cannot be modeled analytically except in the most idealized cases. Rather, either experiments or CFD are required to understand both the *continuous phase* (the air) and the *discrete phase* (the aerosols) transport mechanisms.

1.1.2.1 Modeling airflow

Solving the continuous phase (air) in ventilation flow requires the integration and solution of mass, momentum, and energy equations, normally using finite volume discretiztion methods [63].

The fluid flow regime is determined largely by the Reynolds and Grashof numbers, to be defined in section 1.2.1. Depending on the room geometry, transition from laminar to turbulent flow occurs at $Re \sim O(10^3)$ and buoyancy-driven flows (e.g. thermal plumes) become important for $Gr/Re^2 > O(10)$. The process of airborne infection in a room involves widely differing scales. For example, the flow in the vicinity of a cough or sneeze is highly turbulent and not strongly influenced by gravity or buoyancy. In contrast, over longer times (minutes) and larger length scales (full room), the turbulence intensity is less and the influence of gravity or buoyancy may be larger. The heat and mass transfer to an expiratory droplet is determined by flow conditions in the immediate vicinity ($1-100\ \mu m$) around the droplet, which is always laminar due to the small droplet length scale and the small aerosol-air relative velocity.

Typically, some form of turbulence modeling is needed for simulations, yet modeling turbulence accurately is the limiting factor for continuum phase modeling for two reasons: (i) the physics of turbulence is not well understood and (ii) accurate modeling of turbulence is computationally very expensive.

The most accurate way to model turbulence is Direct Numerical Simulation (DNS). In this technique the eddies (fluid structures) of all length and time scales (from small to large) are resolved. This technique, however, demands immense computational power with increasing Re or Gr numbers, and, hence, is not applied in ventilation simulations.

As a compromise, the Large Eddy Simulation (LES) technique has been developed that resolves larger eddies with more precision. The structure of small scale eddies are simple, isotropic, and have more universal characteristics. The basic motivation behind this idea is that large eddies are the primary mechanisms transporting aerosols over large distances. This reduces the computational cost substantially, but it still poses challenges for modeling ventilation airflow: (i) the required computation cost is still high; (ii) many realizations of the airflow are necessary for statistically significant results; and (iii) original perturbation fields for the flow are not known or are difficult to generate [14, 28].

A less computationally costly approach in modeling turbulence is the Reynolds Averaged Navier-Stokes (RANS) technique. This approach does not resolve any real-time structure of the flow but instead considers time-averaged and fluctuating components of the flow separately. These models report time-averaged flow velocity and turbulence parameters such as *kinetic energy* and *dissipation rate*. Many variations of RANS models are available (e.g. $k-\epsilon$, $k-\omega$, v^2f, and Reynolds Stress Model (RSM)). Many researchers have used the standard or realizable $k-\epsilon$ turbulence model in solving ventilation airflow [85, 102, 114]. Other researchers have predicted ventilation airflow using Renormalization Group (RNG) $k-\epsilon$ turbulence model. Compared to the standard and realizable $k-\epsilon$ models, the RNG model has a better ability to model a wider range of Re or Gr numbers in the same flow [28, 36, 58, 81, 82, 102, 105, 115]. The Reynolds Stress Model (RSM) allows for anisotropy of turbulence, complex geometries and circulating flows around objects. It provides better results than other RANS models if the initial solution is guessed properly [103]. However, the biggest drawback of RSM is that the model relies on many tuneable constants as opposed to LES. Most RANS models are computationally economic and provide useful results, particularly when *qualitative* results are sought. However, they do not consider the anisotropy of the turbulence and often have difficulty to reach a converged solution.

An alternative approach is to combine RANS and LES to obtain a Detached Eddy Simulation (DES), in which LES is used in areas of strong large-scale unsteadiness such as in the wake of a person, while RANS is used to model the flow elsewhere. In this technique LES is used where the mesh is sufficiently fine so that large eddies can be resolved accurately [28].

A summary of the advantages and disadvantages of the major turbulence models is provided in table 1.2. Due to its relative computational speed, RANS is the only approach used today in the engineering design of ventilation systems.

Turbulence model	Advantages	Disadvantages	Cells	Time
DNS[1]	Resolves eddies of all lengths	Computationally very expensive	10^{10}	Years
LES[2]	Resolves large eddies	Computationally expensive	10^{8}	Months
DES[3]	Computationally economic	Difficult to implement	10^{7}	Weeks
RANS[4]	Computationally economic	Less accurate, difficult to converge	10^{6}	Days

Table 1.2: Summary of turbulence modeling approaches (with representative number of required computational cells and computational time to simulate one hour of ventilation flow in a hospital inpatient room) ([1]DNS: Direct Numerical Simulation, [2]LES: Large Eddy Simulation, [3]DES: Detached Eddy Simulation, [4]RANS: Reynolds Averaged Navier-Stokes)

1.1.2.2 Modeling aerosol dispersion, heat and mass transfer

Particle dispersion can be modeled using several approaches. The simplest approach is to assume that aerosols behave like gases (true only for submicrometer aerosols) and to solve for gas concentration transport in the conservation equations. Many studies have used this approach [36, 81, 82, 102], but it cannot be used to predict the transfer of heat and mass in the continuum phase. Also aerosols larger than 1 μm are affected by other dispersion forces including gravity, which are not accounted for in gas dispersion modeling.

Alternatively, the trajectory of an aerosol can be determined by the force

balance that equates the aerosol inertia with the forces acting on it [3, 6]:

$$\frac{d\overrightarrow{u}_p}{dt} = F_D(\overrightarrow{u} - \overrightarrow{u}_p) + \frac{\overrightarrow{g}(\rho_p - \rho)}{\rho_p} + \overrightarrow{F} \tag{1.2}$$

where $\overrightarrow{u}_p$ is the aerosol velocity, $\overrightarrow{u}$ is the continuum phase velocity, F_D is drag acceleration per unit velocity (determined by Stokes law for the smallest aerosols or empirical drag coefficients for larger aerosols), $\overrightarrow{g}$ is gravitational acceleration, ρ_p is aerosol density, ρ is continuum phase density, and $\overrightarrow{F}$ is the acceleration caused by the Brownian force.

Neglecting radiation, the mechanisms of aerosol mass and temperature change are convection and evaporation. Having the time rate of change of aerosol mass and the convective heat transfer coefficient, the energy balance equation for an aerosol may be written as,

$$m_p c_p \frac{dT_p}{dt} = hA_p(T_\infty - T_p) + \frac{dm_p}{dt} h_{fg} \tag{1.3}$$

where m_p is aerosol mass, c_p is aerosol specific heat capacity, T_p is aerosol temperature, h is convective heat transfer coefficient, A_p is aerosol surface area, T_∞ is the far-field continuum phase temperature, and h_{fg} is the latent heat of vaporization.

For cases where DNS or LES are not used, to produce statistically significant results a large ensemble of droplets of various sizes are tracked stochastically using the Discrete Random Walk (DRW) model, and bin-based mean dispersion locations and diameters are reported for a distribution of aerosols [38]. Many literature studies adopt this modeling approach [58, 85, 102, 105, 114].

1.1.3 Viability and infectivity

The term *viability* refers to the survival of pathogens in a given set of environmental conditions. Pathogens are termed *infective* only if they are able to attack host cells and reproduce themselves [44]. Viability is about how likely is a pathogen to survive and initiate infection. Infectivity is about how likely is a pathogen to infect the host (or deterministically, how many of the pathogens will be needed to infect the host). For example, from a probabilistic point of view, if an intake dose of 10 units of pathogen A will cause 90 % chance of infection in the host, while only an intake dose of only 2 units of pathogen B will cause 90 % chance of infection in the host, pathogen B is more infective than pathogen A. From a deterministic point of view, the smaller the tolerance dose, the more infective the pathogen. All

infective pathogens are also viable, but the converse is not necessarily true [23, 37].

This thesis does not focus on detailed and complex mechanisms of infection; however, a cursory review is needed here because the uncertainty in infectivity data can dominate risk estimates and strongly influence ventilation design.

During aerosolization, fluid shear stresses can inactivate some pathogens. Furthermore, following aerosolization, the viability of a pathogen changes as a function of various environmental conditions, including the relative humidity, temperature, oxygen and ozone concentrations, Open Air Factor (OAF), and electromagnetic radiation [23]. On the other hand, the infectious disease process in a host depends on the pathogen concentration (infection dose) and virulence (disease promoting factors) that enable an agent to overcome the physical and immunologic defense mechanisms in the host [20].

It is important to note that innate and adaptive host immune responses (e.g. past-exposures and/or vaccination) will modify the response to any exposure considerably. The following responses may be possible: (i) exposed but not infected; (ii) exposed and infected but not diseased (due to rapid immune clearance primed by past exposures and/or vaccination; (iii) exposed, infected, and diseased. In addition, infectivity of a virus depends on previous infection of a host with another disease. Hall et al. [41] studied viral shedding patterns of ambulatory children with influenza B. They found that the infection symptoms varied in type and time depending on previous infections/diseases that the children already had. These intra-host mechanisms/factors are not within the scope of this thesis.

1.1.3.1 Environmental factors affecting infectivity and viability

Many environmental stressors are responsible for the loss of viability and infectivity in aerosolized pathogens. Table 1.3 shows the stresses and the target cell components in order of significance [23].

Upon aerosolization, bacteria and viruses desiccate, when dispersed in liquid suspensions such as saliva, and then are surrounded by relatively dry air. Loss of water is the greatest environmental stressor to pathogens and results in a loss of viability. On the other hand, the high relative humidity level in the respiratory tract promotes aerosol growth and affects the deposition site and efficiency, as well as some repair mechanisms in the viability of microbes upon inhalation. Table 1.4 shows a summary of the effect of temperature and relative humidity on the survival of airborne

Stress	Most probable target molecules
Relative humidity and temperature	Outer membrane lipids, proteins
Oxygen	Lipids, proteins
Ozone	Lipids, proteins
Open Air Factor ($O_3 + olefins$)	Lipids, proteins, nucleic acids
γ-rays, X-rays, UV radiation	Lipids, proteins, nucleic acids

Table 1.3: Summary of most probable target molecules [23]

pathogens.

Pathogen Type	Temperature	Relative humidity
Viruses	Decrease by higher temperature	Variable
Bacteria	Decrease by higher temperature	Variable
Fungi	Increase by higher temperature	Increase by higher relative humidity

Table 1.4: Summary of the effect of temperature and relative humidity on airborne pathogen viability and infectivity [22, 23, 48]

Comparing the survival of pathogens in the laboratory with those outdoors shows that, under the same conditions of photoactivity, relative humidity, and temperature, outdoor air is often more toxic to pathogens than indoor air, especially in urban areas [22, 23]. Cox [22] attributes this inactivation to the Open Air Factor (OAF). OAF inactivation is probably caused by a multitude of factors including pollutant concentration, relative humidity, pressure fluctuations, and air ions [23].

Aerosol inactivation caused by electromagnetic radiation is observed to be wavelength dependent. Also relative humidity, oxygen concentration, aerosol age, and presence of other gases affect the electromagnetic radiation damage to viability. Shorter and more energetic wavelengths (X-rays and gamma rays) can break the DNA of pathogens. UV radiation acts as an energy source for the production of thymidine dimers. Longer and visible wavelengths are shown to affect cytochromes in the mitochondria of yeasts and bacteria. Another study also shows that survival of aerosolized bacteria

around sewage treatment plants was higher at night compared to daytime [48].

1.1.3.2 Viability and infectivity models

Viability and infectivity are often difficult to separate, so it is common to model their product as a single parameter (equivalent to assuming that all viable organisms are infective). Inactivation of microbial aerosols is a function of many parameters: temperature, suspension fluid chemistry, relative humidity, oxygen, and time. However, integration of all of these factors in a model is a complicated task because the exact inactivation mechanisms for many microbes are not well understood. In addition, many factors have synergistic effects (e.g. temperature and relative humidity), making it difficult to formulate a comprehensive model. Finally, the response to environmental stressors is unique to each organism (e.g. genetic predisposition). Thus, most developed models in the literature are empirical, only considering a few of these factors; usually time and another factor like temperature or relative humidity. The model parameters are fit experimentally for the viability decay of each microbial aerosol of interest.

During and after the aerosolization of a microbial solution, there is a period of stabilization. During this initial time period, many microbes experience shear stresses and disintegrate. Also, aerosols of interest that remain airborne experience rapid evaporation (during the first 10 s) with temperature, relative humidity, and concentration of certain solutes in the droplet varying rapidly to a level that may be toxic to the microbes. The initial stabilization period is fast relative to the airborne lifetime of aerosols. Also, the interplay of various environmental stressors are far too complicated to be understood and modeled with the current methodologies [80].

Exponential decay is often used to model viability; although a gross simplification, it often performs as well as detailed models with twenty or more parameters [48]. For any set of environmental conditions, the exponential decay model is given by,

$$V_t = V_0 e^{-kt} \tag{1.4}$$

where V_0 is % viability at time zero, V_t is viability at time t, and k is decay constant. Many studies have used the standard exponential decay model to fit curves to viability data or predict viability in some other modeling context [50, 55, 98]. Some researchers have extended the standard exponential model by expressing the decay parameter as a variable governed by water activity

and critical water activity in the suspension solution. Posada et al. [80] fit other constants to obtain an exponential expression for the decay variable.

Although the exponential decay model (equation 1.4) offers many advantages and it is easy to use, it has one major drawback. It predicts the viability to be near zero when the aerosol age is large. This is contrary to experimental data that show an initial fast decay followed by a slow decay causing viability to asymptotically approach a non-zero minimum value [22]. As a result, particularly when using the exponential decay model for airborne infection risk prediction over long periods (one hour), extreme care must be taken not to underestimate the risk.

To overcome this difficulty with the exponential decay model, a series of higher order kinetic models have been developed by Cox [22]. As explained, each model considers only up to two parameters, one of which is time and the other the relative humidity, temperature, or oxygen concentration. As described before, relative humidity has the greatest impact on microbial survival. To use higher order kinetic models one needs to have experimental data for a given set of relative humidities, temperature, or oxygen for a particular pathogen. One then fits the data with a few constants to obtain the model.

The other alternative to the exponential model (equation 1.4) is the catastrophe model. In classical treatments, chemical reactions are assumed to proceed continuously whereas close examination suggests this is only an approximation because at the molecular level, individual reactions are not continuous events. The continuum approximation becomes more accurate as the number of molecules becomes large. Loss of viability in a small aerosol has a discontinuous nature since only a small number of microbes are concerned. A microbe is either alive or dead and the sudden change between these two states is termed catastrophe [22]. The mathematical model of catastrophe theory involves describing the potential energy of the system in terms of control parameters. For some range of values for the control parameters, the potential energy curve has a stable equilibrium, which represents the viable state. If the control parameters are changed, there may result a catastrophic drop in potential energy, which leads to the inactivated or non-equilibrium state [22].

High-order kinetic and catastrophe models for pathogen inactivation are more biologically plausible than the exponential model, but seldom is there sufficient data to support usage of more sophisticated models. The advantages and disadvantages of the viability models described above are listed in table 1.5 .

In order to conduct meaningful ventilation experiments or numerical

Viability model	Advantages	Disadvantages
Exponential	Simple, easy to fit, reasonable agreement with experiments	Underestimation of viability at long durations
Higher order kinetic	Physically plausible, good agreement with experiments	Difficult to fit
Catastrophe	Physically plausible, good agreement with experiments	Difficult to fit, too many model varieties

Table 1.5: Summary of advantages and disadvantages of different viability models

models concerning infection risk, it is necessary to have an estimate for the typical viability drop of airborne species upon release in indoor air. Depending on species of interest and the environmental factors described in section 1.1.3.1, 90 % inactivation can be achieved as quickly as 10 min or as long as 60 min [21–24, 48]. This hints that, for ventilation experiments or numerical models predicting airborne droplet concentration or infection risk, it is sufficient to study dispersion within a few tens of minutes and not hours.

1.1.4 Inhalation and deposition

1.1.4.1 Respiratory system construction

The human respiratory system is comprised of three regions: (i) an upper respiratory portion consisting of the nasopharynx and mouth; (ii) conducting air passages of the larynx, trachea, and large bronchi; (iii) a respiratory gaseous exchange region formed by secondary bronchi, terminal bronchioles and alveoli [23]. Cells lining these areas have different functions, with ciliated, mucous producing cells in the nasopharynx, descending to single cells in contact with interstitial fluid forming the alveoli.

1.1.4.2 Deposition mechanisms

Deposition of aerosols in the respiratory tract occurs via different physical mechanisms. Aerosols smaller than 0.1 μm in diameter are transported onto human airway surfaces by Brownian diffusion. For aerosols roughly in the

range $0.1-1.0\ \mu m$, deposition may occur due to the combined action of Brownian diffusion and impaction. For aerosols of size from $1\ \mu m$ to about $1000\ \mu m$, the deposition mechanism shifts from impaction to sedimentation (i.e. gravitational settling) [48].

Deposition of aerosols in the respiratory tract depends on the tract morphology. In addition, both the respiration mode and breathing pattern must be considered in modeling aerosol deposition in the human lung. Humans have the ability to breath through either the nose or the mouth. The breathing pattern can occur either as regulated or spontaneous breathing. The breathing pattern is often described in terms of tidal volume and flow rate. Larger tidal volumes result in higher aerosol deposition in the lung as aerosol-laden air penetrates deeper into the lung. Lower flow rates also result in higher aerosol deposition by sedimentation and diffusion processes [45, 90].

Temperature and relative humidity in the respiratory tract vary with type of respiration and anatomical location. Generally, a temperature of 37 ^oC and a relative humidity of 99.5 % may be assumed for nasal respiration. For oral respiration a temperature of 37 ^oC and a relative humidity of 90 % may be assumed. The relative humidity can be assumed to increase 1 % per airway generation (branching) until a maximum of 99.5 % is reached. Relative humidity and temperature affect the growth of hygroscopic aerosols in the human lung. This causes the aerosol diameter and density to change. As a result, actual aerosol sizes for *in vivo* and *in vitro* experiments may be different [90].

1.1.4.3 Respiratory tract deposition models

Aerosol deposition in the lungs has been modeled both empirically and mechanistically. In empirical models the fluid and aerosol dynamics associated with respiration are incorporated by simplified expressions [90]. Mechanistic modeling of the deposition of aerosols in the respiratory tract requires the description of the morphology of the airways. Both the overall branching structure of the airway tree and dimensions (e.g. diameters and lengths) of each airway must be considered. Both idealized morphology models and models based on specific experimental observations have been used in aerosol deposition modeling [90].

1.1.5 Summary: infection risk models

The physical and biological processes reviewed up to this section determine (explicitly or implicitly) the airborne transmissibility of disease from the

source to receptor. A model of this transmission process is referred to here as an *infection risk model*.

Infection risk models can be either *deterministic* or *stochastic*. In deterministic models, each individual is hypothesized to have an inherent tolerance dose for an infectious agent. When he or she intakes a dose higher than this tolerance, infection occurs. Otherwise it does not. On the other hand, stochastic models do not determine whether an individual will fall sick under certain dosage conditions. Instead, the model estimates a probability of acquiring the infection under the intake dosage [40, 97]. The distinction between stochastic and deterministic models is more philosphical than practical because even if an underlying infection process is deterministic, there are always a host of unresolved parameters (ranging from genetic variations of host and pathogen, to the turbulent transport from source to receptor) such that all practical models reduce to a probabilistic calculation.

A further categorization of infection risk models is *threshold* versus *non-threshold*. Threshold models assume that a minimum number of pathogens are necessary to infect a subject whereas non-threshold models assume that any number of pathogens, in principle, can cause infection [97].

1.1.5.1 Wells-Riley infection model

Riley et al. [86] developed the first airborne infection model in an epidemiological study in a measles outbreak. Their formulation (equation 1.1) is based on the concept of *quanta of infection*. This quantum is defined as the number of infectious airborne aerosols required to infect a person. The Wells-Riley equation assumes a *well-mixed* room air and a steady state infectious aerosol concentration which varies with the ventilation rate (Q). The biological decay of the airborne pathogens are not explicitly considered in this equation; however, this information is implicitly embedded in the model by the quantum generation (q). Since Wells-Riley model is used with experimental measurements of the quanta of infection, it considers many implicit complexities.

Various researchers have used the *well-mixed* Wells-Riley model to predict infection risk [33, 55]. To improve the model, other studies have incorporated effects of respirator filtration, viability loss of the pathogens, deposition loss of infectious pathogens, and inactivation of pathogens by ultraviolet irradiation [17, 97]. Although these efforts have come a long way, they do not provide details of spatial distribution of risk in a given space. To overcome these difficulties, Qian et al. [81] integrated the Wells-Riley equation into a CFD model to predict the spatial distribution of risk in

a ventilated space. Essentially, the well-mixed model is applied to small sub-domains of the room.

1.1.5.2 Dose-response infection model

Dose-response models require infection dose data to construct the dose-response relationship. This data is obtained experimentally in such a way that a large susceptible population is exposed to different doses of a pathogen, and it is observed what fraction of the population develop an infection. For example, the dosage that causes 50 % of the population to fall sick is called ID_{50}.

The tolerance dose concept is biologically plausible since it considers the variation of immune status and the host's sensitivity in the subjects. There are two opposing views of the process of microbial infection of a host in so far as derivation of dose-response relationship is concerned. The first model can be described as the deterministic hypothesis, which assumes complete cooperation among pathogens to cause infection in the host. Under this hypothesis, each host organism is assumed to have an inherent minimal infective dose, and if it is exposed to a dose in excess of this minimal amount, then an observed response will result. The second model can be described as stochastic hypothesis, which assumes pathogens work independently and each of them can potentially cause infection in the host (single hit) [40].

Deterministic dose-response models are direct implementations of the tolerance dose concept. These models require experimental infection data for a population to fit a curve for the distribution of tolerance dose. Some experimental infection results suggest that the distribution of the tolerance dose can be described log-normally [40, 70, 97],

$$P(Z) = \frac{1}{\sqrt{2\pi}} \int_{-\infty}^{Z} exp\left(\frac{x^2}{2}\right) dx \tag{1.5}$$

$$Z = \frac{lnN - \mu}{\sigma} \tag{1.6}$$

where $P(Z)$ is the frequency distribution of the tolerance dose, Z is the normalized tolerance dose, N is the intake dose, and μ and σ are the mean and standard deviation of natural logarithm of the tolerance dose, respectively. These statistics are determined by fitting the infection dose data for a pathogen in an experiment. Sze-To and Chao [97] consider Weibull distribution as another possibility.

Stochastic interpretations of the dose-response model also exist. Due to mathematical complexities these models predict infection risk only for

one subject (as opposed to a population). Generally, the greater the intake dose, the greater the probability of infection. In stochastic single hit models, the host must intake a dose containing at least one pathogen that reaches the infection site and survives until symptoms develop. For aerosolized pathogens, exponential and Beta-Poisson models have been suggested [40, 97]. The exponential model is given by,

$$P_I = 1 - exp(-rN) \tag{1.7}$$

where r is infectivity of pathogens and N is the intake dose. If there is only one available infection dose value, only the exponential model can be used as the other models require at least two infectious dose values to calculate the fitting parameters.

Sze-To and Chao [97] developed an infection risk model that can incorporate aerosol size, spatial, and temporal factors into a dose-response model. By this approach, a model can be formed that gives the airborne infection risk for a subject (moving or stationary) as a function of time. The exposure level of the pathogen at location x and during time interval t_0 is given by,

$$E(x,T) = cp \int_0^T v(x,t) f(t) dt \tag{1.8}$$

where c is the pathogen concentration in the respiratory fluid (i.e. oral mucus and saliva), $f(t)$ is the viability function of the virus or bacteria in the aerosols, and $v(x,t)$ is the volume density of expiratory droplets at the location. $v(x,t)$ can be obtained by CFD modeling. As it is a time consuming computation to determine exposure levels for every expiratory action (like a cough or a sneeze) and in all locations, one can compute the exposure level for one expiratory action and then multiply the exposure level by the number of expirations during the exposure time interval. By this approach a stochastic and non-threshold dose-response model for the airborne infection risk can be formed.

$$P_I(x,T) = 1 - exp\left(- \sum_{j=1}^{m} r_j \beta_j f_s cp \int_0^T v(x,t)_j f(t) dt \right) \tag{1.9}$$

where m is the total number of aerosol size bins, $v(x,t)_j$ is the volume density of droplets of the j^{th} size bin and f_s is the expiration frequency. As the infectivity (reflected in r) and deposition fraction of infectious aerosols (reflected in β) are aerosol size dependent, $v(x,t)$ is thus split into different size bins.

1.1.5.3 Population infection model

Some studies in the literature model airborne infection risk for a *population* of individuals, as opposed to a single subject [17, 18, 96]. Such models are termed *population* or *epidemic* infection models and simulate dynamics in a total population (N) that consists of the susceptible (S), infected (I), and recovered (R) sub-populations [17, 74]. The relationships among these sub-populations are expressed using a series of differential equations that relate physical and biological parameters. The model complexities depend on the number of parameters considered. Various researchers have considered aerosol size, probability of infection by an inhaled pathogen, physical removal of airborne pathogens, infection recovery rate, inactivation rate of airborne pathogens, airborne pathogen generation rate, and many more parameters [17, 18, 74, 75, 96]. For example, the work of Noakes et al. [74] has integrated the Wells-Riley model into a *population* infection model. Noakes and Sleigh [75] also developed a *population* model that finds infection rate for a multi-zone health care facility.

Although these models extend airborne infection risk prediction to a population, they do not resolve infection risk spatially since they assume well-mixed distribution for airborne pathogens. Inclusion of spatial resolution will result in many mathematical complexities for such models. On the other hand, the Wells-Riley (equation 1.1) and dose-response models (e.g. equations 1.5, 1.6, and 1.7) predict the infection probability for a single subject, but they can resolve spatial and temporal components of risk (e.g. equations 1.8 and 1.9) and hence suffice to guide ventilation design.

As investigated in this section, an important step in the airborne infection pathway is the transport of pathogens from a source, such as expiration by an infected person, to a receptor, such as a healthy individual. Although environmental conditions such as temperature, relative humidity, and lighting also impacts the infection pathway, the main focus of any ventilation system design should be the transport aspect of pathogen delivery to subjects. This is critical since exposure level at the breathing zone of a healthy individual is a key parameter in airborne infection risk. The following section focuses on physics of transport for droplets, released by injections, in a ventilated space.

1.2 Mathematical framework and scaling analysis

Before developing specific experimental and numerical methodologies to solve a problem, scientists ought to express the problem using the simplest

mathematical expressions, incorporating all known physical phenomena that may be present. Then, based on these physics, they can determine which ones have significance over the others. They then simplify the mathematical equations and develop subsequent experimental, numerical, or analytical methodologies to find solutions.

For ventilation flows and contaminant dispersion, the process described above involves writing equations of mass, momentum, and energy conservation, as well as equation of motion for discrete aerosol phase. We will develop these equations in this section and investigate important physics that need to be accounted for in order to arrive at sensible, plausible, and useful solutions. These equations are analyzed in two time and length scales.

- Near-field: dispersion behavior at short time scales and small length scales at the vicinity of fast injection events, representing coughs and sneezes, that release contaminants in ventilated space. These scales are in the order of milliseconds and centimeters.
- Far-field: dispersion behavior at long time scales and large length scales relevant to spreading of contaminants over the entire ventilated space. These scales are in the order of seconds, if not minutes, and meters.

The mathematical modeling in this section is rather too simplistic for our problem. In chapter 5 we will refine these models by adding turbulence modeling, discrete phase heat and mass transfer modeling, and species transport modeling, but for now, this rudimentary treatment suffices to develop experimental and numerical methods to solve the problem of contaminant dispersion in ventilation space.

1.2.1 Continuum phase mass, momentum, and energy transport processes

Consider that the ventilation space of interest is modeled in the Cartesian coordinates in which y represents the vertical direction (against gravity) and the x and z coordinates represent the horizontal directions. The non-dimensional equation for the mass conservation for incompressible flow is given by,

$$\frac{\partial u^*}{\partial x^*} + \frac{\partial v^*}{\partial y^*} + \frac{\partial w^*}{\partial z^*} = 0 \tag{1.10}$$

where u^*, v^*, and w^* are non-dimensional velocities and x^*, y^* and z^* are non-dimensional coordinates given in table 1.6. Further assume that the Boussinesque approximation applies. This means that density differences are significant only in terms of the momentum equation that contain gravitational field. Further, one may assume the density variation is only a function of temperature [46],

$$\beta = \frac{1}{V}\left(\frac{\partial V}{\partial T}\right)_p = \frac{1}{V_{ref}}\frac{V - V_{ref}}{T - T_{ref}} = \frac{\rho_{ref} - \rho}{\rho(T - T_{ref})} \tag{1.11}$$

$$(\rho_{ref} - \rho)g = \rho_{ref}\beta(T - T_{ref})g \tag{1.12}$$

where β is the coefficient of thermal expansion and V is volume. Certainly, this is only valid when deviation from reference conditions is small. As a result, the momentum equations for incompressible flow are given by,

$$\frac{\partial u^*}{\partial t^*} + u^*\frac{\partial u^*}{\partial x^*} + v^*\frac{\partial u^*}{\partial y^*} + w^*\frac{\partial u^*}{\partial z^*} = -\frac{\partial P^*}{\partial x^*} + \frac{1}{Re}\left(\frac{\partial^2 u^*}{\partial x^{*2}} + \frac{\partial^2 u^*}{\partial y^{*2}} + \frac{\partial^2 u^*}{\partial z^{*2}}\right) \tag{1.13}$$

$$\frac{\partial v^*}{\partial t^*} + u^*\frac{\partial v^*}{\partial x^*} + v^*\frac{\partial v^*}{\partial y^*} + w^*\frac{\partial v^*}{\partial z^*} = -\frac{\partial P^*}{\partial y^*} - \frac{Gr}{Re^2} + \frac{1}{Re}\left(\frac{\partial^2 v^*}{\partial x^{*2}} + \frac{\partial^2 v^*}{\partial y^{*2}} + \frac{\partial^2 v^*}{\partial z^{*2}}\right) \tag{1.14}$$

$$\frac{\partial w^*}{\partial t^*} + u^*\frac{\partial w^*}{\partial x^*} + v^*\frac{\partial w^*}{\partial y^*} + w^*\frac{\partial w^*}{\partial z^*} = -\frac{\partial P^*}{\partial z^*} + \frac{1}{Re}\left(\frac{\partial^2 w^*}{\partial x^{*2}} + \frac{\partial^2 w^*}{\partial y^{*2}} + \frac{\partial^2 w^*}{\partial z^{*2}}\right) \tag{1.15}$$

where P^* is the non-dimensional pressure, t^* is non-dimensional time, also given in table 1.6, Re is the Reynolds number, and Gr is the Grashof number. These numbers are given by the following relationships,

$$Re = \frac{Inertial\ forces}{Viscous\ forces} = \frac{L_{ref}U_{ref}}{\nu} \tag{1.16}$$

$$Gr = \frac{Buoyant\ forces}{Viscous\ forces} = \frac{g\beta L_{ref}^3(T - T_{ref})}{\nu^2} \tag{1.17}$$

where ν is the air kinematic viscosity. Note that the momentum equation in the y direction has one extra term due to the buoyant force. This term is given by,

$$\frac{Gr}{Re^2} = \frac{g\beta(T - T_{ref})L_{ref}}{U_{ref}^2} \tag{1.18}$$

When this number approaches or exceeds unity, we expect to have strong buoyancy contributions to the flow. On the other hand, if this number is small, buoyancy effects may be ignored. Ignoring any source or sink terms, the energy equation for the incompressible flow is given by,

$$\frac{\partial T^*}{\partial t^*} + u^*\frac{\partial T^*}{\partial x^*} + v^*\frac{\partial T^*}{\partial y^*} + w^*\frac{\partial T^*}{\partial z^*} = \frac{1}{RePr}\left(\frac{\partial^2 T^*}{\partial x^{*2}} + \frac{\partial^2 T^*}{\partial y^{*2}} + \frac{\partial^2 T^*}{\partial z^{*2}}\right) + \phi \tag{1.19}$$

where T^* is non-dimensional temperature, also shown in table 1.6, Pr is Prandtl number, and ϕ is the viscous dissipation. Prandtl number is defined by,

$$Pr = \frac{Viscous\ diffusion\ rate}{Thermal\ diffusion\ rate} = \frac{\mu c_p}{k} \tag{1.20}$$

where μ is air dynamic viscosity, c_p is specific heat capacity, and k is thermal conductivity. The group $RePr$, also known as Péclet (Pe) number, signifies the relative importance of convection versus conductive mechanisms. The viscous dissipation rate ϕ is defined by,

$$\begin{aligned}
\phi &= \frac{Ec}{Re}\left(\left(\frac{\partial u^*}{\partial y^*} + \frac{\partial v^*}{\partial x^*}\right)^2 + \left(\frac{\partial v^*}{\partial z^*} + \frac{\partial w^*}{\partial y^*}\right)^2 + \left(\frac{\partial w^*}{\partial x^*} + \frac{\partial u^*}{\partial z^*}\right)^2\right) \\
&+ \frac{Ec}{Re}\left(2\left(\left(\frac{\partial u^*}{\partial x^*}\right)^2 + \left(\frac{\partial v^*}{\partial y^*}\right)^2 + \left(\frac{\partial w^*}{\partial z^*}\right)^2\right)\right) \\
&- \frac{Ec}{Re}\left(\frac{2}{3}\left(\frac{\partial u^*}{\partial x^*} + \frac{\partial v^*}{\partial y^*} + \frac{\partial w^*}{\partial z^*}\right)^2\right)
\end{aligned} \tag{1.21}$$

where Ec is the Eckert number given by,

$$Ec = \frac{Kinetic\ energy\ rate}{Enthalpy} = \frac{U_{ref}^2}{c_p T_{ref}} \tag{1.22}$$

The Eckert number expresses the relationship between a flow's kinetic energy and enthalpy, and is used to characterize dissipation. Small values of $\frac{Ec}{Re}$ indicate negligible viscous dissipation.

Unknown	Non-dimensionalization
Time	$t = t^* L_{ref}/U_{ref}$
Position	$x = x^* L_{ref}$
Position	$y = y^* L_{ref}$
Position	$z = z^* L_{ref}$
Velocity	$u = u^* U_{ref}$
Velocity	$v = v^* U_{ref}$
Velocity	$w = w^* U_{ref}$
Pressure	$P = P^* \rho_{ref} U_{ref}^2$
Temperature	$T = T^* T_{ref}$

Table 1.6: Dimensionless unknowns in the continuum phase conservation equations

1.2.2 Discrete phase motion

The trajectory of a discrete phase droplet can be determined by integrating the force balance written in the Lagrangian reference frame. This force balance equates the particle inertia with the forces acting on the droplet. If we only consider drag and gravitational forces and also use Stokes and continuum approximation for particle drag (reasonable for particles with diameter between 0.5 μm and 100 μm in ventilation flows), the particle equation of motion in the Cartesian coordinate can be written as follows.

$$\frac{d\overrightarrow{u^*}_p}{dt^*} = Dr(\overrightarrow{u^*} - \overrightarrow{u^*}_p) + \frac{1}{Fr^2}\hat{g} \tag{1.23}$$

where $\overrightarrow{u^*}_p$ is non-dimensional particle velocity, Dr is a particle coefficient of drag, and Fr is the particle Froude number. Particle drag and particle Froude numbers are given by,

$$Dr = \frac{Viscous\ forces}{Inertial\ forces} = \frac{18\mu L_{ref}}{\rho_p d_p^2 U_{ref}} \tag{1.24}$$

$$Fr = \frac{Inertial\ forces}{Gravity\ forces} = \sqrt{\frac{U_{ref}^2}{L_{ref} g}} \tag{1.25}$$

were ρ_p is the density of the droplet, and d_p is the droplet diameter.

1.2.3 Scaling analysis for conservation and particle motion equations

A blunt, but useful, assessment of the non-dimensional terms in the previous sections guides us in the understanding of dominant physics of the problem. We assess all of these terms for both near-field and far-field sub-domains. For each sub-domain, we assume a set of reference values defined in table 1.7.

Reference parameter	Order (Near-field)	Order (Far-field)
$L_{ref}[m]$	10^{-2}	10^{1}
$U_{ref}[m/s]$	10^{2}	10^{-1}
$\rho_{ref}[kg/m^3]$	10^{1}	10^{1}
$T_{ref}[K]$	10^{2}	10^{2}
$\nu[m^2/s]$	10^{-5}	10^{-5}
$\mu[kg/ms]$	10^{-5}	10^{-5}
$g[m/s^2]$	10^{1}	10^{1}
$\beta[1/K]$	10^{-3}	10^{-3}
$T[K]$	$10^{2}+10$	$10^{2}+10$
$c_p[J/kgK]$	10^{3}	10^{3}
$k[W/mK]$	10^{-2}	10^{-2}
$\rho_p[kg/m^3]$	10^{3}	10^{3}
$d_p[m]$	10^{-5}	10^{-5}

Table 1.7: Reference values for scaling analysis

The order of magnitude values for non-dimensional terms in conservation and particle motion equations are shown for scaling analysis in table 1.8. Comparison of $1/Re$ and Gr/Re^2 magnitudes in the momentum equations reveals that natural convection effects can be safely neglected in the near-field, but they play a significant role in the far-field. The comparison of $1/(RePr)$ and Ec/Re magnitudes reveals that viscous dissipation effects are present in the near-field, but they do not play a significant role in the far-field. Likewise, comparing Dr with $1/Fr^2$ magnitudes reveals that gravity effects are far more important in the far-field than near-field. This scaling analysis supports the adequacy of separate near- and far-field treatments for contaminant dispersion in ventilation flow released by fast injections.

Non-dimensional terms	Order (Near-field)	Order (Far-field)
$1/Re$	10^{-5}	10^{-5}
Gr/Re^2	10^{-7}	10^{2}
$1/(RePr)$	10^{-5}	10^{-5}
Ec/Re	10^{-6}	10^{-12}
Dr	10^{-1}	10^{5}
$1/Fr^2$	10^{-5}	10^{4}

Table 1.8: Scaling analysis for non-dimensional terms in conservation and particle motion equations

1.3 Objectives and research plan

As investigated in section 1.1, research in preventive approaches to block any stage of the airborne infection pathway can be pursued in many dimensions. However, study of low energy ventilation systems for mitigating airborne infection risk is particularly useful since improved air quality will be achieved with the bonus benefit of reduction in energy demands of buildings.

North American building codes are very conservative and require high ventilation rates in most health care functional spaces. The European building codes, however, allow other forms of ventilation (e.g. displacement and natural) on the grounds that they possibly improve air quality by enhanced aerosol separation/removal while reducing the building carbon footprint. Careful research in the performance of low-energy ventilation systems (e.g. displacement) may reduce their perceived risks and allow more widespread adoption. The grand objective of this thesis is to investigate the effects of expiratory injection properties, direction, spatial locations of source and suspect, and the thermal plumes in the airborne transmission of contaminants in an underfloor air distribution system.

Figure 1.2 shows the research plan for this thesis. In chapters 2 and 3 we review the physics of airborne droplet transport at near and far-field scales. Some aspects of contaminant transport in the near-field have been studied well in the literature. For example, mean droplet size dispersion and velocity for steady sprays are known, but size-specific dispersion and velocity for transient sprays, representative of coughs and sneezes, need to be studied in more detail. Likewise, some aspects of contaminant transport in the far-field have been investigated in the literature. Relevant studies focus

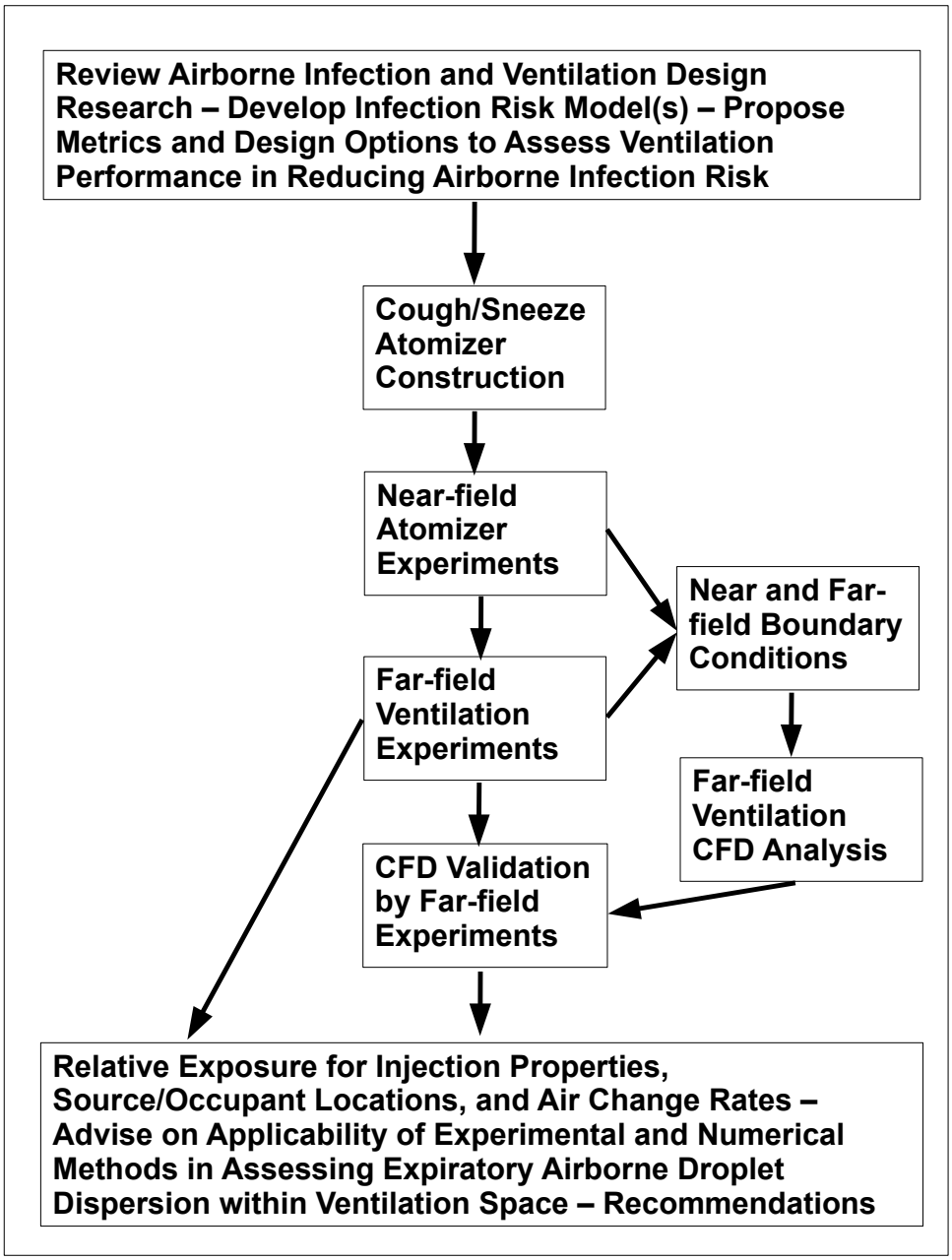

Figure 1.2: Research plan

on steady tracer gas transport, ventilation type, diffuser and exhaust types, effects of heating and cooling modes, supply temperature, auxiliary heating and cooling, heat gains and losses, ventilation rate, and occupancy. However, dispersion of droplets produced by transient injections (coughs and sneezes), placement of subjects within the room, and orientation and momentum of injections can be considered in more detail in the performance of low energy ventilation systems. We will investigate properties of steady and transient sprays, which represent expiratory injections. We will also investigate important parameters in the room that affect contaminant dispersion. These reviews guide designing a suitable pseudo cough/sneeze injector to be used in near-field and far-filed ventilation experiments. Further, we will investigate adequate indices to assess the effects of these parameters on ventilation performance.

Chapter 4 develops the experimental methodology for near and far-field dispersion of droplets. The experimental methodology presented in section 4.1 is designed to study dispersion of a wide size range of droplets, released by various injection momenta, in axial and radial directions. In the near-field, we ignore the effects of natural convection and gravity and consider dispersion of droplets under forced convection. A cone air-assist internally mixing atomizer (cough/sneeze emulator) is developed for this purpose. In these experiments, the droplet dispersion characteristics are sought under both steady and transient operation modes, including spatially resolved size distributions for droplets. The first part of the near-field experiments focuses on steady spray dispersion behavior. The specific research objectives for this part are: (i) determine the effect of droplet breakup in the dispersion of droplets downstream of the spray; (ii) determine the relationship between droplet size and radial dispersion with a focus on the size distribution of droplets. The second part extends the measurements to transient sprays. Specific objectives of this part are: (i) determine the self-preserving dispersion of the overall transient spray and compare it to that of transient continuous phase starting jets; (ii) determine the droplet size distribution, Sauter mean diameter, and concentration for the leading and trailing edges of the transient spray as a function of time and the axial distance from the atomizer, and compare these with steady sprays; (iii) determine the velocity distribution as a function of axial distance and droplet size in the leading and trailing edges of the transient spray, and compare it with steady sprays; (iv) explain the behavior of droplet dispersion and velocity using mean, Kolmogorov and turbulent Stokes numbers.

In the far-field, we consider natural convection, forced convection, and gravity effects on droplet dispersion. The far-field experiments are to investi-

gate the effect of variations in room boundary and initial conditions. Section 4.2 develops methodologies for a ten-parametric case study, in which we vary injection momentum, injection direction, strength and placement of a thermal plume, and the air change rate in the ventilation domain. Since the near- and far-field processes are coupled, all of these parameters could potentially affect contaminant dispersion in the room in significant ways. The cumulative concentration of airborne droplets is measured at various locations of sitting, breathing, and upper zones in the room. Cumulative droplet concentration is directly proportional to the total hypothetical pathogen dosage. The relative normalized cumulative droplet concentrations (or relative exposures) in the parametric study indicate how important relative boundary and initial conditions are for the underfloor air distribution ventilation system to mitigate infection risk under various real-life-like room conditions. A space-resolved study is conducted to assess the contaminant dispersion in various locations within the room for one set of boundary and initial conditions.

Chapter 5 develops a complete Computational Fluid Dynamics (CFD) model that incorporates the physics described above in the far-field dispersion of droplets in the ventilation domain. The near-field and far-field experiments help assigning boundary and initial conditions (e.g. wall temperatures, injection velocities, injection droplet size distribution, etc...) for the numerical model. The same ten-parametric and space-resolved studies are simulated to compare the model against the experiments.

Chapters 6, 7, 8, and 9 discuss the experimental results, the numerical results, the conclusions, and future work respectively.

Chapter 2

Review of Dispersion Mechanisms in Injections (Near-field)

Expiratory actions such as coughs and sneezes are transient injections that introduce and disperse contagious droplets within ventilation domain. Of course, one way to study coughs and sneezes within ventilation domain is to use real injections by human subjects and monitor the subsequent dispersion of droplets. However, some difficulties are to expect with this approach. First, the variability in flow dynamics is high among subjects and even for the same subject injecting multiple times. Second, the resulting droplet concentration within a room is too low to be measured by most experimental techniques successfully. As a result, it is desired to develop an artificial cough or sneeze simulator to produce these droplets at higher concentrations for ventilation studies.

Flow and droplet dynamics of coughs and sneezes were introduced in section 1.1.1.2. In this thesis, an atomizer is developed to produce expiratory injections with representative key parameters found in real coughs and sneezes. These parameters are injected volume of gas, injection time, injection velocity, and droplet size. These parameters are discussed in section 4.2.8.1. In this chapter we review droplet and flow dynamics of transient and steady air-assist atomizers found in the literature.

2.1 Droplet dispersion in steady air-assist atomizers

Droplet dispersion from air-assist atomizers in axial x and radial r directions may be a function of many parameters. These include the type (e.g. internally versus externally mixing) and geometry (exit diameters for liquid and gas streams) of the air-assist atomizer, droplet diameter d, the gas to liquid mass loading ratio $\dot{m}_g/\dot{m}_l$, the gas to liquid momentum loading ratio p_g/p_l,

the gas Weber number We_g, the gas and liquid Reynolds numbers Re_g and Re_l, droplet evaporation rate, gravitational effects and the spray breakup structure. The near-field study considers the effects of droplet diameter, gas and liquid Reynolds numbers, Weber number, and mass loading ratio.

The overall shape of a round air-assist spray can be characterized using the penetration, cone angle, and equivalent spray angle [89]; however, none of these measurements provide any information regarding the droplet size within the spray. Instead, some studies report droplet size in a spray using Sauter Mean Diameter (SMD) or d_{32}, the overall volume-to-surface ratio. Eroglu and Chigier [32], Hardalupas and Whitelaw [43], and Karl et al. [52] performed measurements of d_{32} as a function of axial and radial distances for externally mixing air-assist atomizers. Karl et al. [52] found that d_{32} increases at the spray periphery due to the greater momentum of larger droplets and their ability to migrate to the side given the initial velocity in the radial direction. Hardalupas and Whitelaw [43] found a decreasing d_{32} versus radial distance. To the contrary, given different operating liquid and gas pressures, Eroglu and Chigier [32] found that d_{32} could rise, fall, or stay the same with increasing radial distance. These studies did not report a major shift in the value of d_{32} as a function of axial distance for steady sprays.

Empirical correlations of d_{32} have been developed for air-assist atomizers [87, 89, 91]. Rizkalla and Lefebvre [89] developed the following correlation for d_{32} for an internally mixing atomizer:

$$d_{32} = 0.95\frac{(\sigma\dot{m}_l)^{0.33}}{U_r\rho_l^{0.37}\rho_g^{0.30}}\left(1+\frac{1}{ALR}\right)^{1.70} + 0.13\left(\frac{\mu_l^2 d_g}{\sigma\rho_l}\right)^{0.5}\left(1+\frac{1}{ALR}\right)^{1.70} \tag{2.1}$$

where ALR is the Air to Liquid mass Ratio $\dot{m}_g/\dot{m}_l$ and U_r is the relative velocity between air and liquid. Water, kerosene, and other fluids were employed in these tests. The air velocity was held in the range $70-125$ m/s. ALR was in the range $3-9$. Experiments were run at room and elevated temperatures. This correlation is accurate within 8 % over a broad range of air and liquid properties that include our operating conditions for nitrogen and water.

Size-resolved droplet concentration and velocity within a spray also describe the dispersion behavior. Eroglu and Chigier [32], Hardalupas and Whitelaw [43], Karl et al. [52], and de Vega et al. [27] performed measurements of droplet concentration and mean velocity as a function of axial and radial distances for steady externally mixing air-assist atomizers. Nij-

dam et al. [72] provided comparable measurements for an internally mixing air-assist atomizer. Also, Kennedy and Moody [53] performed velocity and radial dispersion measurements of monodisperse droplets in a steady gas jet as a function of gas Reynolds number and position. It was found that total concentration at large axial distances follow a self-similar Gaussian distribution versus non-dimensional radial distance [27, 52]. Also, it was found that non-dimensional axial velocity profiles are self-similar and appear as Gaussian when plotted against non-dimensional radial distance [7, 27, 49, 52, 53, 62]. de Vega et al. [27] and Nijdam et al. [72] verified that smaller droplets have higher turbulent intensities in sprays, both axially and radially. Kennedy and Moody [53] verified, experimentally, that smaller droplets disperse more effectively in the radial direction. These studies hint that, in a full size distribution, smaller droplets diffuse more quickly in the radial direction, but the validity of this statement in the context of air-assist atomization using liquid breakup is yet to be confirmed.

Axial deceleration of continuous phase jets and sprays is an important measure for droplet dispersion in sprays. Gases and particle-laden jets are characterized by a decreasing centerline axial mean velocity (deceleration) U_c as a function of axial distance x, upstream gas velocity U_g, virtual origin x_0, nozzle gas exit diameter d_g, and a constant B, in such a way that,

$$\frac{U_g}{U_c} = \frac{1}{B}\left(\frac{x}{d_g} - \frac{x_0}{d_g}\right) \tag{2.2}$$

The values of B and x_0 vary among continuous phase jets, particle-laden jets, and sprays. For continuous phase jets, Hussein et al. [49] gave $B \simeq 6$ and $x_0 \simeq 3d_g$; for particle-laden flows with low mass loadings, Hardalupas et al. [42] gave $B \simeq 7.2$ and $x_0 \simeq 3.5d_g$; and for sprays, de Vega et al. [27] gave $B \simeq 10$ and $x_0 \simeq -15d_g$. de Vega et al. [27] found a faster deceleration for smaller droplets. Droplet mean axial velocity is dependent on droplet size and gas axial velocity, both of which must be measured accurately to describe the axial dispersion behavior.

Proper understanding of droplet dispersion in air-assist atomization requires knowledge of continuous phase (gas) jets. Firstly, dispersion of fine droplets in dilute sprays can be approximated by that of gas jets since fine droplets behave like fluid elements. Secondly, spray dispersion results from the interaction of droplets with the gas mean and turbulent flow components. The work of Sangras et al. [92] and others [54, 57, 88, 109] allow comparison between dilute air-assist spray penetration and the penetration of continuous phase puffs, starting jets, and jets. The work of Hussein et al.

[49] can be used to provide estimates for velocity distribution, kinetic energy, and dissipation rate in high-Reynolds-number axisymmetric turbulent jets and subsequently dilute sprays.

Droplet dispersion follows from the breakup processes that occur during the early stages of atomization [31, 59, 104]. Shi and Kleinstreuer [94] classify different breakup regimes for coaxial air-assist atomizers. The first step, called primary breakup, is due to the formation of ligaments and other irregular liquid elements along the surface of the liquid column. These irregular shapes break into large droplets. The droplets then undergo different forms of breakup, called secondary breakup that includes 'bag', 'stripping', and 'catastrophic' mechanisms.

The physics that govern primary and secondary breakup mechanisms are different [59]. For small Weber numbers ($We_g < 110$) surface tension dominates the droplet formation. For larger Weber numbers ($We_g > 100$) fiber-type ligaments begin to form and they break into droplets by the Rayleigh-type capillary breakup mechanism. The intact liquid core in air-assist atomizers further persists downstream to a distance correlated to the gas to liquid momentum ratio. The smaller this ratio the further the liquid stream travels before breakup. The secondary breakup of droplets results from the relative velocity between the droplet and the mean motion of the gas (slip velocity) or from the turbulence of the carrier gas. The former breakup process is termed 'shear breakup' and the latter process is termed 'turbulent breakup'.

Lasheras et al. [59] attribute the accumulation of larger droplets on the periphery of the spray due to different breakup regimes. The primary breakup is more dominant near the edge of the spray where shear forces are maximum at the gas-liquid interface. This mechanism is responsible for large droplet formation. On the other hand, the secondary breakup mechanisms (pressure and viscous forces by turbulent motion) are dominant at the center of the spray. These forces are responsible for smaller droplet formation. The radial profiles of d_{32} reduce in slope at larger axial distances since fine droplets migrate to the periphery faster than large droplets. Explanation of droplet dispersion in an air-assist atomizer requires an understanding of primary and secondary breakup regimes in the spray.

The evaporation rate can significantly affect droplet dispersion if droplets are small and their evaporation time is comparable to their life time. For example, at 20 % relative humidity and room temperature, 1 μm droplets evaporate in 1 ms, 5 μm droplets evaporate in 35 ms, and 100 μm droplets evaporate in 10 s [69]. To reduce the effect of evaporation on size and dispersion measurements, it is desirable to analyze droplets for which the

evaporation time is at least an order of magnitude larger than maximum time of flight. This will be the case for this study and will be explained in detail in section 4.1.7.

Wells and Stock [107] investigated the effect of body forces such as gravity on the dispersion of droplets in turbulent flows. They claimed that the impact of gravity will be negligible if the droplet terminal velocity v_t is less than the root mean square of fluid fluctuating velocity, which is the case for this study. Otherwise, gravitational and other body forces must be considered.

A droplet of diameter d, density ρ_l, suspended in a gas with dynamic viscosity μ_g, interacts with the mean and turbulent components of the gas flow. The droplet response in the flow can be understood comparing the droplet relaxation time $\tau_d = \rho_l d^2/(18\mu_g)$ with other time scales in the flow. These time scales are mean flow time scale $\tau_g = x/U_g$, Kolmogorov time scale $\tau_k = \sqrt{\nu_g/\epsilon}$, and characteristic eddy time scale $\tau_e = Ck/(\sqrt{2/3}\epsilon)$. The turbulent dissipation rate ϵ, kinetic energy k, and constant C can be estimated by those of gas jets in the case of dilute sprays [53]. The Stokes number non-dimensionalizes the droplet relaxation time using these flow time scales. Table 2.1 demonstrates possible Stokes numbers for spray dispersion.

Stokes number	Symbol	Definition
Mean Stokes number	St_m	τ_d/τ_g
Kolmogorov Stokes number	St_k	τ_d/τ_k
Turbulent Stokes number	St_t	τ_d/τ_e

Table 2.1: Stokes numbers in spray droplet dispersion

Radial dispersion of droplets in air-assist atomizers can be quantified using droplet diffusivity and non-dimensionalized using the convective time scale of the gas flow to yield a Lagrangian Péclet number [53]. Droplet diffusivity $\epsilon(d)$ and Lagrangian Péclet number $Pe_L(d)$ are defined as,

$$\epsilon(d) = \frac{1}{2}\frac{d}{dt} < r(d,t)r(d,t) > \tag{2.3}$$

$$Pe_L(d) = \frac{U_g d_g}{\epsilon(d)} \tag{2.4}$$

This Péclet number can be calculated either locally or as an average over a distance.

2.2 Droplet dispersion in transient air-assist atomizers

Droplet dispersion is less studied for transient air-assist atomizers. Most studies in the literature concerning transient sprays relate to liquid jets in engine fuel injectors (e.g. Diesel engines). Arcoumanis and Gavaises [7] have studied atomization from Diesel injectors. They reported decreasing d_{32} as a function of time at larger axial distances. They also performed velocimetry measurements as a function of time and position. Their study, however, did not provide detailed dispersion and velocimetry results for a complete droplet size distribution.

The overall transient dispersion of droplets in a round air-assist spray can be characterized in a similar way to those of continuous phase starting jets. Sangras et al. [92] have shown that downstream of a continuous puff or starting jet, the flow evolves into a self-preserving structure such that dimensionless axial penetration $\frac{x-x_0}{d_g}$ is correlated with dimensionless time $\frac{(t-t_f)U_g}{d_g}$, and the dimensionless radial penetration $\frac{r}{x-x_0}$ is correlated with dimensionless axial penetration. These correlations are provided by,

$$\frac{x-x_0}{d_g} = C_x \left(\frac{(t-t_f)U_g}{d_g} \right)^n \tag{2.5}$$

$$\frac{r}{x-x_0} = C_r \tag{2.6}$$

where C_x, C_r, and n are constants. n is usually 0.5 for starting jets and 0.25 for puffs. t_f is the time delay for the injected phase to reach its maximum flow rate [92]. It is speculated that the same correlation will explain the overall dispersion for dilute air-assist sprays with very fine droplets.

2.3 Concluding remarks

As described in this chapter, the literature is rich in specifying droplet and flow dynamics of steady sprays and flow dynamics of transient gas jets. There are established correlations that give steady spray quality, droplet breakup, and radial dispersion of droplets. There are also correlations that give transient axial and radial development of gas jets.

There is, however, knowledge to be gained in understanding droplet and flow dynamics of transient sprays. The experimental work of this thesis reveals droplet and flow dynamics of transient sprays. Specifically, atomization quality as a function of time delay, axial, and radial dispersion as a

function of droplet size, time, and space are studied. Our findings contribute to fundamental research in atomization and sprays, and also assists the development of a robust transient atomizer to produce artificial expiratory injections for use in ventilation tests.

Chapter 3

Review of Building Ventilation Design Parameters on Infection Risk (Far-field)

Before developing specific experimental and numerical methodologies, it is necessary to review parameters that affect cross infection risk due to expiratory injections within ventilated rooms. These pertain to ventilation type, temperature, relative humidity, air change rate per hour, ventilation effectiveness, diffuser type, contaminant type, heat gains and losses, occupancy, room geometry, and engineered disinfection of air. This chapter provides a thorough review of literature for the effect of such parameters.

3.1 Categories of ventilation systems

Ventilation systems can be classified according to the mechanisms driving airflow. *Mechanical ventilation* systems are fan driven. *Positive pressure* mechanical ventilation systems supply more air at the inlet than they remove through the exhaust. This results in exfiltration of space (i.e. air tends to leak out of ventilated space) with a net positive pressure in space compared to the outside. On the other hand, *negative pressure* mechanical ventilation systems remove more air at the exhaust than they supply at the inlet. This results in infiltration of space and a net negative pressure in space compared to the outside[11, 95]. Various other spaces can be pressure neutral, with the same amount of air supplied and exhausted.

Natural ventilation systems rely on natural forces such as wind or a density generated pressure differences between indoor and outdoor to drive air through building openings. Some purpose-built openings include doors, windows, solar chimneys, wind towers, and more [11, 95]. Advanced natural ventilation systems with passive cooling or heating have also been developed.

In these systems, outdoor air is supplied via stacks fed from below-ground concrete plena providing passive cooling or heating. Air leaves the space through stacks. In some advanced systems central control units operate dampers at inlet and outlet locations for each space [95].

Hybrid (mixed-mode) ventilation systems rely on natural driving forces when sufficient and use mechanical ventilation for augmentation as necessary. These systems use mechanical ventilation whenever the natural ventilation system cannot maintain the required indoor conditions. Sometimes, exhaust fans are used to assist natural ventilation in a negative pressure arrangement [11]. In some systems Passive Down-draught Cooling (PDC) encourages air to fall through chilled water pipes at a high level during hot weather. During cool weather some systems use exhaust flows to warm the incoming air (heat recovery). Usually sensors and control technologies are required for optimum performance of hybrid systems [95]. Table 3.1 shows major advantages and disadvantages associated with the ventilation systems described above [11].

Another categorization for ventilation type relates to the structure of the air motion. Two important variations are mixing and displacement ventilation systems. *Mixing* ventilation aims at creating a uniform low concentration of infected air that is subsequently extracted. The air is supplied along the ceiling with high turbulence for effective mixing [99]. *Displacement* ventilation flows are driven by air density differences in the room (buoyancy). In practice, neither pure mixing nor pure displacement ventilation can be achieved. There is always a combination of the two mechanisms with one being dominant in different zones in a room [99].

Ventilation system	Advantages	Disadvantages
Mechanical	Suitable for all climates, more controlled and comfortable environment	Expensive installation and maintenance, noisy, not fail-safe
Natural	Suitable for warm climates, inexpensive, capable of achieving high air change rates	Difficult to predict actual performance, affected by outdoor conditions, reduced comfort level, high-tech versions difficult to implement and control
Hybrid	Suitable for most climates, energy savings, more flexible	May be expensive, difficult to design and control

Table 3.1: Summary of advantages and disadvantages of different types of ventilation systems for hospitals [11]

In mechanical ventilation, one strategy to reduce infection risk is to use displacement ventilation. The vertical upward type displacement ventilation introduces fresh cool air near the bottom of the room. The air temperature rises by the heat from warm objects (like human bodies) and the buoyant force takes the warm and polluted air (possibly containing airborne pathogens) close to the ceiling and subsequently the exhaust for removal [99]. Laminar or plug flow ventilation, on the other hand, introduces cool and heavy air at the top with the exhaust removal at the bottom. The cool air drops due to negative buoyancy and reaches the floor if air mixing is avoided. This ventilation scheme, if it could be properly designed and operated, would be ideal for removing large droplets [82, 99]. For upward displacement ventilation, high ceilings are required and the heat gains by walls and equipment must be minimized. For laminar or plug flow ventilation, air mixing should be avoided as much as possible.

For naturally ventilated buildings the prediction of airflow distribution structure is more difficult since outdoor air movement behavior is less predictable. Two major factors affecting this are wind pressure and stack (or buoyancy) pressure. When wind strikes a building, it induces a positive pressure on the windward face and a negative pressure on the leeward face. This drives airflow through the building from the positive to the negative pressure openings. The stack (or buoyancy) pressure is generated by the air temperature (or density) difference between indoor and outdoor air. This difference generates an imbalance in the pressure gradients of the inside and outside air columns causing a vertical pressure difference [11].

Natural ventilation systems can be categorized into four groups. In *cross flow* systems, there are no obstacles on either side of the prevailing wind. In *wind tower* systems, the wind is caught on the positive pressure side and extracted on the negative pressure side. In *simple flue stack* systems, a vertical stack at each room allows for air movement to the roof. In a *solar atrium stack*, a large stack is heated by solar radiation, assisting the air movement and removal in the upward direction [11].

Hybrid ventilation system design methods can be grouped into three major categories. In *fan-assisted stack* systems, a fan supplements the extraction of air at the exhaust location of stack. In *top-down* systems, the air extraction is assisted by a wind tower. In *buried pipe* systems, when land is available, ventilation pipes (earth tubes) are used to bring air temperature to steady state values [11].

Major design elements for natural or hybrid ventilation systems require *site analysis, building design analysis, and vent opening design.* The site analysis concerns building location, layout, orientation, and landscaping;

building design analysis involves the type of building, functions, form, envelope, internal distribution of spaces, and thermal mass; and vent opening design concerns the position, type, size, and control of openings [11].

3.2 Ventilation performance indices

Numerous metrics are available to assess the performance of a ventilation system to the point that it is sometimes difficult to decide which metrics to use for a particular analysis. Fortunately, these metrics are provided with their specific applications in the American Society of Heating, Refrigerating and Air Conditioning Engineers (ASHRAE) fundamentals handbook [8]. The following sections only refer to the metrics that are useful to assess the ability of a ventilation system in removing contaminants from space.

3.2.1 Temperature and relative humidity

The most natural indices to use for ventilation performance are temperature and relative humidity. As discussed in section 1.1.3.1, temperature and relative humidity affect pathogen viability. The building code has not yet been fully refined to require specific combinations of temperature and relative humidity to reduce airborne infection risk. Neither does it make any recommendations specific to the type of pathogen that is being considered. For example, ASHRAE 170 and Canadian Standards Association CSA−Z317.2−10 do not require specific temperature or relative humidity levels for some functional spaces in health care facilities, but they do stipulate specific temperatures and relative humidities for critical units such as the operating room [10, 25]. Part of the difficulty is the lack of knowledge for aerosolized pathogen survival behavior in various environmental conditions. Also, some environmental conditions are against human comfort or the recovery process. More research is needed in this field to improve the building code.

Another area of concern is microbial growth in humid environments within the HVAC system (e.g. ducts, humidifiers, evaporative air coolers, cooling coil drain pans, and condensation sites). Kowalski and Bahnfleth [55] report that spores in particular take advantage of humid conditions to germinate and multiply. ASHRAE 170 limits the amount of relative humidity to a maximum value of 90 % throughout the duct work of any HVAC system [10].

3.2.2 Air changes per hour

Air Changes per Hour (ACH) gives the volume fraction of the ventilated space that is replaced by fresh air every hour. The choice of time unit is arbitrary, but the hour is the most commonly used unit. If the volumetric flow, Q, is expressed in m^3/h, and the volume of the room, V, is in m^3, then ACH is

$$ACH = \frac{Q}{V} \tag{3.1}$$

Air Changes per Hour (ACH) is defined differently for positive and negative pressure rooms. For positive pressure rooms, it is the ratio of the volume of air flowing into a given space in an hour divided by the volume of that space. For negative pressure rooms the exhaust airflow rate is used for this calculation [11]. Typically, a higher ACH results in more dilution of pathogens and reduced airborne infection risk [11, 95]. If the outdoor conditions are favourable (e.g. temperature differences and wind patterns), naturally ventilated buildings have higher ACH than mechanically ventilated buildings.

Most building codes mandate a minimum ACH to prevent airborne disease transmission by sufficient air dilution. For example, US Center for Disease Control (CDC) and prevention, World Health Organization (WHO), and the American Society of Heating, Refrigeration, and Air-conditioning Engineers (ASHRAE) all require a minimum of 12 ACH and negative pressure for newly built airborne infection isolation rooms [10, 15, 108]. Table 3.2 shows a list of health care facility functional spaces, with examples of subspace ACH and pressure requirements published by Standard 170 of the ASHRAE [10].

Critical care units such as wound intensive care units (e.g. burn units) are required to be provided with zone humidity control. Typically, the humidification is in the Air Handling Unit (AHU) with sensors in the critical spaces. Sometimes room level control is provided with portable units. These areas require to be positively pressurized. *Airborne Infection Isolation* (AII) rooms are defined as spaces to isolate patients with highly infectious diseases (e.g. *Tuberculosis* and influenza). For these rooms, the code requires continuous negative differential air pressure. Further, the exhaust position is recommended (but not required) to be above the patient's bed. *Protective Environment* (PE) rooms are designed to protect immunocompromised patients (e.g. AIDS) from human and environmental airborne pathogens. The code requires these rooms to be well-sealed and to provide continuous

Functional space category	Supspace functions (minimum required ACH±[1])
Surgery and critical care	Class A (15+), B (20+), and C (20+) operations, newborn intensive care (6+), triage (12+)
Inpatient nursing	Patient recovery (6), protective environment (12+), airborne infection isolation (12−), corridor (2)
Skilled nursing facility	Resident (2), gathering/activity/dining (4)
Laboratories	Diagnostic radiology (6), surgical radiology (15+), bacteriology (6−), microbiology (6−), autopsy (12−), sterilizing (10−)
Diagnostic and treatment	Examination (6), medication (4+), treatment (6)
Sterilizing and supply	Sterilizing equipment (10−)
Central medical and surgical supply	Clean workroom (4+), sterile storage (4+)
Service	Food preparation (10), laundry (10−), bathrooms (10−)
Support	Hazardous material storage (10−)

Table 3.2: Functional spaces in health care facilities [10] ([1]+ : Positive pressure required − : Negative pressure required)

positive differential air pressure. Also, the air inlet diffuser is required to be above the patient's bed, and the exhaust return is required to be near the door. *Surgery* rooms are classified in three major subcategories (A, B, and C). Class A surgery provides minor surgical procedures without preoperative sedation. Class B surgery is minor surgery with oral, parenteral, or intravenous sedation or under analgesic or dissociative drugs. Class C surgery provides major surgical procedures that require general or regional block anesthesia and support of vital bodily functions. The code requires positive pressure differential for class B and C surgery rooms. In addition, the inlet diffusers should be placed on top of the surgical bed, and the return exhaust grilles should be near floor level. For *Morgue* and *Autopsy* rooms, the code requires that the exhaust air should not be combined with air from any other exhaust systems.

Contrary to the ASHRAE 170 standard, which requires mechanical ventilation in all functional spaces, other standards have promoted the use of natural ventilation. For example, the United Kingdom National Health Service (NHS) policy mandates mechanical ventilation only for principal medical treatment areas such as airborne infection isolation rooms, operating theatres and associated rooms. Inpatient rooms are not required to be ventilated mechanically [11].

3.2.3 Ventilation effectiveness

Increasing ACH (higher dilution) is not the only way to reduce airborne infection risk. ACH is a useful but blunt instrument to assess the ventilation rate of a space. A room may have a high overall ACH, but with low ventilation in specific areas. Various formulations have been developed to account for this difference. Ventilation effectiveness follows the same concept as air changes per hour, but it is used to reveal air refresh rate for a specific point in the ventilation domain. A higher ventilation effectiveness indicates a more effective mechanism for the removal of contaminants in a given location. The hypothetical completely mixed ventilation systems has the same ventilation efficiency everywhere. If it is greater than one for a given location, then it surpasses the performance of a highly mixed system. Rooms with short-circuited airflow patterns have very high ventilation effectiveness in some areas while stagnant air in other areas correspond with very low ventilation effectiveness [11]. A complete ventilation study must consider both ACH and space-resolved air change effectiveness.

3.3 Parameters affecting ventilation performance

As mentioned in section 3.2, the most important indices to assess the ability of the ventilation system in removing or disinfecting airborne contaminants are the ventilation effectiveness, Air Changes per Hour (ACH), temperature, and relative humidity. As a result, only those parameters that affect these indices are of great importance in ventilation design and will be discussed in this section. The ventilation space of interest is a single patient hospital recovery room.

3.3.1 Ventilation type

A study by Escombe et al. [33] in Peruvian hospitals in Lima revealed that opening doors and windows could provide a median ventilation of 28 ACH for inpatient rooms. They also report that facilities built more than 50 years ago, with large doors, windows, and high ceilings, provided a median ventilation of 40 ACH. This is remarkably higher than typical high air change rates in hospital rooms ventilated mechanically at 12 ACH. They used CO_2 tracer gas experiments to demonstrate high air change rates for natural ventilation in ideal conditions.

Yin et al. [112] studied dispersion of tracer gas and fine mono-disperse non-evaporating aerosols in mixing and displacement ventilation systems for mock-ups of fully occupied hospital wards. They used a tracer gas (SF_6), 1 μm, and 3 μm aerosols that were released at steady rate at patient bed. A photo-acoustic multi-gas analyzer with a multipoint sample was used to measure SF_6 concentration at various locations. An Aerodynamic Particle Sizer (APS) was used to measure the aerosol concentration. It was shown that displacement ventilation with 4 ACH removes tracer gas and fine aerosols more effectively than the mixing type ventilation with 6 ACH.

Zhang and Chen [114] studied the dispersion of fine mono-disperse and non-evaporating aerosols in ventilation systems with ceiling supply, side wall supply, and underfloor airflow distribution systems. A condensation aerosol generator was used to generate aerosols in the range $0.31-4.5$ μm. A particle counter was used to measure concentration at different heights. They observed that the underfloor system has a better aerosol removal performance than the ceiling type and side wall supply systems. They found that for the ceiling supply and underfloor systems the particle concentration was stratified both horizontally and vertically, while the particle concentration in a room with the side wall supply was uniform.

Wan et al. [105] performed CFD simulations and Interferometric Mie

Imaging (IMI) experiments to determine expiratory droplet dispersion in a hospital ward with a mixing type ventilation system. They used an air-blast nozzle for droplet generation. This nozzle provided an injection velocity of 10 m/s, an air temperature of 34 ^oC, and an airflow rate of 0.4 L/s. The volatile fraction of the surrogate fluid was 0.94, which was representative of oral fluid. In their simulations they used droplets of various size bins in the range $1.5-1500$ μm with a mode of 12 μm. For a perfectly mixed system the decay of aerosols due to removal in a ventilation system is exponential. They found, however, that decay rate is faster in reality due to deposition of droplets and the fact that most mechanical ventilation systems operate in conditions between perfectly mixed and perfectly displaced ventilation. Two distinctive behaviors were observed: small size group aerosols (smaller than 45 μm) exhibited airborne transmittable behavior, whereas large size group aerosols (larger than 87.5 μm) settled quickly under gravity. Also, the dispersion of droplets exhibited different regimes with elapsed time. This was due to momentum interaction of the jet with the background flow and also the size change of aerosols due to evaporation.

Using simulations, Xu et al. [110] demonstrated that a displacement ventilation with an air change rate of 4 ACH performs better than a mixing type ventilation system with 6 ACH so that it provides a higher ventilation effectiveness (greater than one) in the breathing zone.

Lee et al. [60] performed a simulation study to observe the effect of air change rate in the performance of displacement ventilation systems. They observed that increasing the air change rate enhances mixing and competes with thermal and contaminant vertical stratification in the room. As a result, the ventilation effectiveness declines.

A study by Yu et al. [113] shows that naturally ventilated high-rise buildings with interconnected flats benefit from high air change rates, but the airborne pathogens can travel between flats, usually to higher levels, where the infection risk will be the highest.

A recent addendum to ASHRAE 170 [10] allows use of group D diffusers (displacement ventilation) for single bed patient rooms with a minimum of 6 ACH. The standard, however, requires group E diffusers for all class surgery rooms, Protective Environment (PE) rooms, wound intensive care units, and group A or E diffusers for airborne infection isolation rooms. For these spaces, the principal guideline by ASHRAE is to increase airborne pathogen dilution and hence to reduce infection risk. Other guidelines allow for displacement ventilation in health care facilities. CSA−Z317.2−10 [25] is silent on displacement ventilation. CDC [15] suggests downward laminar flow ventilation for isolation wards.

3.3.2 Diffuser type

The type and location of air supply and removal systems are key factors affecting the airflow distribution in ventilation spaces. For mechanical ventilation, ASHRAE defines various air supply diffuser types according to table 3.3.

Diffuser type	Description
Group A	In or near ceiling, horizontal discharge (e.g. multi-way)
Group B	In or near floor, vertical non-spreading discharge (e.g. perforated)
Group C	In or near floor, vertical spreading discharge (e.g. high throw swirl)
Group D	In or near floor, horizontal discharge (e.g. traditional displacement)
Group E	In or near ceiling, vertical discharge (e.g. linear)

Table 3.3: Supply diffuser types [10]

Various types of diffusers are possible to use for a ventilation strategy. A numerical and experimental study was performed by Lee et al. [61] to test the effect of perforated corner, swirl, linear, and perforated floor panel diffusers on the ability of the displacement ventilation to remove contaminants from a room. They found that swirl and linear diffusers have highest velocities (1.5 m/s) while perforated diffusers exhibit lower velocities ($0.1-0.3$ m/s). Linear diffusers throw air at high velocities so that the average velocity in the occupied zone was higher than 0.2 m/s. This caused thermal discomfort or draft. Other diffusers imposed lower air velocities in the bulk of the room and did not cause thermal discomfort due to velocity of air. Another source for thermal discomfort is a high temperature gradient. Under ideal displacement ventilation, it is possible to observe vertical temperature gradients as high as 3 ^oC per height of the person. Lee et al. [61] found that the traditional displacement ventilation with a corner diffuser injecting air horizontally exhibits the highest ventilation effectiveness in the lower part of the room. Linear and swirl diffusers on the other hand cause more mixing and therefore exhibit lower effectiveness in the lower part of the room. However, considering the total occupied zone, the corner and swirl diffuser achieve a similar overall ventilation effectiveness while the linear

diffusers achieves a lower overall ventilation effectiveness. They also studied the temperature vertical stratification as a function of diffuser type. Corner diffusers achieved the highest gradient, followed by low throw underfloor diffusers and then high throw underfloor diffusers. They also found that the corner diffuser generated the smoothest air flow pattern with the lowest turbulence intensity in the room. Other diffusers created more turbulence intensity with the linear diffuser disturbed the room air flow to the greatest amount.

Another simulation study by Lee et al. [60] also confirmed a higher ventilation effectiveness for traditional displacement ventilation compared to low and high throw under floor air distribution systems.

For mixing type ventilation and in extreme winter conditions, Memarzadeh and Manning [68] used simulations to show that radial diffusers are the best in combination with baseboard heating as opposed to linear slot diffusers that impose high jet velocities. These diffusers are not recommended for summer cases since they create a cold dump of air right on top of the patient. For summer cases the sensitivity of the ventilation performance indices to the type of diffuser is reduced since most of them provide good mixing. In modest winter or summer cases, the use of remote diffusers directed vertically downward is dangerous. In such arrangements the high momentum jet of air penetrates and reaches the occupied zone. Rather, a two-way diffuser is recommended.

3.3.3 Contaminant type and injection

Human respiratory activities also affect the airflow distribution structure. Breathing, coughing, and sneezing may all affect the room airflow. Zhu et al. [116] studied dispersion behavior mono-disperse droplets numerically. They tried 30, 50, 100, 200, 300, and 500 μm droplets injected in a cough and found that droplets 30 μm in diameter are not affected by gravity and inertia forces and follow fluid motion closely while droplets in the range $50-200$ μm are significantly affected by gravity. They found that droplets larger than 300 μm are more affected by inertia than gravity. They studied near-field droplet dispersion for actual coughs of three human subjects. Their PIV measurements found cough velocities up to 22 m/s with $6.1-7.7$ mg of saliva expelled into background air. They studied the effect of the injection direction (horizontal and vertical) on contaminant transport in an overhead ventilation system. Transient treatment of the injection was not complete in their study since time averaging of the momentum boundary condition is implemented rather than simulating an instantaneous flow velocity.

Zhao et al. [115] used 1 μm droplets to simulate droplet dispersion in an indoor environment. The small size chosen by this group eliminated inertial and gravitational effects on droplet dispersion. They studied expiratory droplet dispersion as a function of injection momentum. Three injection velocities of 6, 20 and 100 m/s were used to enter droplets in an overhead ventilation system. Normal respiration, which corresponds to a small injection velocity, has a small influence on indoor environment. However, coughed and sneezed droplets traveled as far as 3 m.

The study of Yin et al. [112] was not detailed enough as far as droplet size and transient injection of droplets are concerned. It is desired to test droplets in size distribution varying from sub-micrometer to a few tens of micrometers. In their study there is no mention of transient injection of droplets, nor is the injection velocity or direction varied.

Particle release in the study of Zhang and Chen [114] was steady at a rate of 0.07 L/s that is equivalent to normal breathing. The study can be improved by transient injections with varying momentum and direction.

In the study of Wan et al. [105], the dispersion of droplets exhibited different regimes with elapsed time. This was due to momentum interaction of the jet with the background flow and also the size change of aerosols due to evaporation. The injection was upward at the center of the room and at a height of 0.8 m. After an initial downward motion, which was induced by the bulk air current, the small droplets nuclei were then transported towards the exhaust air vent at the ceiling. The lateral dispersion of the droplets exhibited a two-stage behavior as well. A rapid increase in the lateral mean dispersion distance was observed in the early stage of dispersion. This was followed by a relatively stable trend afterwards.

A simulation study by Gao and Niu [36] revealed that normal breathing does not pose great exposure for contaminants in a room for healthy individuals, but coughs and sneezes can effectively transport contaminants as far as 3 m in a displacement-ventilated room.

Qian et al. [82] performed experimental and simulation studies for contaminant dispersion in a downward ventilation system. Two injection directions were considered, vertical towards the ceiling and horizontal towards the subject. The diffuser was placed on the ceiling and the exhaust was placed either close to the floor or higher on the wall. When the exhaust was placed close to the floor, the face-to-face arrangement resulted in a lower exposure index. On the other hand, when the exhaust was placed higher on the wall, the face to face arrangement resulted in a higher exposure index.

A simulation study by Xu et al. [110] demonstrated that constant breathing boundary condition is the same as the actual, transient breathing bound-

ary condition if considered over time and length scales large enough in the room with respect to the breathing cycle and the size of the patient. Further, they claim that breathing activity has little impact on the general flow and temperature distribution in the room. Constant and transient breathing have very similar effects in contaminant transport in the room (except for the immediate neighborhood of the patient head).

Xu et al. [110] performed a simulation study for a vertical cough injection in displacement and mixing ventilation schemes. They modeled transport of a tracer gas and found that although the cough time was very short (about 0.73 s) the concentration around the patient bed increased over the total simulation time of 5 min. The concentration of coughed gas around the patient bed is lower for displacement ventilation than the mixing ventilation. This means that the ventilation effectiveness is higher for the displacement ventilation around the occupied zone. Nevertheless, for the room as a whole, the difference between two ventilation systems in terms of response to coughing is almost identical.

3.3.4 Heat gains and losses

Lee et al. [61] observed that high heat sources in a room can help thermal vertical stratification in displacement ventilation but can cause large temperature gradients that result in thermal discomfort. For example, under cooling mode in displacement ventilation, a temperature difference as high as 3 ^oC was observed over the height of a person.

Lee et al. [60] showed that increasing the cooling load of a room with displacement ventilation improves the ventilation effectiveness slightly. This is expected since stronger thermal plumes and cooler air supply improve the thermal and contaminant vertical stratification in a room.

A simulation study by Xu et al. [110] demonstrates that in both displacement and mixing type ventilation schemes, thermal comfort suffers from solar radiation such that it should be minimized in inpatient rooms. Also, solar loading of displacement ventilation in the summer causes ventilation effectiveness to reduce.

3.3.5 Occupancy

Occupation density is an important factor affecting airflow distribution in a space. Overcrowding is often correlated with increased rates of infection. Not only does the high thermal load of people make the airflow distribution unpredictable, but also droplet mode and contaminated surfaces contribute

towards disease transmission. Some physicians believe there should be a minimum of two arm's length between patients [69].

Human occupants also generate thermal plumes that interact with ventilation airflow and other plumes in ventilated space. In some situations (e.g. upward displacement ventilation) these plumes can assist aerosol removal. Thermal plumes can also prevent aerosol removal from ventilated spaces. For example, a malfunctioning upward displacement ventilation system can create recirculation zones that keep aerosols in the domain for long periods of time. Also, thermal plumes increase mixing in downward laminar flow ventilation systems, impeding aerosol removal through low level exhausts [82].

Qian et al. [82] performed experimental and numerical studies to show that thermal plumes increase mixing in downward laminar flow ventilation systems, blocking aerosol removal through low level exhausts.

Xu et al. [110] used simulations to show coughed gas concentrations around the patient bed although they did not consider the effect of the location of the thermal source. They demonstrated that, away from the patient, the concentration is lower.

Occupant motion and other activities also perturb the airflow in the ventilation domain. For example, the wake of a person when walking from one location to another may be responsible for mixing of air and hence increasing airborne infection risk. Other actions such as opening or closing doors and windows can also be important [99].

Mazumdar et al. [65] studied the effects of occupant movement, changing bed sheets, and opening doors on contaminant dispersion numerically. The effect of object movement was studied for both displacement and mixing ventilation types. They observed that variation of average contaminant concentration due to moving objects was within 25 % for all cases studied. For most cases the effect of movement on contaminant dispersion only lasted up to 90 s, after which time the concentration reverted to normal decay. It was hypothesized that these variations would not likely change the risk level in the room.

In many cases, the impact of occupancy is poorly understood and much research is needed for the improvement of building codes and design standards.

3.3.6 Room geometry

The location, size, and volumetric airflow of supply and extraction openings affect flow patterns and airborne infection risk levels. The arrangement of

inlet and outlet openings can cause different flow recirculation scales which may change the mean age of indoor contaminants.

Chung and Hsu [19] studied the effect of diffuser and exhaust locations on the removal of contaminants. They observed how ventilation effectiveness changes at various locations. Interestingly, although the total air change rate is insensitive to the location of the diffuser and exhaust, the local ventilation effectiveness varies greatly from one case to another. For example, excluding the effect of occupancy and buoyancy, the most efficient design is to locate diffuser and exhaust face to face at the same height and at opposite sides of the room. The complexities arise for actual rooms with occupancy and heat gains, in which scenario a detailed study must be performed.

Yin et al. [112] observed that the performance of the displacement ventilation system is very sensitive to the location of all exhausts. If any exhaust is located at low level, the pollutant concentration at breathing zone will be worse than mixing type ventilation. All exhausts must be located at high levels, preferably closer to the pollutant source.

A simulation study by Lee et al. [60] showed that using a higher number of diffusers (with lower airflow rate per each diffuser) reduces mixing and results in higher ventilation effectiveness, particularly in lower heights of the room.

Contrary to the common belief, Lee et al. [60] argued that high throw underfloor air distribution systems can sometimes be desirable, especially for high ceilings in classrooms. In such situations most mixing occurs above the breathing zone of the occupant so that ventilation effectiveness in this configuration is higher in the breathing zone than it is for low ceiling rooms with low throw ventilation systems. They recommended that higher ceilings be designed since they help with thermal and contaminant vertical stratification in the room.

A study by Qian et al. [82] used N_2O tracer gas to observe the effect of diffuser and exhaust locations on the performance of ventilation system to remove pollutants in a mock-up hospital ward with thermal manikins. In their experiments, the diffuser was placed over the patients head, but the location of the exhaust was varied. All experiments were run at 4 ACH. They observed that downward ventilation systems could not produce a unidirectional airflow pattern since thermal plumes of manikins induced mixing and disturbed pollutant removal. On the other hand, a higher location for the exhaust caused more effective removal of pollutants.

Memarzadeh and Manning [68] showed that for mixing type ventilation, particularly during cold winter conditions, it is better to place the exhaust at a lower level. This provides better mixing and, as a result, higher values

for thermal comfort.

For upward displacement ventilation, Xu et al. [110] also confirmed by simulations that a higher location of exhaust (or equivalently a higher ceiling) improves vertical thermal and contaminant vertical stratification.

3.4 Engineered disinfection of air

3.4.1 Filtration

Two sources of clean air can be used to refresh indoor air: outside air and recirculated indoor air. Sometimes a combination of these are also used. Conditioning outside air can be energy intensive, but, on the other hand, using recirculated air provides substantial opportunities to save energy in buildings. Kowalski and Bahnfleth [55] show that under certain conditions, using recirculated air with High Efficiency Particulate Air (HEPA) filters reduces particulate concentration for indoor air similar to full outside air systems. Cole and Cook [20] also report that ventilation plus recirculating air filtration could reduce droplet nuclei concentrations with $30-90$ % effectiveness.

ASHRAE 170 requires up to two filter banks in the design of some health care unit ventilation systems. Filter bank No. 1 is placed upstream of the heating and cooling coils and the supply fans to filter all of the incoming mixed air. Filter bank No. 2 is installed downstream of all wet air cooling coils and supply fans.

A few challenges remain in the filter design and fabrication technology. For example, more efficient filters cause more pressure drop, and hence may require auxiliary fans to supply the required pressure. This increases energy consumption of the HVAC system. Also, filters are difficult to use with natural ventilation systems since the pressure differential in such systems is not enough to drive adequate flow through filters. The other challenge is filtration of aerosols in the range $0.1-0.3$ μm economically. Aerosols smaller than 0.1 μm are efficiently captured by diffusional forces, and aerosols larger than 0.3 μm are efficiently captured by impaction.

3.4.2 Ultra violet radiation

Ultra Violet (UV) radiation can play a key role in disinfecting pathogens or limiting their growth. For example, UV radiation has been used to limit microbial growth in cooling coils. UV radiation impairs fungal growth and

in some cases kills spores. Key factors to consider are air velocity, local airflow patterns, degree of maintenance, resistance of microbes, and humidity. Chronic dosing with UV radiation can also have a major impact on disinfecting airborne viruses and bacteria. One-pass exposure of pathogens to UV light may not be effective to disinfect them, but recirculating air through the UV radiation unit can be more effective [20, 55]. UV disinfection equipment is either placed upstream of air supply system or within the ventilated space close to the ceiling, where human exposure is minimal.

3.5 Concluding remarks

As described in this chapter, many parameters pertaining to ventilation design have been studied in the literature to assess dispersion and removal of pollutants within a ventilation domain. These were the type of ventilation system, the type of diffuser, the type and source of contaminant, the heat gains and losses, the occupancy, the room geometry, and the disinfection of air. It is not clear, however, how the injection parameters, such as momentum and direction, the spatial location of the source with respect to the suspect, and the thermal plumes within the room affect pollutant dispersion and removal. In this thesis, we study these effects in some greater depth to investigate the performance of an underfloor air distribution system in dispersion and removal of contaminants introduced by expiratory injections.

Chapter 4

Experimental Methodology

4.1 Near-field atomizer test methodology

An air-assist internally mixing cone atomizer was integrated in a machine to simulate cough/sneeze droplet generation. A similar technique has been used by Wan et al. [105] to inject droplets in a room with mixing type ventilation. Section 4.1.2 provides a methodology to measure the overall axial and radial development of a transient spray as a function of time. Sections 4.1.3 and 4.1.4 provide a methodology to measure the same axial and radial developments but as a function of droplet size.

4.1.1 Atomizer setup

The atomizer used in this study consists of an air nozzle assembly, two separate valves driven by a solenoid, a relay, a liquid tank, a pressure regulator, and two supply pressure lines. The nozzle assembly traverses in the horizontal, x, and vertical, r, directions. The gas and liquid lines are pressurized and the solenoid valves are operated by the relay. Two simultaneous pulses are supplied to the relay that powers the solenoids. The pulses actuate the valves and allow liquid and pressurized gas to flow and produce the spray.

The nozzle (SUQR-220B) was manufactured by Spraying Systems Co. with an orifice output diameter of $d_g = 2.4\ mm$ and an internal liquid jet diameter of $d_l = 1\ mm$. The fluid mixing is shown in figure 4.1. The Liquid cap has the center orifice that carries the liquid into the air cap. Around the fluid cap, near the front gasket, there are four orifices that introduce the atomizing air into the liquid stream. The full nozzle assembly is shown in figure 4.2. Deionized water was used as liquid, and pressurized nitrogen was used as gas for the spray tests. The temperature and relative humidity in the laboratory were $22-24\ ^oC$ and $45-55\ \%$ respectively.

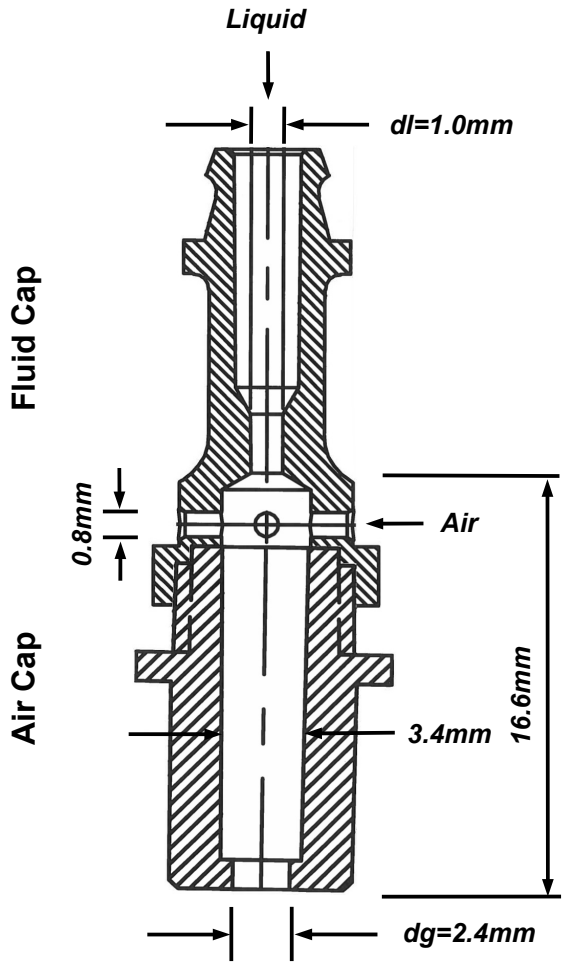

Figure 4.1: Fluid mixing schematic (with permission of Spraying Systems Co.)

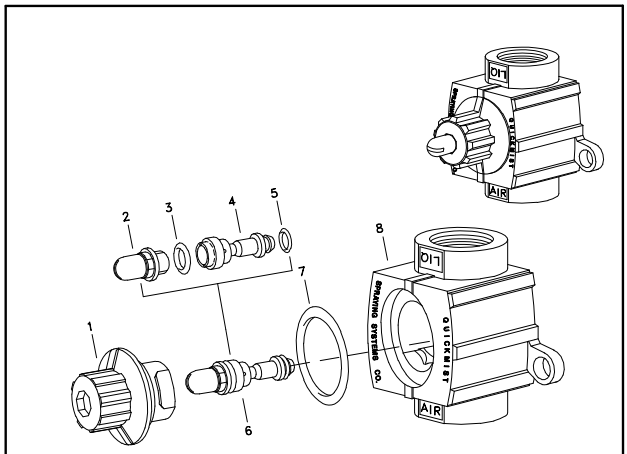

ITEM	PART NO.	DESCRIPTION
1	CP38862-KY	RETAINER CAP, KYNAR (GRAY)
2	PAQ*	AIR CAP, KYNAR
3	CP7717-2/11-VI	O'RING, VITON®
4	PFQ*	FLUID CAP, KYNAR
5	CP7717-3-VI	O'RING, VITON®
6	SUQ**	SPRAY SET-UP (INCLUDES ITEMS 2 THRU 5)
7	CP7717-2/117-VI	O'RING, VITON®
8	CP38867-1-KY	BODY, KYNAR (BLACK) FOR MODEL 1/4QMJML
	CPB38867-1-KY	BODY, KYNAR (BLACK) FOR MODEL B1/4QMJML
1/4QMJML QUICKMIST™ AIR ATOMIZING NOZZLE, KYNAR [1/4" NPT (F) INLET CONN.]		
B1/4QMJML QUICKMIST™ AIR ATOMIZING NOZZLE, KYNAR [1/4" BSPT (F) INLET CONN.]		

*SPECIFY AIR & FLUID CAP SIZES

**SPECIFY SPRAY SET-UP

DESCRIPTION:
1/4QMJML & B1/4QMJML
QUICKMIST
AIR ATOMIZING NOZZLES
WITH MOUNTING LUGS

Spraying Systems Co.®
Spray Nozzles and Accessories
P.O. Box 7900 - Wheaton, Il. 60189-7900

Rev. No.
Ref.

Parts List No.
PL 1/4QMJML & B1/4QMJML
SHEET OF

Figure 4.2: Nozzle assembly (with permission of Spraying Systems Co.)

4.1.2 Spray penetration test setup

A 'forward lighting' arrangement was used to take images of the spray using a LaVision Imager Intense Camera. A continuous light source was used so that a powerful backscattered signal from the droplets could be recorded. The physical distance between the camera and the atomizer was 2.7 m. A 50 mm 1 : 1.2 Nikon lens (386671) was used to provide a wide field of view of 475 mm. The area behind the atomizer was covered by a black mat. The camera exposure time was set to 500 μs. A complete schematic for the spray penetration test is shown in figure 4.3.

The atomizer and imaging were timed using a LabView system (consisting of a computer and a National Instruments BNC-2121 pulse generator) and a LaVision system (consisting of a computer and a Programmable Timing Unit (PTU) board to trigger the camera). First, a pulse was generated by the LabView system to trigger the solenoids and therefore initiated the injection. The same pulse was supplied to the LaVision system. Then, the LaVision Sizemaster/Davis 7.2 program signaled the camera for imaging by a pulse that was delayed by various times so that penetration of the spray could be observed at different times after valve opening. The delay time ranged logarithmically from 10 ms to 40 ms in 20 steps. Two flow conditions were considered in this study (table 4.1). The time resolution for the PTU sequencer I/O was 10 ns. The typical jitter between all outputs was less than 1 ns.

Test	1	2
Nitrogen Pressure $[psi]$	30	50
Water Pressure $[psi]$	15	25
$U_g[m/s]$	$[237]^1$	[351]
$U_l[m/s]$	[0.37]	[0.25]
$Re_g = U_g d_g/\nu_g$	34600	51200
$Re_l = U_l d_l/\nu_l$	370	260
$We_g = \rho_g(U_g - U_l)^2 d_l/\sigma$	940	2070
$\dot{m}_g/\dot{m}_l = (\rho_g A_g U_g)/(\rho_l A_l U_l)$	1.23	0.60
$p_g/p_l = (\rho_g A_g U_g^2)/(\rho_l A_l U_l^2)$	830	830

Table 4.1: Flow conditions for the spray tests (^{1}[]: Velocities are estimated using gas and liquid flow rates, exit diameters, and densities at room temperature provided by the manufacturer)

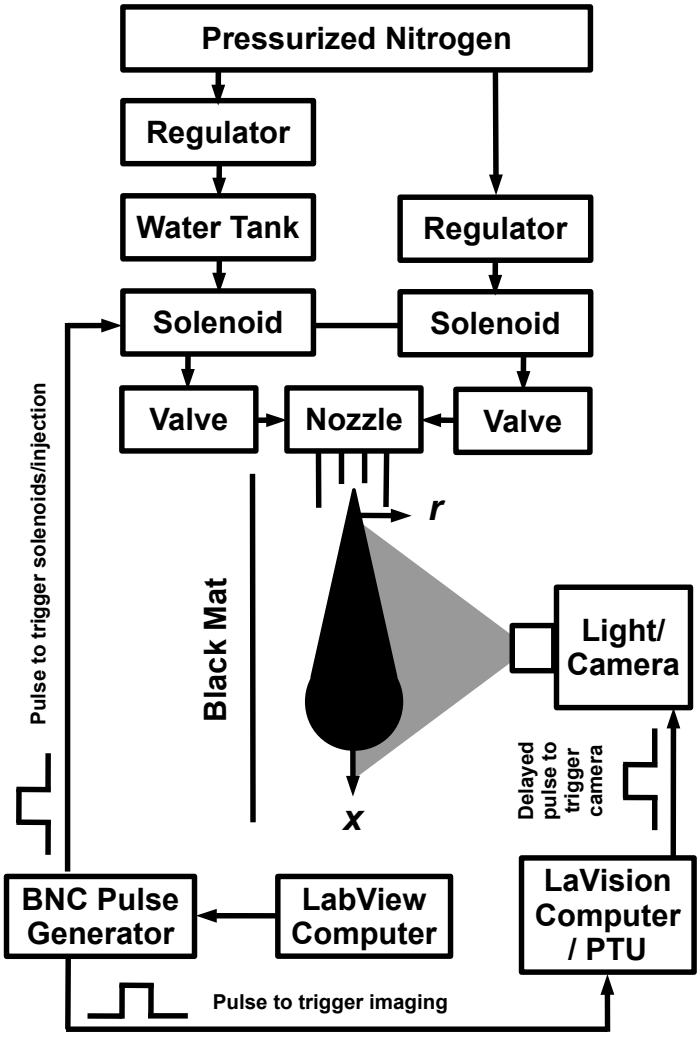

Figure 4.3: Schematic for spray penetration test system

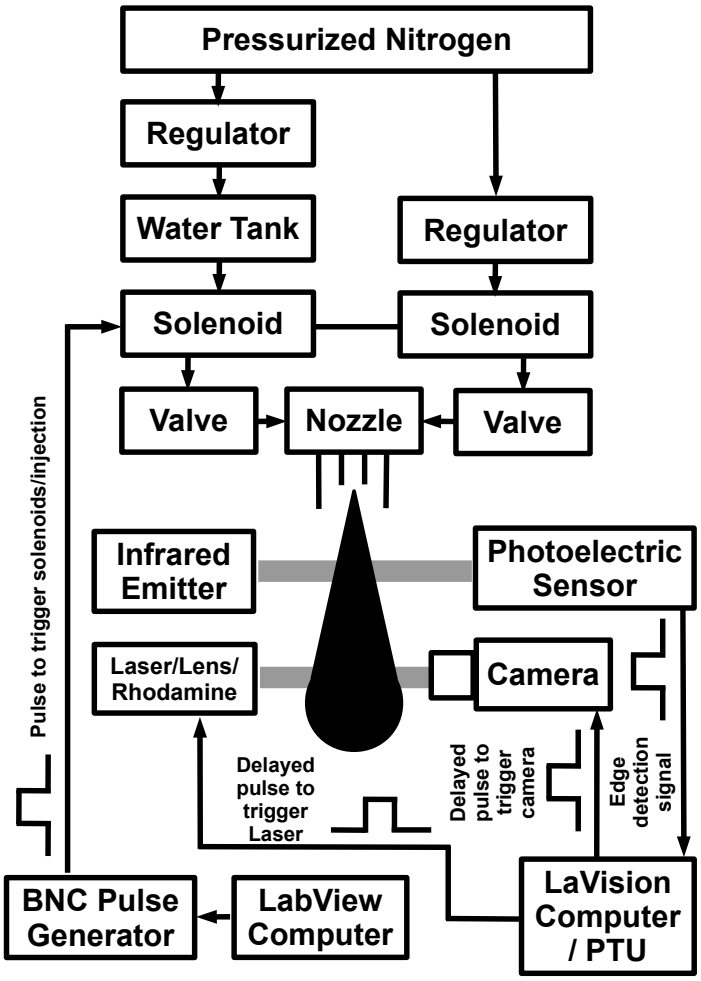

Figure 4.4: Schematic for spray shadowgraphy/PTV test system

4.1.3 Spray shadowgraphy test setup

A shadowgraphy technique was used to take close-up images of individual droplets. A 'backlighting' arrangement was used to take images of the spray using the LaVision Imager Intense Camera. A pulsed Laser (Big Sky Ultra) was used as a light source to shine a collimated beam of green light (532 nm). The beam was passed through a lens so that the beam was traced as a round circle of about 2 cm in diameter on a flat container of diffuse and fluorescent medium (liquid Rhodamine). The physical distance between the camera and the atomized spray was about 10 cm. A $14X$ magnification Navitar lens was used to provide a narrow field of view of about 0.5 mm by 0.3 mm. The camera exposure time was set to 500 μs and the Laser light source was fired at the end of the exposure time by the PTU. The actual exposure was just under 10 ns (the pulse width of the Laser). Only Test 1 flow conditions in section 4.1.2 were used. It was desired to measure the droplet size distribution at a location at a known elapsed time after the spray injection. To obtain precise elapsed times, the valve actuation time variability must have been eliminated. As a result, a pair of photoelectric sensor and an infrared emitter were arranged in a 'through-beam' setup at the exit of the spray near the nozzle tip. The receiver (C5R-AN-1A) and the emitter (C5E-ON-1A) were supplied by Automation Direct. If the spray blocked the infrared beam path, the receiver would produce a triggering signal for the PTU board. A complete schematic for this system is shown in figure 4.4.

The same LabView and LaVision systems were used for timing the injection and imaging. Again, a valve actuation signal was sent by the LabView system. Upon sensing the spray at the nozzle tip by the infrared sensor, a trigger signal (corresponding to either the leading or trailing edges of spray) was sent to the LaVision system. The LaVision system then sent two delayed pulses to both the Laser and camera for imaging. The delay helped determine droplet sizing at various times during the spray development.

In our experiment, LaVision's DaVis 7.2 Sizemaster program determined the droplet size using the following algorithm. The source images were acquired without smoothing, recommended when high quality images contain low noise or only a few hot/cold pixels. Then a smooth reference image was created for each source image with equal or more photon counts for all pixels. Subsequently the source image was normalized and inverted by the reference image. The resultant image contained droplets with high photon count pixels. Then global segmentation of the image was performed, where areas of the image with a higher than set point photon count were chosen

for analysis. Then, the particle segmentation was performed finding the average particle diameter for two areas associated with each global segmentation. One area covered a section with a high and another area covered a section with the low photon count thresholds. Usually a minimum and maximum pixel area are set for the software to avoid detecting noise or very large particles. All parameters set for shadowgraphy are given in figure 4.2. Droplets that are not in the depth of field may appear faintly with irregular shapes, but their intensity contrast with the background is not high enough so that the global segmentation does not consider them for counting.

Category	Sub-category	Value/Technique
Preprocessing	Image processing	No smoothing
Preprocessing	Reference image	Calculate for each image
Preprocessing	Reference calculation	Strict sliding max. filter
Preprocessing	Filter length	200 pixels
Particle recognition	Reference	Normalize by ref. image
Particle recognition	Global segmentation	40 % global threshold
Particle recognition	Particle segmentation	40 % low, 60 % high
Particle recognition	Particle segmentation	5 % AOI expansion
Particle recognition	Particle segmentation	Fill particles
Recognition filter	Maximum low level area	200 % of high level area
Recognition filter	Minimal area	25 pixels
Velocity parameters	Initial/final window size	$x = 0.5\ mm \times r = 0.2\ mm$
Velocity parameters	Number of passes	1
Velocity parameters	Diameter deviation	15 %
Velocity parameters	Initial shift	$x = 0.5\ mm \times r = 0.0\ mm$
Statistical results	Correct depth of field	100 μm reference

Table 4.2: Summary of shadowgraphy and particle tracking velocimetry parameters

Figure 4.5 shows the number distribution N_f for 6 μm diameter calibration microspheres suspended in liquid water. The microspheres were manufactured by Polyscience with a diameter standard deviation of 0.165 μm. A total of 4135 droplets in 30 images were detected. For this measurement, $d_{10} = 6.4$ μm. The shadowgraphy technique, like other droplet measurement techniques, 'broadens' the distribution, with a standard deviation of $\sigma = 2.2$ μm. As the result of this broadening, the measured d_{32} increases slightly to 8.2 μm. Figure 4.6 shows a sample image of droplets and the corresponding shadowgraphy technique that sized the droplets.

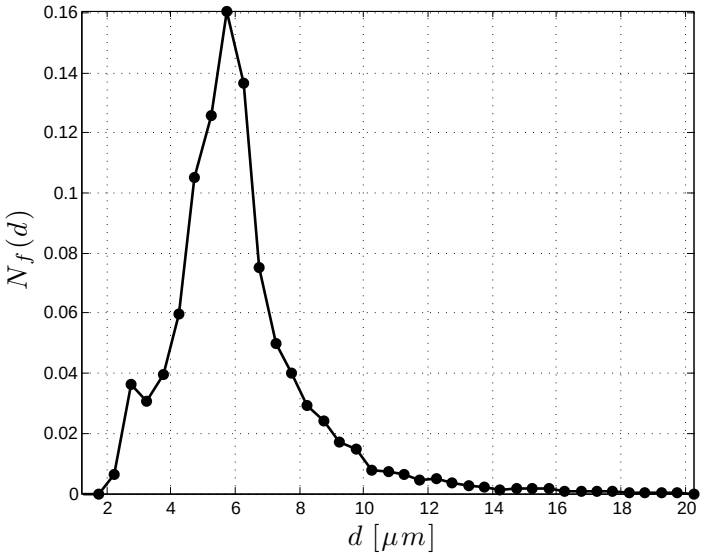

Figure 4.5: Number size distribution for 6 μm diameter calibration microspheres measured by the shadowgraphy technique

4.1.4 Spray particle tracking velocimetry test setup

The same optical system as in section 4.1.3 was used for size dependent Particle Tracking Velocimetry (PTV). A dual-head Laser generated two light pulses separated by 10 μs. The LaVision Imager Intense Camera was used to grab a double-frame image timed with Laser firing. Again, only Test 1 flow conditions in section 4.1.2 were used.

LaVision's DaVis 7.2 Sizemaster program determined the droplet ve-

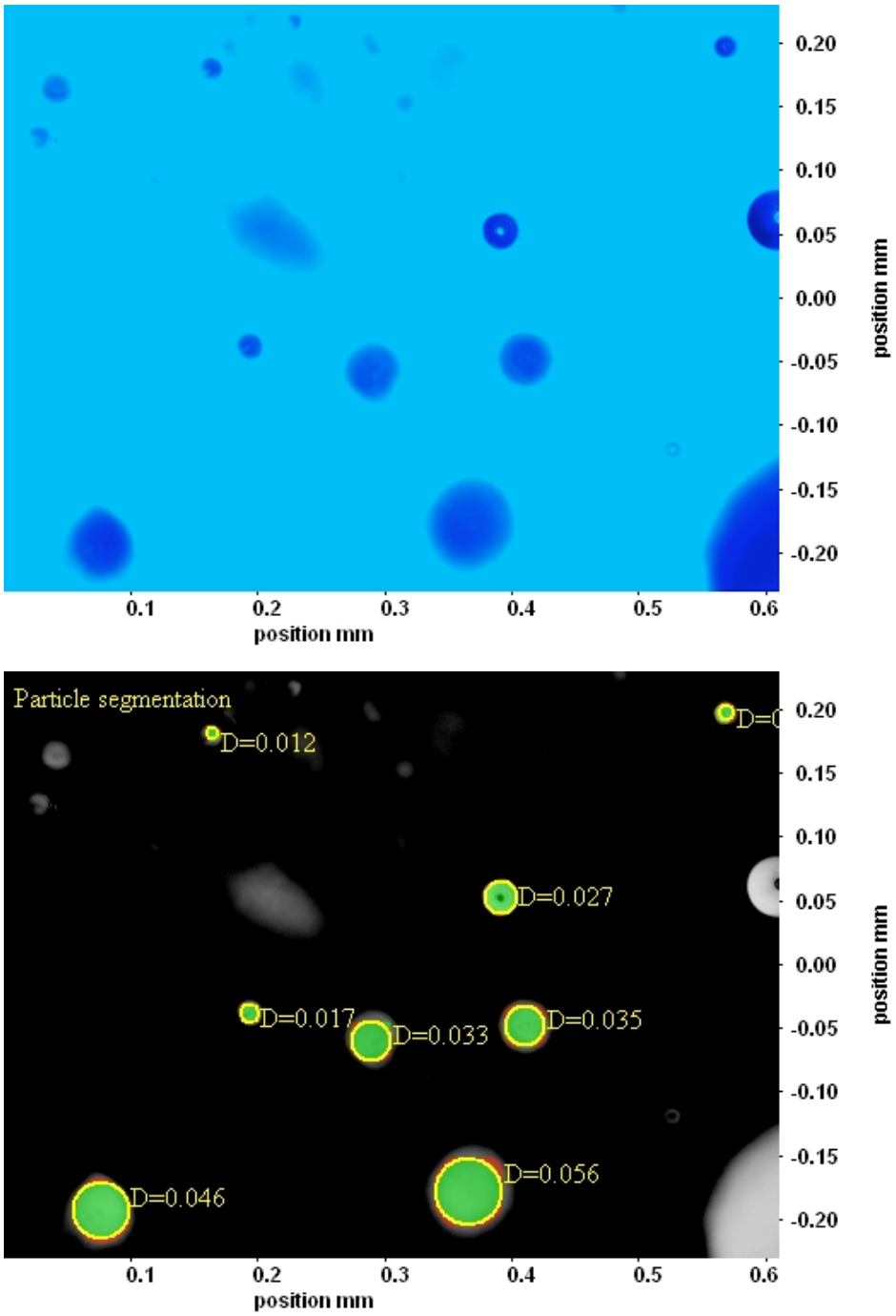

Figure 4.6: Sample droplet image (top) and shadowgraphed droplet size (bottom)

locity using the following algorithm. First the sizing algorithm described in section 4.1.3 determined the particle size for each frame of the image. The position and size for each particle were stored. The velocity algorithm identified two pairs of particles with two conditions: the allowed shift and the size. The initial and final window sizes determined the two windows in which particles were analyzed. The initial shift defined the center position of the final window, in which particles are accepted, relative to each particle location in the initial window. This shift was chosen in the direction of the axial flow of spray so that no reverse motion could be detected. The other parameter determined how much a particle size was allowed to vary between the two windows. All parameters set for PTV are given in table 4.2.

4.1.5 Valve actuation and rise time

For transient spray measurements, it is important to know the uncertainties in valve opening time as well as the delay for flow to reach maximum rate. The former ensures accuracy of the measurements of droplet size as a function of time delay. The latter informs the far-field study by indicating, for what fraction of the injection time, the spray quality is constant.

To test the valve 'actuation' time and flow 'rise' time, a pressure transducer was placed in front of the atomizer at a distance of 1 cm along the central axis. A PCB pressure transducer (model 112A05), a Kistler dual mode amplifier (model 5004), an iotech wave data logger (model WaveBook/512) and iotech wave recording software (model WaveView7) were used to read and log pressure data. The system sampled $500,000$ data points during 50 s with a sampling frequency of 10 kHz. Twenty five injections were made and the pressure trace was monitored.

The maximum cycle-to-cycle actuation time variability for all twenty five injections was 8 ms. The twenty five injections resulted in a pressure trace with a standard error ($P = 68$ %) that is plotted in figure 4.7. The reason for high fluctuations was individual droplet impaction on the sensor. The rise time t_f for the pressure was a good indicator of time required for liquid/gas flows to reach maximum value. The rise time was taken as the time required to reach 90 % of maximum for a smooth fit to the pressure and was estimated to be 9 ms. The actuation and rise time are also shown in figure 4.7.

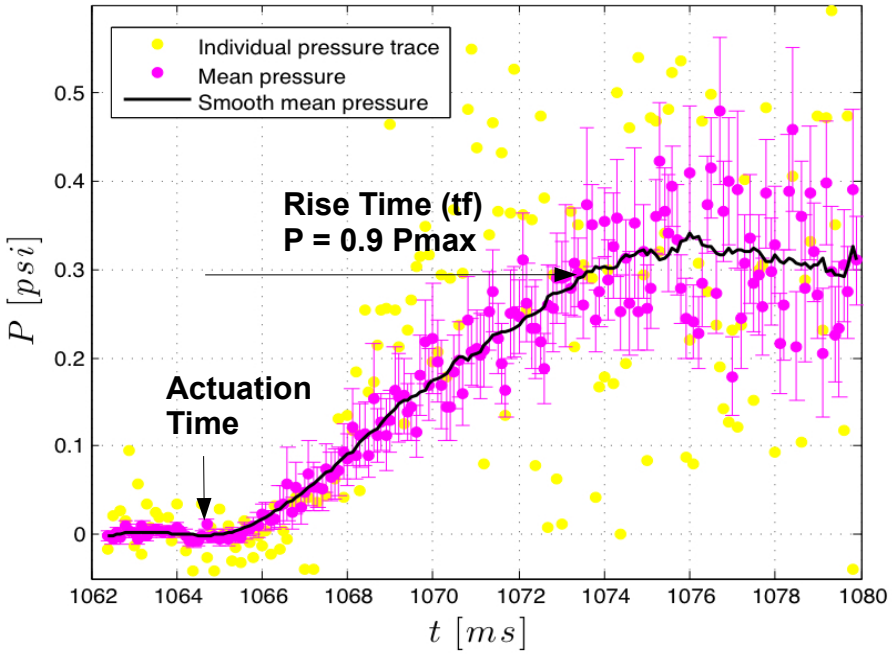

Figure 4.7: Pressure rise time at a distance of 1 cm in front of the nozzle due to valve actuation (Test 1 flow conditions)

4.1.6 Statistical analysis

Concentration, d_{32}, volume fraction, number fraction, velocity, and Péclet number were reported using three measurements, each calculated from 100 images. A t distribution was assumed for the data so that $x_{best} = \overline{x} \pm t_{P,\nu} \frac{\sigma_x}{\sqrt{N}}$ with $P = 68$ %, $N = 3$, $\nu = 2$, and σ_x the standard deviation for the three measurements. The mean values $\overline{x}$, the standard errors $t_{P,\nu} \frac{\sigma_x}{\sqrt{N}}$, and the curve fitting coefficient of determination R^2 were reported.

4.1.7 Droplet size range for analysis

To determine the atomization quality the droplets were analyzed in the range $2-100$ μm. For dispersion measurements, however, a smaller range ($5-60$ μm) was considered. Increasing the minimum droplet size reduced the effect of evaporation as described in section 2.1. Also, decreasing the maximum droplet size improved the statistics of large droplets as they occur less frequently in the flow.

4.2 Far-field ventilation test methodology

The far-field ventilation tests were performed in the Center for Interactive Research on Sustainability (CIRS) building located at 2260 West Mall, Vancouver, BC. The ventilation domain was a single room with an underfloor air distribution ventilation system. A swirl diffuser (Figure 4.8) was used, located on the floor near the window. The exhaust was located at a high elevation over the door. The window was kept closed at all times and an aluminum cover radiation shield minimized solar gains in the room during the experiments. This is recommended for stratified ventilation systems which are prone to air circulation disturbances causing the vertical stratification of temperature and pollutants to break down.

The room was set up with two thermal manikins (patient and nurse/visitor) and an atomizer injector placed on top of the patient. Thirty two sensors measured temperature on all the boundaries (walls, ceiling, floor, and diffuser) and the internal space of the room (5 poles). The aerosol concentration was measured in the range $0.5-5.0$ μm at three elevations on a moving pole (#1). Four anemometers measured the airflow rate at diffuser, exhaust, and internal locations in the room. Figures 4.10 and 4.9 show the schematic and the interior for ventilation test room.

The room x, y, and z dimensions were 2.93 m, 3.68 cm, and 3.77 m, respectively. The diffuser diameter was 0.25 m, and it introduced air at an

Figure 4.8: Swirl diffuser

upward angle of 35 ^{o} from the floor. The exhaust grill was 0.25 m × 0.50 m. The bed dimensions were $x = 0.56$ m × $y = 0.45$ m × $z = 2.15$ m. The atomizer assembly dimensions were $x = 0.31$ m × $y = 0.60$ m × $z = 0.62$ m.

Except for ventilation design of patient recovery rooms in hospitals described in chapter 2, there is no general standard on room geometry design. The mockup of the room in this study is representative and contains the major features that could potentially affect contaminant stratification and dispersion. These are placement of diffuser and exhaust, locations of the source and suspect, location of the atomizer, and the thermal plumes generated by manikins.

4.2.1 Temperature measurement

Thirty-two type T thermocouples manufactured by Omega were used to measure the temperature at the boundaries and internal space of the room. Five poles measured internal temperature at various elevations. These elevations were $LL = 0.10$ m, $L = 0.85$ m, $M = 1.63$ m, and $H = 3.00$ m. Wall temperatures were measured at similar elevations. The temperature range within the internal space of the room was expected to vary by

Figure 4.9: Ventilation test room

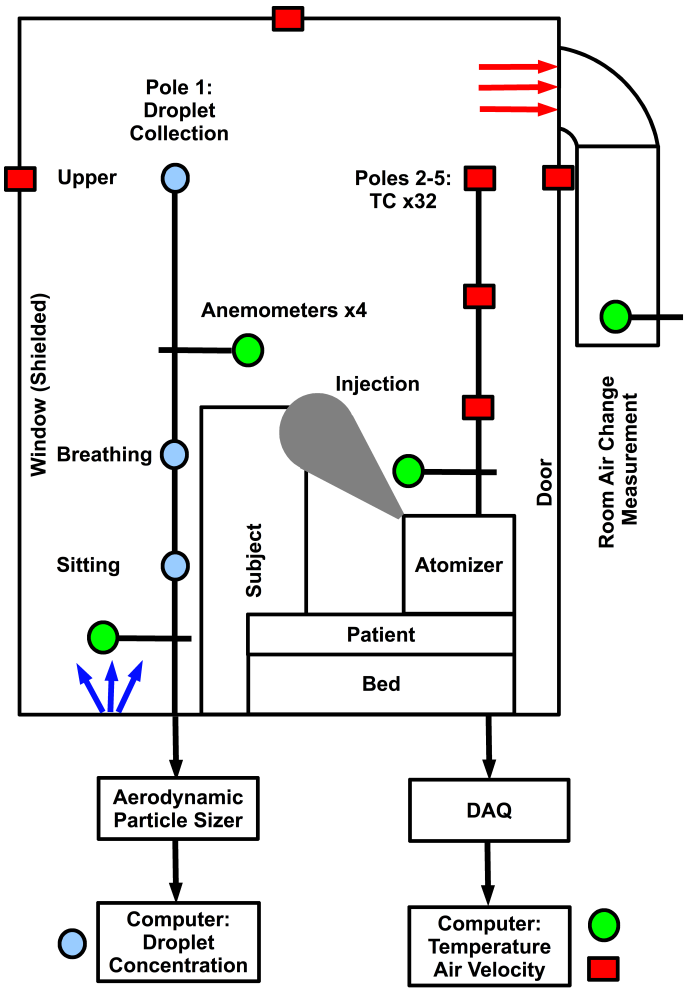

Figure 4.10: Schematic for ventilation test room

a few degrees and the gradient to be usually vertical due to thermal vertical stratification. Since this gradient is small, it was desired to calibrate the thermocouples with high accuracy and precision so that even a weak thermal vertical stratification could be noticed.

All 32 thermocouples were calibrated in a water bath whose temperature varied from 15 ^oC to 45 ^oC. A large plate of aluminum, which has high thermal conductivity, was used, and all thermocouples were taped and gently squeezed by an insulating foam on the plate so that good thermal contact could be achieved. Figure 4.11 shows the 32 thermocouples that were taped on the aluminum plate. The plate was immersed half way in water. The water temperature was varied using a hot plate that provided heat very gradually to the water. At the same time the water was mixed to ensure a homogeneous distribution of temperature around the aluminum plate.

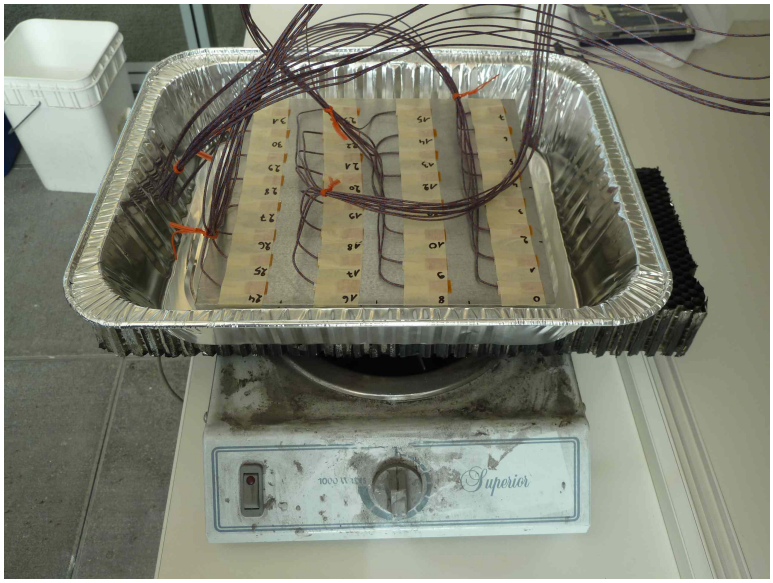

Figure 4.11: Thermocouple calibration device

The absolute temperature measurement was not a stringent requirement for this study, but the relative error among thermocouples was very important and should have been minimized. Therefore, all 32 thermocouples were calibrated with reference to thermocouple number 0. For this purpose a straight line was fitted through temperatures measured by all thermocouples versus thermocouple number 0. The fit coefficients were then entered

into the Tracer DAC Pro software. This software was used to log temperatures for all thermocouples simultaneously. Figure 4.12 shows the measured temperature for thermocouple number 1 versus thermocouple number 0.

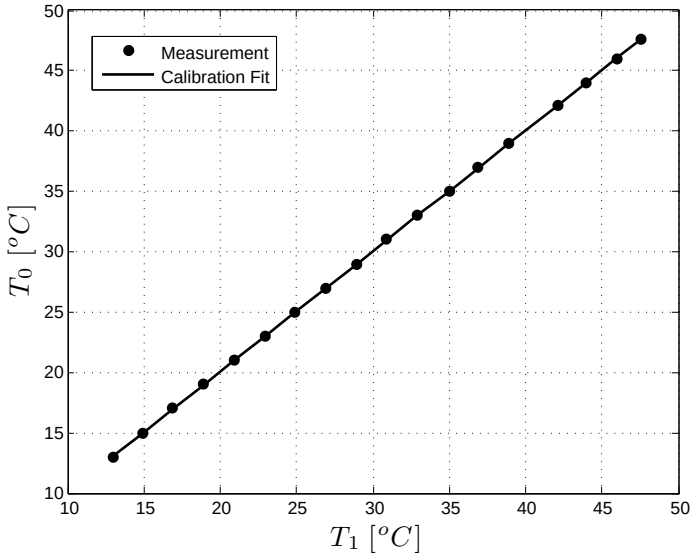

Figure 4.12: Calibration curve for thermocouple number 1

4.2.2 Velocity measurement

Four Thermo Air 6 omnidirectional anemometers were used to measure air velocity in the range $0.01-1\ m/s$. These thermoelectric probes were suitable for measuring small flow ranges of gaseous media. They were calibrated for air with temperature compensation. Figure 4.13 shows the anemometer used for the ventilation experiments. Two of the four anemometers were placed at the diffuser inlet and the exhaust duct for all experiments. The other two were placed in various locations. Most notably, one anemometer measured the thermal plume associated with the caregiver manikin by measuring velocity at a distance of $0.2\ m$ above the manikin.

4.2.3 Aerosol measurement

An Aerodynamic Particle Sizer (APS) manufactured by TSI Inc. (model 3321) was used to measure aerosol concentration in air. The instrument

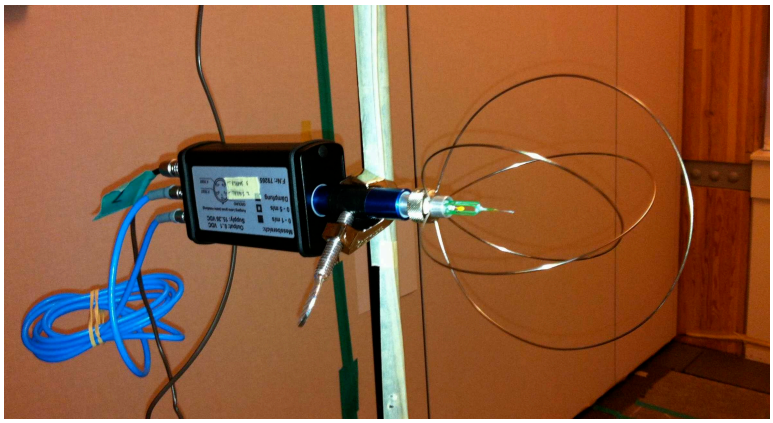

Figure 4.13: Thermoelectric anemometer

was able to measure droplets in the size range $0.5-20\ \mu m$, but due to sampling losses only a size range $0.5-5.0\ \mu m$ were measured. Pole 1 was equipped with aerosol sampling collectors at three elevations (sitting= 1.13 m, breathing= 1.64 m, and upper= 2.98 m). The location of this pole is given in table 4.7. These collectors delivered aerosols to the APS for concentration measurements.

The APS uses a sophisticated time-of-flight technique that measures aerodynamic diameter in real time. Because time-of-flight aerodynamic sizing accounts for particle shape and is unaffected by index of refraction or Mie scattering, it is superior to sizing by light scattering. In addition, the monotonic response curve of the time-of-flight measurement ensures high-resolution sizing over the entire particle size range. The drawback of this technique is that aerodynamic size may be significantly different than actual size if density of droplets is much greater or less than the density of water, for which the instrument is calibrated. This instrument measured particle concentrations in the range $0.001-1000\ pt/cm^3$. The instrument sampled air at a rate of 1 L/min with a sheath airflow of 4 L/min.

Typically, the sampling line itself accounts for a major fraction of particle loss in aerosol measurement systems. The sampling line geometry and material affects the particle collection efficiency significantly. A 0.19 in inner diameter conductive tube from TSI (model 3001788) was used to sample the air. Also, in order to avoid particle loss due to sharp bends, a selection manifold was designed that mixed three quasi parallel flow streams. These three samples correspond to the three heights for aerosol sampling in the

room (sitting, breathing, and upper levels). For every experiment, the manifold allowed selecting only one from the three sampling lines using shut off valves. The APS instrument and the sampling manifold are shown in figure 4.14.

Figure 4.14: Aerodynamic particle sizer and sampling manifold

Most aerosol measurement systems apply correction factors to account for particle losses in sampling lines. The three major particle loss mechanisms are diffusion, gravitation, and impaction. From the three mechanisms mentioned, only impaction losses are significant for the aerosol size range that APS measures [12]. Diffusional losses are significant only for aerosol less than 100 nm [56] while gravitational losses are significant for droplets greater than 100 μm [93].

The droplet collection efficiency for the entire sampling line was found experimentally. In the first test, the APS was placed at some distance in front of the atomizer without the sampling line. Then an injection was made with a total sampling time of 60 s. The total size distribution of the droplets was recorded. In the second test, the droplets were collected by the APS, but this time using the sampling line with a few arbitrary traces of the

sampling line. Then an injection was made with a total sampling time of 60 s as well. Three measurements were taken for each test. Comparing the size distributions gave the collection efficiency directly. Figure 4.15 shows the APS sampling collection efficiency for a range of droplet sizes that is critical. For droplets smaller than 4 μm in diameter, the collection efficiency is nearly 100 %, but for droplets larger than 5 μm in diameter the collection efficiency drops below 35 %. Although droplets as large as 10 μm were detected, 5 μm was considered as the cut off diameter for the experimental results in the far-field studies. The collection efficiency shown in the figure is used directly to correct for losses in the sampling line.

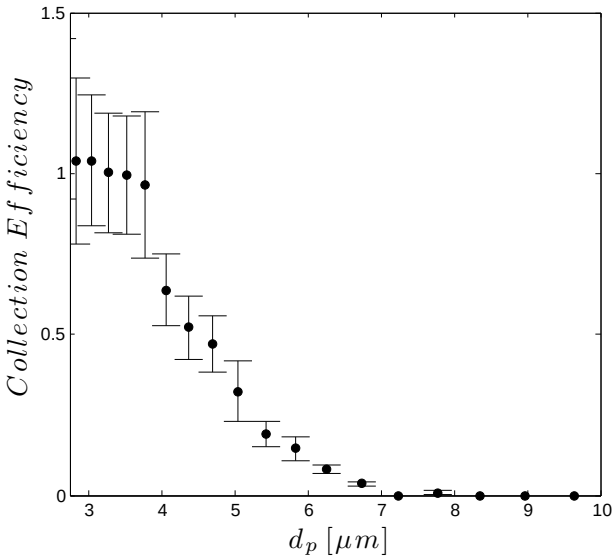

Figure 4.15: APS aerosol sampling collection efficiency

Another issue was the background aerosol concentration in the room. The background air in the room contained aerosols with diameter less than 2.5 μm or $PM_{2.5}$, however with very low concentrations. If we had desired to reduce $PM_{2.5}$, a high efficiency filtration system (better than MERV 14 rating) would have been required. However, filtering fine droplets comes at the expense of losing airflow rate in the room. We found that even a MERV 12 rated filter placed underneath the diffuser would cut the ventilation flow in half. As a result, no filter was used, but the background aerosol concentration was subtracted from the measured aerosol concentration. Nevertheless,

the total mass carried by $PM_{2.5}$ is smaller compared to PM_5.

4.2.4 Thermal manikins

4.2.4.1 Approach

Humans generate heat from their bodies, and the heat affects the airflow around them. To properly simulate a hospital room, we built vertical and horizontal human manikins that could release heat. They were made from a light steel frame and wood panels. Inside each manikin, two light bulbs acted as the heat sources of the human body.

4.2.4.2 Human dimensions

When creating human analogs for our tests, it is important to closely match the dimensions of an average adult. It was found that the average adult height in North America (Canada and US) is approximately 1.7 m. It was also found that the average human body surface area is approximately 1.73 m^2. The width and length of 3 adults were measured, and a width-length ratio was found to be two. Due to the limitations of the lengths of the frames that were available for purchase, the manikins had a height of 1.83 m, a width of 0.3 m, and a length of 0.15 m. Wood panels were attached to all faces of the frame, and provided a surface area of 1.76 m^2, close to the average human body surface area. Figures 4.16 and 4.17 show the vertical and horizontal thermal manikins.

4.2.4.3 Heat source

Humans generate heat through the metabolic process, a process that burns the food humans eat as fuel, leaving heat as a byproduct. To find a good range of metabolic rates to test, we consulted an ASHRAE table with metabolic rates for typical tasks [9]. The activities we wished to simulate were based on activities done in a hospital room, and these range from lying in bed to moving and lifting objects around. It was found that the metabolic rate for a person at complete rest is 45 W/m^2, and the metabolic rate for doing arm activities while standing is 80 W/m^2. For a person standing but without arm activities the metabolic rate is 70 W/m^2. Based on the surface area of 1.76 m^2, the heat range required to match the range of metabolic rates was calculated to be roughly 70 W to 150 W.

Each manikin uses two matching light bulbs located one fourth of total length at each end to ensure that the temperature was spread out on the

Figure 4.16: Vertical thermal manikin

Figure 4.17: Horizontal thermal manikin

manikin surface as best as possible. The wood panels were painted black inside to absorb as much heat as possible. Light bulbs inside each manikin simulated human heat generation. Three levels of activities are simulated: lying down, standing at rest, and standing while doing arm activities. The laying manikin used two 40 W light bulbs to simulate the body heat of a person at complete rest with a metabolic rate of 45 W/m^2. The vertical manikin at rest used two 60 W light bulbs to simulate a person at rest with a metabolic rate of 70 W/m^2 or two 75 W bulbs to simulate the body heat of a person standing while doing arm activities with a metabolic rate of 80 W/m^2.

4.2.4.4 Measuring the average temperature

To calculate the average temperature for each of the three levels of activities, the manikins panels were divided into 0.5 ft squares (cells). The light bulbs were left on for about an hour and a half, to allow the manikin to heat up and reach a steady temperature. For the manikins, the faces that were visible were measured (in other words, the face in contact with the ground was not measured).

The average temperatures and corresponding error bars for the three

metabolic rates were calculated using a MATLAB code. The temperature of each cell was measured three times and then averaged. The average of each cell is then used to calculate the average of the overall temperature of the manikin. The equilibrium temperature of the manikin balanced radiative and convective heat transfer with the room. These temperatures have been checked with standard convective and radiative heat transfer calculations for vertical and flat plates. Table 4.3 shows the results.

Metabolic rate $[W/m^2]$	Average temperature $[^oC]$	Error ($P = 68$ %) $[^oC]$
45 (horizontal)	26.41	± 0.05
70 (vertical)	28.51	± 0.06
80 (vertical)	30.77	± 0.09

Table 4.3: Metabolic rate and manikin temperature

4.2.4.5 Statistical analysis

The temperature of each 0.5 ft square (cell) was measured three times. To calculate the error at each cell, a t distribution was assumed for the data so that, $T_{best} = \overline{T} \pm t_{P,\nu} \frac{\sigma_T}{\sqrt{N}}$. N is the number of measurements, P is 68 %, σ_T is the standard deviation for the measurements, and ν is degrees of freedom ($\nu = N - 1$).

To calculate the temperature for the entire manikin, a straight average was used. The error could be calculated using the error propagation principle,

$$u_T = \pm \sqrt{\frac{\sum_{i=1}^{N} u_{Ti}^2}{N}} \tag{4.1}$$

where N is the number of cells and u_{Ti} is the uncertainty (or error) associated with temperature for cell i. The horizontal manikin had 52 cells and the vertical manikin had 74 cells.

4.2.4.6 Limitations of manikin design

Although the total heat dissipation of manikins were matched by metabolic rates of real occupants doing relevant activities, the non-uniform distribution

of heat around real bodies was not accounted for in detail. For example, no clothing was put on the standing manikin, or no blanket was used to cover the horizontal manikin. In addition, the manikins were simplified in geometry, not including the fine features and curvatures of real occupants, yet the overall surface area was matched with that of real occupants. These simplifying assumptions were made on the basis that, at room scale, air flow would primarily depend on total heat dissipation, surface area, and orientation, and not other delicate features of the manikins.

4.2.5 Room air change rate measurement

Measuring airflow rate at the room inlet is a difficult task since most diffusers (such as swirl) have a complex flow pattern with a varying velocity in three dimensions. As a result, it is easier to measure the airflow in the exhaust duct. For this purpose, a circular exhaust duct was extended, and an anemometer was placed in it at a location where the flow was fully developed. Figure 4.18 shows the set up for exhaust airflow measurement.

ASHRAE fundamentals handbook [8] provides a standard for this purpose. Because velocity in a duct is seldom uniform across any section, and a pitot tube reading or thermal anemometer indicates velocity at only one location, a traverse is usually made to determine average velocity. Generally, velocity is lowest near the edges or corners and greatest at or near the center. To determine the velocity in a traverse plane, a straight average of individual point velocities will give satisfactory results when point velocities are determined by the log-linear rule for circular ducts. Table 4.4 shows the specific distances relative to the duct inner wall where the airflow speed needs to be measured. An eight-point measurement was performed in the circular duct to measure the exhaust airflow speed and consequently the room air change rate. Any opening in the room (e.g. space under the door) was sealed with extreme care.

4.2.6 Oral fluid surrogate

Actual human oral fluid consists of ions, water, and proteins. The ion content is dominated by monovalent species, and the molar concentrations of cations and anions are approximately 150 mM. Table 4.5 shows the major components in human oral fluid [30] .

Treating the ion content in the oral fluid as $NaCl$ (molecular weight 58.5 g/M), the mass concentration of ions would be 8.8 g/L. The protein concentration of 76 g/L is about an order of magnitude higher. As a result

Figure 4.18: Exhaust flow measurement setup for ventilation tests

No. of measuring points per diameter	Position relative to inner wall (as fraction of diameter)
6	0.032, 0.135, 0.321, 0.679, 0.865, 0.968
8	0.021, 0.117, 0.184, 0.345, 0.655, 0.816, 0.883, 0.981
10	0.019, 0.077, 0.153, 0.217, 0.361, 0.639, 0.783, 0.847, 0.923, 0.981

Table 4.4: Log-linear rule for circular ducts [8]

Species	Molecular Weight or Atomic Mass	Concentration
Na^+	23 g	91 ± 8 mM
K^+	39.1 g	60 ± 11 mM
Cl^-	35.5 g	102 ± 17 mM
Lactate	89 g	44 ± 17 mM
Glycoprotein	Not given	76 ± 18 g/L

Table 4.5: Oral fluid composition [30]

of its large contribution to the equilibrium particle size, the effect of protein on final particle size must be considered [71].

Since the final desiccated size of generated aerosols is important, it was essential to prepare a surrogate that contained the same volume fraction of non-volatile content. The surrogate was prepared by dissolving 76 g (60 mL) of pure glycerin (at least 99.6 % pure) with pure deionized water to produce a total 1 L volume. This resulted in a 6 % volume of non-volatile content in each droplet. A similar approach was taken by Wan et al. [105] although no salt was added to the surrogate for health and safety considerations.

Actual human oral fluid is non-Newtonian and exhibits shear thinning and visco-elasticity. It also exhibits a different viscosity and surface tension compared to water. However, these properties were not matched with the actual oral fluid since, upon atomization, these properties have less effect on final droplet size than the non-volatile fraction of the droplet. The surrogate atomization was fully characterized by shadowgraphy and Particle Tracking Velocimetry (PTV).

4.2.7 Injection air temperature

Actual exhaled air temperature is above ambient, so it was desired to create similar conditions for the injected air temperature. A 4 ft and 144 W heat tape (McMaster Carr 3631K22) was wrapped around the incoming gas line to raise the air temperature. To ensure that most of the heat released is absorbed by the incoming gas, a 4 ft long and 0.5 in thick Melamine insulation foam (McMaster Carr 93495K11) was wrapped around the heated line. This also ensured that the thermal plume strength associated with the heat tape in the room is minimized. In this way the air temperature was raised to 32 ^oC at a distance of 1 cm away from the atomizer exit.

4.2.8 Parametric study

Ten parametric cases were chosen for this study. These parameters involved changing airflow rate, injection momentum, injection direction, occupant location, and occupant metabolic rate (shown in table 4.6 and figure 4.19). The specific metric that was measured in the parametric study was the aerosol concentration at three elevations (sitting, breathing, and upper zones).

The reference case (1) represented a mid velocity injection of aerosols at a 45 ^{o} angle from the floor. A regular metabolic rate for the occupant and a resting metabolic rate for the patient were used with ACH= 0.8. Cases 2

and 3 injected aerosols at high and low nitrogen velocities. Case 4 injected aerosols at 45 ^{o} angle away from the bed and at 45 ^{o} angle from the floor. Cases 5 and 6 injected aerosols horizontally and vertically, respectively. Case 7 reduced the occupant metabolic rate to a light activity. Cases 8 and 9 moved the occupant away from and behind the injection source respectively. Case 10 increased air change rate to ACH=3.7. A total of 9 tests were performed for each case. For each case there was a set of 3 measurements for sampling air at each elevation (sitting, breathing, upper), so any statistical variations could be observed. As a result, each case required a total of 9 tests. Table 4.7 gives the location of each object in the room based on the distance between the closest vertex of the object and the origin.

Case	Injection Momentum	Injection Direction 1	Injection Direction 2	Metabolic Rate	Occupant Location	Airflow Rate
Ref.(1)	Mid	Inline	Inclined	Mid	Mid	Mid
2	High	Inline	Inclined	Mid	Mid	Mid
3	Low	Inline	Inclined	Mid	Mid	Mid
4	Mid	Away	Inclined	Mid	Mid	Mid
5	Mid	Inline	Horizontal	Mid	Mid	Mid
6	Mid	Inline	Vertical	Mid	Mid	Mid
7	Mid	Inline	Inclined	Low	Mid	Mid
8	Mid	Inline	Inclined	Mid	Far	Mid
9	Mid	Inline	Inclined	Mid	Close	Mid
10	Mid	Inline	Inclined	Mid	Mid	High

Table 4.6: Parametric study for the ventilation experiments

Object	$x[m]$	$y[m]$	$z[m]$
Bed	1.15	0.00	1.23
Patient	1.27	0.45	1.39
Atomizer	1.27	0.60	2.61
Diffuser	1.45	0.00	0.66
Exhaust	1.20	3.18	3.00
P1 (base)	1.88	0.00	1.67
P1 (away)	1.88	0.00	2.68
P1 (behind)	2.65	0.00	0.72
P2	1.84	0.00	2.14
P3	1.00	0.00	1.47
P4	1.00	0.00	2.84
P5	1.34	0.00	0.60
Nurse (base)	1.81	0.00	1.23
Visitor (away)	2.57	0.00	0.25
Nurse (behind)	1.81	0.00	2.23

Table 4.7: Object locations in the ventilation test setup

4.2.8.1 Injection momentum

In order to study the effect of injection momentum, the air-assist internally mixing cone atomizer was run at three different sets of liquid and gas pressures that all produced the same size distribution of droplets. The injected gas velocity and volume were representative of actual coughs and sneezes outlined in section 1.1.1.2. The injections also contained droplets in a size range shared with actual expirations although a very limited size range $0.5-5.0\ \mu m$ was measured. Table 4.8 shows the flow conditions for the atomizer.

4.2.8.2 Injection directions

Four injection directions were used, three in the same vertical plane containing the diffuser, patient, and exhaust and one in another vertical plane that made a $45\ ^{o}$ angle with the first plane. Figure 4.20 shows the atomizer as it was set up to inject in an inclined direction for the reference case.

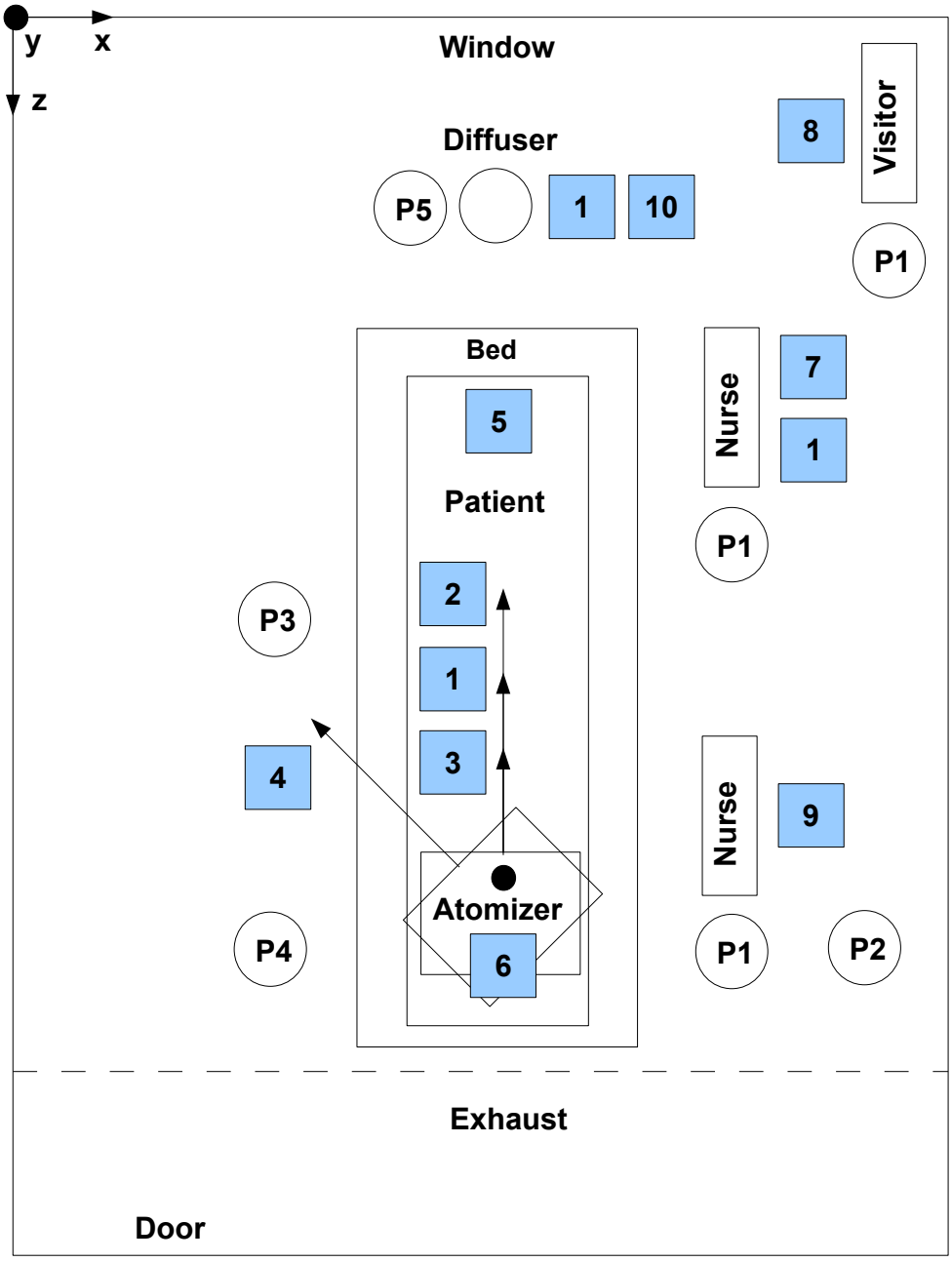

Figure 4.19: Diagram of ventilation test cases for experiments - Case numbers are shown in squares

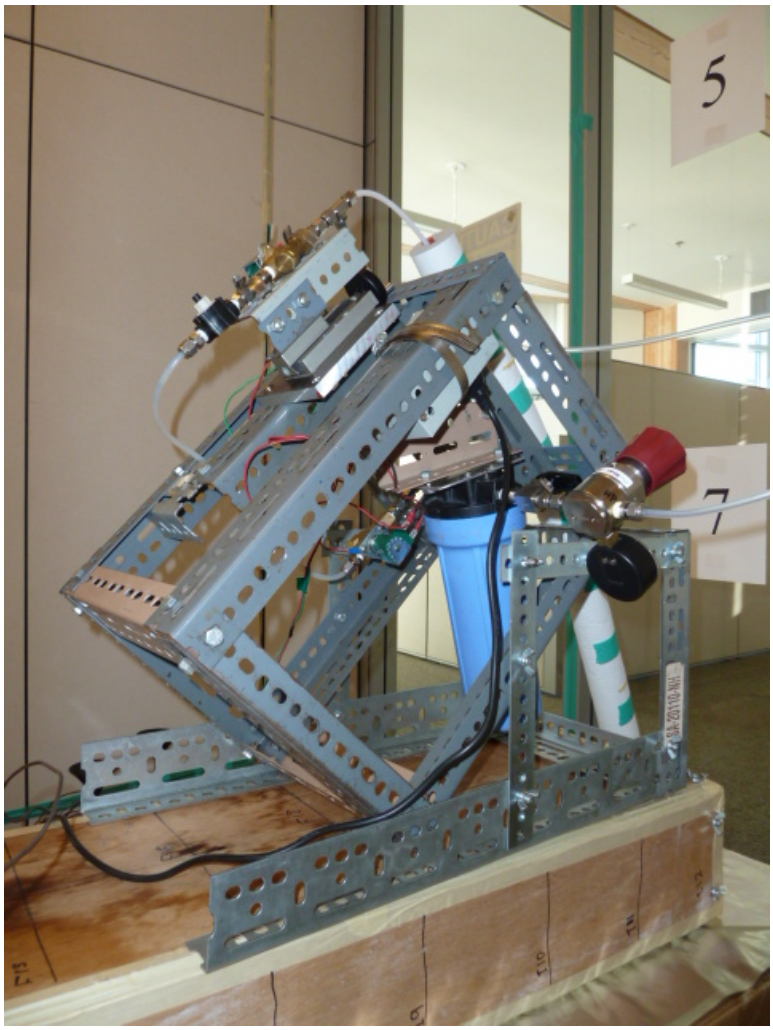

Figure 4.20: Atomizer orientation for the reference case (1) in the ventilation tests

Flow Condition	Low	Mid	High
Nitrogen $[psi]$	20	30	40
Liquid $[psi]$	9	13	20
Nitrogen $[L/s]$	0.85	1.13	1.37
Liquid $[mL/s]$	5.1	7.5	9.6
Nitrogen Velocity $[m/s]$	185	247	299
Liquid Volume $[mL]$	3.8	3.8	3.8
Injection Time $[s]$	0.75	0.51	0.40
Nitrogen Volume $[L]$	0.63	0.57	0.54

Table 4.8: Atomizer flow conditions for the far-field ventilation test

4.2.8.3 Metabolic rate

Two metabolic rates were considered for the vertical manikin. 70 W/m^2 corresponds to a person at rest and 80 W/m^2 corresponds to a standing person doing arm activities.

4.2.8.4 Occupant location

Three occupant locations were used. The close location was beside the patient mouth, the mid location was at the end of the bed, and the far location was at the corner of the room.

4.2.8.5 Airflow rate

The building underfloor distribution system was set to maintain a static pressure above the ambient. This pressure in turn drove airflow at a given rate through the room. The diffuser damper in the system could be set to a value in the range $0-100$ %. Varying the damper opening area changed the air change rate of the room. When the static pressure was set to its maximum value and the diffuser damper was fully open, the room ventilation rate was 0.8 ACH. In order to achieve a higher air change rate representative of hospital patient recovery rooms, an inline fan (Greenhech CSP A390) was used below the diffuser which increased the air change rate to 3.7 ACH.

Lower air change rates were used in nine cases and the higher air change rate was used for one case. This was due to limitations and special circumstances. First, the CIRS building allowed only a maximum air change rate of about 0.8 ACH in our experiments. The inline fan was too noisy and was added later in the study after most cases were already experimented or

modeled. Second, sensitivity of contaminant exposure to parametric variations described above was expected to be more pronounced at low ventilation rates.

4.2.9 Space-resolved ventilation tests

Section 4.2.8 described a parametric test study where important room operating and occupational conditions varied from case to case. Although these variations reveal relative exposure to droplets at the occupant location (sitting, breathing, and upper elevations), they do not resolve droplet dispersion spatially. It is desired to know the performance indices (e.g. droplet concentration) in more than three sampling locations. Such information is particularly useful in assessing the adequacy and performance of computational fluid dynamics simulations to be addressed in detail in chapters 5 and 7.

For this purpose, the reference case (1) was chosen, and pole 1, which carries droplet sampling collectors, was moved in the z direction, all the way from one wall to the other in 0.5 m increments from $z = 0.17$ m to $z = 3.67$ m. The result was eight sampling locations for pole 1 as depicted in figure 4.21.

4.2.10 Ventilation test protocol

Often in experimental research it is difficult to produce a large number of sensible results that fit together, especially when a large number of experiments are to be conducted. One usually suffers from the volume of information that needs to processed in the mind, on paper, or computers, and by the time the experiments are half way done, the test protocol is already forgotten or altered unwantedly. The magnitude of this crisis is multi-fold, especially when one desires to repeat similar experiments that involve many tenuous parametric changes. Appendix A contains a detailed test protocol (Standard Operating Procedure (SOP)) that was prepared and executed line by line for each experiment.

4.2.11 Performance indices

4.2.11.1 Normalized concentration and cumulative concentration for the reference case

Real time and cumulative air pollutant concentration in a location is of extreme importance. The cumulative concentration is a direct measure of

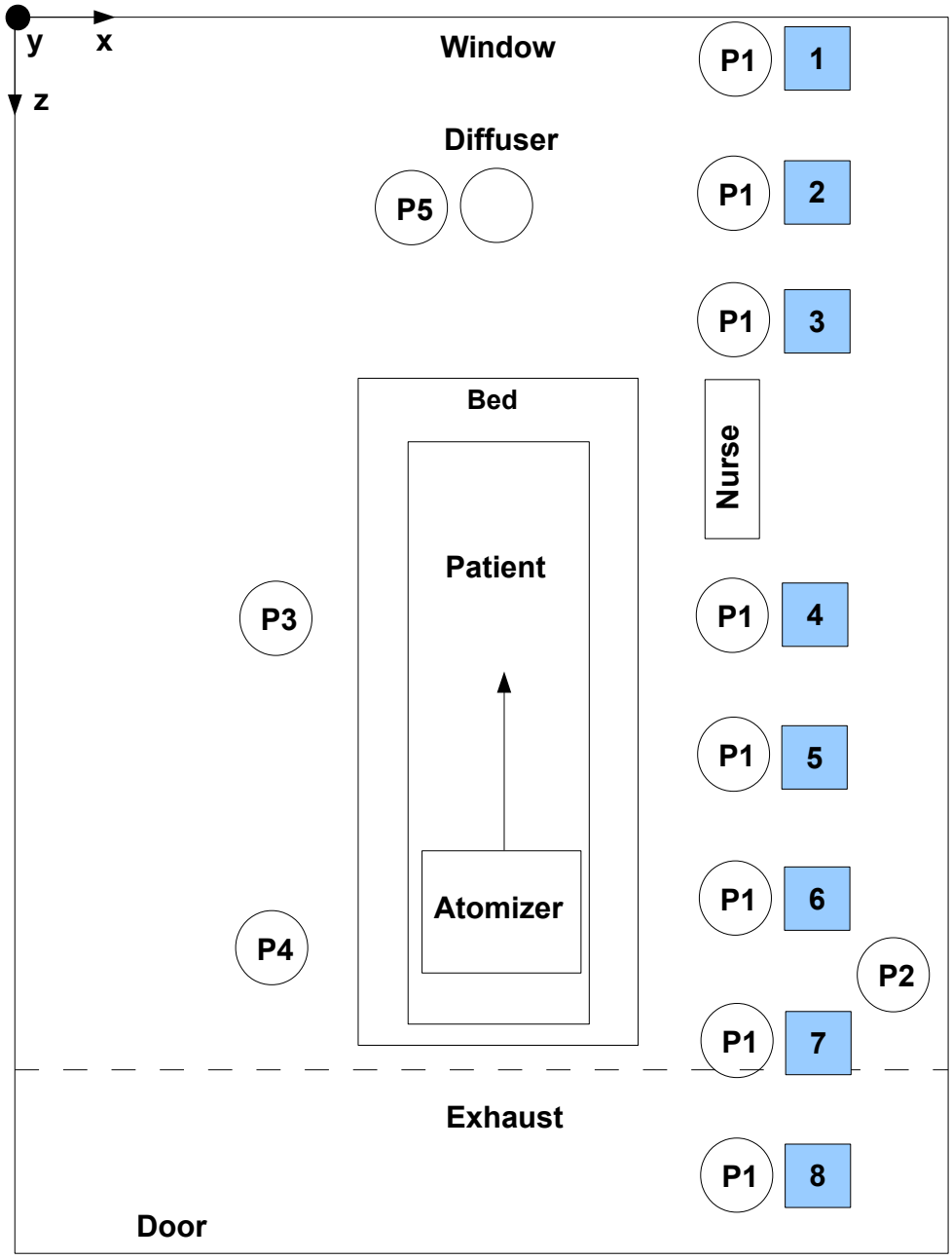

Figure 4.21: Diagram of ventilation test cases for space-resolved experiments - Sampling locations are shown in squares

exposure to pollutants and is inversely proportional to the ventilation effectiveness. In other words, the lower the cumulative concentration is, the higher the ventilation effectiveness will be. Cumulative concentration is defined by,

$$\overrightarrow{C(T)} = \int_{t=0}^{t=T} C(t)dt \tag{4.2}$$

where t is real time, T is the elapsed time of exposure, and $C(t)$ is real time concentration.

The reference case real time and cumulative concentrations can be normalized with respect to the injection concentration. This is useful since the dilution of the contaminants within space is monitored at each measurement point. Also, any differences between concentrations at various heights can be noticed on a size bin-specific or whole size distribution basis. Finally, the reference case results produced by experiment and model can be directly compared. The normalized concentration and cumulative concentration can be defined by,

$$\frac{C(t)}{C_{inj}} \tag{4.3}$$

$$\frac{\overrightarrow{C(T)}}{C_{inj}} \tag{4.4}$$

where C_{inj} is concentration of atomized droplets in the volume of gas injected. If volume concentration is desired, it is convenient to consider the volume of droplets after they have shrunk to the droplet nuclei by evaporation. Note that these equations can be written for any droplet size bin of interest. The concentrations in our studies are reported based on four size bins of $0.5-1\ \mu m$, $1-2.5\ \mu m$, $2.5-5\ \mu m$, and $0.5-5\ \mu m$. Also note that the unit for concentration is arbitrary, but we used volume concentration in our measurements.

4.2.11.2 Relative exposure

For ease of comparison, the relative normalized cumulative concentration (or relative exposure) can be used for the parametric and space-resolved studies. This is particularly useful for comparing experimental results to models when differences among various cases are sought. Relative exposure can be defined as,

$$\hat{C}(T) = \frac{\overrightarrow{\overline{C(T)}}}{\overrightarrow{\overline{C(T)_{ref}}}} \tag{4.5}$$

where $\overrightarrow{\overline{C(t)_{ref}}}$ is the cumulative concentration for the reference case. Such parameters affecting $\overrightarrow{\overline{C(T)}}$ are described in section 4.2.8 (e.g. supply airflow rate, thermal load, placement of objects and occupants, etc...). If $\hat{C}(T)$ for a parameter is much greater or less than 1, then the parameter is important.

4.2.11.3 Temperature

The temperature profiles were observed, but only reported for the reference case, to assess the ability of the ventilation system under the operating conditions to maintain thermal vertical stratification.

4.2.11.4 Airflow speed

Airflow speed was also observed, but only plotted for the reference case, to give relative strength of thermal plumes and the flow rates in the boundaries of of the test room (diffuser and exhaust). Calculation of room air changes per hour was only possible knowing the airflow speed in the exhaust duct.

4.2.12 Statistical analysis

A t distribution was assumed for the experimental performance indices so that $x_{best} = \overline{x} \pm t_{P,\nu}\frac{\sigma_x}{\sqrt{N}}$ with $P = 68$ %, $N = 3$, $\nu = 2$, and σ_x the standard deviation for the three measurements. The mean values $\overline{x}$ and the standard errors $t_{P,\nu}\frac{\sigma_x}{\sqrt{N}}$ are reported.

Chapter 5

Numerical Methodology

5.1 Modeling

Continuum phase mass, momentum, and energy transport processes as well as discrete phase motion were described briefly in section 1.2. Our treatment of the mathematical model was preliminary, but in this section we continue the modeling in more detail, using methodologies that enable us to arrive at numerical solutions with reasonable accuracy and economic computational resources. The detailed model is used to predict droplet dispersion in both parametric and space-resolved studies.

5.1.1 Turbulence: renormalization group $k - \epsilon$

The RNG $k - \epsilon$ model was derived using a rigorous statistical technique (called renormalization group theory). It is similar to the standard $k - \epsilon$ model, but includes many refinements. This model has an additional term in its ϵ equation that greatly improves the accuracy for rapidly strained flows. This model also enhances the accuracy of swirling flows. The RNG theory provides an analytical formula for the turbulent Prandtl number as opposed to using constant values. While standard $k - \epsilon$ model is a high-Reynolds-number model, the RNG theory provides an analytically-driven differential formula for effective viscosity that accounts for low-Reynolds-number effects [1].

5.1.2 Multicomponent mixture properties

For situations that we have a mixture fluid and should consider the mass, momentum and energy transport, we must approximate the properties of the mixture fluid. In our case, the species of interest in the mixture are nitrogen, oxygen, water vapor, and carbon dioxide (ranked in abundance respectively). To estimate the density of the mixture, we can use the ideal gas law for the incompressible flow. This method ignores the pressure contribution to change density. However, it will consider the mixture fraction

and the temperature to approximate the density [1].

$$\rho = \frac{P_0}{RT \sum_i \frac{Y_i}{M_{w,i}}} \tag{5.1}$$

where P_0 is the background pressure, R is the universal gas constant, T is temperature, Y_i is mass fraction of species i, and $M_{w,i}$ is the molecular weight of species i. When the Boussinesq approximation is not used, the operating density ρ_0 appears in the body-force term in the momentum equation as $(\rho - \rho_0)g$. This form of the body-froce term follows from the redefinition of pressure by,

$$P'_s = P_s - \rho_0 g y \tag{5.2}$$

The hydrostatic pressure in a fluid at rest is then $P'_s = 0$. By default FLUENT computes the operating density by averaging over all cells. In some cases, specifying an explicit operating density helps obtaining better results. When solving natural-convection problems the operating pressure specified is P'_s in the previous equation. Although one knows the actual pressure P_s, one needs to know the operating density in order to determine P'_s from P_s. Therefore, we need the operating density to be explicitly specified rather than use of the computed average [1].

Since we have a mixture fluid, we must define other fluid properties based on the mixture. The specific heat capacity of the mixture is defined using the mixing-law by,

$$c_p = \sum_i Y_i c_{p,i} \tag{5.3}$$

To estimate the diffusion flux of chemical species we must consider the mass diffusion, turbulent diffusion, and thermal (Soret) diffusion processes. In turbulent flow the diffusion flux can be shown by,

$$J_i = -(\rho D_{m,i} + \frac{\mu_t}{Sc_t})\nabla Y_i - D_{T,i}\frac{\nabla T}{T} \tag{5.4}$$

where $D_{m,i}$ is the mass diffusion coefficient for species i in the mixture, μ_t is turbulent viscosity, Sc_t is the effective Schmidt number for turbulent flow defined as $\frac{\mu_t}{\rho D_t}$ (D_t is the effective mass diffusion coefficient due to turbulence), and $D_{T,i}$ is the thermal diffusion coefficient. Turbulent viscosity, μ_t is calculated by the RANS turbulence model [1]. The thermal diffusion of species is negligible in comparison to other processes. Furthermore, carbon dioxide and water vapor mass fractions in the mixture are very small so

that the dilute approximation applies. Hence, we can consider a constant mass diffusion coefficient in an air background for all species. This is fair assumption since turbulent diffusion dominates other diffusion processes in high shear and turbulent flows. Other fluid properties of interest are thermal conductivity and viscosity. Thermal conductivity and viscosity can be approximated by that of air.

5.1.3 Discrete phase heat and mass transfer processes

The simplest mode of heat transfer between the discrete phase and the continuous phase is inert heating or cooling. These processes apply when the droplet temperature T_p is less than the vaporization temperature T_{vap} and after the volatile fraction $f_{v,0}$ of a droplet has been consumed,

$$T_p < T_{vap} \tag{5.5}$$

$$m_p < (1 - f_{v,0})m_{p,0} \tag{5.6}$$

where m_p is droplet mass and $m_{p,0}$ is droplet mass before evaporation begins. Radiation heat transfer is insignificant compared to convective heat trasnfer for transparent expiratory droplets in room conditions. In this situation a simple heat balance equation can be used to relate the droplet temperature $T_p(t)$ to the convective heat transfer to the background medium [1].

$$m_p c_p \frac{dT_p}{dt} = hA_p(T_\infty - T_p) \tag{5.7}$$

where c_p is droplet heat capacity, h is convective heat transfer coefficient, A_p is droplet surface area, and T_∞ is far-field temperature. The heat transfer coefficient h is evaluated using the correlations of Frössling and Ranz and Marshal [35, 83, 84].

$$Nu = \frac{hd_p}{k} = 2.0 + 0.6Re_l^{\frac{1}{2}} Pr^{\frac{1}{3}} \tag{5.8}$$

where Nu is the Nusselt number, k is the thermal conductivity of the continuous phase, Re_l is the Reynolds number based on the droplet diameter and the droplet-gas relative velocity, and Pr is the Prandtl number of the continuous phase.

Vaporization of a liquid droplet begins upon injection and continues until the droplet has shrunk to its nonvolatile core. During such a process, the temperature of the droplet remains below the boiling point T_{bp} since the droplet is continually cooled by vaporization,

$$T_p < T_{bp} \tag{5.9}$$

$$m_p > (1 - f_{v,0})m_{p,0} \tag{5.10}$$

Vaporization is halted if the droplet temperature falls below the dew point. The rate of vaporization is governed by gradient diffusion, in which the flux of droplet vapor into the gas is related to the gradient of the vapor concentration between the droplet surface and the bulk gas [1].

$$N_i = k_c(C_{s,i} - C_{\infty,i}) \tag{5.11}$$

where N_i is molar flux of vapor for species i, k_c is mass transfer coefficient, $C_{s,i}$ is vapor concentration at the droplet surface, and $C_{\infty,i}$ is the vapor concentration in the bulk gas. The concentration of vapor at the droplet surface is evaluated by assuming that the partial pressure of vapor at the interface is equal to the saturated vapor pressure P_{sat} at the droplet temperature [1].

$$C_{s,i} = \frac{P_{sat}(T_p)}{RT_p} \tag{5.12}$$

where R is universal gas constant. The concentration of vapor in the bulk gas is already known from the solution of the transport equation for all the species of interest.

$$C_{\infty,i} = X_i \frac{P}{RT_\infty} \tag{5.13}$$

where X_i is the local bulk mole fraction of species i, P is the local absolute pressure, and T_∞ is the local bulk temperature in the gas. The mass transfer coefficient in equation 5.11 is calculated using the Sherwood number correlations [35, 83, 84],

$$Sh_{AB} = \frac{k_c d_p}{D_{m,i}} = 2.0 + 0.6 Re_d^{\frac{1}{2}} Sc^{\frac{1}{3}} \tag{5.14}$$

where $D_{m,i}$ is the diffusion coefficient of vapor in the bulk gas, Sc is the Schmidt number ($\frac{\mu}{\rho D_{m,i}}$). The droplet mass can then be governed by the following equation,

$$\frac{dm_p}{dt} = -N_i A_p M_{w,i} \tag{5.15}$$

where $M_{w,i}$ is the molecular weight of species i. In order to correctly predict droplet mass change we need to define the vapor pressure as a polynomial

or piecewise linear function of temperature, $P_{sat}(T)$. The polynomial must cover the full range of temperatures that the droplet is expected to experience in the computational domain.

Knowing the mass change, we can predict the heat transfer, and subsequently the temperature change in the droplet. If we assume a bulk system (true for small droplets of interest as the Biot number is small), we get the following expression,

$$m_p c_p \frac{dT_p}{dt} = hA_p(T_\infty - T_p) + \frac{dm_p}{dt} h_{fg} \tag{5.16}$$

where h_{fg} is latent heat of vaporization [1].

5.1.4 Discrete phase motion

When the flow is turbulent, we can predict the trajectories of droplets using the fluid phase mean velocity, $\overline{u}$, and fluctuating component of velocity, u', in the trajectory equations. Optionally, we can include the instantaneous value of the fluctuating gas flow velocity,

$$u = \overline{u} + u' \tag{5.17}$$

In stochastic DRW approach, we can predict the turbulent dispersion of droplets by integrating the trajectory equations for individual droplets by using the instantaneous fluid velocity along the droplet path during the integration. If we compute the trajectory for a large ensemble of droplets, then the random effect of turbulence has been accounted for. In DRW model, the fluctuating velocity components are discrete and piecewise constant functions of time. Their random value is kept constant over an interval of time given by the characteristic lifetime of the eddies. Extreme care must be applied 'not using' DRW in 'diffusion dominated flows' where droplets predicted by DRW appear to concentrate in low-turbulence regions in the flow [1].

Prediction of droplet dispersion makes use of the concept of the integral time scale T that describes the time spent in turbulent motion along the droplet path ds,

$$T = \int_0^\infty \frac{u_p'(t) u_p'(t+s)}{\overline{u_p'^2}} ds \tag{5.18}$$

The integral time is proportional to the droplet dispersion rate, as larger values indicate more turbulent motion in the flow. It can be shown that the

droplet turbulent diffusivity is given by $\overline{u_i' u_j'} T$. For small 'tracer' droplets moving with the fluid with negligible drift velocity, the integral time becomes the fluid Lagrangian integral time T_L since small droplets only marginally deviate from the motion of fluid elements [1]. This time scale can be approximate as follows,

$$T_L = C_L \frac{k}{\epsilon} \tag{5.19}$$

where C_L is to be determined since it is not generally known. By matching the diffusivity of tracer droplets, $\overline{u_i' u_j'} T_L$, to the scalar diffusion rate predicted by the turbulence model, we can obtain the following expression,

$$T_L \simeq 0.15 \frac{k}{\epsilon} \tag{5.20}$$

This expression can only be used for $k - \epsilon$ turbulence models and its variants [1].

In the DRW model, the interaction of a droplet with a succession of discrete stylized fluid phase turbulent eddies is simulated. Each eddy is characterized by a Gaussian distributed random velocity fluctuation (u', v', w') and a time scale (τ_e). This fluctuating values can be sampled assuming they obey a Gaussian probability distribution,

$$u' = \zeta \sqrt{\overline{u'^2}} \tag{5.21}$$

where ζ is a zero mean and unit variance Gaussian random variable. Since the kinetic energy of turbulence is known at each point in the flow, one can calculate the right hand side of the previous equation assuming isotropy of turbulence [1]. Therefore, for $k - \epsilon$ models, the following expression can be written,

$$\sqrt{\overline{u'^2}} = \sqrt{\overline{v'^2}} = \sqrt{\overline{w'^2}} = \sqrt{\frac{2k}{3}} \tag{5.22}$$

The characteristic lifetime of an eddy can be defined either as a constant or random variable using the following expressions,

$$\tau_e = 2T_L \tag{5.23}$$

$$\tau_e = -T_L log(r) \tag{5.24}$$

where r is a uniform random number between 0 and 1 and T_L is given as mentioned earlier. The random definition of eddy lifetime gives more realistic results. The droplet eddy crossing time is defined as follows,

$$\tau_{cross} = \tau ln \left[1 - \left(\frac{L_e}{\tau \mid u - u_p \mid} \right) \right] \tag{5.25}$$

where τ is the droplet relaxation time, L_e is the eddy length scale, and $\mid u - u_p \mid$ is the magnitude of the relative velocity. The droplet is assumed to interact with the fluid phase eddy over the smaller of the eddy lifetime and the eddy crossing time. When this time has been reached, a new value of the instantaneous velocity is sampled and the calculation is repeated [1].

For better presentation of droplet dispersion in CFD modeling, one can 'stagger' droplets spatially and/or temporally. With spatial staggering, the trajectory calculations originate from a region of space rather than a point. When tracking droplets in a transient calculation using relatively a large time step in relation to the spray event, the droplets can clump together in discrete bunches. These clumps do not look like physical reality. To obtain a smoother statistical representation of the spray, the droplets can be staggered in time as well.

5.1.5 Coupling between the discrete and continuous phases

A realistic modeling of volatile droplet dispersion requires the consideration of heat, mass, and momentum exchanges between the discrete and continuous phases. For example, in a real volatile droplet system, droplets tend to evaporate hence losing heat to the continuous phase. Also, the concentration of the volatile species increases in the continuous phase by evaporation. Furthermore, the interaction of the droplet momentum by that of the continuous phase results in momentum exchange between the phases. A two-way coupling is necessary when heat and mass transfers to or from the discrete phase need to be considered. A two-way coupling is accomplished by alternately solving the discrete and continuous phase equations until the solutions in both phases have converged within the required tolerances.

The momentum transfer from continuous phase to the discrete phase is computed by finding the change in momentum of a droplet as it passes through each control volume in the solution domain. The momentum exchange appears as a momentum 'sink' in the continuous phase momentum balance, which needs to be accounted for in two-way modeling. The heat transfer from the continuous phase to the discrete phase is found by the

change in thermal energy of a droplet as it passes through each control volume. Mass transfer from the discrete phase in the continuous phase can be found by predicting the change in mass of particle as it passes through each control volume. This mass usually appears as a source term in the continuous phase because in most cases droplets evaporate. To improve convergence stability, the interphase exchange of heat, mass, and momentum is under-relaxed during the calculations. The more under-relaxation the more stable the convergence will be. When stochastic DRW model is performed, the interphase exchange terms are computed for each stochastic trajectory with the droplet mass flow rate divided by the number of stochastic tracks computed. This implies that an equal mass flow of droplets follows each stochastic trajectory [1].

5.2 Boundary and initial conditions

5.2.1 Injection

Our droplet sampling setup allowed droplets to be detected only as large as 10.0 μm in diameter. As a result, it was desired to use an injection volume distribution that resulted in a maximum droplet diameter of 10.0 μm after evaporation. Of course it would have been possible to use distributions covering a broader range, but for two reasons this was not preferred. Firstly, modeling of the dispersion behavior for larger droplets is difficult to validate since our experimental facility does not allow measurements of droplets larger than 10 μm in diameter. Secondly, using a droplet distribution model for a larger size range reduces the accuracy of the model approximating the actual experimental distribution. For this purpose, a linear number distribution in the range $0.5-30$ μm was used. This distribution results in a volume fraction distribution that closely approximates the experimental volume fraction distribution in the same range. A total of 10,000 droplets were injected in the CFD model. Figure 5.1 shows the experimental distribution measured by the setup in section 4.1.3 and the model distribution that was used in the CFD analysis. The translation of distributions after complete evaporation is also shown. As discussed in section 6.1.4, the transient injection properties are short-lived compared to the total injection time. As a result, usage of the steady spray droplet size distribution is a safe choice. A nitrogen tracer gas was assumed at injection for tracer gas modeling of contaminant dispersion.

Of course, it was possible to fit other complex distributions to the experimental data, but FLUENT only provided standard distributions such as

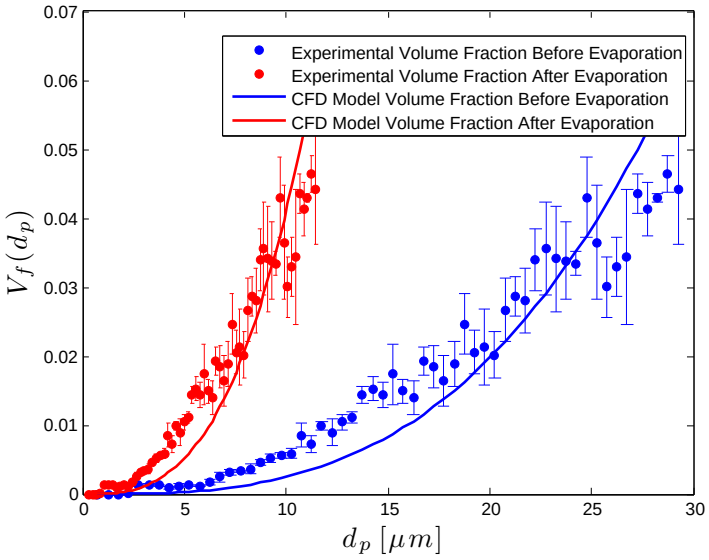

Figure 5.1: Injection volume fraction for experiment and CFD model (Blue legends: before evaporation, Red legends: after evaporation)

Weibull and linear. The particular choice of distribution does not affect the results if normalized volume concentration is reported per each size bin.

5.2.2 Diffuser

The flow pattern for the swirl diffuser was investigated using smoke tube experiments. It was found that the velocity vector makes an angle of 35 ^{o} with respect to the floor. For modeling, the same angle was assumed in a 'velocity inlet' boundary condition. In addition, the velocity vector was defined with the same magnitude over the entire diffuser area. All vectors were tangential to the circle that was co-centric with the diffuser center (figure 5.2). The magnitude of this velocity vector was calculated using the air change rate of the room measured by anemometry at the exhaust pipe. ACH for cases 1 to 9 was set to 0.8 and for case 10 was set to 3.7.

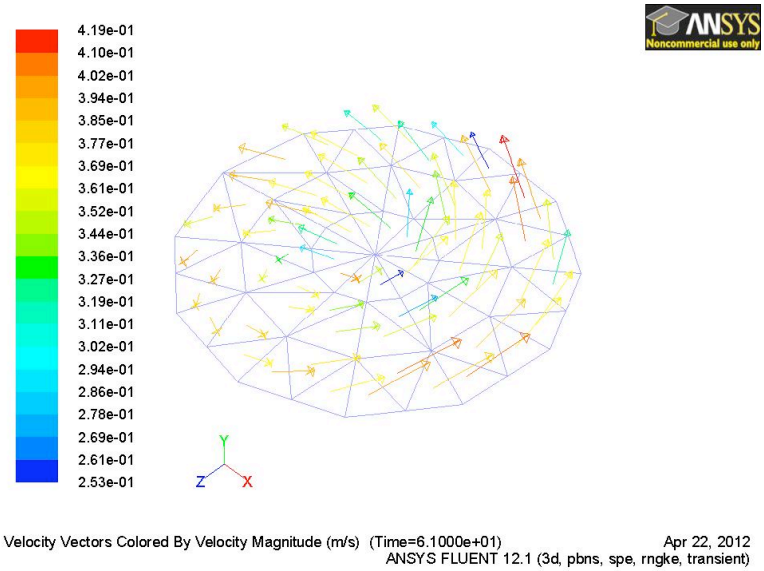

Figure 5.2: Modeling swirl diffuser flow pattern

5.2.3 Initial conditions

The relative humidity in the room was set to 50 %, a condition that was maintained in the experiments as well. The initial temperature of the room was set to 296 K. The mass fraction for nitrogen, oxygen, water vapor,

and carbon dioxide were initially set to 0.76939, 0.221, 0.009, and 0.00061, respectively.

5.2.4 Exhaust

The exhaust boundary condition was treated as a 'pressure outlet' with flow direction according to neighboring cells. If a backflow of air was necessary in part of the exhaust area, the same temperature and species mass fractions were used as the initial condition. So, the mass fraction for nitrogen, oxygen, water vapor, and carbon dioxide were set to 0.76939, 0.221, 0.009, and 0.00061, respectively.

5.2.5 Envelope

The thermocouple measurements helped set the temperature boundary conditions for the envelope surfaces. As confirmed by the experiments, the temperature on the surfaces did not vary substantially for each test, so a constant temperature boundary condition was assumed. Table 5.1 shows the temperatures used for the room envelope. In addition, the no slip condition was assumed at the walls.

Surface	1	2	3	4	5	6	7	8	9	10	1*
West (low)	295.9	295.2	296.0	296.3	297.9	296.5	295.5	295.6	296.7	295.6	296.0
West (mid)	296.0	295.3	296.1	296.3	298.2	296.6	296.6	295.8	297.0	295.7	296.8
West (high)	295.8	295.1	295.9	296.1	298.2	296.4	295.4	295.8	297.1	295.6	297.1
East (low)	295.8	295.1	295.8	296.1	298.0	296.4	295.5	295.9	296.9	295.5	296.0
East (mid)	295.9	295.2	296.0	296.2	298.2	296.5	295.5	296.0	297.1	295.7	296.7
East (high)	295.6	294.9	295.7	296.0	298.1	296.3	295.3	295.7	297.1	295.5	296.9
North (low)	294.7	294.2	294.8	294.9	296.5	295.1	294.7	294.8	295.9	294.7	295.9
North (mid)	294.6	294.0	294.7	294.9	296.5	295.1	294.6	294.8	295.8	294.7	296.1
North (high)	296.5	295.9	296.7	296.8	298.4	297.1	296.3	296.7	297.4	296.5	297.7
North (very high)	295.2	294.6	295.4	295.6	297.3	296.0	294.9	295.4	296.4	295.4	297.0
South (low)	293.6	292.7	293.8	294.2	295.2	294.5	293.9	294.1	294.3	294.1	294.0
South (mid)	294.8	293.6	294.5	295.2	299.0	295.7	294.8	294.9	298.0	295.0	297.5
South (high)	295.6	294.8	295.6	296.0	300.0	296.3	295.3	295.5	298.5	295.6	298.5
Ceiling (very high)	296.2	295.6	296.3	296.6	298.7	297.0	295.9	296.1	297.6	296.3	297.4
Floor (very low)	296.2	295.6	296.3	296.5	297.4	296.6	295.6	295.9	296.2	295.6	294.0
Diffuser (very low)	296.9	296.3	297.0	296.8	297.2	296.9	295.6	296.1	297.0	295.5	292.8
Heater (very low)	294.6	293.9	294.7	295.1	297.2	295.4	296.1	297.8	296.5	295.9	293.5
Exhaust (very high)	295.8	295.1	295.9	296.2	299.1	296.4	295.6	295.9	298.0	295.8	298.1

Table 5.1: Surface temperature boundary conditions (units are in K) (*: Case 1 for the space-resolved ventilation test)

5.3 Solution methods

5.3.1 Coupled continuous and discrete phase calculations

In a coupled two-phase simulation, an iterative approach is taken to account for momentum, heat, and mass exchanges between the two phases. This iterative approach is outlined below.

- Solve the continuous phase flow field prior to the introduction of the discrete phase.
- Introduce the discrete phase by calculating the droplet trajectories for each discrete phase injection.
- Recalculate the continuous phase flow, using the interphase exchanges of momentum, heat, and mass during the previous droplet calculation.
- Recalculate the discrete phase trajectories in the modified continuous phase flow field.
- Repeat the previous two steps until a converged solution is achieved, in which both the continuous phase flow field and the discrete phase droplet trajectories have converged within the specified tolerance.

For stochastic prediction of turbulent dispersion in the coupled two-phase flow calculations, the frequency for droplet trajectory calculations is set in the 'number of continuous phase iterations per discrete phase iteration'. For example, if this frequency is set to five, with every five continuous phase calculations the droplet trajectory will be calculated once.

5.3.2 Pressure discretization

The general scalar transport equations can be discretized and solved using the control-volume-based technique. The control volume technique consists of integrating the transport equation about each control volume, yielding a set of discrete equations that express the conservation laws on a control-volume basis. If the pressure field and face mass fluxes are known, the discrete equations can be solved and a velocity field can be obtained. However, the pressure field and the face mass fluxes are not known *a priori* and must be obtained as a part of the solution. There are important issues with respect to storage of pressure and the discretization of the pressure gradient term. Many solution methods use a co-located scheme, where pressure and

velocity are both stored at cell centers. It is required to have the value of the pressure at the face between the cells. Therefore, an interpolation scheme is required to compute the face values from the cell values.

The default scheme is to interpolate the pressure values at the faces using momentum equation coefficients. This procedure works well when the pressure variation between cell centers is smooth. However, in the presence of large gradients at the cell faces, this scheme results in overshoots/undershoots of cell velocity. Such cases include the presence of body forces such as in strongly swirling flows, in high-Rayleigh-number natural ventilation and the like. In such cases, it is necessary to pack the mesh in regions of high gradient to resolve the pressure variation adequately.

Another source of error is the assumption that the normal pressure gradient at the wall is zero. This is valid for boundary layers, but not in the presence of body forces or curvature. Again, the failure to correctly account for this wall pressure gradient is manifested in velocity vectors pointing in/out of the walls. One remedy to avoid such problems is the use of PRESTO! (PREssure STaggering Option) scheme that uses the discrete continuity balance for a 'staggered' control volume about the face to compute the 'staggered' (i.e. face) pressure. This procedure is similar in spirit to the staggered-mesh schemes used with structured meshes. For triangular, tetrahedral, hybrid, and polyhedral meshes, comparable accuracy is obtained using a similar algorithm. The PRESTO! scheme is available for all meshes.

In the staggered-mesh approach, different variables to be solved for are stored at alternate locations. For example, the pressure is stored at a cell center, and the velocity is stored on the cell faces on which they acted or vice versa. The solution procedure usually uses the SIMPLE algorithm for pressure-velocity coupling. This solution technique is extended to turbulent calculations as well. A major disadvantage of the staggered-mesh approach is that the different variables have different control volumes. For a three-dimensional staggered-mesh, four different control volumes are required; four different sets of metrics are required for general, non-orthogonal coordinate systems [77].

5.3.3 Continuous phase solver

An 'implicit', 'pressure based' solver with 'absolute velocity formulation' was used. 'Green-Gauss cell based' option was chosen for the gradient option. A 'second order implicit' time discretization was used. Due to the possible variations of temperature we coupled the 'energy' and 'momentum' equations. The Renormalization Group (RNG) $k - \epsilon$ turbulence model was

chosen.

5.3.4 Discrete phase solver

The trajectory equations, and for that matter any auxiliary equations describing heat or mass transfer to/from the droplet, are solved by stepwise direct integration over discrete time steps. The motion of droplets is governed by a set of coupled ordinary differential equations [1].

$$\frac{d\overrightarrow{u}_p}{dt} = F_D(\overrightarrow{u} - \overrightarrow{u}_p) + \frac{\overrightarrow{g}(\rho_p - \rho)}{\rho_p} + \overrightarrow{F} \tag{5.26}$$

$$\frac{d\overrightarrow{x}}{dt} = \overrightarrow{u}_p \tag{5.27}$$

where $\overrightarrow{u}_p$ is the droplet velocity, $\overrightarrow{u}$ is the continuum phase velocity, F_D is drag acceleration per unit velocity (determined by Stokes law for the smallest droplets or empirical drag coefficients for larger droplets), g is gravitational acceleration, ρ_p is droplet density, ρ is continuum phase density, and $\overrightarrow{F}$ is the acceleration caused by the Brownian force, and $\overrightarrow{x}$ is position. In turbulent dispersion of discrete phase, most solvers do not account for Brownian dispersion on the grounds that the computation becomes extremely complex, and magnitude of Brownian dispersion is insignificant compared to turbulent dispersion. The integration of the above equations is possible using a variety of methods. The 'analytic' scheme is very efficient, but it can become inaccurate for large steps and in situations where the droplets are not in hydrodynamic equilibrium with the continuous flow. The numerical 'implicit' and 'trapezoidal' schemes, on the other hand, consider most of the changes in the forces acting on the droplets. The 'Runge−Kutta' schemes are recommended for non-drag force changes along a particle integration step. As a result, the 'implicit' and 'trapezoidal' schemes are preferred with careful consideration of time step [1].

5.4 Numerical errors

Numerical errors arise from discretization (both in space and time) and modeling approaches adopted. Space discretization relates to the quality of the spatial mesh used. Various methods have been used to quantify space discretization errors in CFD solutions. Time discretization errors may also become large when time step is increased beyond a critical value. Poor quality space and time discretization may result in incorrect solutions that

could also become unstable and diverge. Aside from discretization errors, there are modeling errors that include physical over simplifications in the formulation of the problem (e.g. turbulence models). Section 5.5 addresses discretization quality in the numerical work of this thesis.

5.5 Space and time discretization quality

The gist of Computational Fluid Dynamics (CFD) is a process through which a numerical solution is obtained to a set of discretized differential equations. The discretization is performed on both space and time dimensions. The importance of discretization quality in order to arrive at sensible and correct solutions cannot be emphasized enough. Paradoxically, one needs to have a good idea about the solution beforehand, in order to generate a proper space and time discretization scheme to arrive at a converged solution. If the solution is not known in good detail beforehand, the mesh design can be a tedious and repetitive task so that one needs to obtain a crude solution first to improve the space and time discretization quality.

5.5.1 Time discretization

Of 'critical' importance is the apt selection of the flow simulation and particle advancement time steps. This is true since 'careless' selection of these time steps results in obtaining erratic results 'easily'. Part of the difficulty is that the correct selection of time step depends on many other parameters such as, transient nature of the flow, the space mesh refinement, and turbulent characteristics of the flow (eddy life time and length scale).

Temporal discretization for the continuous phase involves the integration of every term in the differential equations over a time step. A generic expression for the time evolution of some variable Φ is given below [1].

$$\frac{\partial \Phi}{\partial t} = F(\Phi) \tag{5.28}$$

where Φ is a solution of interest and F incorporates any spacial discretization (some times referred to as 'flux integral'). If the time derivative is discretized using backward differences, the first and second order accurate temporal discretizations are given below.

$$\frac{\Phi^{n+1} - \Phi^{n}}{\Delta t} = F(\Phi) \tag{5.29}$$

$$\frac{3\Phi^{n+1} - 4\Phi^n + \Phi^{n-1}}{2\Delta t} = F(\Phi) \tag{5.30}$$

where $n-1$, n, and $n+1$ designate solution at time levels $(n-1)\Delta t$, $(n)\Delta t$, and $(n+1)\Delta t$. An important choice is the selection of time level for Φ in evaluating $F(\Phi)$. If time level n is used for this evaluation, the integration is called 'explicit', and Φ^{n+1} can be found in one step in terms of the existing solution values Φ^n. With 'explicit' time stepping, the maximum value of Δt is restricted to the stability limit of the underlying solver. A time step is usually limited by the Courant−Friedrich−Lewy (CFL) condition [1].

Another method to evaluate $F(\Phi)$ is referred to as 'implicit' integration by using time level $n+1$. If so, the 'implicit' equation can be solved iteratively at each time level before moving to the next time step. The major advantage of the fully implicit scheme is that it is unconditionally stable with respect to the time step size. In other words, any flow simulation time step may be used to obtain a converged solution, provided that in 'implicit' temporal discretization is used. Uninformed selection of the time step, however, may result in a large discretization error for particle tracking. Therefore, it is recommended to obtain as much resolution for the flow time as is justified by the computational cost [1].

For the droplet tracking time step many considerations are necessary. Each process that contributes to the droplet dispersion puts a restriction on the time step. So it is needed to make a compromise among all restrictions present. The first restriction is imposed by the required 'length scale' L. This parameter controls the integration time step size used to integrate the equations of motion for the particles. This length scale sets as much tracking space resolution as we need. A smaller value for the length scale increases the accuracy of the trajectory and heat/mass transfer calculations for the discrete phase. Practically, it can be as fine as the mesh space resolution. One way to estimate the required time step given L is,

$$\Delta t_1 \simeq \frac{L}{u_p + u} \tag{5.31}$$

where u_p is the instantaneous droplet velocity and u is instantaneous continuous phase velocity. Note that L, u_p, and u are all functions of both space and time. Therefore Δt_1 may vary accordingly [1].

As far as turbulent dispersion modeling is involved, other restrictions apply for the dispersion time step. The unique characteristic feature of the DRW model (an eddy interaction model), as opposed to other dispersion models, is that in the duration of the aerosol interaction with the eddy,

u, remains constant in space and time, however this is valid only within the time and space where the eddy is present. At some later time, both the eddy and the aerosol will have moved in space, perhaps according to the fluid mean velocity. So the eddy translates with the mean instantaneous velocity of the fluid. The aerosol, however, does not translate with the eddy because it probably has a velocity different than that of the eddy. The droplet remains influenced by the eddy until either its traveling time exceeds the eddy life time $\Delta t_2 = \tau_e$ or the separation distance of the continuous phase and droplet exceeds the eddy length. The time for this latter process to occur was calculated earlier in equation 5.25 ($\Delta t_3 = \tau_{cross}$). Again observe that both Δt_2 and Δt_3 are functions of space and time [1].

A proper selection of the tracking time step must satisfy all three time steps to account for the physics of dispersion correctly. Therefore, a time step that is the minimum of these three time steps is adequate for the simulation [1].

$$\Delta t \simeq minimum(\Delta t_1, \Delta t_2, \Delta t_3) \tag{5.32}$$

For our simulations we specified a fine length scale equal to the smallest mesh element size. We further allowed the solver to refine the time step up to a set number of sub time steps to meet the accuracy control with a set tolerance. If still more time steps were to be required than the maximum allowed, then the solver flagged an 'incomplete' trajectory. The accuracy control enabled the solution of equations of motion for the discrete phase to be within a specified tolerance. This was done by computing the error of the integration step and reducing the integration step if the error was too large. If the error was within the given tolerance, the integration step was also increased in the next steps. The relative error estimation for implicit Euler and trapezoidal schemes was computed by comparing the results of the integration step with the outcome of a two step procedure with half the step size,

$$\epsilon = \frac{\Phi_{\frac{\Delta t}{2}} - \Phi_{\Delta t}}{\Phi_{\Delta t}} \tag{5.33}$$

where Φ is the solution to the equation of motion (i.e. position of the droplet), and Δt is the current time step [1].

Transient simulations were performed to solve for aerosol dispersion during 600 s after injection using the following flow time steps. At first the background ventilation was solved during the first 60 s. Then, nitrogen and aerosols were injected. The time advance was resolved close to the injection

event. The time resolutions used for fluid flow solution were 6 s, 0.01 s, 0.1 s, 1 s, and 10 s for simulation times of 60 s, 61 s, 70 s, 200 s, and 660 s respectively. The particle tracking time resolution was either the same as the fluid flow time step or more refined if required.

5.5.2 Space discretization

The complexity of the geometry of interest demands an unstructured mesh to be used. For this purpose, tetrahedral elements were chosen. An important factor in generating good quality mesh is packing the control volume density in areas of the domain where solution gradients are high. These are particularly areas around nozzle, patient, occupant, exhaust, diffuser, and sharp corners in the room including the bed, the atomizer, the light, and the ceiling. Figure 5.3 shows the complete mesh for the room. Three meshes, coarse, mid, and fine, were created that contained 278669, 316645, and 359402 control volumes respectively.

The general methodology was to create the mesh by defining length scales for control volumes on surfaces of interest and then fill the volume using the 'on proximity' scheme given a growth rate. Table 5.2 summarizes the growth rates and surface control volume sizing for coarse, mid and fine meshes.

Mesh	Growth rate	Nozzle $[m]$	Diffuser $[m]$	Exhaust $[m]$	Walls $[m]$
Coarse	1.50	0.001	0.04	0.085	0.35
Mid	1.45	0.001	0.04	0.085	0.32
Fine	1.42	0.001	0.03	0.075	0.20

Table 5.2: Mesh generation parameters for coarse, mid and fine meshes in the ventilation simulation

Figures 5.4, 5.5, and 5.6 show close up images of the nozzle, diffuser, and exhaust face meshes for the mid size mesh.

The maximum length scales for all boundary walls in the room are set to 0.35 m for coarse mesh, 0.32 m for mid mesh, and 0.20 m for the fine mesh. To assess the adequacy of these settings it is necessary to review the turbulent boundary layer theory briefly.

Consider a turbulent boundary layer in which the fluid with density ρ and kinematic viscosity ν is moving with average velocity u parallel to a wall boundary and y is distance from the wall. The turbulent boundary layer

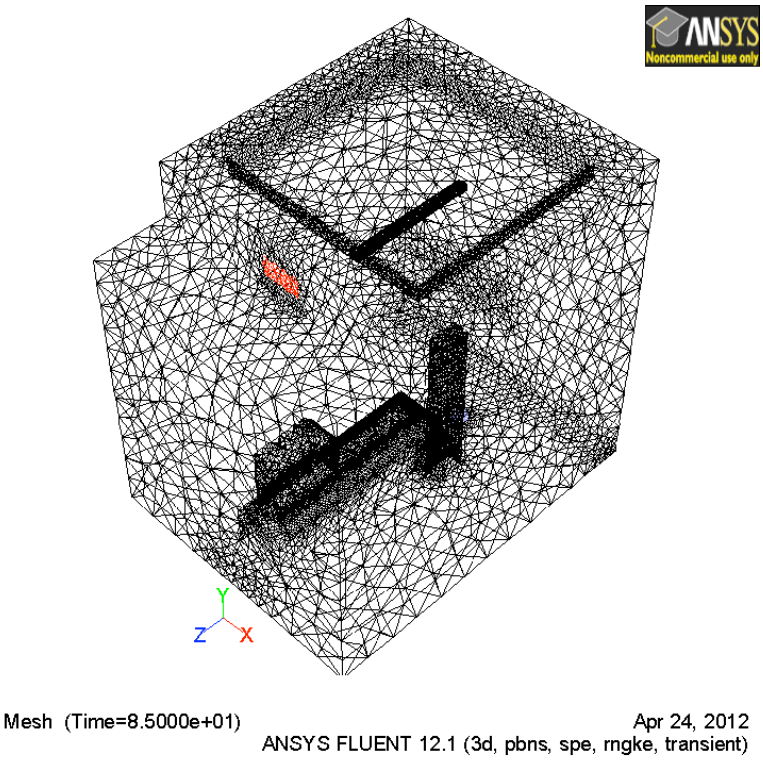

Figure 5.3: Complete mesh for the reference case (1) in ventilation simulations

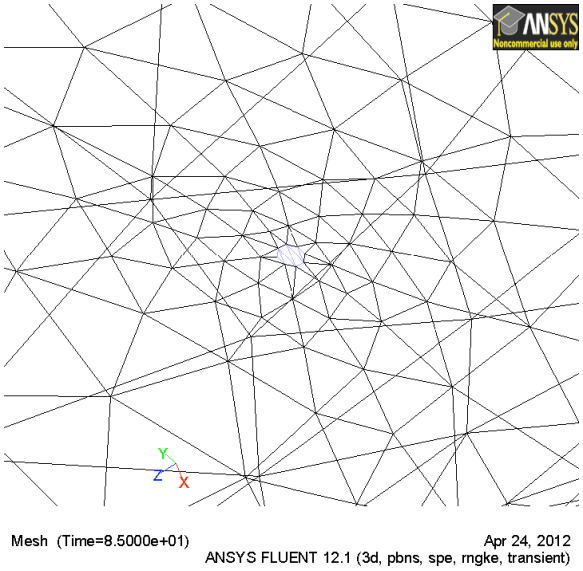

Figure 5.4: Nozzle face mesh for the reference case in ventilation simulations

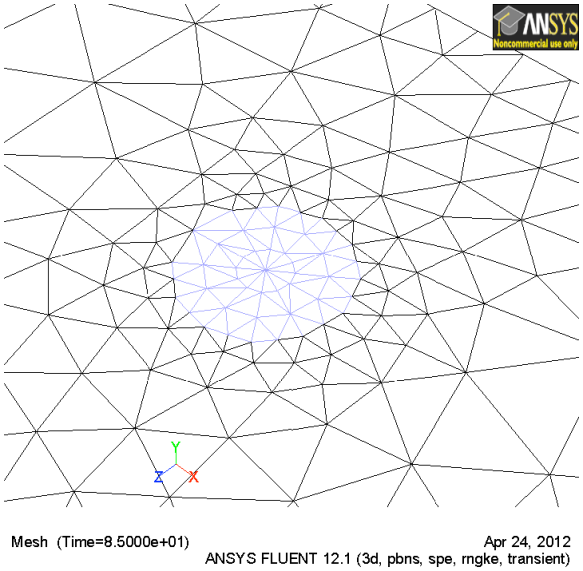

Figure 5.5: Diffuser face mesh for the reference case in ventilation simulations

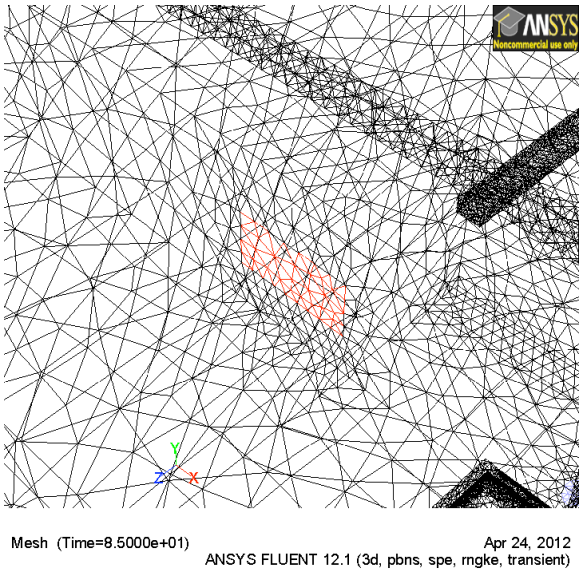

Figure 5.6: Exhaust face mesh for the reference case in ventilation simulations

regimes can be analyzed by non-dimensionalizing u and y according to the following formulae,

$$u_\tau = \sqrt{\frac{\tau_w}{\rho}} \tag{5.34}$$

$$u^+ = \frac{u}{u_\tau} \tag{5.35}$$

$$y^+ = \frac{y u_\tau}{\nu} \tag{5.36}$$

where τ_w is wall shear. The relationship between u^+ and y^+ is given by a chart known as 'law of the wall'. When it is desired to resolve the velocity profile in the turbulent boundary layer for all viscous, buffer, log-law, and outer layers, it is necessary to choose a mesh with length scale $y^+ \sim 1$ adjacent to the wall and then gradually increase mesh length scale towards the inner volume of the spacial domain for fluid flow. This requirement can impose colossal memory and computational demand for a large domain for which full resolution of the flow close to the boundary may not be necessary. The wall functions with $k - \epsilon$ turbulence models relax this requirement to

$50 < y^+ < 500$, and, hence, result in significant savings in mesh size and computational cost.

For most low energy ventilation systems the fluid velocity close to the boundary wall is moderate so that a speed of $u = 0.1\ m/s$ may be assumed. This gives the required mesh length scale close to the wall using the 'law of the wall' chart. Table 5.3 gives the required length scale for the boundary control volumes in the range $50-500$ for y^+. It is evident from this table that the chosen lengths scale for the boundary control volumes in all mesh sizes are reasonable.

y^+	u^+	$u[m/s]$	Required $y[m]$
50	14	0.1	0.11
250	19	0.1	0.74
500	20	0.1	1.57

Table 5.3: Required length scale for wall control volumes in ventilation simulations according to the 'law of the wall' turbulent boundary layer theory

5.5.3 Time and space discretization error estimation

5.5.3.1 Order of convergence

The order of grid convergence involves the behavior of the solution error defined as the difference between the discrete solution and the exact solution,

$$E = f(h) - f_{exact} = Ch^p + H.O.T \tag{5.37}$$

where C is a constant, h is some measure of mesh spacing, and p is the order of convergence. The Higher Order Terms (HOT) are negligible compared to Ch^p. A representative cell mesh size h can be defined as,

$$h = \left(\frac{1}{N} \sum_{i=1}^{N} \Delta V_i \right)^{\frac{1}{3}} \tag{5.38}$$

where ΔV_i is the volume of cell i, and N is the total number of cells. A 'second order' discretization for either space or time means that p is equal, or at least very close, to 2. A CFD code uses a numerical algorithm that will provide a theoretical order of convergence; however, the boundary conditions,

numerical models, and mesh will reduce this order so that the observed order of convergence will likely be lower. Neglecting HOT and taking the logarithm of both sides of the above equation result in,

$$ln(E) = ln(C) + pln(h) \tag{5.39}$$

The order of convergence p can be obtained from the slope of the curve of $ln(E)$ versus $ln(h)$. If such data points are available, the slope can be read from the graph or the slope can be computed from a least-squares fit to the data.

A more direct evaluation of p can be obtained from three solutions. We select three significantly different sets of meshes and run our simulations to determine values of key solutions needed for error estimation study. For example assume Φ is critical to the conclusions being reported (i.e. velocity, relative exposure, temperature, etc...). Third, we assume $h_1 < h_2 < h_3$. We define the mesh refinement ratio to be $r_{mn} = \frac{h_m}{h_n}$ and further $\Phi_{mn} = \Phi_m - \Phi_n$. If using a constant mesh refinement ratio $r = r_{32} = r_{21}$,

$$p = \frac{ln\left(\frac{\Phi_{32}}{\Phi_{21}}\right)}{ln(r)} \tag{5.40}$$

The order of accuracy is determined by the order of the leading term of the truncation error and is represented with respect to the scale of the discretization, h. The local order of accuracy is the order for the stencil representing the discretization of the equation at one location in the mesh. The global order of accuracy considers the propagation and accumulation of errors outside the stencil. This propagation causes the global order of accuracy to be, for most cases, one degree less than the local order of accuracy. The order of accuracy of the boundary conditions can be one order of accuracy lower than the interior order of accuracy without degrading the overall global accuracy.

Assessing the accuracy of the code and caluculations requires that one sufficiently refines the mesh such that the solution is in the asymptotic range of convergence. The asymptotic range of convergence is obtained when the mesh spacing is such that the various mesh spacings h and errors E result in the constancy of C:

$$C = \frac{E}{h^p} \tag{5.41}$$

5.5.3.2 Grid convergence index

Richardson extrapolation and the Grid Convergence Index (GCI) methods are commonly used to quantify discretization error estimation. We will use GCI. GCI provides a consistent manner in reporting the results of grid convergence studies. It can be computed using two levels of meshes; however, three levels are recommended in order to accurately estimate the order of convergence and to check that the solutions are within the asymptotic range of convergence.

A consistent numerical analysis is one which provides a result approaching an asymptotic value as the mesh resolution approaches zero. Thus, the discretized equations will approach the solution of the original differential equations. One significant issue in numerical computations is to decide what level of mesh resolution is appropriate. This is a function of the flow conditions, type of analysis, geometry, and other variables. One is often left to start with a coarse mesh resolution and then conduct a series of mesh refinements to assess the effect of mesh resizing. This is known as a mesh refinement study.

One must recognize the distinction between a numerical result which approaches an asymptotic value and one which approaches the true solution. Even when the asymptotic solution to a set of differential equations is found, it may be different from the true physical solution.

The GCI is a measure of the percentage the computed solution is away from the asymptotic computed solution. It indicates an error band on how far the solution is from the asymptotic value and how much the solution would change with a further refinement of the mesh. A small value of GCI indicates that the computation is within the asymptotic range. The GCI is defined as,

$$GCI_{mn} = \frac{F_s \mid \epsilon_{mn} \mid}{r^p - 1} \tag{5.42}$$

where F_s is a factor of safety. The refinement may be in either space or time. The factor of safety is recommended to be 3.0 for comparisons of two meshes and 1.25 for comparison over three meshes or more. The relative error ϵ_{mn} is defined by,

$$\epsilon_{mn} = \frac{\Phi_m - \Phi_n}{\Phi_n} \tag{5.43}$$

It is assumed that the mesh refinement ratio r is applied equally in all coordinate directions (i, j, k) for steady state solutions and also time t for

time dependent solutions. If this is not the case, then the grid convergence indices can be computed for each direction independently and then added to give the overall grid convergence index by,

$$GCI = GCI_t + GCI_x + GCI_y + GCI_z + ... \tag{5.44}$$

Chapter 6

Experimental Results and Discussion

6.1 Near-field atomizer test results

6.1.1 Spray penetration

A total of 200 images were taken for each test described in section 4.1.2. The injection (and therefore imaging) was repeated every 2.5 s. The raw images were later processed by a MATLAB code so that the spray axial and radial penetration distances could be determined with ease. First, each image was converted into a binary image with its pixel value assigned to 'one' if the intensity was above a given threshold, and 'zero' if the intensity was below it. Second, the image was filtered for noise (random pixels with high intensity). The spray axial and radial penetration distances were measured by constructing a box around the spray whose length and width represented x and r respectively. The final image was used in the penetration study. Figure 6.1 shows the raw and filtered binary images obtained by the camera. Appendix B contains the algorithm that was used in image processing.

Dimensionless axial penetration is plotted versus dimensionless time in figure 6.2. Dimensionless radial penetration is plotted versus dimensionless axial penetration in the same figure. t_f is estimated in section 4.1.5. Two lines on each plot have been fitted to the last 11 data points to describe the self-preserving scaling of the starting jet ($R^2 = 0.99$) according to equations 2.5 and 2.6. The virtual origin, x_0, is calculated to be $-0.005\ m$. These lines are expected to overlay closely on top of each other. The fitted constants to the self-preserving scaling of the starting jet are provided in table 6.1. The constants found are close to those of starting continuous phase jets in the literature.

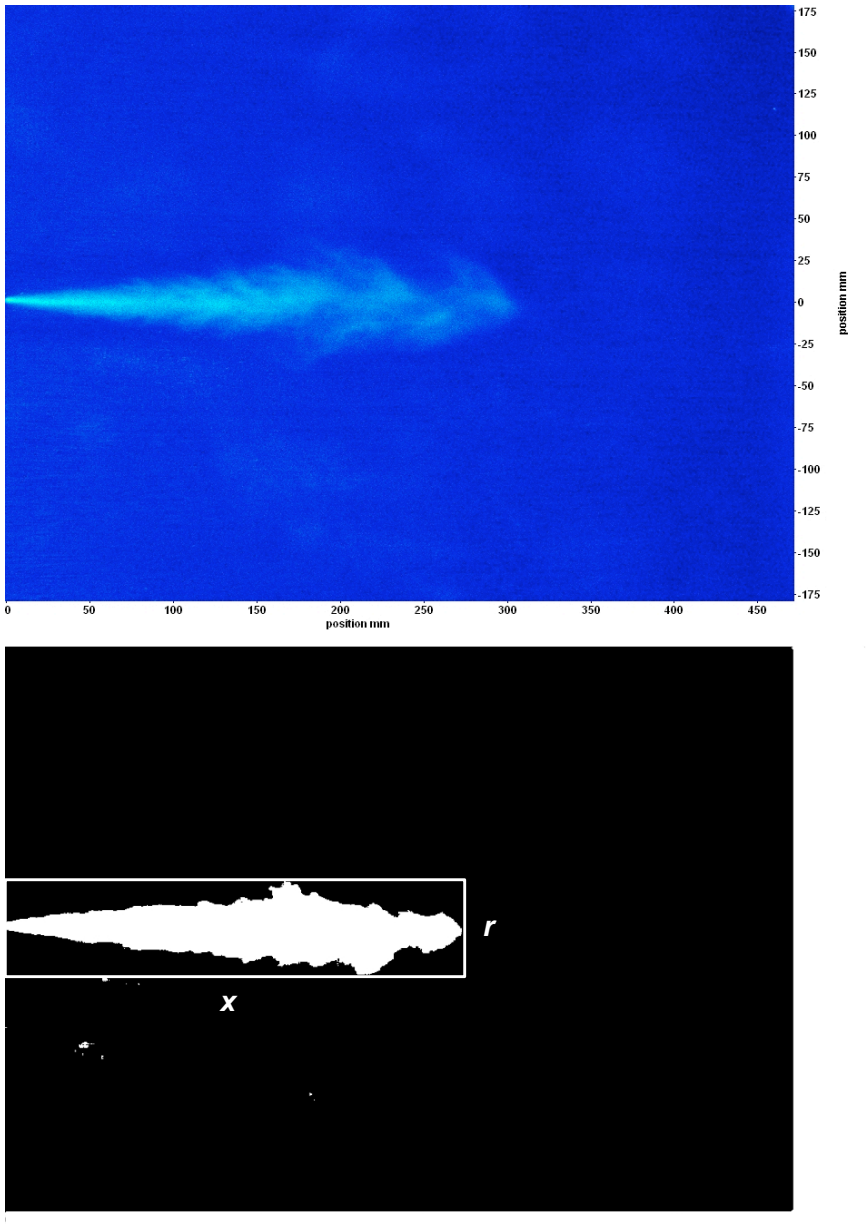

Figure 6.1: Spray at $t = 24\ ms$ for Test 1 raw image (top) and filtered binary image (bottom)

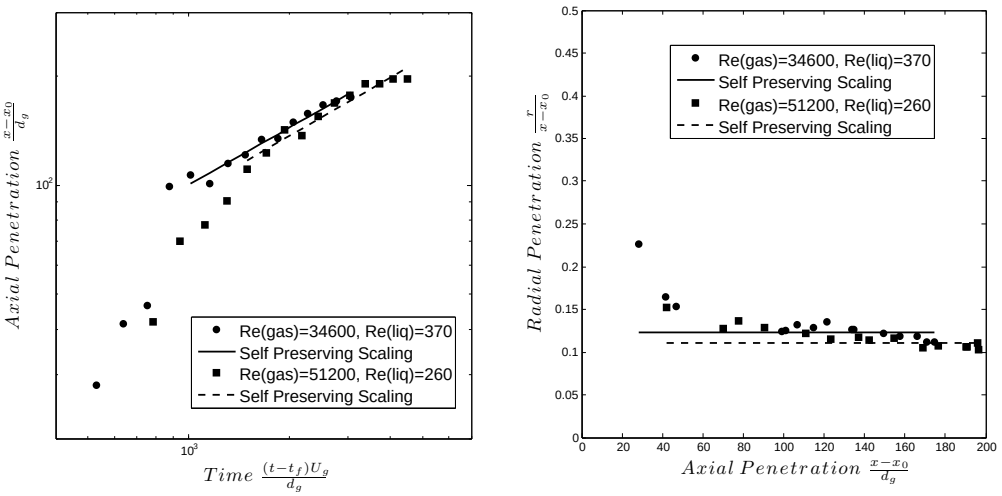

Figure 6.2: Dimensionless axial penetration versus dimensionless time (left) and dimensionless radial penetration versus dimensionless axial penetration (right) (Test 1 and 2 flow conditions)

Medium	Re_g	n	C_x	C_r
Liquid [92]	3000−12000	0.5	2.6	0.16
Liquid [54]	53000	-	-	0.09-0.10
Liquid [57]	2600	0.5	2.9	-
Liquid [88]	-	-	-	0.13
Gas [109]	2400−9200	0.5	2.5−3.2	-
This Study	34600−51200	0.5	2.19-2.48	0.10−0.11

Table 6.1: Summary of self-preserving properties for round turbulent starting jets and transient sprays

6.1.2 Sauter mean diameter, droplet size, and concentration distributions for steady spray

The spray was imaged at three axial locations: 50 mm ($\frac{x}{d_g} = 20.7$), 100 mm ($\frac{x}{d_g} = 41.4$), and 200 mm ($\frac{x}{d_g} = 82.9$) away from the nozzle tip. A radial traverse was performed at each axial location. The radial total concentration is plotted in figure 6.3. As expected the data collapse on a Gaussian curve ($R^2 = 0.96$). Figure 6.3 also shows the radial profiles of d_{32} at three different axial locations. d_{32} rises as the spray periphery is approached. These results are in agreement with those found in previous studies [27, 52, 59] indicating that close to the nozzle, larger droplets were more prevalent on the spray periphery.

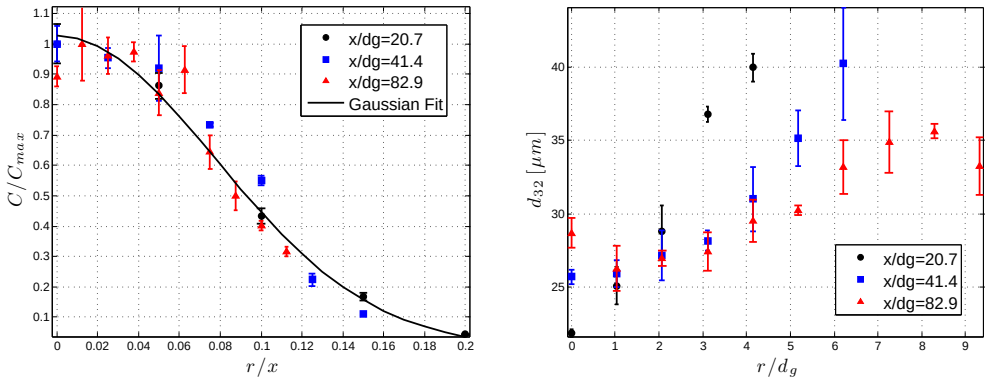

Figure 6.3: Total radial concentration of droplets (left) and d_{32} (right) at three different axial distances (Test 1 flow conditions)

The correlation of Rizkalla and Lefebvre [89] predicts $d_{32} = 20.8$ μm for the same atomizer flow conditions, exit diameters, and liquid and gas properties. This value is remarkably close to our experimentally measured value ($d_{32} = 20.8 \pm 0.3$ μm) at $\frac{x}{d_g} = 20.7$ for droplet sizes in the range 2−100 μm as described in section 4.1.7. This leads to confidence in our size measurements.

6.1.3 Sauter mean diameter and concentration distribution for transient spray

The leading and trailing edges of the spray are shown, schematically, in figure 6.4. The arrival of the leading edge at a particular location is considered when at least 100 droplets are detected, on average, for the three sets of 100 images taken. Likewise, for the trailing edge, there should be at least 100 droplets detected, on average, for the three sets of 100 images taken. The transient behavior of the spray is studied by delaying imaging with respect to the infrared sensor trigger signal. The leading edge of the spray is measured when the infrared beam is blocked (high to low edge trigger), and the trailing edge of the spray is measured when the infrared beam is unblocked (low to high edge trigger).

Figure 6.5 plots d_{32} and normalized concentration profiles against non-dimensional time delay for the leading and trailing edges at the centerline of spray. At the trailing edge the value of d_{32} is higher at larger axial distances. This can be attributed to two effects. Firstly, small droplets may shrink slightly and leave the measurement droplet size limits due to evaporation at long time delays. Secondly, the small droplets depart from the centerline more quickly by turbulent dispersion. These two mechanisms can result in higher d_{32} values at the centerline of the spray.

6.1.4 Droplet size distribution for transient spray

Figure 6.6 shows the volume size distributions for the leading and trailing edges at the centerline of the spray with respect to time delay for $\frac{x}{d_g} = 20.7$, 41.4, and 82.9. The time delay is non-dimensionalized by $t^* = \frac{t_d U_g}{d_g}$.

Figures 6.5 and 6.6 show that for $\frac{x}{d_g} = 20.7$ the leading edge of the transient spray contains more fine droplets than the steady spray. In contrast, the leading edges for $\frac{x}{d_g} = 41.4$ and 82.9 contain larger droplets so that the volume size distribution is gradually shifted to the right. It is speculated that fine droplets respond to the high flow speed near the nozzle more quickly. In addition, larger droplets originally form closer to the periphery of the spray and do not interact with high flow velocities at the center. As a result, smaller droplets penetrate faster in the axial direction near the nozzle. On the contrary, at larger axial distances ($\frac{x}{d_g} = 41.4$ and 82.9) larger droplets have gained momentum and penetrate with higher speed in the axial direction. No obvious trend is observed for the trailing edge. It is noted that at larger non-dimensional time delays, the transient spray approaches steady state conditions so that the plots reflect any differences.

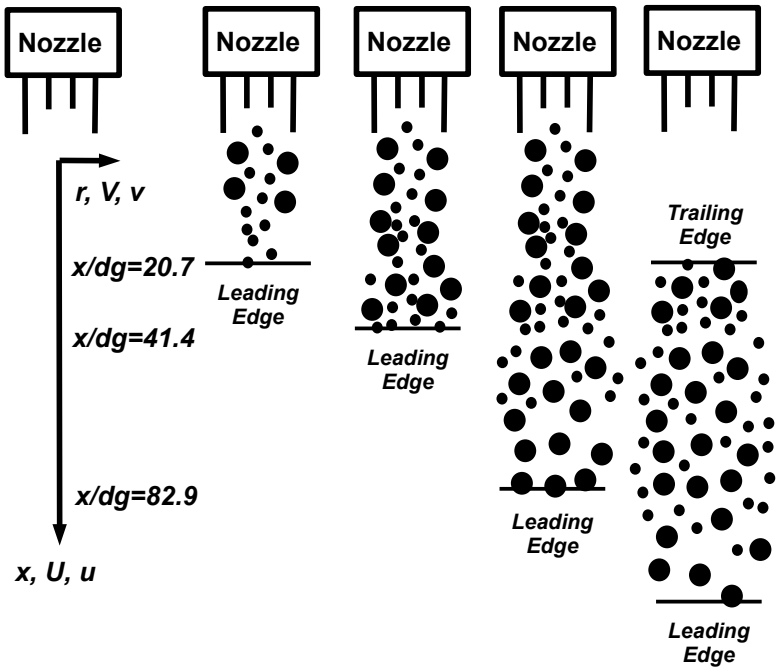

Figure 6.4: Schematic for leading and trailing edges of the transient spray

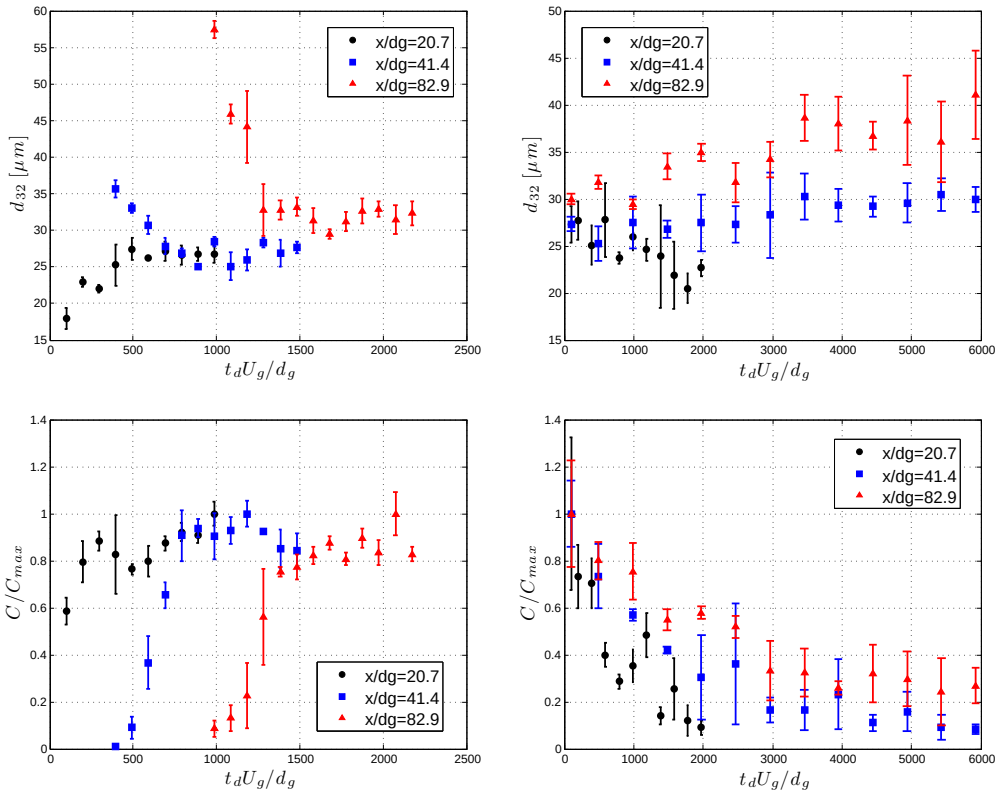

Figure 6.5: d_{32} (top) and normalized concentration (bottom) in the leading (left) and trailing (right) edges of the spray on central axis (Test 1 flow conditions)

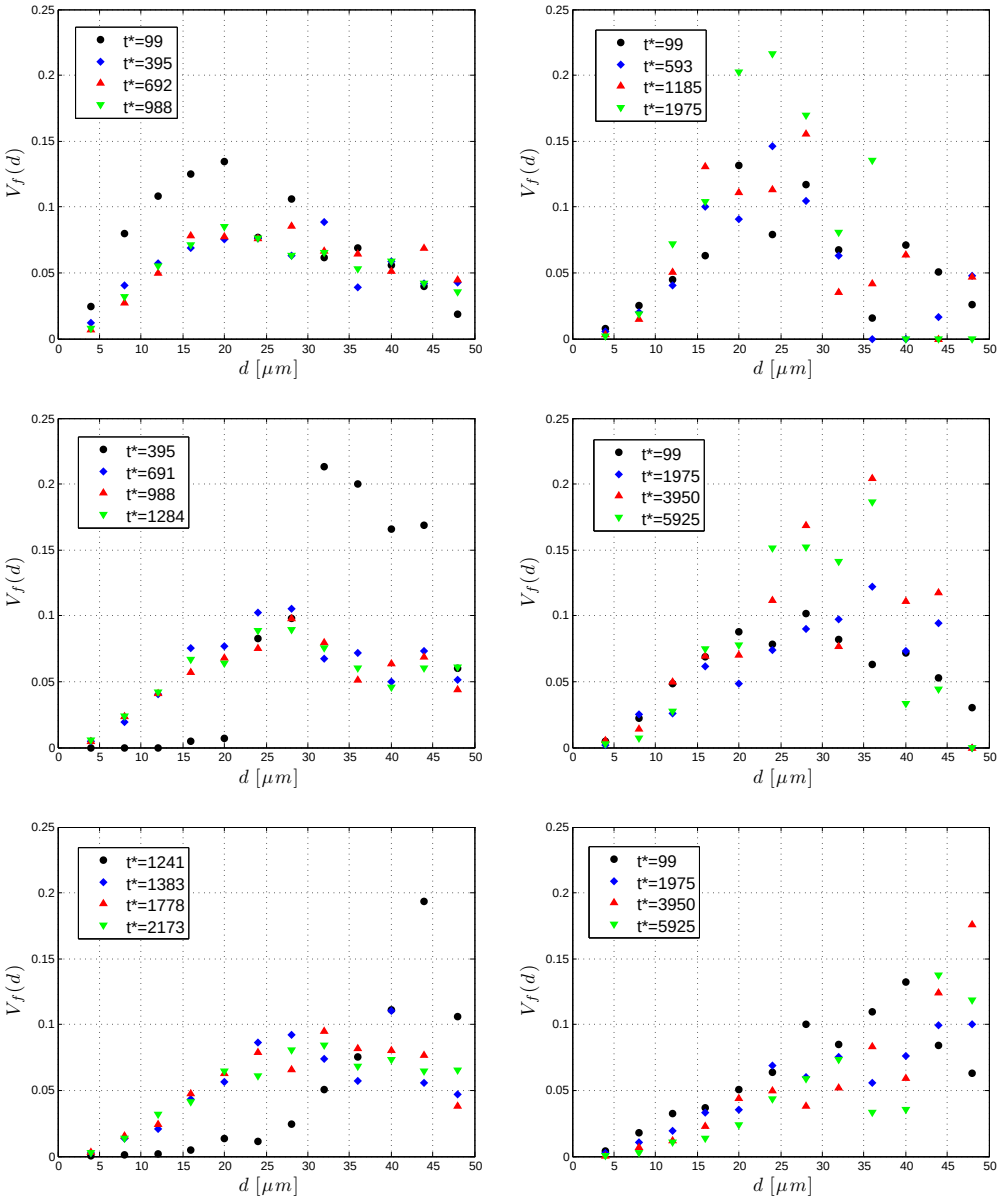

Figure 6.6: Volume size distribution on central axis in the leading (left) and trailing (right) edges of the spray at $\frac{x}{d_g} = 20.7$ (top), $\frac{x}{d_g} = 41.4$ (middle) and $\frac{x}{d_g} = 82.9$ (bottom) ($t^* = \frac{t_d U_g}{d_g}$) (Test 1 flow conditions)

These results can be better understood considering the mean Stokes number (defined in table 2.1). The mean Stokes number for the peak droplet size in the leading edge is calculated as St_m = 5.3, 7.2, and 6.4 for $\frac{x}{d_g}$ = 20.7, 41.4, and 82.9 respectively. For the trailing edge, it is calculated as St_m = 7.6, 8.6, and 5.4 accordingly. The mean Stokes number suggests that the relaxation time τ_d for the dominant droplet size in the leading or trailing edges of the spray scales with the mean characteristic time of the flow τ_g at each axial distance of interest.

6.1.5 Steady spray deceleration

The steady spray deceleration is shown in figure 6.7. The values of B and x_0 in equation 2.2 are found experimentally. B is 6.5, 11.8, 7.4, 5.5, and 5.8 for each droplet size bin from smallest to largest. Likewise, x_0 is $-131d_g$, $-232d_g$, $-114d_g$, $-63d_g$, and $-57d_g$ for each droplet size bin from smallest to largest (R^2 = 0.84, 0.75, 0.68, 0.71, and 0.59). Large droplets are detected less frequently in the flow, so the statistical errors for these droplets are expected to be higher. The B values, negative virtual origins, and faster deceleration of smaller droplets in the spray are consistent with results found in the literature [27]. The virtual origin decreases as the droplet diameter increases.

6.1.6 Velocity distribution for steady spray

Figure 6.8 shows the velocity distribution as a function of radial distance at the axial location of $\frac{x}{d_g}$ = 41.4. In particular, profiles of axial velocity U, normalized axial velocity $\frac{U}{U_c}$, axial fluctuating velocity $\overline{u^2}$, and radial fluctuating velocity $\overline{v^2}$ have been chosen for demonstration. The velocity profiles for other axial locations show a similar trend and therefore they are not shown for conciseness.

The first trend observed is that larger size bin droplets have higher mean velocities in the axial direction. This is expected since larger droplets have higher momentum and are disturbed less by turbulent eddies in the gas phase. Moreover, these velocity profiles are self-similar and appear as Gaussian in the radial direction, as confirmed by the literature [7, 27, 49, 52, 53, 62].

The fluctuating profiles indicate to what extent particles of a certain size bin follow the turbulent fluctuations in the fluid. Smaller droplets assume higher fluctuating velocities than larger droplets [27, 72]. This can be understood in light of turbulent and Kolmogorov Stokes numbers (defined

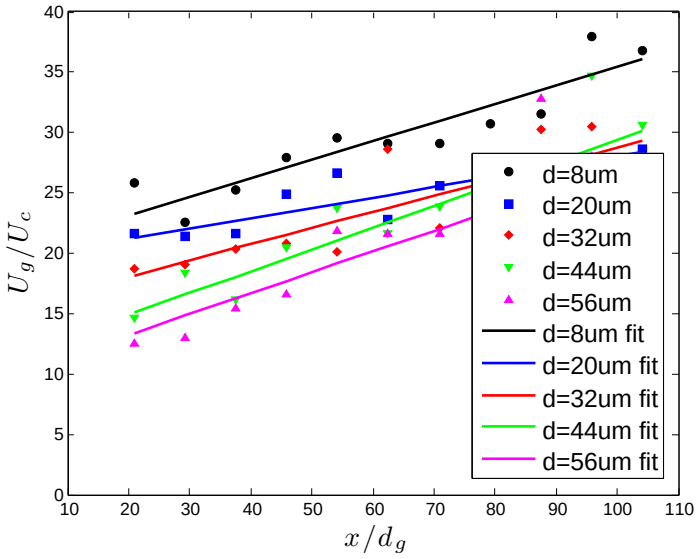

Figure 6.7: Steady spray deceleration (Test 1 flow conditions)

in table 2.1). The values of k and ϵ for turbulent and Kolmogorov Stokes numbers calculations have been approximated by considering the turbulent kinetic energy and dissipation rate on the central axis of gas jets. Figure 6.9 shows that, at all axial distances the values of turbulent and Kolmogorov Stokes numbers are higher for larger droplets. This means that as droplets become larger, they disperse in a more dissimilar way than the fluid elements since the ratios of droplet relaxation time to turbulent eddy or Kolmogorov characteristic times become higher.

6.1.7 Péclet number for steady spray

The turbulent dispersion of droplets in the radial direction can be non-dimensionalized using droplet diffusivity and the Lagrangian Péclet number in equations 2.3 and 2.4. Since the droplet response to turbulence is more predictable at larger distances from the nozzle, the average Péclet number is calculated from $\frac{x}{d_g} = 41.4$ to $\frac{x}{d_g} = 82.9$. Figure 6.10 shows the Péclet number as a function of droplet size. Larger droplets show a higher Péclet number than smaller droplets. This confirms the hypothesis in section 6.1.6 that smaller droplets disperse more effectively in the radial direction due to

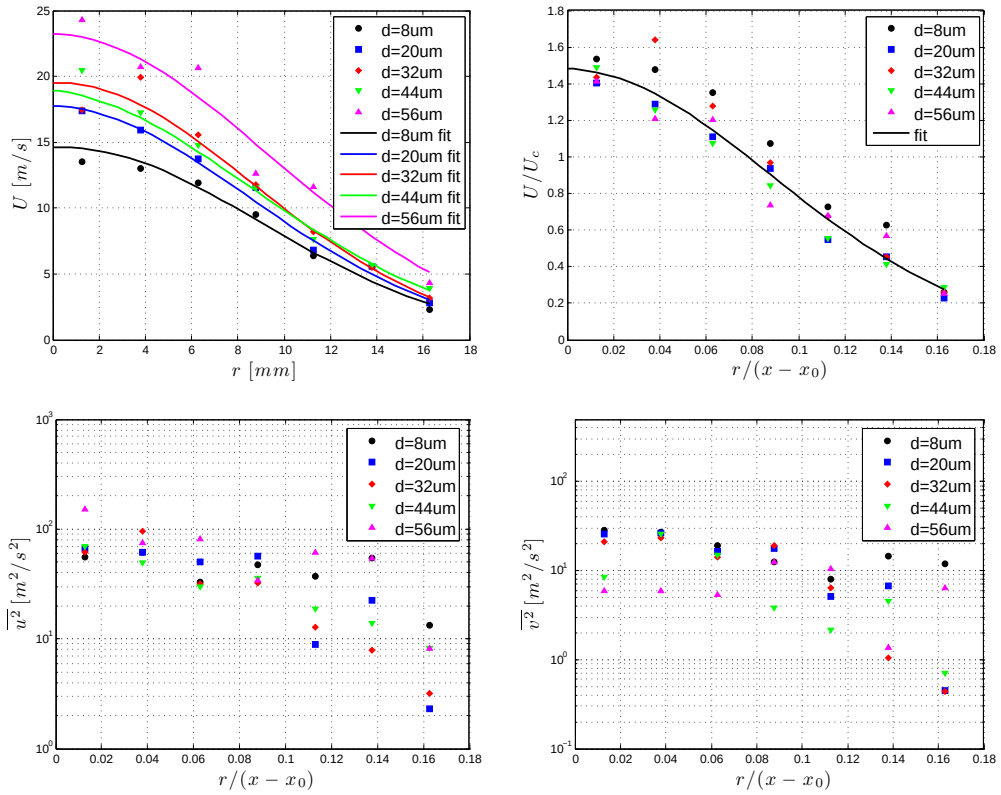

Figure 6.8: Axial velocity (top left), normalized axial velocity (top right), axial fluctuating velocity (bottom left), and radial fluctuating velocity (bottom right) for $\frac{x}{d_g} = 41.4$ (Test 1 flow conditions)

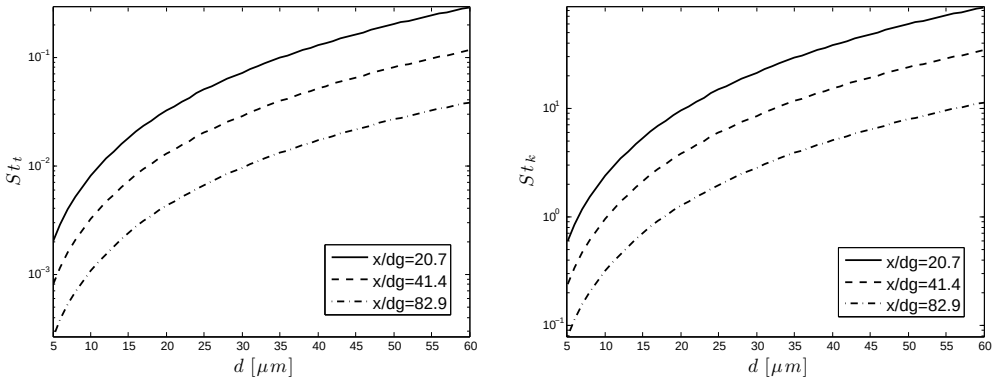

Figure 6.9: Turbulent Stokes number (left) and Kolmogorov Stokes number (right) for axial locations $\frac{x}{d_g} = 20.7$, 41.4 and 82.9 (Test 1 flow conditions)

turbulent fluctuations [53].

6.1.8 Velocity distribution for transient spray

Figure 6.11 shows the velocity distribution as a function of time delay at the axial location of $\frac{x}{d_g} = 41.4$ on the center line of the spray. In particular, profiles of axial velocity U, axial fluctuating velocity $\overline{u^2}$, and radial fluctuating velocity $\overline{v^2}$ have been chosen for demonstration. Again, the data have been plotted on the same scale as for the steady spray (figure 6.8) so that the relative magnitude of the quantities of interest could be compared. For conciseness, the results for other axial locations are not shown but are similar.

For the leading edge, the mean axial velocity for larger droplets is higher than that of smaller droplets. The magnitude of this velocity does not change notably as a function of time delay. The velocity magnitude is also similar to those observed for steady sprays. The unchanging value of this velocity as a function of time delay in the leading edge shows similarity between continuous phase starting jets and transient sprays. As one would anticipate, the magnitude of the axial velocity at the trailing edge is smaller compared to the leading edge. This magnitude is similar for all droplet sizes, and it declines slowly for larger time delays.

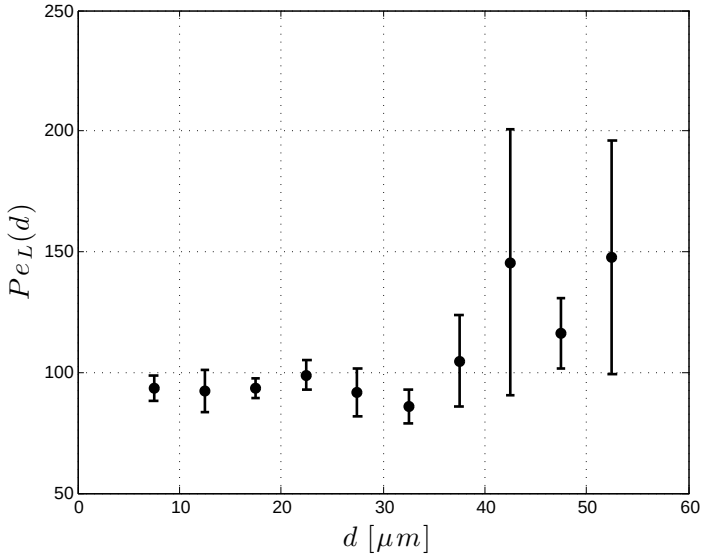

Figure 6.10: Average Péclet number from $\frac{x}{d_g} = 41.4$ to $\frac{x}{d_g} = 82.9$ (Test 1 flow conditions)

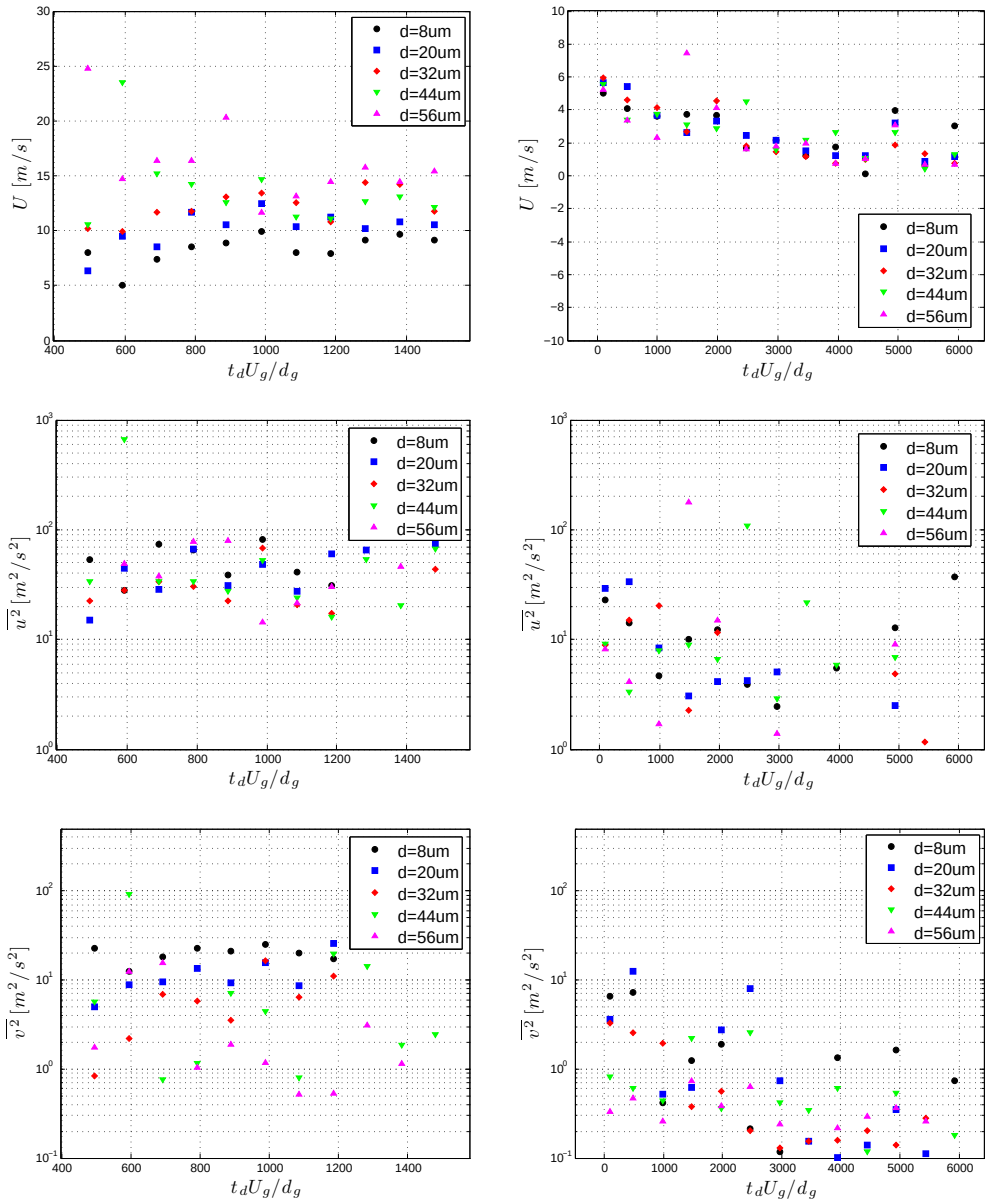

Figure 6.11: Axial velocity (top), axial fluctuating velocity (middle), and radial fluctuating velocity (bottom) for leading (left) and trailing (right) edges of the transient spray at $\frac{x}{d_g} = 41.4$ on central axis (Test 1 flow conditions)

At the leading, edge the magnitude of axial and radial fluctuating velocities are about the same as the equivalent steady case. Again, small droplets move with higher fluctuating velocities than large droplets. For the trailing edge, these velocities drop an order of magnitude and no correlation can be observed between velocity and droplet size. The velocity data is rather very scattered. It is speculated that the magnitude of turbulent and Kolmogorov Stokes numbers drop quickly when the injection momentum is cut. As a result, all droplets track fluid turbulent motion more easily. In this region the flow reaches very low Reynolds numbers where all droplets follow the random fluid motion with the same likelihood.

6.2 Far-field ventilation test results

The temperature for the boundaries and internal space of the room was monitored over 24 hours to find the best time period for testing. Ideally, one would like steady temperatures for the boundaries so that the experiments are repeatable. Appendix C shows the boundary and internal temperature as measured by the thermocouples on January 22 and 23, 2012. The sampling for this test started at 3 pm and continued for 24 hours. It is observed that the boundary and internal temperatures are steady over 24 hours except for a period of time in the late afternoon, when the solar gain in the building is dominant. The overall temperature of the room peaks at about 3 pm. To avoid such temperature fluctuations, a time window before noon was chosen for conducting the experiments. All tests were performed from 9 am until 12 pm on consecutive days.

6.2.1 Reference case (1)

6.2.1.1 Temperature, velocity, and air change rate

Reference case boundary temperatures, internal temperature, air velocities, and air change rate are shown in Appendix D. The air change rate of the room stayed nearly constant for the entire duration of the test. Also the thermal vertical stratification of the room was maintained during each test. The airflow speed at diffuser and exhaust were stable over the total experiment time. The thermal plume associated with the nurse is measured on top of the nurse's head. The air velocity in this location is about 0.15 m/s.

6.2.1.2 Concentration and cumulative concentration

The background aerosol concentration is insignificant compared to concentrations when injections are made. Figure 6.12 shows the concentration and cumulative concentration in the background. Although insignificant, this background concentration is subtracted from measurements when injections are made.

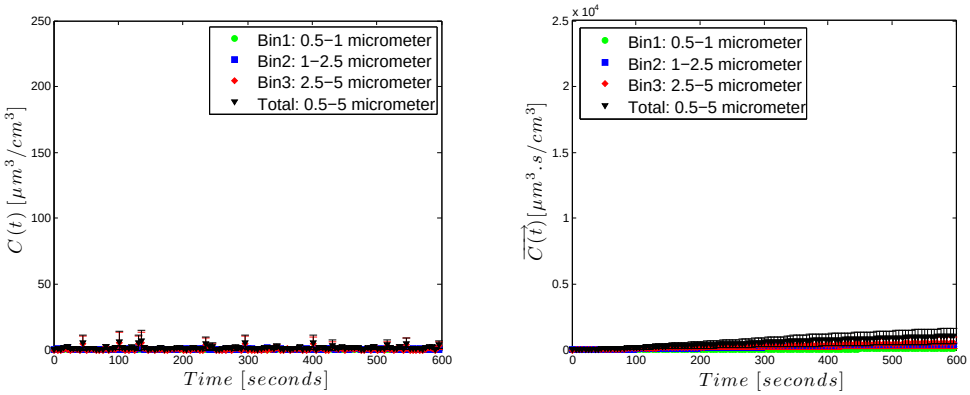

Figure 6.12: Background concentration (left) and cumulative concentration (right)

Figure 6.13 shows the real time measured concentration and cumulative concentration for the reference case in the parametric study. Observe that the majority of droplet volume is carried by size bin 3. Also observe that the concentration and cumulative concentration are greater at the sitting zone than for the upper zone.

6.2.1.3 Normalized concentration and cumulative concentration

For the purpose of comparison with modeling results, it is necessary to normalize the concentration and cumulative concentration by the injection concentration. Figure 6.14 shows the normalized concentrations and cumulative concentrations at sitting, breathing, and upper zones. Normalized by the injection concentrations, droplets in size bins 2 and 3 make the greatest contribution in cumulative concentration, followed by size bin 1. In other words, a greater fraction of droplets injected in size bins 2 and 3 actually reach the measurement point, while smaller droplets in bin 1 are quickly dispersed and diluted. Again, observe that the overall exposure at the sitting

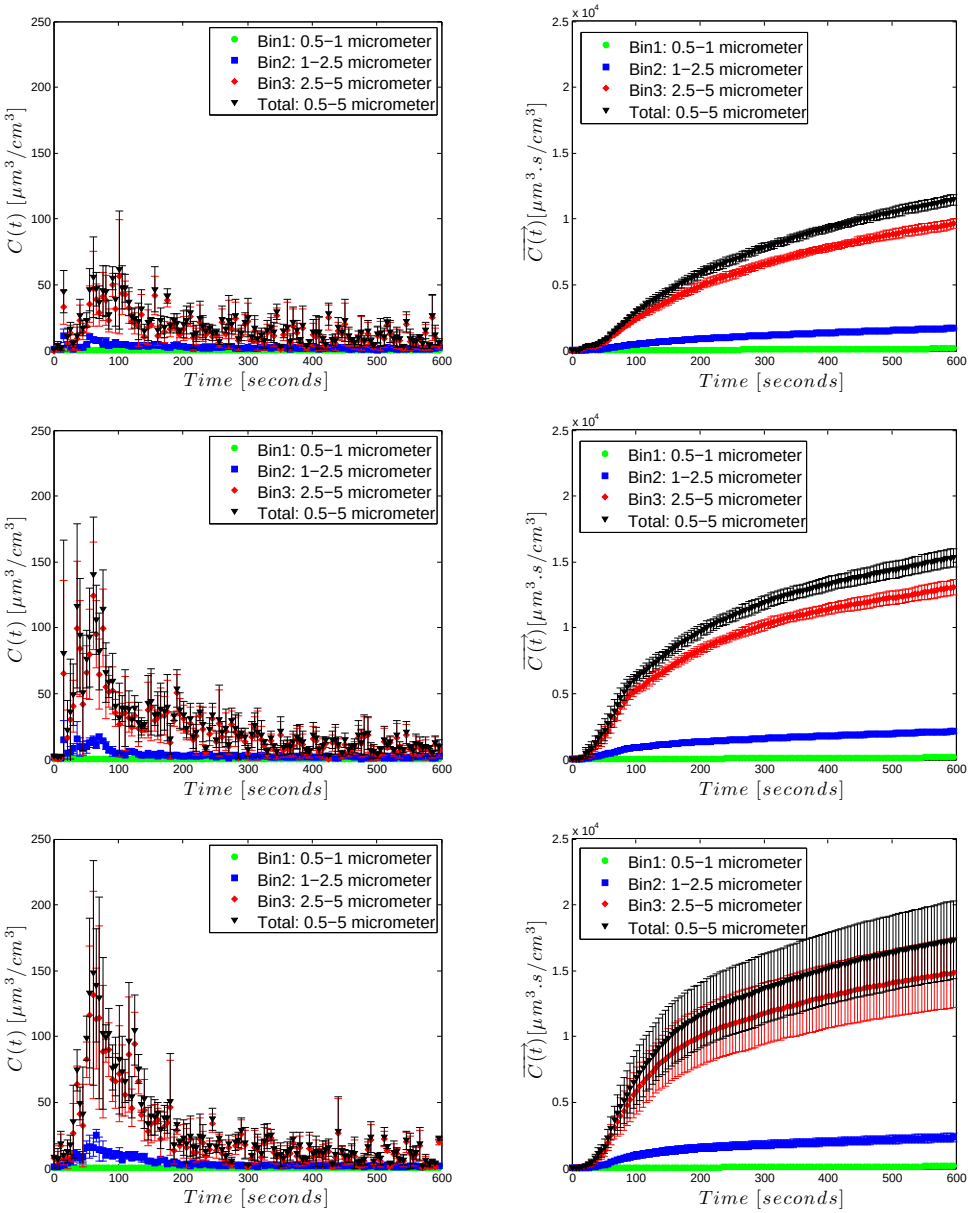

Figure 6.13: Experimental concentration (left) and cumulative concentration (right) at the sitting (bottom), breathing (middle), and upper (top) zones for the reference case (1)

zone is higher than the breathing and upper zones.

The size bin behavior in dispersion is best demonstrated using the normalized concentration fraction for droplets in injection compared to the normalized cumulative concentration fraction for droplets at sitting, breathing, and upper zones. Figure 6.15 shows these fractions. Observe that droplets in bins 2 and 3 succeed more in reaching the measurement locations. Also a subtle dependence in the size distributions are noticed as a function of height. Droplets in bin 1 have a higher fraction at higher zones while droplets in bins 2 and 3 have a higher fraction near lower zones. This is expected since small droplets are not affected by gravity and are easily transported upwards due to ventilation flow and turbulent diffusion. On the other hand, gravitational settling tends to move larger droplets downwards.

6.2.2 Parametric study

6.2.2.1 Total relative exposure

The reference case (1) cumulative concentration at the breathing zone is used to normalize cumulative concentrations for all other cases and zones. Since the total amount of injected mass and droplet size distribution for all experiments are the same, the relative exposure shall be directly compared to the reference case to study the effects of variations in boundary and initial conditions. The results are reported for short ($T = 140\ s$) and long ($T = 600\ s$) exposure times at sitting, breathing, and upper elevations.

Figure 6.16 summarizes the total relative exposure at all zones for short and long times respectively. For the reference case (1), the relative exposure is higher at the sitting zone and lower at the upper zone. In other words, exposure is not vertically stratified. We speculate that the inclined spray crosses the plume in the room, so aerosols do not follow the plume streamlines. This can occur with mixing and recirculation of the spray in the room. In addition, gravitational settling and relaxation time effects result in a dispersion behavior that is different from gases.

The following observations can be made regarding the effects of boundary and initial conditions on the relative exposure. High injection velocity of case 2 increases mixing in the room so that relative exposure increases (more pronounced at long time). Lower injection velocity of case 3 has the opposite effect so the relative exposure reduces. Cases 4 and 6 transport aerosols away from the occupant so they decrease relative exposure. Case 6 (vertical injection) is ideal since it results in a better exposure vertical stratification, and it is the only case that actually achieves the desired ver-

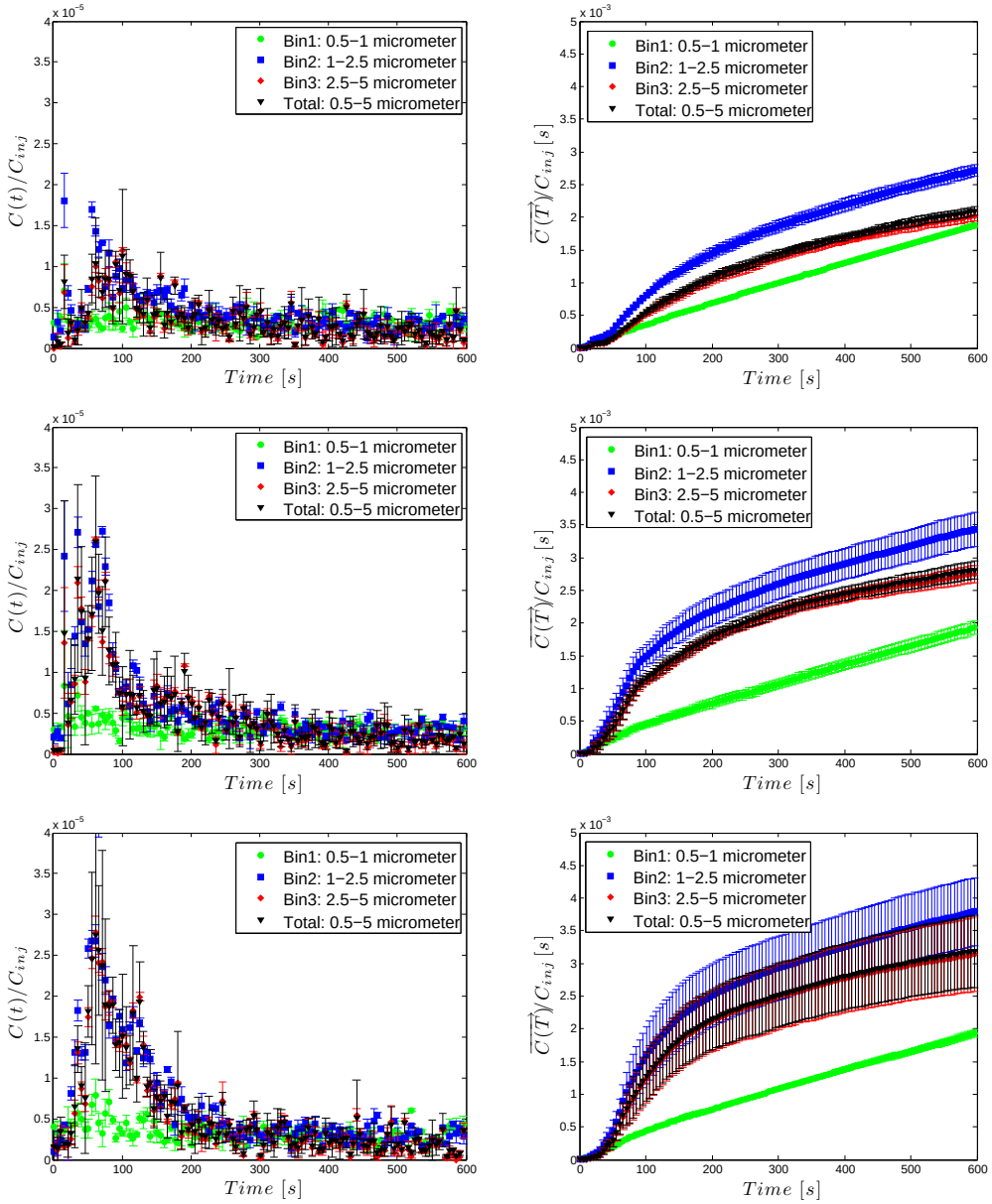

Figure 6.14: Experimental normalized concentration (left) and cumulative concentration (right) at the sitting (bottom), breathing (middle), and upper (top) zones for the reference case (1)

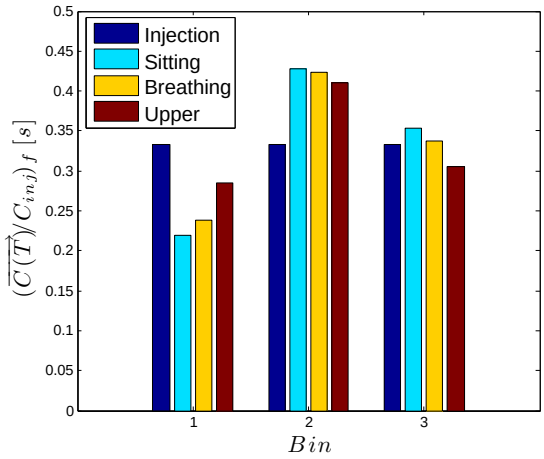

Figure 6.15: Experimental normalized cumulative concentration fraction near injection and measurement points

tical stratification between sitting versus breathing/upper zones. Case 5 (horizontal injection) impacts aerosols on the wall, so it reduces the relative exposure. The lower metabolic rate in case 7 slightly increases relative exposure for all zones at long time. We suspect that a less fraction of aerosols in the room are removed by a weaker plume so lower metabolic rates increase relative exposure. Albeit, this result is not statistically significant, since the measured average exposure is within the error bars calculated in the reference case. Cases 8 and 9 place the occupant at a farther distance from the contaminants in a way that relative exposure reduces. In Case 8 the occupant is still in front of the injection so more droplets reach the sampling pole compared to case 9, where the sampling pole is behind the injection. The higher air change rate of 3.7 in case 10 reduces relative exposure at both short and long times. This can occur by several mechanisms. The higher turbulence of air in this case quickly dilutes air in the room. Also with more air change rate, more droplets are transported to the ceiling and removed. Still, exposure is not vertically stratified, as it is in case 6 (vertical injection).

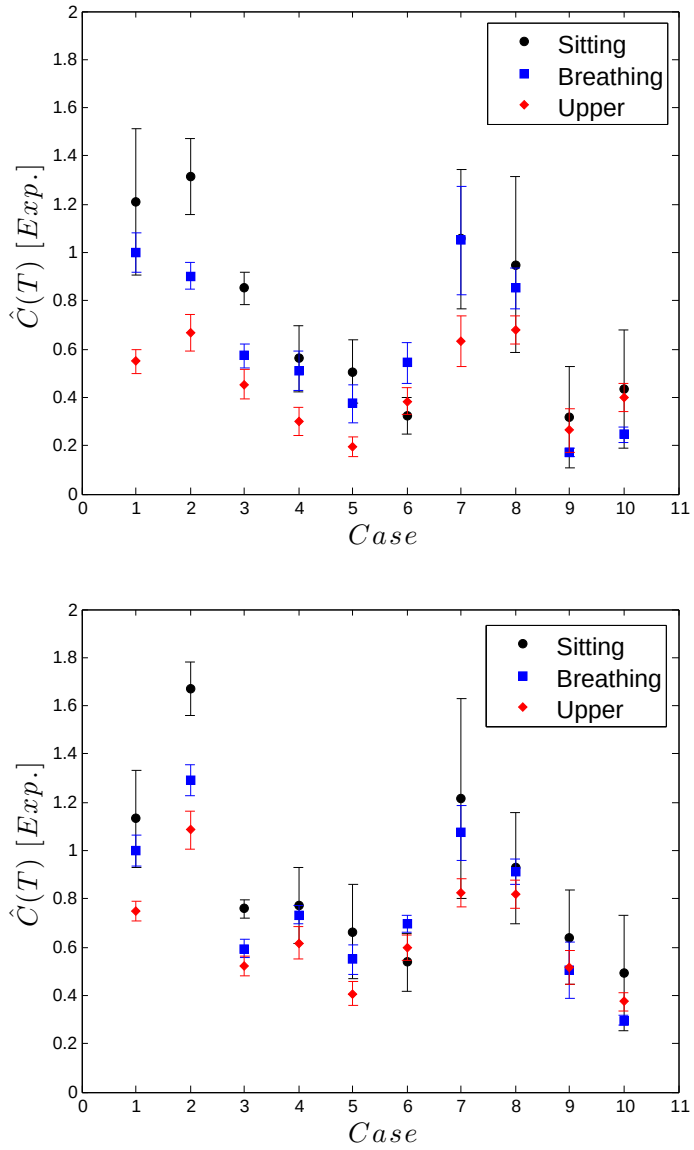

Figure 6.16: Short (top) and long (bottom) time measured (Exp.) relative exposure at all zones for parametric study

6.2.2.2 Size bin-resolved relative exposure

Figure 6.17 shows size bin-specific relative exposure for short and long times at all zones. Generally, size bin 1 droplets are observed to move upwards more easily than size bins 2 and 3 droplets. This can be noticed by green legend data points at the upper zone graphs. The following statements can be made about the size bin-specific dispersion of droplets among the ten parametric cases.

Case 1: the total relative exposure is highest for the sitting zone. Size bin-specific relative exposure is slightly reversed in vertical stratification from sitting zone to the upper zone. This is noticed by a reversed color legend. Finer droplets in bin 1 transport upwards more easily than larger droplets, and larger droplets tend to stay closer to the sitting zone. This may be due to the effect of gravity. The dispersion is alike in both short and long times.

Case 2: size bin-specific relative exposure is similar to case 1 albeit the short and long time dispersion characteristics are different. At short time, the relative exposure rise is moderate for all size bins, perhaps because the high injection momentum has transported most droplets above measuring heights. At long time, the relative exposure takes a second surge for bins 2 and 3 because the droplet cloud could circulate or fall due to gravity back to the measuring collectors.

Case 3: for most cases relative exposure at all sampling heights are lower compared to cases 1 and 2. Large droplets in bin 5 are measured at higher concentrations at sitting zone.

Case 4: for the sitting zone, relative exposure is reduced compared to case 1 since droplets are injected away from the measurement pole. A fraction of these droplets do however return at the breathing zone to be measured at higher concentrations compared to case 3.

Case 5: due to impaction of droplets on the window, this configuration also effectively removes larger droplets in bins 2 and 3 compared to most previous cases. Droplet removal due to impaction is slightly improved compared to case 4.

Case 6: this is the only configuration where vertical stratification of exposure in most size bins is achieved. Except for bin 1, the sitting zone exhibits the lowest concentration for all size bins among most previous cases. Bin 1 droplets are measured at a high concentration at the upper zone compared to all other cases. The vertical momentum of injection easily transports these droplets upward, and the gravity does not pull them back down.

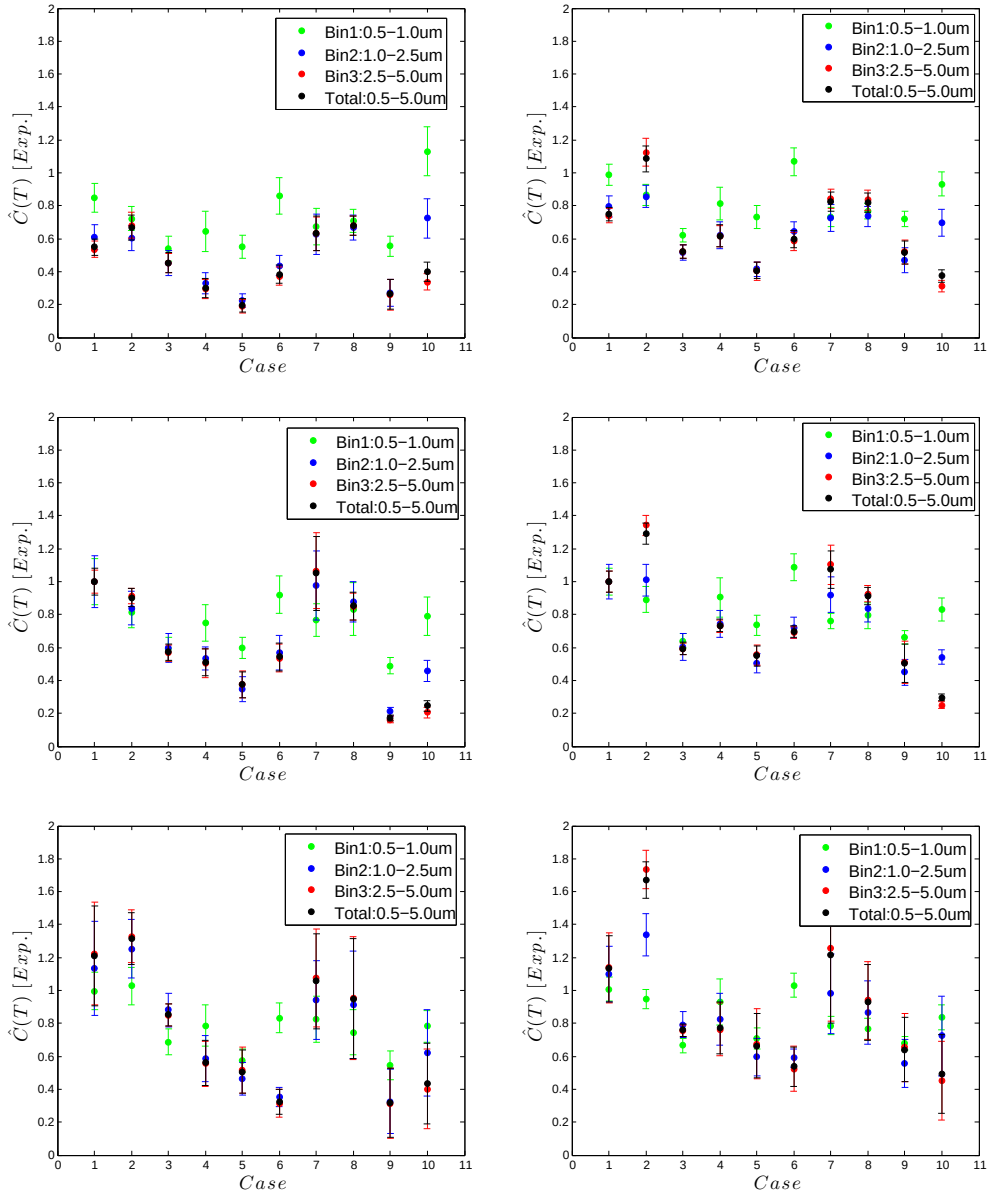

Figure 6.17: Short (left) and long (right) time measured (Exp.) relative exposure for sitting (bottom), breathing (middle), and upper (top) zones for parametric study

Case 7: size bin characteristics are similar to case 1, although due to weaker thermal plume, more droplets are measured at sitting and breathing zones, while less droplets are measured at the upper zone. Again, these results are not statistically significant because the measured average concentration is within the error bars reported for the reference case.

Case 8: since the sampling pole is moved away from the injection, to the corner of the room, less droplets are counted in most size bins compared to the previous cases.

Case 9: the results for this configuration are similar to case 8, but the magnitude of relative exposure is even lower for most size bins.

Case 10: the higher air change rate reduces overall relative exposure at all zones considerably. Although relative exposure for most size bins are reduced compared to the reference case, the amount of reduction is dependent on size bin. The higher turbulence and air mixing with increased air change rate result in a higher concentration for bin 1 than for bins 2 and 3. This can be noticed by the ordered vertical separation of color legend for case 10. Size bin-specific exposure vertical stratification is slightly enhanced between breathing and upper zones compared to case 1 for all droplet sizes.

6.2.3 Space-resolved study

Similar to the parametric study, the space-resolved tests were conducted during similar hours on consecutive days so that temperature boundary conditions would stay as nearly constant as possible. These tests were started on July 16, 2012.

6.2.3.1 Total relative exposure

The relative exposure is reported per the same size bins described in section 4.2.11. We normalize the cumulative concentration by the reference case (1) breathing zone. The results are reported for short ($T = 140\ s$) and long ($T = 600\ s$) times at sitting, breathing, and upper elevations. Figure 6.18 summarizes the total relative exposure at all zones and times. The figure shows that exposure is generally stratified, horizontally, with higher magnitudes near the window, where the injection is directed at, and lower magnitudes behind the injection. This horizontal stratification is greater at short time while at long time the relative exposure tends to even out.

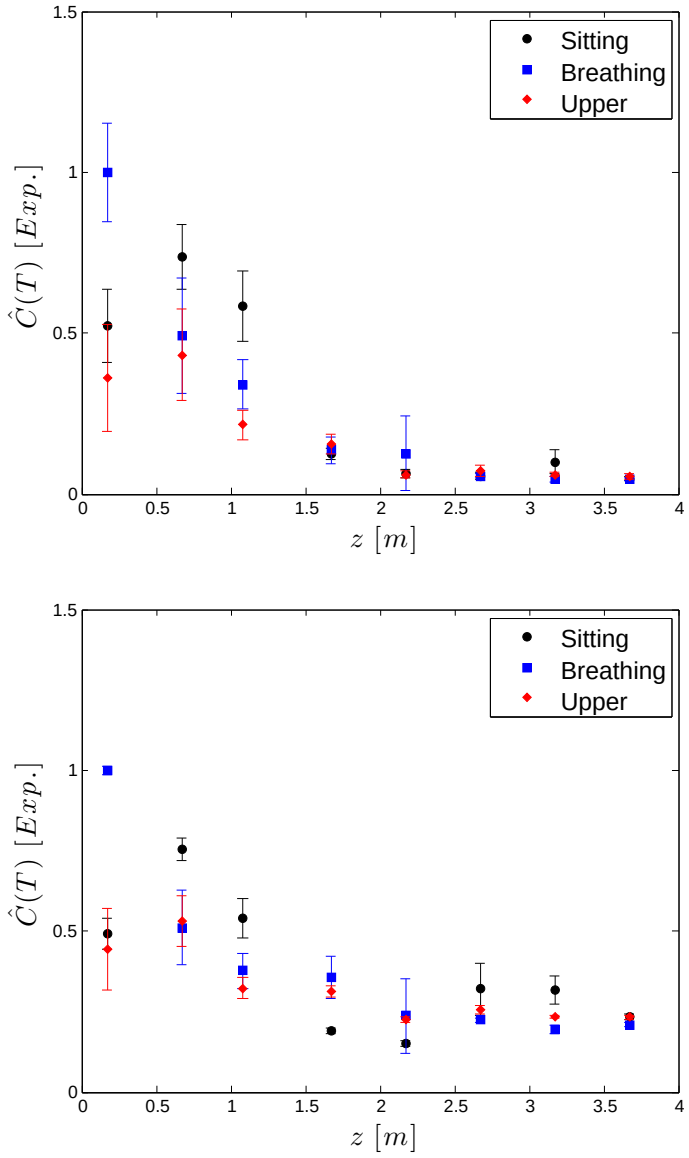

Figure 6.18: Short (top) and long (bottom) time measured (Exp.) relative exposure at all zones for space-resolved study (z is distance from the window.)

6.2.3.2 Size bin-resolved relative exposure

Figure 6.19 shows size bin-specific relative exposure for short and long times at all zones. The following statements can be made about the size bin-specific dispersion of droplets among the eight space-resolved cases.

Concerning horizontal variation in dispersion, the reduced relative exposure at a location behind the injection is common among all size bins, but the reduction rate is different for each size bin. The relative exposure reduction for the size bin 1 is very moderate at short time, but essentially nil at long time. The relative exposure reduction is more pronounced for the larger size bins of 2 and 3. We speculate that fine droplets make it to the opposite direction behind injection by turbulent diffusion, while many larger droplets settle, due to gravity, before having a chance to be carried by the flow in the opposite direction. Further research is needed to confirm these hypotheses more accurately.

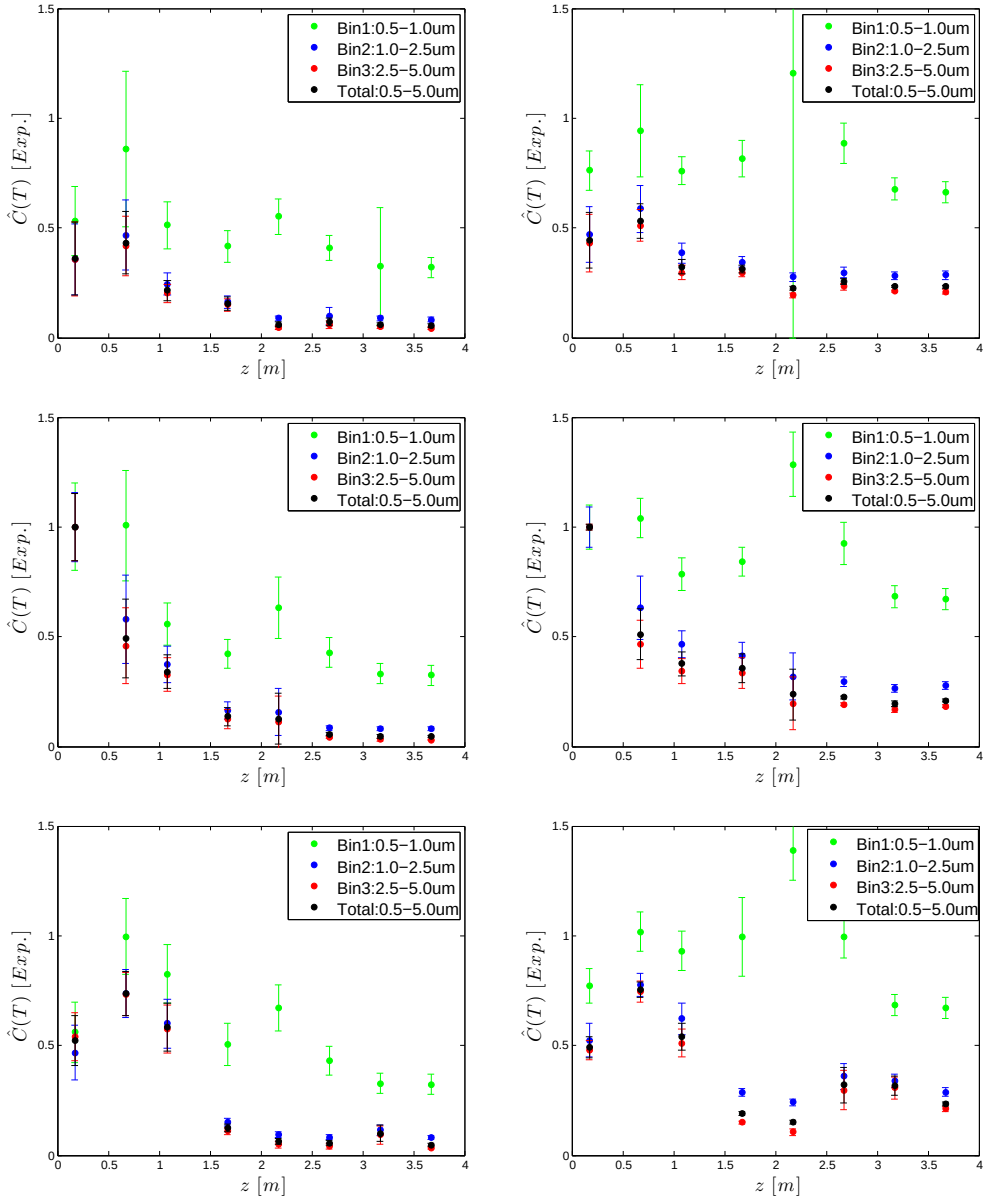

Figure 6.19: Short (left) and long (right) time measured (Exp.) relative exposure for sitting (bottom), breathing (middle), and upper (top) zones for space-resolved study (z is distance from the window.)

Chapter 7

Numerical Results and Discussion

7.1 Far-field solution convergence

The solution convergence was tested using the methodology of section 5.5.3. The total room volume V was 39.4 m^3. Three meshes were used for convergence study. These meshes contained 278669, 316645, and 359402 control volumes (N) from low to high resolution. The nominal mesh refinement ratio (r) was 1.135. The corresponding mean mesh spacing (h) values were 0.0521 m, 0.0499 m, and 0.0479 m respectively.

The solution of interest for studying convergence was chosen as cumulative total volume concentration of aerosols at the breathing zone. This solution assimilates all information in the model in a single number that is directly a measure of exposure and hence infection risk. Based on equation 5.42 the mesh convergence index is calculated for the reference case (1) in the parametric study as $GCI_{21} = 0.0011$. This indicates that we have reached a solution that is within 0.11 % of the theoretical asymptotic solution.

7.1.1 Reference case (1)

7.1.1.1 Velocity

Before discussing numerical relative exposure results in the parametric and space-resolved studies, it is helpful to examine, qualitatively, the flow velocity field calculation by the numerical model. Figures 7.1 and 7.2 show the velocity vectors and contours at 5 s and 600 s after the injection respectively. The velocity solution is shown on planes that slice the patient or the patient/nurse together. Shortly after the injection ($T = 5$ s), the high momentum injected puff gives an upward bulk flow at the center of the room. Long after injection ($T = 600$ s) the weak thermal plume of the patient is attracted towards the stronger plume of the nurse. There are also recirculation zones at the corners of the room. The numerical solution predicts

thermal plume velocity over the head of the nurse in agreement with the experiments (figure 9.5. Both approaches give an approximate plume velocity of 0.15 m/s. This gives some confidence on the ability of the numerical model to solve for the mean flow in selected parts of the domain.

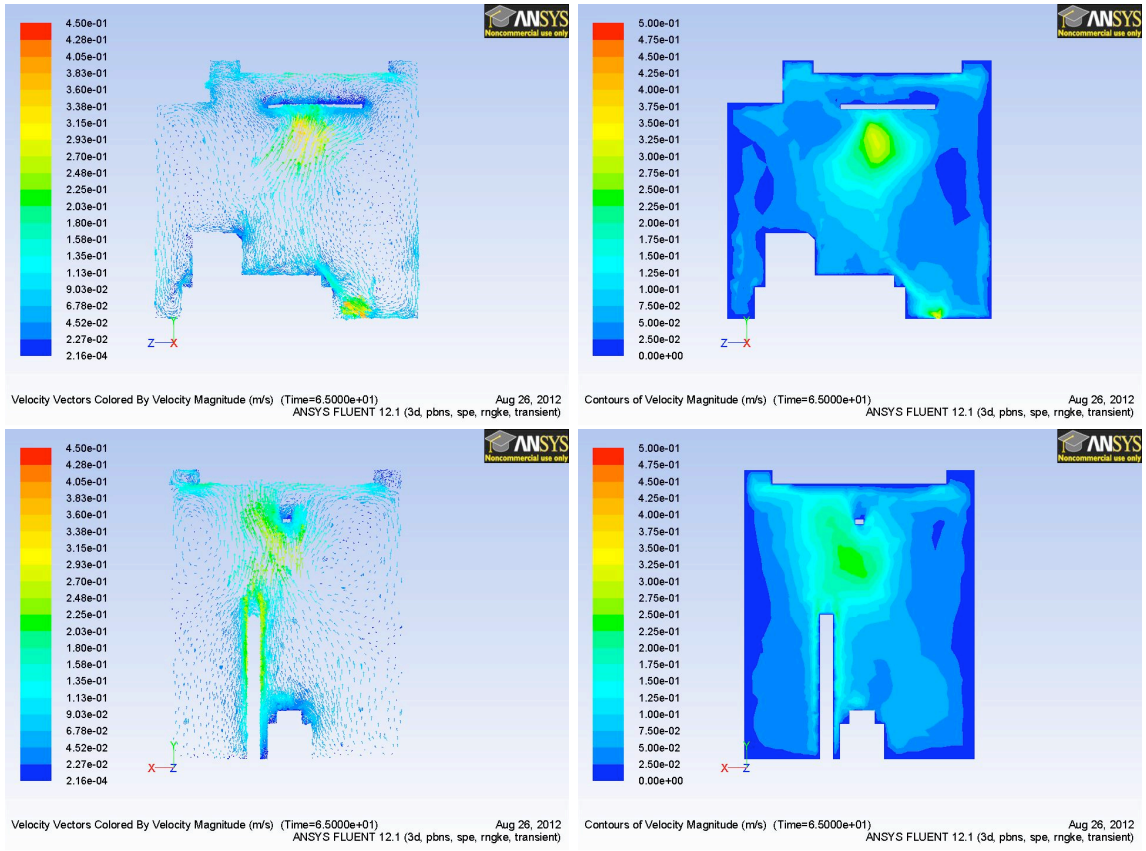

Figure 7.1: Velocity vectors (left) and velocity contours (right) at planes $x = 1.42\ m$ (top) and $z = 1.40\ m$ (bottom) computed by CFD 5 s after injection for reference case (1) for parametric study

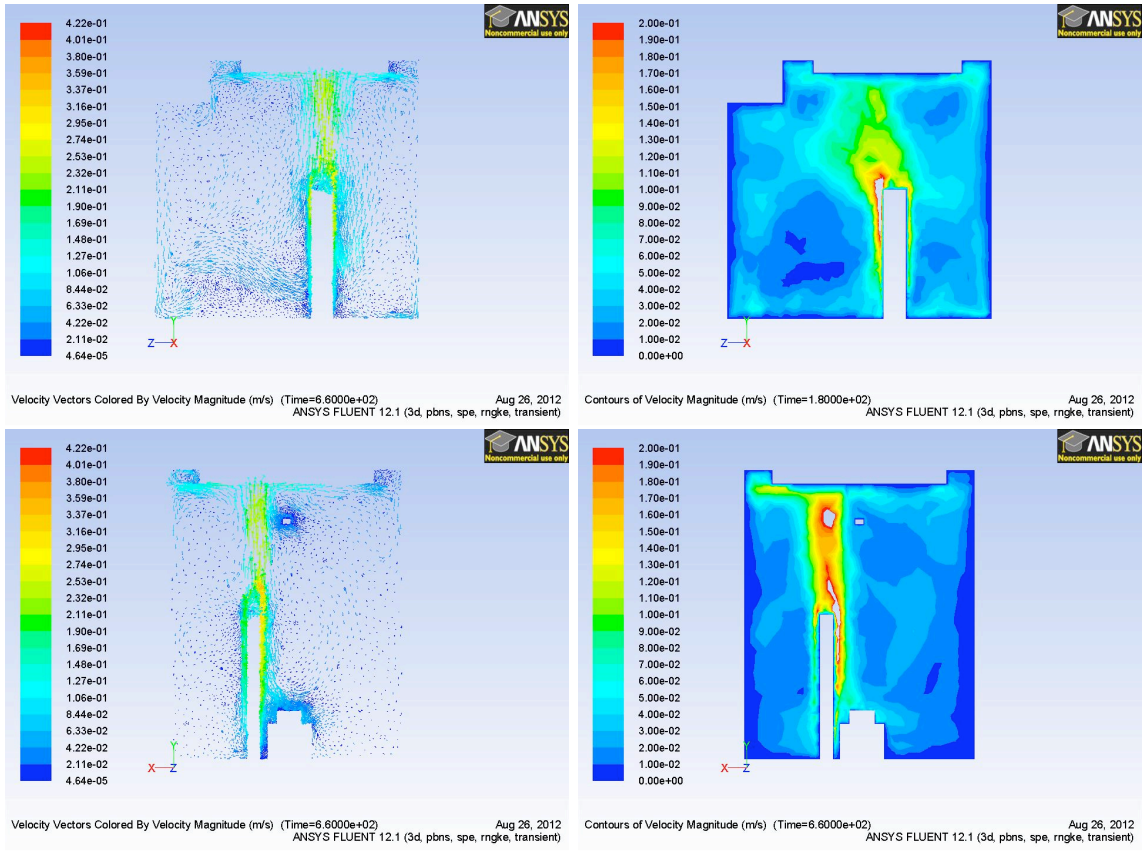

Figure 7.2: Velocity vectors (left) and velocity contours (right) at planes $x = 1.88\ m$ (top) and $z = 1.40\ m$ (bottom) computed by CFD 600 s after injection for reference case (1) for parametric study

7.1.1.2 Normalized concentration and cumulative concentration

Figure 7.3 shows the droplet dispersion in the ventilated space for the reference case (1) in the parametric study 120 s after the injection. The color bar indicates droplet diameter in meters.

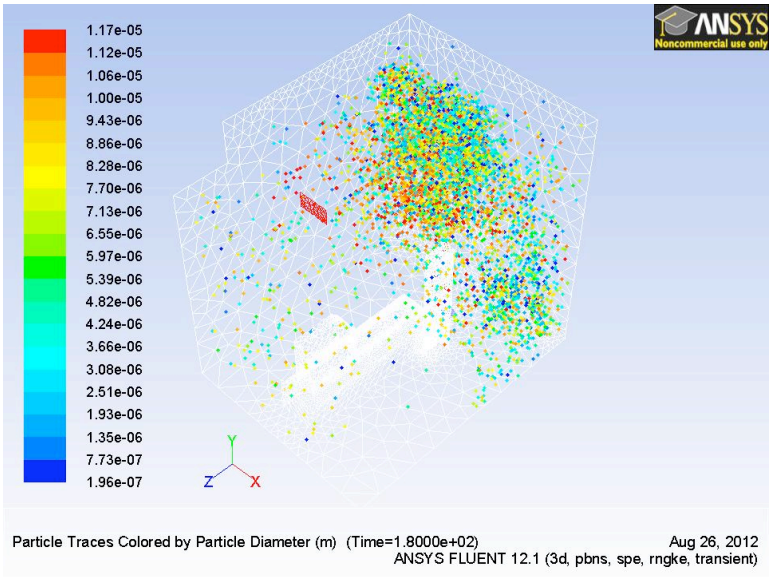

Figure 7.3: Droplet dispersion 120 s after injection simulated by CFD for parametric study reference case (Color bar indicates droplet diameter in meters)

Figure 7.4 shows the normalized concentrations and cumulative concentrations at sitting, breathing, and upper zones. For validation, this figure shall be compared to figure 6.14. For most cases, concentration and cumulative concentration are predicted higher at the upper zone, which is contrary to experiments. Two concentration peaks are observed at the upper zone. It appears that a dense droplet cloud initially passes by the upper zone measurement point, making an initial surge in cumulative concentration. Then, this cloud recirculates, while expanding, and makes a second appearance at the upper zone measurement point, which causes a more moderate increase in cumulative exposure. Also note that sitting zone cumulative concentration begins to rise very late ($\sim$ 100 s) compared to the experiments. This hints that the droplet cloud size growth rate is underpredicted by the model. This is expected since larger eddy dispersion mechanisms are not accounted

for.

The size bin behavior in dispersion is best demonstrated using normalized cumulative concentration fraction for droplets in injection compared to the normalized cumulative concentration fraction for droplets at sitting, breathing, and upper zones. Figure 7.5 shows these fractions. For comparison, this figure also shows experimental fractions discussed in the previous chapter. The relative magnitude of the distribution for each bin is in agreement with the experiments. In other words, bin 1 droplets are dispersed/diluted more quickly that bins 2 and 3 droplets. However the effect of measurement height on the size distribution is not modeled correctly.

7.2 Far-field parametric study

Figure 7.6 compares experimental and CFD relative exposure for short and long times at all zones. In most cases, the CFD model does not predict the correct magnitude and sign of the change in relative exposure resulting from changes in boundary conditions. The predicted relative exposures very seldom fall within error bars of the experiment. We investigate the model and experiment discrepancies in the following sections and speculate on reasons why there is a major disagreement.

7.2.1 Tracer gas model

The predicted tracer gas relative exposure is significantly higher than the experiments at the upper zone. This is expected since contrary to droplets, gravity has no effect in lowering relative exposure at higher elevations for tracer gases. Also there could be inadequate modeling of mean flow patterns in certain parts of the domain so any recirculating mechanisms that transport contaminants to lower levels are not resolved. There could be errors in estimation of turbulent diffusion as well. For example determination of turbulent viscosity in equation 5.4 is not trivial in two-equation RANS turbulence models for universal flow situations.

7.2.2 Discrete phase model

7.2.2.1 Total relative exposure

Similar to tracer gas model, the predicted relative exposure is significantly higher than the experiments at the upper zone. It appears that this model does not properly account for gravity, mean flow, and turbulent dispersion

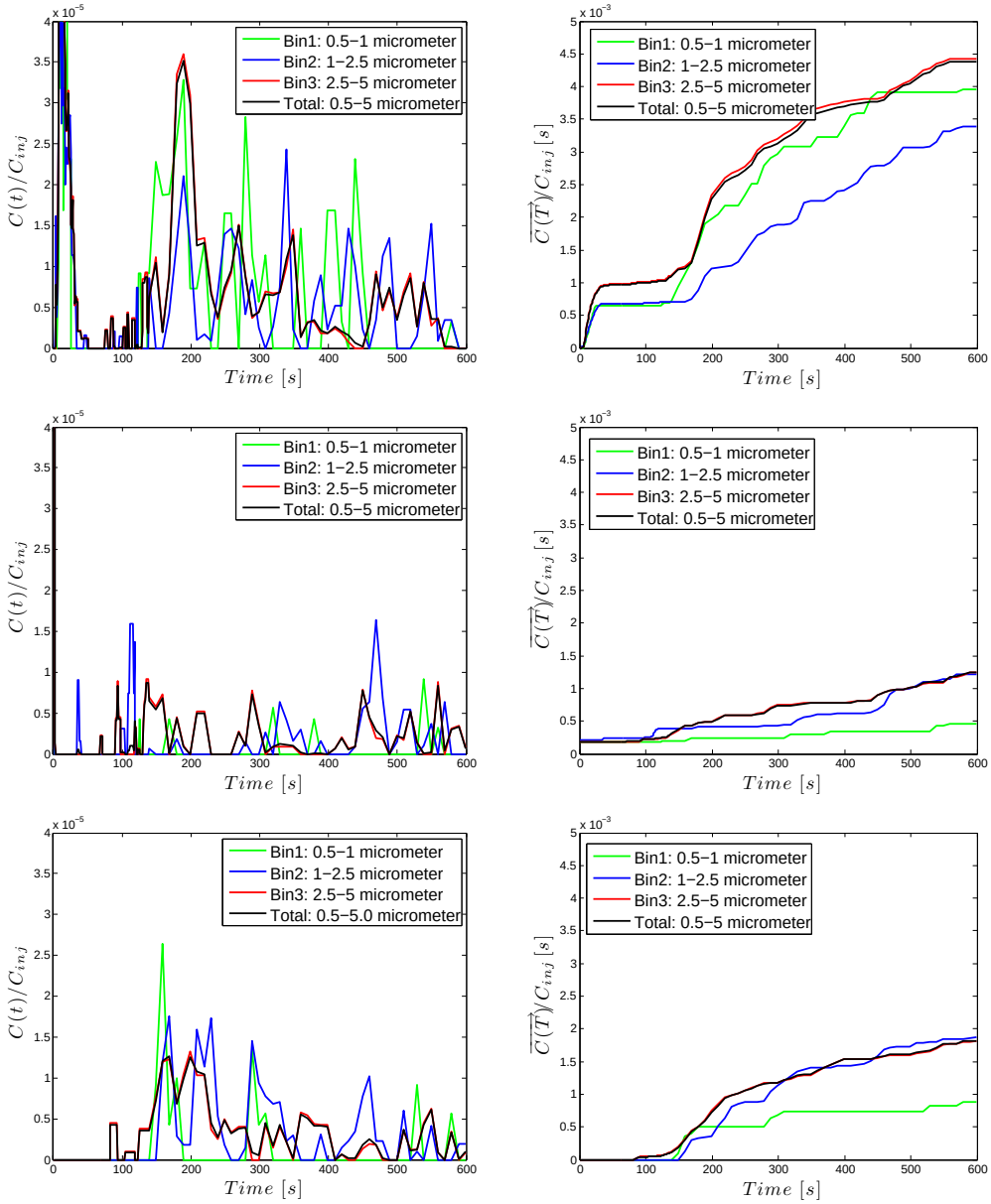

Figure 7.4: Modeled normalized concentration (left) and cumulative concentration (right) at the sitting (bottom), breathing (middle), and upper (top) zones for the reference case (1)

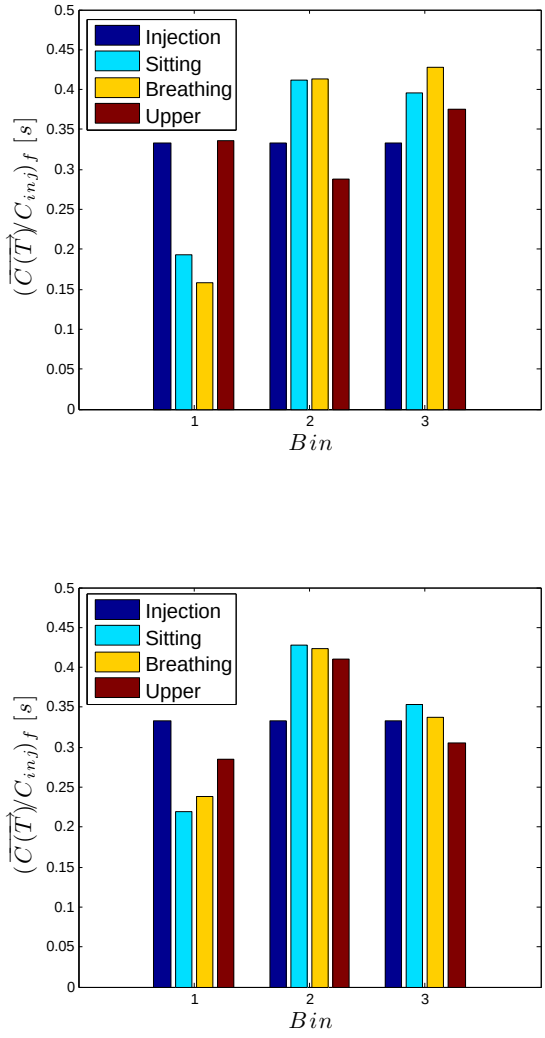

Figure 7.5: Modeled (top) and experimental (bottom) normalized cumulative concentration fraction near injection and measurement points

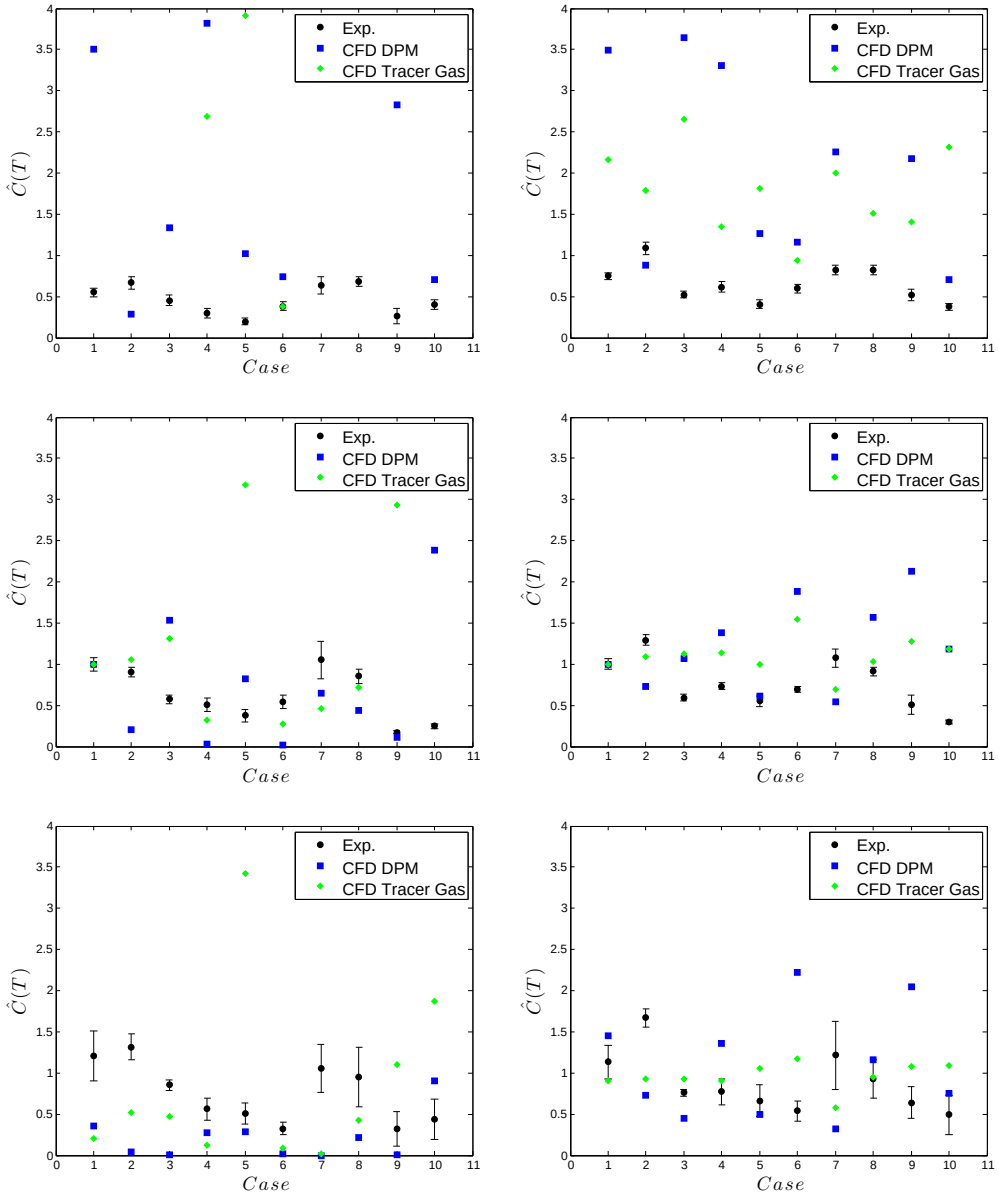

Figure 7.6: Short (left) and long (right) time measured (Exp.) and predicted (CFD DPM and tracer gas) relative exposure for sitting (bottom), breathing (middle), and upper (top) zones for parametric study

effects in lowering the relative exposure at higher elevations either. The Stochastic DRW model tends to underpredict the droplet cloud growth rate. The whole validity of stochastic DRW model is under question for room level ventilation flows. In such flows we have orders of magnitude differences in time and length scales, and non-dimensional groups such as Reynolds and Grashof numbers, while stochastic DRW model works best with isotropic turbulence with a limited (but high) range of Reynolds numbers. In addition, the effect of large and slow eddies that are responsible for particle transport are completely ignored in RANS and DRW models. Most dispersion sampling times and lengths are short with RANS and DRW models, so only smaller and short-lived eddies are accounted for.

7.2.2.2 Size bin-resolved relative exposure

Figure 7.7 shows the bin-resolved relative exposure for short and long times at all zones. For the short time at sitting zone few or no droplets are found, especially for smaller bin sizes. This is expected since the stochastic DRW model underpredicts dispersion. Except for detecting more size bin 1 droplets in long time at upper zones, it appears that the model cannot consistently report a dispersion behavior specific to droplet size bin. Although size bin-specific physics are built into the model (e.g. gravity effects and droplet inertia) the size range studied in our model ($0.5-5.0\ \mu m$) is too narrow for the model to show significant size-specific dispersion behaviors.

Table 7.1 shows a ranking of cases that pose a risk from lowest to highest relative exposure in long time for all zones as suggested by the experiments, the tracer gas model, and the DPM model. Focusing on experiments for sitting and breathing zone relative exposure rankings, staying away from injection source, increasing ventilation rate, and upward injections are the most effective boundary and initial conditions to reduce expiratory airborne droplet exposure. On the other hand, weaker thermal plumes (albeit less statistically significant), fast, and inclined injections are the least effective combinations in boundary conditions to reduce expiratory airborne droplet exposure.

7.3 Far-field space-resolved study

Although the CFD model was not successful predicting outcomes of the experimental parametric study, it was able to predict, at least qualitatively, features of dispersion for the space-resolved study. Figure 7.8 shows the

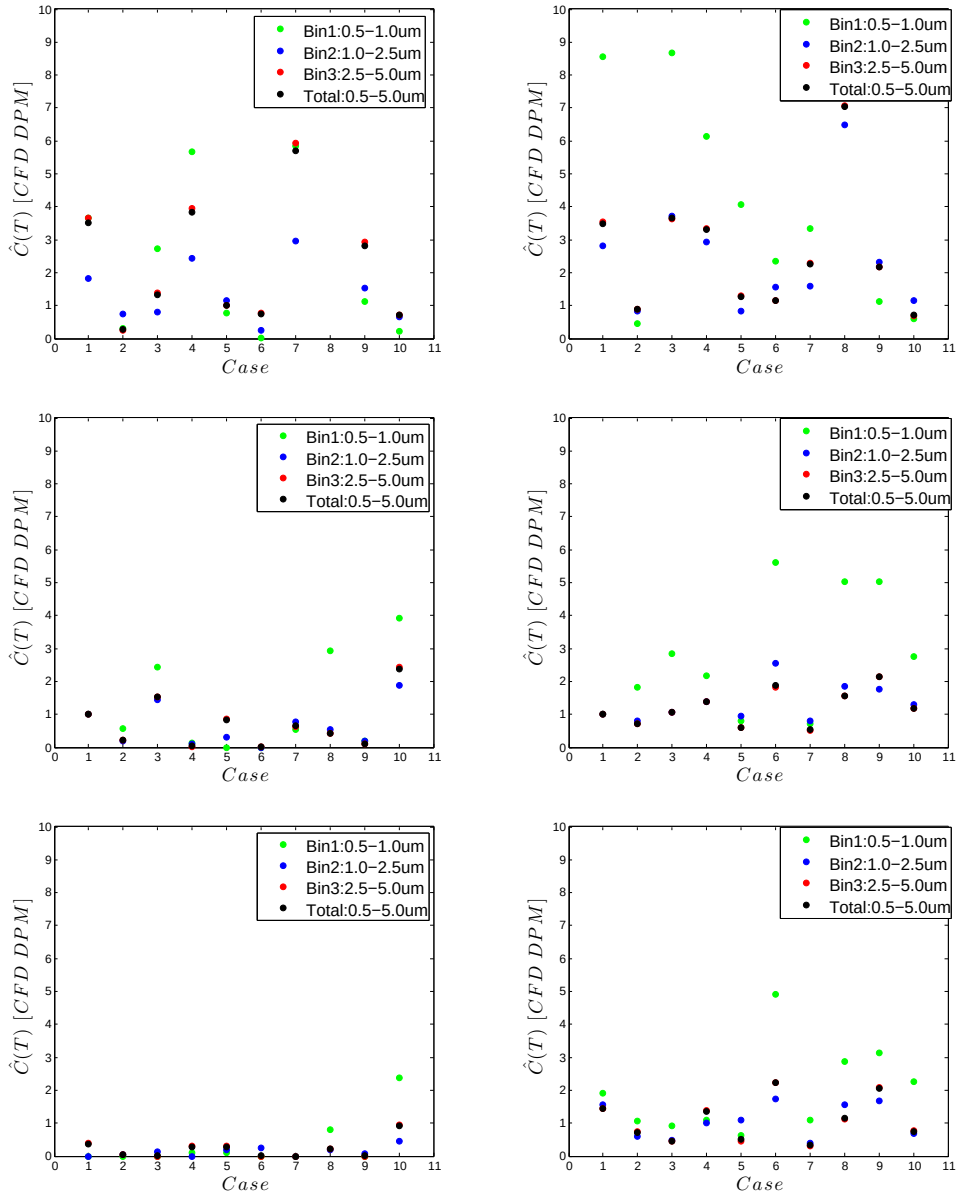

Figure 7.7: Short (left) and long (right) time predicted (CFD DPM) relative exposure for sitting (bottom), breathing (middle), and upper (top) zones for parametric study

Height	Long time ($T = 600\ s$)
Upper Exp.	10, 5, 9, 3, 6, 4, 1, 7, 8, 2
Upper tracer gas	6, 4, 9, 8, 2, 5, 7, 1, 10, 3
Upper DPM	10, 2, 6, 5, 9, 7, 4, 1, 3, 8
Breath Exp.	10, 9, 5, 3, 6, 4, 8, 1, 7, 2
Breath tracer gas	7, 5, 1, 8, 2, 3, 4, 10, 9, 6
Breath DPM	7, 5, 2, 1, 3, 10, 4, 8, 6, 9
Sit Exp.	10, 6, 9, 5, 3, 4, 8, 1, 7, 2
Sit tracer gas	7, 4, 1, 2, 3, 8, 5, 9, 10, 6
Sit DPM	7, 3, 5, 2, 10, 8, 4, 1, 9, 6

Table 7.1: Comparison among experiments, tracer gas, and DPM in parametric study (Ranking from lowest to highest relative exposure)

prediction of the DPM and tracer gas models against the experiments for short and long time at all zones.

7.3.1 Tracer gas model

Both experiment and model show a horizontal stratification for relative exposure at short time, while the concentration spreads out at long time. Tracer gas model overpredicts the relative exposure at the upper zone for reasons suggested in section 7.2.

7.3.2 Discrete phase model

7.3.2.1 Total relative exposure

There is a relative exposure horizontal stratification for the short time while relative exposure spreads out in the room for the long time. Both experiment and model show a drop in relative exposure from case 3 to case 4. This is due to the manikin acting as a barrier for droplets to pass. We notice that droplets actually disperse more in the horizontal direction (z) than the

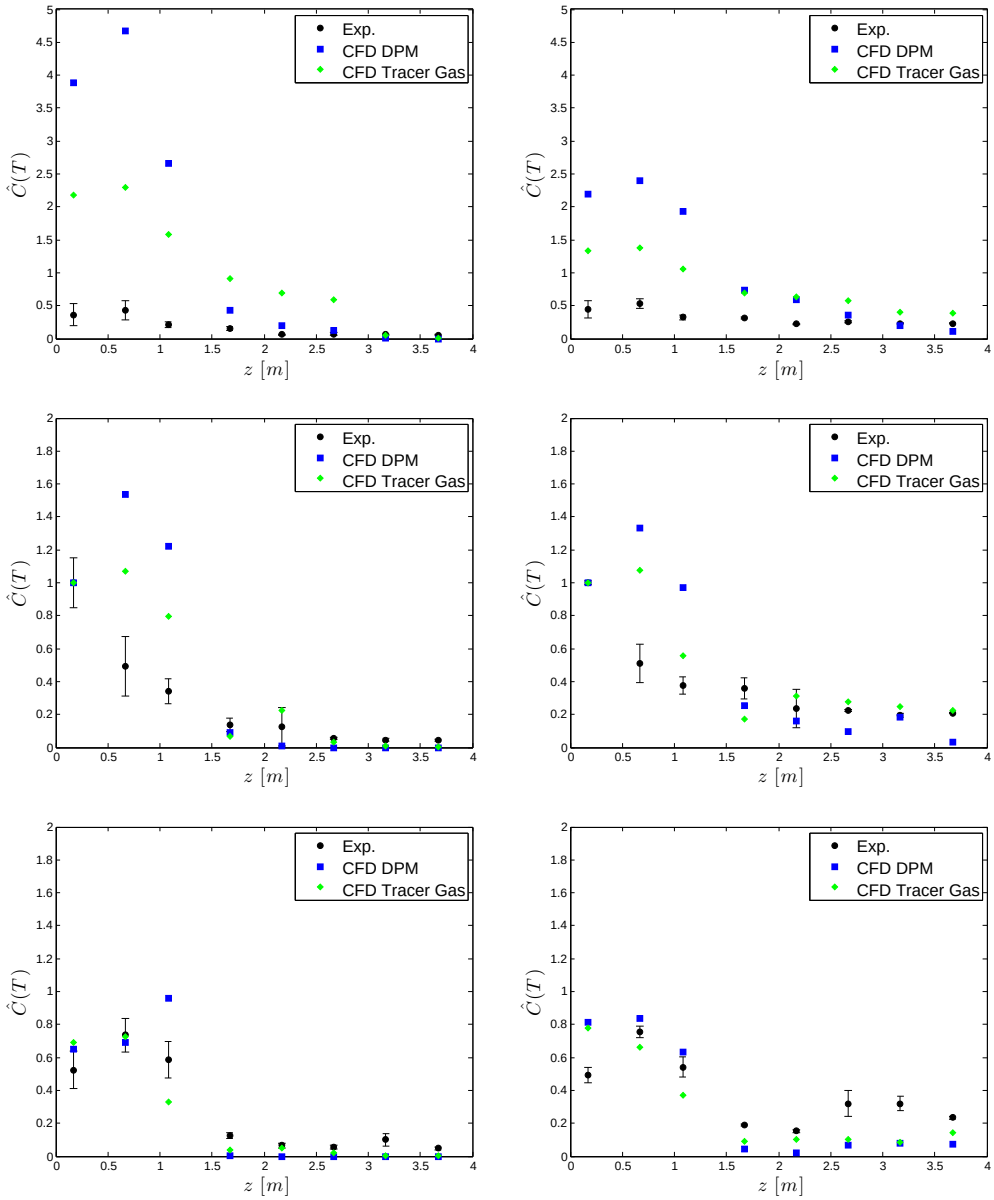

Figure 7.8: Short (left) and long (right) time measured (Exp.) and predicted (CFD DPM and tracer gas) relative exposure for sitting (bottom), breathing (middle), and upper (top) zones for space-resolved study (z is distance from the window.)

model predicts. We expect turbulent dispersion, larger and slow eddies to be responsible for this, features of the flow that RANS turbulence model cannot correctly account for. The relative exposure is in good agreement for the sitting and breathing zones, but it is overpredicted for cases 1, 2, and 3 at the upper zone.

7.3.2.2 Size bin-resolved relative exposure

Figure 7.9 shows the bin-resolved relative exposure for short and long times at all zones. This figure shall be compared to figure 6.19 for validation. The CFD model does not predict the spread of size bin 1 droplets in the horizontal direction as much as the experiment does. The stochastic DRW model used with two-equation RANS turbulence modeling tends to disperse all droplets in our size range equally.

7.4 Limitations of eddy-viscosity turbulence models in ventilation space with injections

The RNG $k-\epsilon$ turbulence model is an example of eddy-viscosity turbulence models commonly used in engineering applications. These models are not computationally expensive, and, if only qualitative results are sought, they offer reasonable solutions for the mean flow characteristics. The primary assumption in these models is that momentum exchange through turbulent eddies is analogous to microscopic momentum exchange by molecular collision. In these models turbulent viscosity is related to the dominant large eddy length and velocity, and the Reynolds stresses are proportional to this turbulent viscosity and the mean rate of strain in fluid elements. Essentially, these models work by replacing the laminar viscosity of the fluid with a larger turbulent effective viscosity [26]. This approach neglects important features of turbulent flow in complex geometries as follows,

1. Turbulent viscosity must be a tensor and not a scalar. This results in inapplicability of eddy-viscosity models for anisotropic turbulence (e.g. stratification and swirl).

2. When mean rate of strain in fluid elements is locally zero, isotropic turbulence is predicted, but in reality anisotropy is transported and 'remembered' in the flow.

3. Reynolds stresses are determined by 'local' rate of strain, not accounting for history of straining in turbulence.

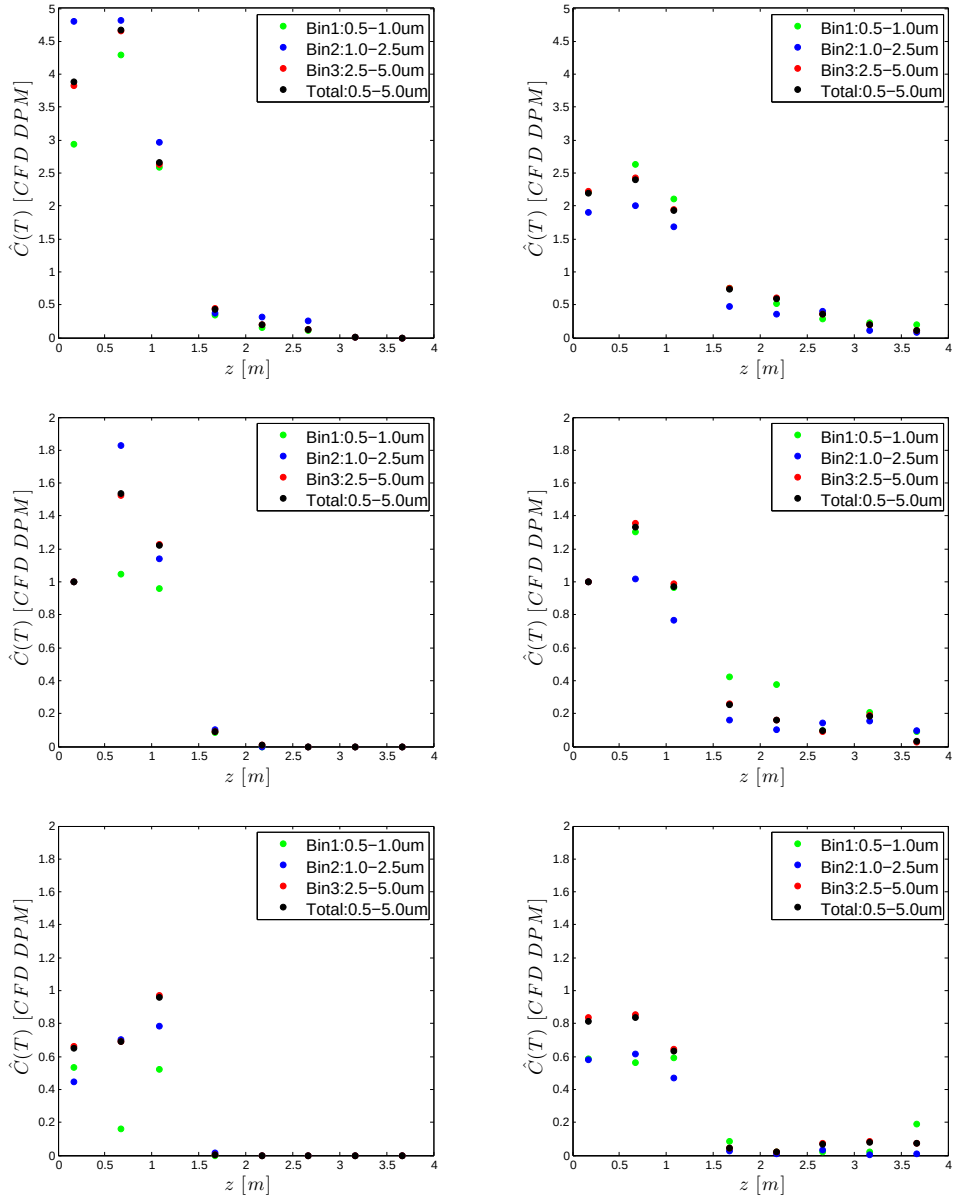

Figure 7.9: Short (left) and long (right) time predicted (CFD DPM) relative exposure for sitting (bottom), breathing (middle), and upper (top) zones for space-resolved study (z is distance from the window)

$k-\epsilon$ turbulence models add two extra transport equations for turbulent kinetic energy, k, and dissipation rate, ϵ, to the mass, momentum, and energy equations. The k equation governs the transport of turbulent kinetic energy, its generation by Reynolds shear stresses, and its sink by dissipation rate. The ϵ equation governs the transport of dissipation rate, forcing the the large scale turbulent vorticity towards the large scale vorticity of the mean flow [79]. Davidson believes that the ϵ equation is pure invention and is not derived from known and universal physical laws. It is simply a rigorous statistical model meant to fit various data sets [26]. Nevertheless, this treatment is applicable for special circumstances,

1. Statistical equilibrium is governed by local conditions and the time scale of turbulent fluctuations, k/ϵ, is short compared to the mean flow time scale.

2. The flow is dominated by simple shear mechanisms and freely decaying and isotropic turbulence.

It is evident from this discussion that transient ventilation flows containing injections do not satisfy the stringent requirements posed by eddy-viscosity and $k-\epsilon$ turbulence models. In such flows we have complex geometry, stratification, and potentiality swirling flows (when swirl diffusers are used). In addition, a wide range of eddy length and time scales are present. It is noteworthy that grid convergence for such situations may be achieved, but the physics of the flow is against the turbulence model assumptions, so that solution residuals may not drop even by a large number of solution iterations.

Another important issue is to realize that both large/slow and small/fast eddies contribute to pollutant dispersion in turbulent flow. If these fluctuations are not resolved correctly by the turbulence model, then erroneous dispersion is predicted, no matter what stochastic droplet tracking model is used or to what resolution is tracking computation performed.

Because of these difficulties, we suggest using the Large Eddy Simulation turbulence model for transient ventilation flows. This technique resolves a wider range of eddy length and time scales with better accuracy that also becomes handy in correctly predicting dispersion, without the need for a stochastic droplet tracking model. This, however, comes at the expense of a very immense computational cost.

Chapter 8

Conclusions and Recommendations

8.1 Conclusions

This thesis studied the relative airborne droplet concentration by simulated respiratory injections from a model patient in a room with an underfloor air distribution ventilation system. The experimental domain provided a mock-up for a single patient hospital recovery room. The ultimate goal was to investigate the effect of variations boundary and initial conditions such as occupant locations, injection direction and strength, thermal plume strength, and ventilation flow rate on the magnitude of total droplet volume inhaled (exposure) by a hypothetical subject. The exposure was directly proportional to the total hypothetical pathogen dosage, so it was a suitable indicator for airborne infection risk. The relative exposures indicated how properly or poorly the ventilation system is performing in mitigating exposure under various real-life-like room conditions.

As a first step, a droplet generator (air-assist atomizer) was built and tested. This machine produced artificial expiratory injections (coughs and sneezes). In various 'near-field' experiments, the steady and transient performance of this atomizer was characterized using Laser illuminated shadowgraphy and Particle Tracking Velocimetry (PTV) techniques. Typical metrics such as droplet Sauter Mean Diameter (SMD), droplet size, and velocity were measured as functions of axial distance, radial distance, and time. The droplet generator was used in the 'far-field' ventilation tests. The droplet size distribution in the injection was also used in the numerical analysis. Using the droplet size distribution, the volume of injected liquid, and the volume of injected gas were used to calculate droplet concentrations in the vicinity of the injection. The 'near-field' concentrations were used to normalize concentrations and cumulative concentrations at various measurement locations for the reference case in the 'far-field' experiment.

As a second step, the droplet generator was used in a mockup of a

single patient hospital recovery room with an underfloor air distribution ventilation system. An Aerodynamic Particle Sizer (APS) was used to measure the droplet concentrations in various size bins at three heights (sitting, breathing, and upper). Ten 'far-field' 'parametric' cases were tested, where boundary conditions, described above, varied, and the relative exposure to airborne droplets were determined. Also for the reference case boundary conditions, a 'space-resolved' test was conducted, where relative exposures were measured in a horizontal sweep in the room at the same heights as in the parametric study. Eight locations from one wall in the room to the opposite wall were considered. This test meant to understand the droplet dispersion characteristics in more detail.

As a third component of the thesis, Computational Fluid Dynamics (CFD) was used to simulate the experiments described above. Contaminant transport was modeled by both tracer gas and stochastic droplet tracking. The experimental results were used to set the injection and wall boundary conditions. The CFD model performance was compared against experimental results. The adequacy of the CFD model was investigated for both tracer gas and droplet approaches in the dispersion of droplet contaminants in the room.

The sections below summarize the main findings of these three thesis sections.

8.1.1 Near-field study

Steady and transient droplet dispersion characteristics of an air-assist internally mixing cone spray have been studied using imaging, shadowgraphy, and Particle Tracking Velocimetry (PTV). While some results confirm previous studies, others are novel. The following conclusions may apply to many dilute sprays at far enough distances from the breakup regime, where flow patterns are self-similar.

8.1.1.1 Steady operation

For the steady operation, the spray quality ($d_{32} = 20.8 \pm 0.3\ \mu m$) satisfies accepted Sauter Mean Diameter correlations that relate d_{32} to fluid properties and flow conditions. Total concentration profiles are distributed in a Gaussian shape when plotted versus radial distance from the central axis. Furthermore, concentration profiles are self-similar so that they all collapse on the same curve when plotted versus non-dimensional radial distance. The mean axial velocity profiles also appear to be Gaussian as a function of radial

distance.

For the steady operation, spatial variation of atomization quality reveals that larger droplets form closer to the periphery of the spray while smaller droplets form close to the central axis. The velocimetry and Péclet number analyses confirm that smaller droplets migrate to the periphery of the spray faster ($Pe_L(d = 7.5\ \mu m) = 93.3$) than larger droplets ($Pe_L(d = 52.5\ \mu m) = 147.7$) due to turbulent dispersion. The deceleration plot and the mean axial velocity profiles indicate that larger droplets move faster than smaller ones in the axial direction.

8.1.1.2 Transient operation

Transient spray penetration test results reveal that the overall spray axial and radial dispersion is self-similar ($C_x = 2.19 - 2.48$, $C_r = 0.10 - 0.11$, and $n = 0.5$) after a certain non-dimensional time and axial distance. In the self-similar region, the spray behaves like a gas jet since the smallest droplets in the spray disperse like fluid elements in the gas background.

The droplet volume fraction for the leading edge peaks at 20 μm, 33 μm, and 44 μm for $\frac{x}{d_g}$ of 20.7, 41.4, and 82.9 respectively. In the trailing edge, droplet volume fraction peaks at 24 μm, 36 μm, and 42 μm for the same non-dimensional axial distances. Likewise, d_{32} varies in the leading edge as a function of time delay and axial distance. This variation for the trailing edges is less pronounced. The mean Stokes number analysis suggests that the relaxation time τ_d for dominant droplet size in the leading and trailing edges of the spray is correlated with the mean characteristic time of the flow τ_g at the axial distances examined. For the leading edge the mean Stokes number is calculated as $St_m = 5.3$, 7.2, and 6.4 and for the trailing edge it is calculated as $St_m = 7.6$, 8.6, and 5.4 for the same axial distances respectively.

PTV of the transient spray in the leading edge reveals similar mean and fluctuating velocities to the steady spray. Large droplets have high mean axial velocities, while small droplets have higher fluctuating radial velocities. These velocities do not change appreciably as a function of time delay. The mean and fluctuating velocities for the trailing edge, however, are an order of magnitude (factor ten) less than those for steady spray. These velocities decrease as a function of time delay. The mean axial and fluctuating radial velocities have equal magnitudes for all droplet sizes. The trailing edge of the spray exhibits low-Reynolds-number and large-eddy flow conditions with low turbulent and Kolmogorov Stokes numbers. Such flows tend to move droplets, whether large or small, with the same likelihood as fluid elements.

8.1.2 Far-field study

8.1.2.1 Parametric study

Vertical temperature stratification was achieved in all experiments, and the injection disturbed the temperature field by only $1-2\ ^oC$ for a few seconds following injection.

The different boundary conditions resulted in exposures that varied by more than a factor of four. Some effects increased exposure: faster injections by ~ 50 %, inclined injections by $\sim 30-50$ %, and lower air change rates by ~ 60 %. Other effects decreased exposure: slow injections by ~ 40 %, vertical injections by ~ 50 %, and far occupant location from the source by $\sim 10-40$ %. The effect of the thermal plume strength on exposure could not be determined reliably by these experiments.

For most cases, the finest droplets ($0.5-1.0\ \mu m$ in diameter) disperse in all directions quickly. It is suggested that this is attributed to higher turbulent diffusion and lower gravitational settling for droplets in this size range. On the other hand, larger droplets ($2.5-5.0\ \mu m$) exhibit less dispersion, so they are measured at lower relative exposures at upper elevations and for cases where injection is directed towards the walls. It is suggested that this is attributed to lower turbulent diffusion and higher gravitational settling for this size range. Other ventilation studies with mixing type ventilation do not observe this effect, reporting that droplets in the same size range ($0.5-5.0\ \mu m$ in diameter) disperse alike. Although air mixing in our experiments is much lower than reported for mixing type ventilation systems in the literature, further research is required to explain these different results more accurately.

State of the art Computational Fluid Dynamics (CFD) simulations were performed to model droplet and gas dispersion introduced by fast injections in the ventilation domain. The boundary conditions (surface temperatures and diffuser velocity) and initial conditions (injection velocity and droplet size distribution) were carefully implemented. The mesh resolution was controlled adequately on surfaces and locations where solution gradients were expected to be high. The time step sizes were also chosen carefully to ensure adequate species tracking.

Despite the efforts, CFD did not provide satisfactory predictions of the experimental relative exposure for the parametric study. Neither qualitative, nor quantitative agreement is obtained. The variations in the boundary and initial conditions are so subtle that the computational model cannot accurately resolve differences in contaminant transport.

8.1.2.2 Space-resolved study

Experiments show that relative exposure is generally stratified, horizontally, at short time with higher magnitudes near the window, towards which the injection is made. At long time, however, relative exposure evens out more with the migration of droplets to the opposite side of the room behind the injection. The finest droplets ($0.5-1.0\ \mu m$) quickly disperse horizontally while larger droplets ($2.5-5.0\ \mu m$) are detected in low concentrations at the opposite side of the room. As noted above, this feature of dispersion in low energy ventilation systems should be researched in more detail.

Contrary to the parametric study, the models in space-resolved study captures the main quality of horizontal dispersion behavior for short and long times. The models also predict the relative magnitude of exposure for sitting and breathing zones well for locations near the injection. However, they overpredict relative exposure at high elevation and underpredict exposure at distances behind the injection.

8.1.3 Adequacy of eddy-viscosity turbulence models for ventilation studies with injections

Many studies in the literature use our CFD methodologies to obtain dispersion solutions that are also validated by experiments, but they do not consider fast injections in ventilation space, neither do they run models where sensitive variations in the boundary conditions are made. The adequacy of two-equation Reynolds Averaged Navier-Stokes (RANS) turbulence modeling for injections within ventilation space is questionable. Such flows exhibit widely differing time and length scales from milliseconds and millimeters to seconds and meters. Also there are widely differing magnitudes for other non-dimensional groups encountered. The Reynolds number close to the injection may reach 50,000 while far away and around objects in the room it will be significantly less. The turbulence in our ventilated room was anisotropic due to objects and swirling air at the diffuser.

We observed that our exposure results were very sensitive to the choice of turbulence model. The solution had difficulty to converge to the specified minimum residuals. This suggests that our flow was highly transitional and the turbulence model could not capture the large scale unsteadiness inherent to such flows. An important observation was that although grid convergence was achieved, the residuals did not drop as expected. This encourages studies in the literature to report both grid convergence and a plot of residuals to show that the choice of any turbulence model is justified.

Turbulent viscosity is not well defined in two-equation RANS models and for anisotropic flows with widely differing time and length scales. In addition, a weak droplet size bin-specific dispersion behavior is observed using the stochastic Discrete Random Walk (DRW) model. We suspect that gravity and inertia effects on size-specific droplet dispersion would be more pronounced if a larger size range of droplets were modeled. The inadequacy in choosing the turbulence model also affects the validity of results obtained by the stochastic DRW model. RANS and DRW models completely ignore large and slow eddy mechanisms that transport droplets into far distances. In other words, large scale flow unsteadiness is crucial in proper dispersion modeling of droplets within the ventilation domain. Stochastic DRW model tends to underpredict droplet cloud growth rate. Again, such techniques work best with a limited range of Reynolds numbers, usually higher than encountered in ventilation domains, in isotropic turbulent flows.

Other turbulence models such as Large Eddy Simulation (LES) may be more appropriate for ventilation flows containing injections. The implementation of more accurate turbulence models in this work such as LES or Direct Numerical Simulation (DNS) was not feasible due to a diverse set of research activities and the computational budget (time and cost).

8.2 Recommendations

As investigated in this thesis, the performance of the underfloor air distribution system in removing injection droplets is very sensitive to injection properties (momentum and direction), occupant location, and air change rate. The performance is, however, less sensitive to the thermal plume variations representative of actual metabolic rates, in a statistically significant ways. Also it is observed that droplet dispersion behavior is dependent on droplet size, with sub micrometer droplets tending to disperse more quickly that larger droplets. Findings in this thesis have implications in ventilation design and usage of single patient hospital recovery rooms.

It is desired to have injections with lower momentum, preferably directed upwards or towards the walls, that result in less airborne droplet concentrations in the breathing zone of the subjects. Also, it is desired to advise subjects to spend most of their times away from the patient (corner of the room or behind the expiratory injections), where droplet concentrations at the breathing zone are likely to be less. The recommended ventilation rate for hospital patient recovery rooms is greater than 4 ACH since high momentum coughs and sneezes are likely to break down the vertical concentration

stratification. It is speculated that stratification alone is not sufficient to reduce exposure to airborne droplets introduced by fast injections. Instead, higher ventilation rates with sufficient dilution may be a better approach. It is likely that variations in subject metabolic rates, and the associated thermal plume strength, do not result in a large airborne droplet exposure difference at the breathing zone that is statistically significant.

It is also likely that finer sub micrometer droplets tend to disperse more quickly compared to larger droplets in actual rooms with injected source and stratified ventilation. This has implications on ventilation design and room usage, based on the size of the pathogen or pathogen carrying drop of concern. In other words, fine viruses carried by sub micrometer droplets may disperse more rapidly than larger bacteria suspended in 5 micrometer droplets.

Chapter 9

Future Work

9.1 Strengths and weaknesses of this thesis

This thesis investigated the interaction of expiratory droplets, produced by coughs and sneezes, with an underfloor air distribution ventilation system in a mockup of a single patient hospital recovery room. Particular attention was paid to quantify exposure to airborne droplets as the main indicator for infection risk.

The strength of this thesis is the experimental work. It was observed that variations in boundary and initial conditions, such as injection direction and momentum, occupant thermal plume and location, and ventilation rate, greatly affect exposure to droplets. The exposure from worst to best conditions changed by a factor of four or more, suggesting that such boundary and initial conditions cannot be ignored in the ventilation and interior design of health care facilities.

The weakness of this thesis is the numerical work. Simulations failed to predict exposure differences as a function of variations in boundary and initial conditions. The simulations, at best, provided qualitative prediction of exposure in various spaces within the ventilation domain for only one set of boundary and initial conditions.

The work in this thesis directly inspires various future research activities to guide ventilation design of single patient hospital recovery rooms.

9.2 Droplet dispersion experiments for air-assist internally mixing atomizers

The near-field droplet dispersion experiments in this thesis were fundamental research but limited only to support the experiments and modeling for the far-field dispersion behavior. Future research should investigate steady and transient air-assist internally mixing atomizers in more detail. For example dispersion behavior can be studied for more varying conditions such as nozzle geometry, liquid/gas mass flow rate, momentum rates, Reynolds

numbers, and Weber numbers. Droplet velocity and size distribution can be characterized for a broader range and/or finer resolution in axial or radial dimensions. Specific correlations can be found between droplet relaxation time and characteristic time in the flow. As an alternative to the shadowgraphy imaging technique, Phase Doppler Anemometry (PDA) can be used.

9.3 Experiments to measure a wider droplet size range in ventilation flow

The droplet sampling technique in this thesis limited the size range of droplets we could measure. The remote sampling techniques utilizing long and potentially curved tubes severely reduce the collection efficiency for droplets larger than 5 μm in diameter. Other in situ techniques such as optical measurements may be used in future works. These techniques may require placement of instruments such as Lasers or cameras within ventilation domain. Consequently, ventilation flow may be disturbed by obstruction, thermal plumes, and air mixing. Such challenges must to be overcome.

9.4 Empirical experiments with actual expiratory actions

Respiratory expirations (speech, cough, and sneeze) generate many viable and infective pathogens from sub-micrometer to millimeter size. Flow and droplet characteristics of actual expirations are highly diverse for different people and even for a single person from one expiration to another. The work in this thesis used an artificial droplet generator that was tuned to produce injections repeatedly that were representative of actual expirations. Future research can conduct empirical studies and field measurements to investigate interaction of actual expirations with ventilation airflow. Of course low droplet concentrations and variations in actual expirations will be experimental challenges, but such variations are most representative of actual dispersion processes and hence airborne infection risk. Aerosol mass spectrometry may be necessary to investigate contaminant transport with actual expiratory injection since the chemistry of oral fluid may be different among different people.

9.5 Effect of ventilation type on transport of expiratory injected droplets

This thesis investigated transport of expiratory injected droplets in an underfloor air distribution ventilation system with a swirl diffuser and a high side wall exhaust for ventilation rates from 0.8 to 3.7 air changes per hour. Future research can investigate the effect of other ventilation systems on dispersion of injected droplets. At this point only a few studies have been published, mainly considering low side wall laminar flow diffusers with high exhausts (traditional displacement ventilation) or turbulent ceiling type diffusers with low or high exhausts (mixing type ventilation). There is need to consider other ventilation systems such as natural, hybrid, or even variations of a single ventilation system (diffuser/exhaust type and position).

9.6 Effect of occupancy on aerosol transport

The effect of occupancy on ventilation of health care functional spaces has not been researched in detail. Occupancy affects the airflow distribution, and therefore, the airborne infection risk significantly. The occupational density of people and also their location in a room relative to the room's interior decoration, diffuser, and exhaust can either reduce or increase airborne infection risk. People, introduce thermal plumes in the ventilation space, and if thermal plumes in a room increase flow circulation and mixing, it will increase the airborne infection risk. In addition, the motion of people, and associated functions such as opening doors or windows, alter the ventilation flow pattern in a room. Such effects must carefully be experimented or modeled to arrive at occupation-specific recommendations in health care ventilation design.

9.7 Prediction of airflow and contaminant distribution

The room airflow distribution can have a major impact on infectious aerosol concentration beyond the simple effect of increased ventilation rate. Computational Fluid Dynamics (CFD) simulations are used to predict the airflow distribution and contaminant dispersion by modeling, but there are many improvements to be made in the simulation methods when injections and discrete phase transport within ventilation domain are considered.

One limiting factor in predicting the airflow distribution in ventilated space is related to air turbulence. Current economic turbulence models, such as Reynolds Averaged Navier-Stokes (RANS), predict some qualitative aspects of airflow in the ventilated space but fail to resolve dispersion of injected contaminants, particularly when changes in boundary and initial conditions are subtle. In such cases, more accurate modeling of turbulence is possible only using more computationally intensive models such as Large Eddy Simulation (LES) and Direct Numerical Simulation (DNS). Aerosol transport is particularly affected by larger eddies, flow separations, recirculation behind objects, and anisotropic turbulence, features of the ventilation flow that RANS models cannot predict accurately. With increased computational power and more advanced CFD simulations, the inclusion of more accurate turbulence models in ventilation airflow simulations can predict the chaotic behavior of airflow in greater detail and hence predict airborne infection risk more accurately.

Actual viruses and bacteria are carried by airborne droplets, and discrete phase dispersion models are more appropriate than tracer gas transport models in predicting their concentration within ventilation space. Particular choice of turbulence model affects predictions of discrete phase dispersion as well. Currently, RANS turbulence models are used in combination with stochastic Discrete Random Walk (DRW) dispersion models. Such approach is only useful for limited Reynolds or Grashof numbers and isotropic turbulent flows since only a limited range of eddy length and life times are considered. Ventilation flows containing injections are different, exhibiting a large range of Reynolds or Grashof numbers in anisotropic turbulence conditions. In these types of flows large scale unsteadiness of the flow is crucial in proper dispersion modeling of droplets, a feature that RANS models cannot account for. For more accurate simulations, other dispersion models should be used or developed, and the stochastic DRW models should be improved or at least used with more accurate turbulence models.

Although there are improvements to be made in the simulation methods, the models are extremely sensitive to initial and boundary conditions. Some of this uncertainty is irreducible. For example, people cough or sneeze with unpredictable directions, strengths, and locations. Further, day to day variations in room use and weather conditions introduce additional variations in aerosol transport. This complexity implies the need to simulate a very large number of cases to assess ventilation performance, but fortunately computing power is becoming inexpensive enough to contemplate integrating such simulations into the building design process.

Bibliography

[1] ANSYS FLUENT 12.0 Theory Guide. Technical report, ANSYS, Inc., 2009.

[2] A. A. Aliabadi, K. W. J. Lim, S. N. Rogak, and S. I. Green. Steady and transient droplet dispersion in an air-assist internally mixing cone atomizer. *Atomization and Sprays*, 21(12):1009–1031, 2011.

[3] A. A. Aliabadi and S. N. Rogak. Lagrangian stochastic particle tracking. *Aerosol Science and Technology*, 45(3):313–314, 2011.

[4] A. A. Aliabadi, S. N. Rogak, K. H. Bartlett, and S. I. Green. Preventing airborne disease transmission: Review of methods for ventilation design in health care facilities. *Advances in Preventive Medicine*, Volume 2011, Article ID 124064(doi:10.4061/2011/124064):21, 2011.

[5] A. A. Aliabadi, S. N. Rogak, and S. I. Green. Displacement ventilation performance of a hospital patient recovery room in airborne infection prevention. In *The Tenth International Conference on Industrial Ventilation*, 2012.

[6] A. A. Aliabadi, S. N. Rogak, S. I. Green, and K. H. Bartlett. CFD simulation of human coughs and sneezes: a study in droplet dispersion, heat, and mass transfer. *Proceedings of ASME International Mechanical Engineering Congress & Exposition*, pages IMECE2010–37331, November 12-18 2010.

[7] C. Arcoumanis and M. Gavaises. Linking nozzle flow with spray characteristics in a diesel fuel injection system. *Atomization and Sprays*, 8:307–347, 1998.

[8] ASHRAE. Fundamentals handbook. Technical report, American Society of Heating, Refrigerating, and Air-Conditioning Engineers, Inc., 2001.

[9] ASHRAE. Thermal environmental conditions for human occupancy. Technical Report ANSI/ASHRAE 55-2004, American Society of Heating, Refrigerating, and Air-Conditioning Engineers, Inc., 2004.

[10] ASHRAE. Ventilation of health care facilities. Technical Report BSR/ASHRAE/ASHE Standard 170-2008, American Society of Heating, Refrigerating, and Air-Conditioning Engineers, Inc., 2008.

[11] J. Atkinson, Y. Chartier, C. L. Pessoa-Silva, P. Jensen, Y. Li, and W. H. Seto. Natural ventilation for infection control in healthcare settings. Technical report, World Health Organization (WHO) Publications/Guidelines, 2009.

[12] I. Balásházy, T. B. Martonen, and W. Hofmann. Simultaneous sedimentation and impaction of aerosols in two-dimensional channel bends. *Aerosol Science and Technology*, 13:20–34, 1990.

[13] C. B. Beggs. The airborne transmission of infection in hospital buildings: fact or fiction? *Indoor and Built Environment*, 12:9–18, 2003.

[14] C. Béghein, Y. Jiang, and Q. Y. Chen. Using large eddy simulation to study particle motions in a room. *Indoor Air*, 15:281–290, 2005.

[15] CDC. Guidelines for environmental infection control in health-care facilities. Technical Report 52(RR-10), United States Centers for Disease Control and Prevention, 2003.

[16] C. Y. H. Chao, M. P. Wan, L. Morawska, G. R. Johnson, Z. D. Ristovski, M. Hargreaves, K. Mengersen, S. Corbett, Y. Li, X. Xie, and D. Katoshevski. Characterization of expiration air jets and droplet size distributions immediately at the mouth opening. *Journal of Aerosol Science*, 40(2):122–133, 2009.

[17] S. C. Chen, C. P. Chio, L. J. Jou, and C. M. Liao. Viral kinetics and exhaled droplet size affect indoor transmission dynamics of influenza infection. *Indoor Air*, 19:401–413, 2009.

[18] Stephen E. Chick, James S. Koopman, Sada Soorapanth, and Mary E. Brown. Infection transmission system models for microbial risk assessment. *Science of the Total Environment*, 274(1-3):197–207, 2001.

[19] K. C. Chung and S. P. Hsu. Effect of ventilation pattern on room air and contaminant distribution. *Building and Environment*, 36:989–998, 2001.

[20] E. C. Cole and C. E. Cook. Characterization of infectious aerosols in health care facilities: an aid to effective engineering controls and preventive strategies. *American Journal of Infection Control*, 26(4):453–464, 1998.

[21] C. S. Cox. Inactivation kinetics of some microorganisms subjected to a variety of stresses. *Applied And Environmental Microbiology*, 31(6):836–846, 1976.

[22] C. S. Cox. *The Aerobiological Pathway of Microorganisms*. John Wiley & Sons Ltd., Great Britain, 1987.

[23] C. S. Cox. Airborne bacteria and viruses. *Science Progress*, 73(292):469–500, 1989.

[24] C. S. Cox, S. J. Gagen, and J. Baxter. Aerosol survival of serratia-marcescens as a function of oxygen concentration, relative humidity, and time. *Canadian Journal of Microbiology*, 20(11):1529–1534, 1974.

[25] CSA. Special requirements for heating, ventilation, and air-conditioning (hvac) systems in health care facilities. Technical Report CAN/CSA−Z317.2−10, Canadian Standards Association (CSA), 2010.

[26] P. A. Davidson. *Turbulence: an introduction for scientists and engineers*. Oxford University Press, Great Clarendon Street, Oxford OX 2 6DP, 2004.

[27] M. de Vega, P. Rodríguez, and A. Lecuona. Mean structure and droplet behavior in a coaxial airblast atomized spray: Self-similarity and velocity decay functions. *Atomization and Sprays*, 10:603–626, 2000.

[28] M. Deevy, Y. Sinai, P. Everitt, L. Voigt, and N. Gobeau. Modelling the effect of an occupant on displacement ventilation with computational fluid dynamics. *Energy and Buildings*, 40(3):255–264, 2008.

[29] J. P. Duguid. The size and duration of air carriage of respiratory droplets and droplet nuclei. *The Journal of Hygiene*, 44:471–479, 1946.

[30] R. M. Effros, K. W. Hoagland, M. Bosbous, D. Castillo, B. Foss, M. Dunning, M. Gare, W. Lin, and F. Sun. Dilution of respiratory solutes in exhaled condensates. *American Journal of Respiratory and Critical Care Medicine*, 165(5):663–669, 2002.

[31] C. Engelbert, Y. Hardalupas, and J. H. Whitelaw. Breakup phenomena in coaxial airblast atomizers. *Proc. R. Soc. Lond. A*, 451:189–229, 1995.

[32] H. Eroglu and N. Chigier. Initial drop size and velocity distributions for airblast coaxial atomizers. *Journal of Fluids Engineering*, 113:453–459, 1991.

[33] A. R. Escombe, C. C. Oeser, R. H. Gilman, M. Navincopa, E. Ticona, W. Pan, C. Martinez, J. Chacaltana, R. Rodriguez, D. A. J. Moore, J. S. Friedland, and C. A. Evans. Natural ventilation for the prevention of airborne contagion. *PLoS Medicine*, 4(2):0309–0316, 2007.

[34] C. I. Fairchild and J. F. Stamper. Particle concentration in exhaled breath. *American Industrial Hygiene Association Journal*, 48:948–949, 1987.

[35] N. Frössling. On the evaporation of drops. *Geophys.*, 52:170–216, 1938.

[36] N. Gao and J. Niu. Transient CFD simulation of the respiration process and inter-person exposure assessment. *Building and Environment*, 41:1214–1222, 2005.

[37] R. J. Goodlow and F. A. Leonard. Viability and infectivity of microorganisms in experimental airborne infection. *Bacteriological Reviews*, 25(3):182–187, 1961.

[38] D. I. Graham and P. W. James. Turbulent dispersion of particles using eddy interaction models. *International Journal of Multiphase Flow*, 22(1):157–175, 1996.

[39] J. K. Gupta, C. H. Lin, and Q. Y. Chen. Flow dynamics and characterization of a cough. *Indoor Air*, 19:517–525, 2009.

[40] C. N. Haas. Estimation of risk due to low doses of microorganisms: a comparison of alternative methodologies. *American Journal of Epidemiology*, 118:573–582, 1983.

[41] C. B. Hall, R. G. Douglas, J. M. Geiman, and M. P. Meagher. Viral shedding patterns of children with influenza B infection. *The Journal of Infectious Diseases*, 140(4):610–613, 1979.

[42] Y. Hardalupas, A. M. K. P. Taylor, and J. H. Whitelaw. Velocity and particle-flux characteristics of turbulent particle-laden jets. *Proceedings of Royal Society of London A*, 426:31–78, 1989.

[43] Y. Hardalupas and J. H. Whitelaw. Characteristics of sprays produced by coaxial airblast atomizers. *Journal of Propulsion and Power*, 10(4):453–459, 1994.

[44] J. F. Heidelberg, M. Shahamat, M. Levin, I. Rahman, G. Stelma, C. Grim, and R. R. Colwell. Effect of aerosolization on culturability and viability of Gram-negative bacteria. *Applied and Environmental Microbiology*, 63(9):3585–3588, 1997.

[45] J. Heyder, J. Gebhardt, G. Rudolf, C. F. Schiller, and W. Stahlhofen. Deposition of particles in the human respiratory tract in the size range $0.005-15\ \mu m$. *Journal of Aerosol Science*, 17(5):811–825, 1986.

[46] J. P. Holman. *Heat transfer*. McGraw-Hill Book Co., New York, sixth edition, 1986.

[47] P. Höppe. Temperatures of expired air under varying climatic conditions. *International Journal of Biometeorology*, 25(2):127–132, 1981.

[48] C. J. Hurst. *Modeling the environmental fate of microorganisms*. American Society for Microbiology, Washington, DC, 1991.

[49] H. J. Hussein, S. P. Capp, and W. K. George. Velocity measurements in a high-reynolds-number, momentum-conserving, axisymmetric, turbulent jet. *Journal of Fluid Mechanics*, 258:31–75, 1994.

[50] M. K. Ijaz, Y. G. Karim, S. A. Sattar, and C. M. Johnson-Lussenburg. Development of methods to study the survival of airborne viruses. *Journal of Virological Methods*, 18:87–106, 1987.

[51] M. W. Jennison. The dynamics of sneezing - studies by high-speed photography. *The Scientific Monthly*, 52(1):24–33, 1941.

[52] J. J. Karl, D. Huilier, and B. Henri. Mean behavior of a coaxial air-blast atomized spray in a co-flowing air stream. *Atomization and Sprays*, 6:409–433, 1996.

[53] I. M. Kennedy and M. H. Moody. Particle dispersion in a turbulent round jet. *Experimental Thermal and Fluid Science*, 18:11–26, 1998.

[54] H. Kouros, R. Medina, and H. Johari. Spreading rate of an unsteady turbulent jet. *AIAA J.*, 31:1524–1526, 1993.

[55] W. J. Kowalski and W. Bahnfleth. Airborne respiratory diseases and mechanical systems for control of microbes. *HPAC Heating, Piping, Air Conditioning*, 70(7):11, 1998.

[56] P. Kumar, P. Fennell, J. Symonds, and R. Britter. Treatment of losses of ultrafine aerosol particles in long sampling tubes during ambient measurements. *Atmospheric Environment*, 42:8819–8826, 2008.

[57] F. Z. Lahbabi, J. Botee, H. J. Nuglisch, and G. Charnay. Analysis of starting and steady turbulent jets by image processing techniques. *Experimental and Numerical Flow Visualization, ASME Fluids Engineering Division*, 172:315–321, 1993.

[58] A. C. K. Lai and Y. C. Cheng. Study of expiratory droplet dispersion and transport using a new eulerian modeling approach. *Atmospheric Environment*, 41:7473–7484, 2007.

[59] J. C. Lasheras, E. Villermaux, and E. J. Hopfinger. Break-up and atomization of a round water jet by a high-speed annular air jet. *Journal of Fluid Mechanics*, 357:351–379, 1998.

[60] K. Lee, Z. Jiang, and Q. Chen. Air distribution effectiveness with stratified air distribution systems. *ASHRAE Transactions*, 115 Part 2:322–333, 2009.

[61] K. Lee, T. Zhang, Z. Jiang, and Q. Chen. Comparison of airflow and contaminant distributions inrooms with traditional displacement ventilation and under-floor air distribution systems (RP-1373). *ASHRAE Transactions*, 115 Part 2:306–321, 2009.

[62] L. K. B. Li, D. M. Dressler, S. I. Green, and M. H. Davy. Experiments on air-blast atomization of viscoelastic liquids, part 1: quiescent conditions. *Atomization and Sprays*, 19(2):1–34, 2009.

[63] H. Lomax, T. H. Pulliam, and D. W. Zingg. *Fundamentals of Computational Fluid Dynamics*. Springer-Verlag Berlin Heidelberg, Germany, 2001.

[64] R. G. Loudon and R. M. Roberts. Relation between the airborne diameters of respiratory droplets and the diameter of the stains left after recovery. *Nature*, 213:95–96, 1967.

[65] S. Mazumdar, Y. Yin, A. Guity, P. Marmion, B. Gulick, and Q. Chen. Impact of moving objects on contaminant concentration distributions in an inpatient ward with displacement ventilation. *HVAC and R Research*, 16(5):545–563, 2010.

[66] F. D. McCool. Global physiology and pathophysiology of cough: ACCP evidence-based clinical practice guidelines. *American College of Chest Physicians*, 129:48S–53S, 2006.

[67] E. R. McFadden, B. M. Pichurko, and H. Frederick Bowman. Thermal mapping of the airways in humans. *Journal of Applied Physiology*, 58(2):564–570, 1985.

[68] F. Memarzadeh and A. P. Manning. Thermal comfort, uniformity, and ventilation effectiveness in patient rooms: Performance assessment using ventilation indices. *ASHRAE Transactions*, 106, June 25 - 28 2000.

[69] L. Morawska. Droplet fate in indoor environments, or can we prevent the spread of infection? *Indoor Air*, 16:335–347, 2006.

[70] M. Nicas and A. Hubbard. A risk analysis for airborne pathogens with low infectious doses: application to respirator selection against *Coccidioides immitis* spores. *Risk Analysis*, 22:1153–1163, 2002.

[71] M. Nicas, W. Nazaroff, and A. Hubbard. Toward understanding the risk of secondary airborne infection: Emission of respirable pathogens. *Journal of Occupational and Environmental Hygiene*, 2(3):143, 2005.

[72] J. J. Nijdam, T. A. G. Langrish, and D. F. Fletcher. Assessment of an Eulerian CFD model for prediction of dilute droplet dispersion in a turbulent jet. *Applied Mathematical Modelling*, 32:2686–2705, 2008.

[73] T. Nishino. Physiological and pathophysiological implications of upper airway reflexes in humans. *Japanese Journal of Physiology*, 50:3–14, 2000.

[74] C. J. Noakes, C. B. Beggs, P. A. Sleigh, and K. G. Kerr. Modelling the transmission of airborne infections in enclosed spaces. *Epidemiology and Infection*, 134:1082–1091, 2006.

[75] C. J. Noakes and P. A. Sleigh. Mathematical models for assessing the role of airflow on the risk of airborne infection in hospital wards. *Journal of the Royal Society Interface*, 6:S791–S800, 2009.

[76] R. S. Papineni and F. S. Rosenthal. The size distribution of droplets in the exhaled breath of healthy human subjects. *Journal of Aerosol Medicine*, 10(2):105–116, 1997.

[77] R. Peyret. *Handbook of Computational Fluid Mechanics*. Academic Press Limited, USA, 1996.

[78] P. Piirilä and A. R. A. Sovijarvi. Objective assessment of cough. *European Respiratory Journal*, 8:1949–1956, 1995.

[79] S. B. Pope. *Turbulent flows*. Cambridge University Press, Cambridge, New York, 2000.

[80] J. A. Posada, J. Redrow, and I. Celik. A mathematical model for predicting the viability of airborne viruses. *Journal of Virological Methods*, 164:88–95, 2010.

[81] H. Qian, Y. Li, P. V. Nielsen, and X. Huang. Spatial distribution of infection risk of SARS transmission in a hospital ward. *Building and Environment*, 44:1651–1658, 2009.

[82] H. Qian, Y. Li, P. V. Nielsen, and C. E. Hyldgaard. Dispersion of exhalation pollutants in a two-bed hospital ward with a downward ventilation system. *Building and Environment*, 43(3):344–354, 2008.

[83] W. E. Ranz and W. R. Marshall. Evaporation from drops, part I. *Chemical Engineering Progress*, 48(3):141–146, 1952.

[84] W. E. Ranz and W. R. Marshall. Evaporation from drops, part II. *Chemical Engineering Progress*, 48(4):173–180, 1952.

[85] J. Richmond-Bryant. Transport of exhaled particulate matter in airborne infection isolation rooms. *Building and Environment*, 44:44–55, 2008.

[86] E. C. Riley, G. Murphy, and R. L. Riley. Airborne spread of measles in a suburban elementary school. *American Journal of Epidemiology*, 107:421–432, 1978.

[87] N. K. Rizk and A. H. Lefebvre. Spray characteristics of plain-jet airblast atomizers. *Trans. ASME J. Eng. Gas Turbines Power*, 106:639–644, 1984.

[88] W. Rizk. Experimental studies of the mixing process and flow configurations in two-cycle engine scavenging. *Proceedings of the Institution of Mechanical Engineering, Series E*, 172:417–424, 1958.

[89] A. Rizkalla and A. H. Lefebvre. The influence of air and liquid properties on air blast atomization. *ASME Journal of Fluids Engineering*, 97(3):316–320, 1975.

[90] L. S. Ruzer and N. H. Harley. *Aerosols Handbook*. CRC Press, United States of America, 2005.

[91] T. Sakai, M. Kito, M. Saito, and T. Kanbe. Characteristics of internal mixing twin-fluid atomizer. *Proceedings of the 3rd International Conference on Liquid Atomization and Sprays*, pages 235–241, 1978.

[92] R. Sangras, O. C. Kwon, and G. M. Faeth. Self-preserving properties of unsteady round nonbuoyant turbulent starting jets and puffs in still fluids. *Journal of Heat Transfer*, 124(3):460–469, 2002.

[93] J. H. Seinfeld and S. N. Pandis. *Atmospheric chemistry and physics - from air pollution to climate change*. John Wiley & Sons, New Jersey, second edition, 2006.

[94] H. Shi and C. Kleinstreuer. Simulation and analysis of high-speed droplet spray dynamics. *Journal of Fluids Engineering*, 129:621–633, 2007.

[95] C. A. Short and S. Al-Maiyah. Design strategy for low-energy ventilation and cooling of hospitals. *Building Research and Information*, 37(3):264–292, 2009.

[96] N. I. Stilianakis and Y. Drossinos. Dynamics of infection disease transmission by inhalable respiratory droplets. *Journal of the Royal Society Interface*, doi:10.1098(rsif.2010.0026):1–12, 2010.

[97] G. N. Sze-To and C. Y. H. Chao. Review and comparison between the Wells-Riley and dose-response approaches to risk assessment of infectious respiratory diseases. *Indoor Air*, 20:2–16, 2010.

[98] G. N. Sze-To, M. P. Wan, C. Y. H. Chao, F. Wei, S. C. T. Yu, and J. K. C. Kwan. A methodology for estimating airborne virus exposures in indoor environments using the spatial distribution of expiratory aerosols and virus viability characteristics. *Indoor Air*, 18:425–438, 2008.

[99] J. W. Tang, Y. Li, I. Eames, P. K. S. Chan, and G. L. Ridgeway. Factors involved in the aerosol transmission of infection and control of ventilation in healthcare premises. *Journal of Hospital Infection*, 64:100–114, 2006.

[100] J. W. Tang, T. J. Liebner, B. A. Craven, and G. S. Settles. A schlieren optical study of the human cough with and without wearing masks for aerosol infection control. *J. R. Soc. Interface*, 6:S727–S736, 2009.

[101] R. Tellier. Aerosol transmission of influenza A virus; a review of new studies. *Journal of Royal Society Interface*, 6:S783–S790, 2009.

[102] Z. F. Tian, J. Y. Tu, and G. H. Yeoh. CFD studies of indoor airflow and contaminant particle transportation. *Particulate Science and Technology*, 25(6):555–570, 2007.

[103] P. Tibaut, B. Basara, and H. Shu. Advanced turbulence models for indoor thermal comfort simulation - operating room. In *The Fourth International Symposium on HVAC*, 2003.

[104] C. M. Varga, J. C. Lasheras, and E. J. Hopfinger. Initial breakup of a small-diameter liquid jet by a high-speed gas stream. *Journal of Fluid Mechanics*, 497:405–434, 2003.

[105] M. P. Wan, C. Y. H. Chao, Y. D. Ng, G. N. Sze-To, and W. C. Yu. Dispersion of expiratory droplets in a general hospital ward with ceiling mixing type mechanical ventilation system. *Aerosol Science and Technology*, 41(3):244–258, 2007.

[106] M. P. Wan, G. N. Sze-To, C. Y. H. Chao, L. Fang, and A. Melikov. Modeling the fate of expiratory aerosols and the associated infection risk in an aircraft cabin environment. *Aerosol Science and Technology*, 43:322–343, 2009.

[107] M. R. Wells and D. E. Stock. The effects of crossing trajectories on the dispersion of particles in a turbulent flow. *Journal of Fluid Mechanics*, 136:31, 1983.

[108] WHO. Infection prevention and control of epidemic- and pandemic-prone acute respiratory diseases in health care - WHO interim guidelines. Technical report, World Health Organization, 2007.

[109] P. O. Witze. Hot-film anemometer measurements in a starting turbulent jet. *AIAA J.*, 21:308–309, 1983.

[110] W. Xu, A. Manning, A. Guity, B. Gulick, P. Marmion, Y. Yin, and Q. Chen. Numerical studies of ventilation systems in a patient room. Technical report, Mentor Graphics Corporation, 2009.

[111] S. Yang, G. W. M. Lee, C. M. Chen, C. C. Wu, and K. P. Yu. The size and concentration of droplets generated by coughing in human subjects. *Journal of Aerosol Medicine*, 20(4):484–494, 2007.

[112] Y. Yin, W. Xu, J. K. Gupta, A. Guity, P. Marmion, A. Manning, B. Gulick, X. Zhang, and Q. Chen. Experimental study on displacement and mixing ventilation systems for a patient ward. *HVAC and R Research*, 15(6):1175–1191, 2009.

[113] I. T. S. Yu, Y. Li, T. W. Wong, W. Tan, A. T. Chan, J. H. W. Lee, D. Y. C. Leung, and T. Ho. Evidence of airborne transmission of the severe acute respiratory syndrome virus. *New England Journal of Medicine*, 350:1731–1739, 2004.

[114] Z. Zhang and Q. Chen. Experimental measurements and numerical simulations of particle transport and distribution in ventilated rooms. *Atmospheric Environment*, 40(18):3396–3408, 2006.

[115] B. Zhao, Z. Zhang, and X. Li. Numerical study of the transport of droplets or particles generated by respiratory system indoors. *Building and Environment*, 40(8):1032–1039, 2005.

[116] S. Zhu, S. Kato, and J. H. Yang. Study on transport characteristics of saliva droplets produced by coughing in a calm indoor environment. *Building and Environment*, 41(12):1691–1702, 2006.

Appendices

Appendix A: Far-field Tests Standard Operating Procedure (SOP)

1. Ensure that the Building Monitoring and Assessment (BMA) laboratory door is open, the storage room door is closed, and the office door is open (The state of the other doors in the BMA area affects steadiness and repeatability of ACH in the test domain).

2. Ensure the static pressure for the underfloor distribution system is set to its maximum value (request that the building operator sets this pressure). This provides a high static pressure (e.g. 200 Pa) for the operation of the diffuser. If possible record the static pressure for the duration of the experiment. If you are using an inline fan, set the speed so that the desired air change rate is maintained.

3. Pick a date and time when the boundary conditions of the room are favorable (i.e. boundary temperatures and exhaust airflow speed). If the boundary conditions are not favorable, wait until a suitable time window is available (Boundary temperatures and exhaust airflow speed must be repeatable and as steady as possible for each group of tests).

4. Record the relative humidity in the room before the experiment.

5. Ensure that the liquid tank has adequate amount of liquid for the duration of the test.

6. Turn on the main valve for the gas supply to the desired pressure (30, 40, or 50 psi).

7. Turn the liquid supply regulator to the maximum pressure.

8. Turn on the supply gas heater to 15 % power at least one hour before starting the experiments. (Caution: increasing the power carelessly poses a local burn damage on the supply gas line to the atomizer or

a fire hazard). Touch the insulator foam to make sure it is warm and heating the incoming gas to the experiment.

9. Turn on the manikins at least one hour before starting the experiments.

10. Turn on the power supply for the anemometers to supply 20 V.

11. Ensure the opening under the door is blocked (e.g. with tape or carpet) so that most of the air in the room exits through the exhaust duct.

12. Be careful upon closing the door so that the wiring for anemometer number 2 is not damaged.

13. Ensure the APS sampling line is not bent sharply at any point. Any sharp bend reduces the aerosol collection efficiency of the device.

14. Turn on APS. Turn on the APS pump using the dial and going to the 'menu'.

15. Perform a few injections before recording to make sure that the atomizer is primed.

16. Sample the background air in the room before the experiment to ensure the background concentration level is low (less than $1-2\ pt/cc^3$). This also helps flushing any aerosols left in the sampling tube from the previous experiment.

17. Select the proper sampling line (1, 2, or 3) for the APS measurement. (Preferably perform three sequential sampling for each line so that a sample for each line is obtained at different times during the day. This accounts for slight building boundary condition variations).

18. Make sure the clocks in the data acquisition computers show identical times down to seconds. It is useful to have both of the clocks open on the screen.

19. Start the experiment by collecting data for 10 min. First start the data acquisition for temperature, air speed, and APS, then command the atomizer to inject after 5 s.

20. Ensure the 'online' viewing option of the MSR program is closed when you start recording anemometer data. If this happens, the data will not be stored. It is OK if you view the anemometer data in 'online' mode after the data acquisition has already started.

21. While taking data, monitor anemometer 2 velocity (exhaust airflow speed) so that it does not show large variations. This speed should be within an acceptable range for experiments for a given air changes per hour in the room. If this velocity changes abruptly, repeat the experiment at a different date and time.

22. Before the next experiment, ensure that the background aerosol concentration has reached a low level and the temperature and air speed data have reached steady states.

23. Record the test date, time, and conditions in the experiment logbook.

24. Save the data text files for thermocouples, anemometers, and APS. Only use the date/time format (dd-mm-yyyy-hh-mm.txt).

25. For APS ensure you export data in $dW/dLogD_p$ and also in 'rows'.

26. After performing the experiments for the day, turn off the main gas supply valve and the APS.

27. Turn off the power supply to the anemometers.

28. Turn off the gas heater power.

29. If it is desired to continue testing to the next day, it is optional to keep the manikin and gas heater power on. (Usually thermal response time of the room takes about an hour and keeping the manikin and heater on will help saving time for the next experiment).

Appendix B: MATLAB image processing algorithm

- Set the image intensity threshold to 0.2 (tuned to detect the spray and output a binary image).
- Set the noise removal constant to 5 (tuned to remove hot pixel noise on the CCD sensor).
- Define the number of pixels in the image per unit length.
- Read 10 images for each time delay in MATLAB using the *imread*() command.
- Convert the images to the binary format using the image intensity threshold and the *im*2*bw*() command. Any pixel with an intensity greater than threshold is assigned an intensity of 1, or otherwise an intensity of 0.
- Filter the binary images for noise using the noise removal constant and the *medfilt*2() command. This command performs median filtering of an image matrix in two dimensions. Each output pixel contains the median value in a neighborhood around the corresponding pixel which is as large as the noise removal constant in length.
- Visually inspect the 10 pictures and crop the spray, which appears as a white region, using the *imcrop* command in each image. This command allows the user to draw a box around the edges of the spray and to store the box width and length in memory in pixels.
- Convert the box dimensions from pixels to meters.
- Calculate the mean and standard deviation for the box dimensions using the data for the 10 images for the same time delay.

Appendix C: Room boundary and internal temperatures over 24 hours

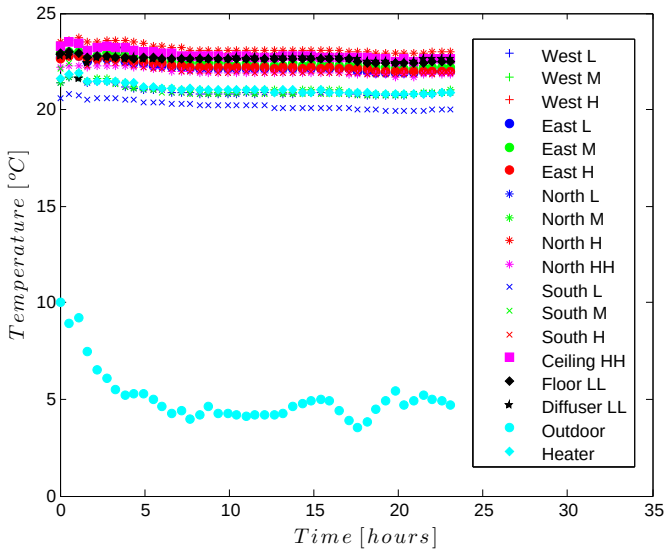

Figure 9.1: Room boundary temperature over 24 hours (Horizontal axis shows time from 3 *pm* to 2:59 *pm*)

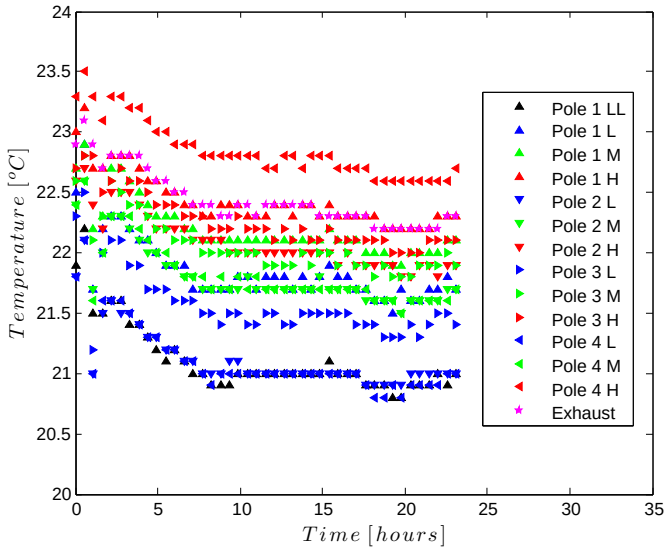

Figure 9.2: Room internal temperature over 24 hours (Horizontal axis shows time from 3 *pm* to 2:59 *pm*)

Appendix D: Room boundary and internal conditions for reference case (1)

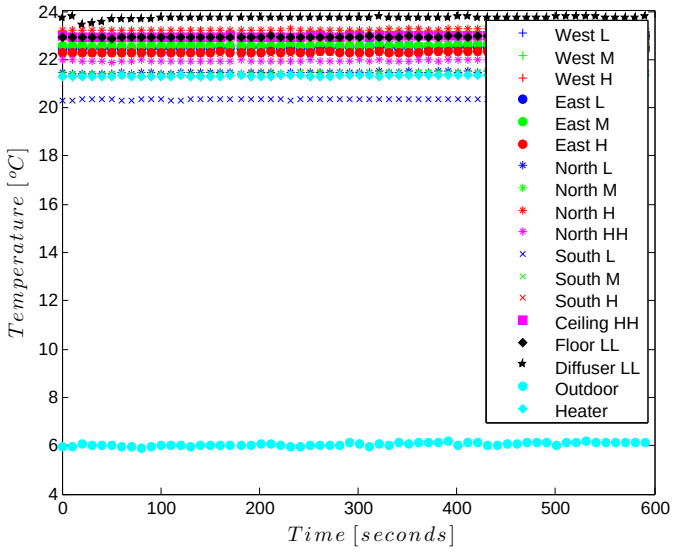

Figure 9.3: Reference case (1) boundary temperatures

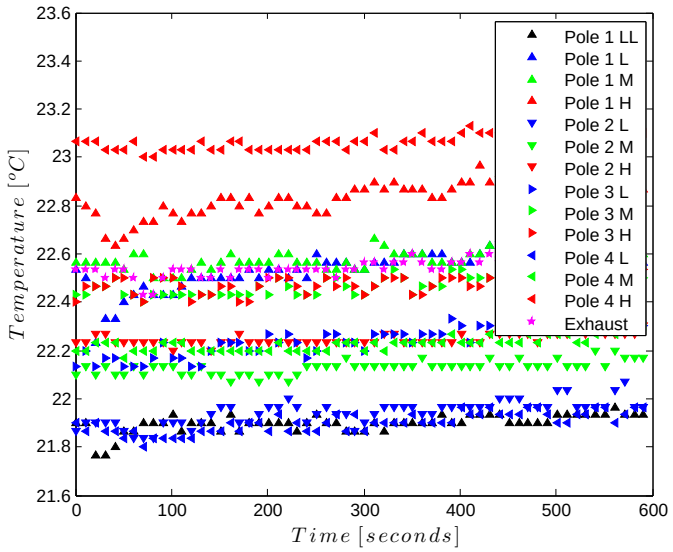

Figure 9.4: Reference case (1) internal temperatures

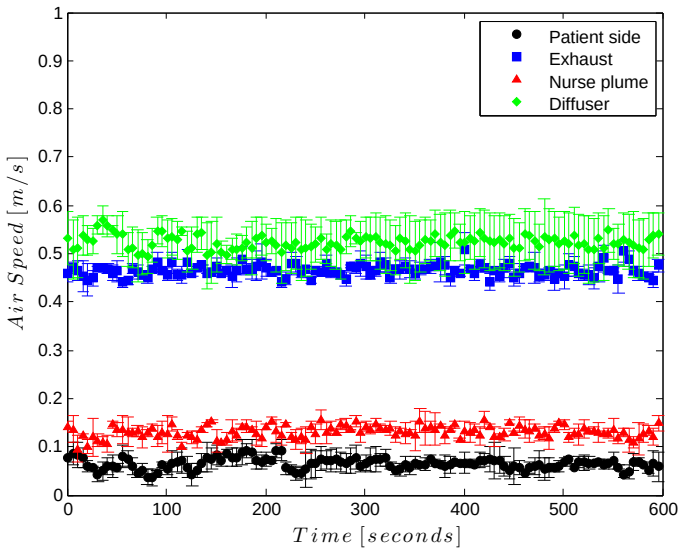

Figure 9.5: Reference case (1) internal air speed in the room

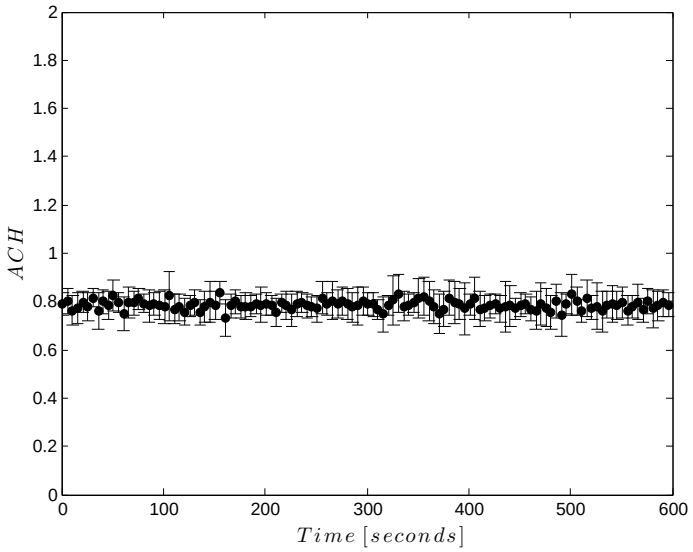

Figure 9.6: Reference case (1) room air changes per hour

Appendix E: Further information

This thesis is registered with Collections Canada and assigned the $ISBN$: $978-0-9809704-6-3$ for the Library and Archives of Canada. For more information regarding the author's other scientific contributions and mission statements please visit the website:

`http://www.aaa-scientists.com`